UNIVERSITÀ
DEGLI STUDI
DI PADOVA

Sede Amministrativa: Università degli Studi di Padova

Dipartimento di Scienze Chimiche

SCUOLA DI DOTTORATO IN SCIENZE MOLECOLARI

INDIRIZZO: SCIENZE CHIMICHE

XXII CICLO

Role and Effective Treatment of Dispersive Forces in Materials

Direttore della Scuola: Chiar.mo Prof. Maurizio Casarin

Coordinatore d'indirizzo: Chiar.mo Prof. Maurizio Casarin

Supervisore: Chiar.mo Prof. Maurizio Casarin

Dottorando: Daniel Forrer

Universa Universis Patavina Libertas

Abstract

In questa tesi è presentata un'indagine computazionale basata sulla Teoria del Funzionale Densità (DFT), eseguita su un ampio range di sistemi che spazia da molecole a polimeri cristallini, grafite, fasi auto-organizzate di molecole organiche su supporti metallici e piccole molecole assorbite in materiali porosi a base organica-inorganica.

Combinando le informazioni ottenute per mezzo di metodi computazionali con i risultati sperimentali, prevalentemente di microscopia a scansione ad effetto tunnel, è stato possibile descrivere il comportamento elettronico e strutturale di tali sistemi e raggiungere una compresione dettagliata del loro comportamento chimico-fisico. Grazie all'implementazione di uno schema correttivo per l'inclusione delle forze di dispersione nella DFT, sono stati effettuati calcoli accurati su sistemi altrimenti inaccessibili, pur contendo lo sforzo computazionale. Questo ha permesso, ad esempio, di capire il ruolo giocato dal ricoprimento della superficie nella transizione di fase osservata per le ftalocianine di ferro depositate su Ag(110) e di modellare con successo l'assorbimento di H_2O in un polimero di Cu(II) bispirazolato.

Abstract

DFT and DFT-D calculations have been carried out on several chemical systems, ranging from molecules to crystalline polymers, bulk graphite, self-assembled phases of large molecules on metal surfaces and small molecules absorbed in porous organic-inorganic materials.

Joining insights from calculations with experimental outcomes, the structural and electronic behavior of complex chemical systems have been described and explained, allowing a deeper understanding of the studied phenomena. Thanks to the implementation of a correction scheme to DFT, allowing the effective treatment of dispersion forces in materials, accurate calculations on previously unaffordable problems have been performed at a reasonable computational effort. This allowed, e.g., to understand the coverage-dependent phase transition of iron phthalocyanine on Ag(110) and the successful modeling of water absorption in a bispyrazolato copper(II) polymer.

Preface

The development of effective and accurate computational tools provides invaluable benefits to the quest for new materials. Indeed, the ability to describe at the atomistic scale the quantum mechanical behavior of interacting nuclei and electrons gives to material scientists the chance of validating ambiguous data from in vitro experiments, and it could also drive the design of new systems with tailored functions. Therefore, at the forefront of current research in theoretical and computational chemistry there is a great effort to increase the accuracy and reliability of available methods. In this respect, a considerable success has been achieved in the last decades by implementations of the density functional theory (DFT).[1, 2] However, the exact form of the electron density functional is still unknown, and there are many cases where the physics of the investigated system is badly described by currently available approximated density functionals. Van der Waals (VdW) interactions, also referred to as dispersion forces, represent an important case of failure of commonly exploited local and semilocal density functionals.[3] VdW forces between two atoms or two molecules arise from the interaction of instant induced dipole moments, because of the fluctuation of electron densities. Despite being usually referred to as 'weak force', dispersion plays a pivotal role in many relevant physicochemical processes.[4] In particular, great attention is devoted to their ability to drive the self-assembly of aromatic molecules to produce three-dimensional lattices or two-dimensional networks supported by surfaces.

Self-assembling techniques allows the production of supramolecular assemblies of macroscopic extent of nanoscale regularity and eligible to be employed

for the manufacturing of new, high-efficiency, materials for light harvesting, energy conversion, thin-film transistors, non-linear optical devices and sensors. For instance, the possibility of obtaining electron donor-acceptor systems that couple macrocyclic dyes with C_{60} is currently explored with the aim of obtaining highly efficient photovoltaic devices and artificial light harvesting systems. Almost all of the applications mentioned above require a certain degree of molecular ordering at an interface, and therefore a detailed understanding of the interface formation and of its electronic properties at the molecular level is required. An other attractive field is the design of porous materials based on molecular frameworks for gas storage application. This crystal engineering process is, however, hampered by the natural tendency of molecular systems to pack as close as possible, intrinsically limiting the number of porous compounds. In this context, a promising class of materials is represented by systems which are able to reversibly change their crystal structure in the presence of guest molecules in such a way as to create otherwise absent pores. This property is achieved thanks to the presence of a network of non-covalent bonding interactions that can be easily broken to promote a structural reorganization of the components, allowing thus the hosting of small molecules, which, in turn, interacts with the hosting materials through non-covalent interactions, conferring reversibility to the absorption.

Although self-assembly is a promising tool, improvements on the control on the growth of supramolecular structures are highly desirable. In this context, computational chemistry methods can be exploited to improve our knowledge of self-assembled properties of molecules and develop a rational approach to the design of new materials.

The correct accounting of non-covalent interactions is crucial for an accurate theoretical description of these systems. However, VdW forces are non-classical and nonlocal interactions that need a proper treatment of electronic dynamic correlation. This could be achieved by the so-called post Hartree-Fock (post-HF) methods, in particular by the many-body perturbation theory and coupled cluster approaches.[5] The 'chemical accuracy' of post-HF methods

is unfortunately balanced by demanding computational burden, which practically limits their use to small molecular systems. On this basis, it would be extremely convenient to include an effective description of dispersion forces within the framework of DFT. Indeed, this goal is currently being pursued by many groups working in the research field of VdW complexes, see refs. [6] and [7] for recent reviews of the proposed solutions. A particularly effective and computationally convenient scheme to include dispersion has been achieved by adding a semiempirical correction term to the Kohn-Sham energy functional. [8]

Contents

Chapter 1

Theory of electronic structure

Most of the properties of systems studied by chemists are intimately related to the behavior of electrons. In the present chapter, the elementary theory of electrons in atoms, molecules and solids is presented. Particular attention is paid to the Density Functional Theory, on which the most widespread used computational tools are based.

1.1 Introduction

Quantum Chemistry aims to study the behavior of electrons in atoms, molecules and materials. In this habit, electrons are typically described through their wavefunction Ψ, which is a solution to the Schrödinger's equation:

$$-i\hbar\frac{\partial\Psi}{\partial t} = \hat{H}\Psi, \tag{1.1.1}$$

where $\hat{H}$ is the Hamiltonian of the system. When $\hat{H}$ does not depend explicitly by the time, it coincides with the energy operator:

$$\hat{H}\Psi_i = \varepsilon_i \cdot \Psi_i, \tag{1.1.2}$$

where the eigenvalue ε_i is the energy associated to the i-th eigenstate Ψ_i of the chemical system. It should be pointed out that the eigenstates Ψ_i of the Hamiltonian are orthogonal by definition and form a complete basis set in the Hilbert space of the system.

The wavefunction itself have an obscure physical meaning, but its square modulus is related to the electron density ρ by the

$$\rho(\mathbf{r}) = N \int d\mathbf{r}_2 d\mathbf{r}_3 \cdots d\mathbf{r}_N |\Psi(\mathbf{r}_1, \mathbf{r}_2, \mathbf{r}_3, \cdots, \mathbf{r}_N)|^2. \tag{1.1.3}$$

In fact, for the 1.1.3 to be valid, wave functions are required to be normalized accordingly to:

$$\langle \Psi_i | \Psi_j \rangle = \delta_{ij}, \tag{1.1.4}$$

to let the electron density ρ to integrate to the total number of electrons N.

$$\int \rho(\mathbf{r}) d\mathbf{r} = N. \tag{1.1.5}$$

In the non relativistic framework, the Hamiltonian $\hat{H}$ of a chemical system composed by M nuclei and N electrons is written as:

$$\hat{H} = -\sum_{p=1}^{M} \frac{1}{2m_p} \nabla_p^2 - \sum_{i=1}^{N} \frac{1}{2} \nabla_i^2 + \sum_{p<q}^{M,M} \frac{Z_p Z_q}{R_{pq}} + \sum_{i<j}^{N,N} \frac{1}{r_{ij}} - \sum_{p,i}^{M,N} \frac{Z_p}{r_{ip}}. \tag{1.1.6}$$

though, for most chemical applications, the electronic and the nuclear motions can be decoupled so that the Hamiltonian is separable in a nuclear plus an electronic term. This is known as the *Born-Oppenheimer approximation* [9]. Within this approximation, the electronic term, hereafter called simply $\hat{H}$, becomes:

$$\hat{H} = -\sum_{i=1}^{N} \frac{1}{2} \hat{\nabla}_i^2 + \sum_{i<j}^{N,N} \frac{1}{r_{ij}} + \sum_{p,i}^{M,N} \frac{Z_p}{r_{ip}}, \tag{1.1.7}$$

where nuclear coordinates are treated as parameters.

Looking at the 1.1.7, it can be seen that the actual system of interest is involved in the Hamiltonian only through the position and the nature of its nuclei and the total number of electrons N. Indeed, the Hamiltonian presents a finite amount of singularities for $|\mathbf{R}_p - \mathbf{r}_i| = 0$, i.e. when the electron approaches that nucleus. The latter causes a cusp to appear in the electron density 1.1.3 just at the position of each nucleus. Interestingly, the shape of the cusp is related to the atomic number of the underlying atom by the limit:

$$\lim_{r_{ip} \to 0} \left[\frac{\partial}{\partial r} + 2Z_p \right] \overline{\rho}(\mathbf{r}) = 0, \tag{1.1.8}$$

where $\overline{\rho}(\mathbf{r})$ is the spherical average of $\rho(\mathbf{r})$. This means that the electron density defines both the position of the nuclei and their kind. Thus, the 1.1.8 with the normalization condition 1.1.5 completely defines the Hamiltonian of the chemical system.

1.2 Density Functional Theory

In the first section, some hints of the Density Functional Theory (DFT) has been reported. Here, the basis of DFT are presented in a more systematic way. The kernel of modern DFT is rather recent and is due to P. Hohenberg and W. Kohn, who enunciated their two theorems in 1964 [10].

Let us define the external potential $v(\mathbf{r})$ due to the nuclear charge as:

$$v(\mathbf{r}) = -\sum_{p} \frac{Z_p}{r_{ip}} \tag{1.2.1}$$

The **first theorem** states that *the external potential* $v(\mathbf{r})$ *is determined, within an additive constant, by the electron density* $\rho(\mathbf{r})$. Since ρ integrates to the number of electrons N, it follows that the ground state wave-function and all other electronic properties of the chemical system are uniquely defined by the electron density. Its proof is rather simple: it employes only the minimum-energy principle for the ground-state. Consider the electron density $\rho(\mathbf{r})$ of the non-degenerate ground state of a certain N-electron system, it determines the number of electrons N by simple quadrature 1.1.5. It could be shown that it determines also $v(\mathbf{r})$ and hence all the electronic properties. Assume that there are two external potentials $v(\mathbf{r})$ and $v'(\mathbf{r})$, differing by more than a constant, giving the same ground state density ρ. We would have two different Hamiltonian, $\hat{H}$ and $\hat{H}'$ whose ground state densities are identical, although the ground state wave-functions Ψ and Ψ' would be different. Recalling the minimum-energy principle and taking Ψ' as trial wave function for

the $\hat{H}$ problem we write:

$$\begin{aligned} E_0[\Psi] < \langle \Psi' | \hat{H} | \Psi' \rangle &= \langle \Psi' | \hat{H}' | \Psi' \rangle + \langle \Psi' | \hat{H} - \hat{H}' | \Psi' \rangle \\ &= E_0'[\Psi'] + \int dr \rho(\mathbf{r})[v(\mathbf{r}) - v'(\mathbf{r})]. \end{aligned} \tag{1.2.2}$$

Similarly, taking Ψ as trial function for the $\hat{H}'$ problem

$$\begin{aligned} E_0[\Psi'] < \langle \Psi | \hat{H}' | \Psi \rangle &= \langle \Psi | \hat{H} | \Psi \rangle + \langle \Psi | \hat{H}' - \hat{H} | \Psi \rangle \\ &= E_0[\Psi] - \int dr \rho(\mathbf{r})[v(\mathbf{r}) - v'(\mathbf{r})]. \end{aligned} \tag{1.2.3}$$

By summing 1.2.2 and 1.2.3 we obtain the contradiction $E_0 + E_0' < E_0' + E_0$. This proofs that there are no two distinct external potentials $v(\mathbf{r})$ and $v'(\mathbf{r})$ that give raise to the same electron density $\rho(\mathbf{r})$. The biunique relationship between ρ and v, together with the normalization condition 1.1.5, legitimates the use of the electron density as basic variable, in place of the wave function, and allows to define the total energy as a functional of the electron density ρ:

$$E = E[\rho] = T[\rho] + V_{ee}[\rho] + \int d\mathbf{r} \rho(\mathbf{r}) v(\mathbf{r}) \tag{1.2.4}$$

where the three terms on the right hand are the electron kinetic energy functional, the electron-electron and the nucleus-electron interaction respectively.

The **second theorem** reads: *for any trial density* $\tilde{\rho}(\mathbf{r})$*, such that* $\tilde{\rho}(\mathbf{r}) \geq 0$ *and* $\int d\mathbf{r} \tilde{\rho}(\mathbf{r}) = N$

$$E_0 \leq E[\tilde{\rho}], \tag{1.2.5}$$

providing the energy variational principle. The previous theorem assures that the $\tilde{\rho}$ determines its own external potential $v(\mathbf{r})$ and the wave function $\tilde{\Psi}$, which can be taken as trial function for the problem of interest having external potential $v(\mathbf{r})$, thus

$$\langle \tilde{\Psi} | \hat{H} | \tilde{\Psi} \rangle = F_{HK}[\tilde{\rho}] + \int d\mathbf{r} \tilde{\rho}(\mathbf{r}) v(\mathbf{r}) = E[\tilde{\rho}] \geq E[\rho] = \langle \Psi | \hat{H} | \Psi \rangle. \tag{1.2.6}$$

It is to worth note that the validity of the Hohenberg and Kohn theorems is limited by the fact that the density ρ have to be associated with the antisymmetric ground-state eigenfunction of an Hamiltonian of the form 1.1.7. This is

known as the *v-representability problem*. In fact, the theorems ceases to apply if the density ρ or the trial densities $\tilde{\rho}$ are non-v-representable; moreover, the conditions for an electron density to satisfy this condition are as yet unknown. Fortunately, the fundamentals of DFT can be enunciated in a way that requires the density to satisfy a weaker condition, the N-representability condition. A density ρ is N-representable if it can be obtained from some antisymmetric wave function. The conditions for a density ρ to be N-representable are well known and are satisfied by any reasonable density [11]:

$$\rho(\mathbf{r}) \geq 0, \qquad \int d\mathbf{r}\rho(\mathbf{r}) = N \qquad \text{and} \qquad \int d\mathbf{r}|\nabla\rho(\mathbf{r})^{1/2}|^2 < \infty \tag{1.2.7}$$

Although they are of pivotal importance in the Density Functional Theory, the Hohenberg and Kohn theorems do not provide any operative strategy for whatever application. Indeed, the density functionals representing the kinetic energy and the electron-electron interaction in 1.2.4 are still unknown and the development of approximated forms is an active field of research. The most successful operative DFT scheme is due to Kohn and Sham [12], who developed an ingenious indirect approach to compute the kinetic energy. Kohn and Sham proposed to reintroduce orbitals into the problem such that the kinetic energy can be computed easily to good accuracy.

As shown by Gilbert [11] and by Harriman [13] any nonnegative, continuous and normalized density ρ is N-representable and can be decomposed accordingly to

$$\rho(\mathbf{r}) = \sum_{i}^{N} |\psi_i(\mathbf{r}, s)|^2 \tag{1.2.8}$$

where $\psi_i(\mathbf{r}, s)$ are spin orbitals. Nonetheless, given a ρ, there is not a unique decomposition in terms of orbitals. Kohn and Sham faced this problem by invoking a reference system of *noninteracting* electrons, without any electron-electron repulsion, and for which the ground-state electron density is exacly ρ. For this system the ground-state wave function is exactly known and it corresponds to a single Slater determinant

$$\Psi_S = \frac{1}{\sqrt{N!}} \det[\psi_1\psi_2\cdots\psi_N], \tag{1.2.9}$$

where the ψ_i are the lowest N eigenfunctions of the one-electron Hamiltonian. The kinetic energy of the reference system is then computed as

$$T_S = \sum_i^N \langle \psi_i | -\frac{1}{2}\nabla^2 | \psi_i \rangle. \tag{1.2.10}$$

Although this quantity have the advantage to be defined uniquely for any density, it is still not exact. The difference between the exact kinetic energy T and T_S, presumably fairly small, is included in the exchange-correlation functional (see below).

The Kohn and Sham treatment runs as follows. For a given external potential $v(\mathbf{r})$, orbitals are obtained by solving the N one-electron equations

$$\left[-\frac{1}{2}\nabla^2 + v(\mathbf{r}) + \int d\mathbf{r}' \frac{\rho(\mathbf{r}')}{|\mathbf{r} - \mathbf{r}'|} + v_{xc}(\mathbf{r}) \right] \psi_i = \epsilon_i \psi_i, \tag{1.2.11}$$

where the exchange-correlation potential v_{xc} is defined as

$$v_{xc}(\mathbf{r}) = \frac{\delta E_{xc}[\rho]}{\delta \rho(\mathbf{r})} \tag{1.2.12}$$

and it will be discussed in detail in the following section. Then, the density ρ is computed through equation 1.2.8 and the new density ρ is substituted in 1.2.11 to recompute orbitals. At each step the total energy is given by

$$E = -\frac{1}{2}\sum_i^N \langle \psi_i | \nabla^2 | \psi_i \rangle + \frac{1}{2}\int d\mathbf{r} d\mathbf{r}' \frac{\rho(\mathbf{r})\rho(\mathbf{r}')}{|\mathbf{r} - \mathbf{r}'|} + E_{xc}[\rho] + \int d\mathbf{r} v(\mathbf{r})\rho(\mathbf{r}). \tag{1.2.13}$$

The cycle is repeated until self-consistency is reached.

1.3 Electron exchange and correlation

Thanks to W. Kohn and L. J. Sham the kinetic energy can be computed, the last term of 1.2.4 to be discussed is the electron-electron repulsion V_{ee}. At this step, it is useful to introduce the pair density

$$\rho_2(\mathbf{r}_1, \mathbf{r}_2) = N(N-1) \int d\mathbf{r}_3 d\mathbf{r}_4 \dots d\mathbf{r}_N |\Psi(\mathbf{r}_1, \mathbf{r}_2, \dots, \mathbf{r}_N)|^2, \tag{1.3.1}$$

representing the probability to find two electrons simultaneously within two volume elements $d\mathbf{r}_1$ and $d\mathbf{r}_2$, while the other $N-2$ electrons may be anywhere. If the pair density is known, the electron-electron interaction is promptly available as

$$V_{ee}[\rho_2] = \frac{1}{2}\int d\mathbf{r}_1 d\mathbf{r}_2 \frac{\rho_2(\mathbf{r}_1,\mathbf{r}_2)}{r_{12}}. \tag{1.3.2}$$

The pair density of a N-electron system can be written as product of the single-particle densities accordingly to

$$\rho_2(\mathbf{r}_1,\mathbf{r}_2) = \rho(\mathbf{r}_1)\rho(\mathbf{r}_2)\left[1 + f(\mathbf{r}_1\mathbf{r}_2)\right], \tag{1.3.3}$$

where $f(\mathbf{r}_1\mathbf{r}_2)$ is the correlation function. For $f(\mathbf{r}_1\mathbf{r}_2) = 0$ the 1.3.3 describes the special case of a non-interacting electron system, where the corresponding V_{ee} is reduced to the classical interaction J within the charge cloud

$$J[\rho] = \frac{1}{2}\int d\mathbf{r}_1 d\mathbf{r}_2 \frac{\rho(\mathbf{r}_1)\rho(\mathbf{r}_2)}{r_{12}}. \tag{1.3.4}$$

It is worth to note that, as $f(\mathbf{r}_1\mathbf{r}_2)$ equals zero, $\rho_2(\mathbf{r}_1,\mathbf{r}_2)$ integrates to N^2 rather than $N(N-1)$; this wrong normalization of ρ_2 causes $J[\rho]$ to contain an unphysical self-interaction of the electron with itself. As we shall see, self-interaction is exactly canceled by exchange.

In order to evaluate the non-classical terms of electron-electron interaction, we introduce the conditional probability $\Omega(\mathbf{r}_1,\mathbf{r}_2)$, which measures the probability to find any electron at position $\mathbf{r}_2$ given that there is one other electron already known to be in $\mathbf{r}_1$:

$$\Omega(\mathbf{r}_1,\mathbf{r}_2) = \frac{\rho_2(\mathbf{r}_1,\mathbf{r}_2)}{\rho(\mathbf{r}_1)}. \tag{1.3.5}$$

The difference between the conditional probability Ω and the uncorrelated probability ρ of finding an electron at $\mathbf{r}_2$ describes the change in the former due to the interaction between electrons and is known as *exchange-correlation hole*

$$h_{xc}(\mathbf{r}_1,\mathbf{r}_2) = \frac{\rho_2(\mathbf{r}_1,\mathbf{r}_2)}{\rho(\mathbf{r}_1)} - \rho(\mathbf{r}_2). \tag{1.3.6}$$

Using 1.3.6 the electron-electron interaction 1.3.2 can be rewritten as

$$\begin{aligned} V_{ee} &= \frac{1}{2}\int d\mathbf{r}_1 d\mathbf{r}_2 \frac{\rho(\mathbf{r}_1)\rho(\mathbf{r}_2)}{r_{12}} + \frac{1}{2}\int d\mathbf{r}_1 d\mathbf{r}_2 \frac{\rho(\mathbf{r}_1)h_{xc}(\mathbf{r}_2,\mathbf{r}_2)}{r_{12}} \\ &= J[\rho] + E_{xc}, \end{aligned} \tag{1.3.7}$$

where $J[\rho]$ is the *classical* repulsion 1.3.4 of a charge distribution and E_{xc} is the exchange-correlation energy. E_{xc} can be further split in two terms by parting the exchange-correlation hole in two part: a Fermi hole h_x, and a Coulomb hole h_c. The former incorporates exchange effects, so-called because they arise from the requirement that $|\Psi|^2$ be invariant to the exchange of the space and spin coordinates of any two electrons. The Fermi hole dominates by far h_{xc} and satisfies the important integral condition or *sum rule*

$$\int d\mathbf{r}_2 h_x(\mathbf{r_1},\mathbf{r_2}) = -1, \tag{1.3.8}$$

which means that h_x contains exactly the charge of one electron and this holds for any $\mathbf{r_1}$. Through this removal of one charge, the Fermi hole takes care of the self-interaction problem already discussed for $J[\rho]$. h_x does not only integrates to -1, but also is negative everywhere and then its contribution to the total energy is negative for any density satisfying 1.2.7.

As pointed out above, the Fermi hole is solely due to the Pauli exclusion principle, while the electrostatic repulsion $1/r_{12}$ between electrons is kept into account by the Coulomb hole h_c. Given their nature, h_c is large and negative at the position of the reference electron, where the repulsion takes the other electrons apart, but since its integral over the whole space is zero, it must be also positive in some regions. Although the whole exchange-correlation energy is dominated by the exchange term and then by the Fermi hole h_x, correlation plays an important role in many cases. In particular, the inclusion of dispersion correlation, fundamental for the modeling of soft matter, will be discussed in the following chapter.

Although the exact exchange-correlation functional $E_{xc}[\rho]$ is still unknown, several approximated forms have been developed and are shown to give fairly accurate results on many chemical systems. The quest of finding even better

approximations to E_{xc} is a very active field of research and, as shown above, it is finally the art of approximating the exchange-correlation hole. The better we model h_{xc}, the better is the accuracy reached by the resulting functional. For sake of completeness, it should be noted that the HK theorems holds for the exact exchange-correlation functional, whereas they are not valid for the approximated forms. This means that, strictly speaking, practical approaches to DFT are no longer variational.

Common exchange-correlation functionals could be parted in four main groups, each of them is related to a different level of approximation. The simplest level is the *Local Density Approximation* (LDA) and functionals belonging to this group depends solely by the local value of the electron density $\rho(\mathbf{r})$:

$$E_{xc}^{LDA} = \int d\mathbf{r}\rho(\mathbf{r})\epsilon_{xc}(\rho), \tag{1.3.9}$$

where ϵ_{xc} is the exchange-correlation energy per particle and within LDA it is given by the free-electron-gas formula. The exchange contribution is known after Dirac to be

$$\epsilon_x^{LDA}(\rho) = -\frac{3}{4}\left(\frac{3}{\pi}\right)^{1/3}\rho(\mathbf{r})^{1/3}, \tag{1.3.10}$$

while the analytical form of the correlation term was obtained by Vosko, Wilk and Nusair [14] by interpolating the quantum Monte Carlo results of Ceperley and Alder [15]. Despite the rather crude approximation, LDA was found to work surprisingly good in many cases. An explanation of the unexpected accuracy of LDA is that it satisfies by construction the sum rule 1.3.8.

To go beyond LDA and reach better accuracy, there is the need to account for the inhomogeneity of the electron density. This is done by introducing a correction term depending on the gradient of the charge density. The functionals of this family are called GGA, where the acronym stands for *Generalized Gradient Approximation*. Here, the exchange energy takes the general form

$$E_x^{GGA} = E_x^{LDA} - \int d\mathbf{r} f(s)\rho^{4/3}(\mathbf{r}); \qquad s(\mathbf{r}) = \frac{|\nabla\rho(\mathbf{r})|}{\rho^{4/3}(\mathbf{r})}, \tag{1.3.11}$$

where the actual shape of $f(s)$ changes from functional to functional. It should

be pointed out that, unlike LDA, GGA functionals do not hold automatically the sum rule 1.3.8, rather, it needs to be enforced.

Another important class of exchange-correlation functionals used within the Kohn and Sham scheme exploits the orbitals of the reference system to compute exchange through its exact formula

$$E_x^{HF} = -\frac{1}{2}\int d\mathbf{r_1} d\mathbf{r_2} \psi_i^*(\mathbf{r_1})\psi_j(\mathbf{r_1})\frac{1}{2}\psi_j^*(\mathbf{r_2})\psi_i(\mathbf{r_2}). \tag{1.3.12}$$

These functionals are called *hybrid* since they make use of a term borrowed from the Hartree-Fock theory. It is worth to note that, although the exchange term 1.3.12 is usually called "exact", it is just computed using an exact formula, while orbitals are those of the reference system of non-interacting electrons.

The last group collects the *meta-GGA* functionals, whose general formula involves a contribution related to the kinetic energy density of the occupied Kohn-Sham orbitals

$$\tau(\mathbf{r}) = \sum_i^{\text{occup}} \frac{1}{2}|\nabla\psi_i(\mathbf{r})|^2. \tag{1.3.13}$$

Chapter 2

Theory of Dispersion Interaction

As seen in the previous chapter, electron-electron interaction can be divided in three terms: the classical repulsion $J[\rho]$, exchange and correlation. The latter is commonly defined as the difference between the exact energy E_{exact}, solution to the many-body Schrödinger equation and the best energy value obtained through the Hartree-Fock theory E_{HF}

$$E_c = E_{\text{exact}} - E_{\text{HF}}. \tag{2.0.1}$$

E_c is sometimes called *dynamical* or *Coulomb correlation*, in contrast with the *statical* or *Fermi correlation* already accounted for by the Hartree-Fock approximation. In fact, the term 'correlation' is commonly employed to indicate just the effects arising from the correlated motion of electrons, while the contribution due to Pauli exclusion principle is referred to as exchange. The present chapter is focused on a particular kind of dynamical correlation, named *dispersion*, originated by the interaction of fluctuating dipoles emerging from the charge density of molecules.

2.1 Perturbation Theory of Dispersion Forces

Dispersion represents the main interaction between non-polar molecules at large distance, when the superposition of the electron clouds become negligible. Let us take two non-polar molecules A and B, whose wave functions Ψ_A and Ψ_B are non-zero in different region of the space. As long as Ψ_A and Ψ_B do not overlap, calculations can be done without requiring antisymmetrization of the global wave function. As a consequence we can identify a set of N_A electrons belonging to molecule A and a Hamiltonian $\hat{H}_A$ can be defined for molecule A in terms of these electrons. Similarly, $\hat{H}_B$ is defined in term of the N_B electrons of molecule B. Let us define the unperturbed Hamiltonian for the coupled system $\hat{H}^0 = \hat{H}_A + \hat{H}_B$, whose eigenfunctions are simple products $\Psi_m^A \Psi_n^B$, hereafter abbreviated to $|mn\rangle$.

$$\begin{aligned} \hat{H}^0|mn\rangle &= \left(\hat{H}_A + \hat{H}_B\right)|mn\rangle \\ &= \left(E_m^A + E_n^B\right)|mn\rangle \\ &= E_{mn}^0|mn\rangle \end{aligned} \tag{2.1.1}$$

Here, m and n labels the electronic states of A and B respectively. The electrostatic interaction between molecules is treated as a perturbation

$$H' = \sum_{a\in A}\sum_{b\in B}\frac{1}{r_{ab}}. \tag{2.1.2}$$

Applying ordinary Rayleigh-Schrödinger perturbation theory, we write the total energy E_{00} for the ground state $|00\rangle$ of the combined system as

$$E_{00} = E_{00}^0 + E_{00}' + E_{00}'' + \cdots, \tag{2.1.3}$$

where

$$E_{00}^0 = E_{00}^A + E_{00}^B \tag{2.1.4}$$

$$E_{00}' = \langle 00|H'|00\rangle \tag{2.1.5}$$

$$E_{00}'' = -\sum_{mn}{}' \frac{\langle 00|H'|mn\rangle\langle mn|H'|00\rangle}{E_{mn}^0 - E_{00}^0}. \tag{2.1.6}$$

The prime on summation implies that m and n can't be simultaneously zero. Notice that similar expressions for the energy E_{mn} can be obtained for excited states $|mn\rangle$ if they are non-degenerate. This condition have to be satisfied also by the ground state for the 2.1.4-2.1.6 to be valid.

The first-order energy 2.1.5 is just the electrostatic interaction between the charge densities of the two molecules

$$E'_{00} = \int d\mathbf{r} d\mathbf{r}' \frac{\rho^A(\mathbf{r})\rho^B(\mathbf{r}')}{|\mathbf{r} - \mathbf{r}'|}, \tag{2.1.7}$$

with obvious meaning of symbols.

The second-order energy 2.1.6 involves both induction and dispersion. In order to separate these two contribution we split E''_{00} in three parts:

$$U^A_{\text{ind}} = -\sum_{m\neq 0} \frac{\langle 00|H'|m0\rangle\langle m0|H'|00\rangle}{E^A_m - E^A_0} \tag{2.1.8}$$

$$U^B_{\text{ind}} = -\sum_{n\neq 0} \frac{\langle 00|H'|0n\rangle\langle 0n|H'|00\rangle}{E^B_n - E^B_0} \tag{2.1.9}$$

$$U_{\text{disp}} = -\sum_{m,n\neq 0} \frac{\langle 00|H'|mn\rangle\langle mn|H'|00\rangle}{E^A_m + E^B_n - E^A_0 + E^B_0}. \tag{2.1.10}$$

Here, 2.1.8 represent the induction energy of molecule A due to the field produced by molecule B, while 2.1.10 is the dispersion energy.

In order to unravel 2.1.10, it is useful to express H' using the multipole expansion [16]:

$$\begin{aligned} H' = &- T_{\alpha\beta}\hat{\mu}^A_\alpha\hat{\mu}^B_\beta - \frac{1}{3}T_{\alpha\beta\gamma}(\hat{\mu}^A_\alpha\hat{\Theta}^B_{\beta\gamma} - \hat{\Theta}^A_{\alpha\beta}\hat{\mu}^B_\gamma) \\ &- T_{\alpha\beta\gamma\delta}(\frac{1}{15}\hat{\mu}^A_\alpha\hat{\Omega}^B_{\beta\gamma\delta} - \frac{1}{9}\hat{\Theta}^A_{\alpha\beta}\hat{\Theta}^B_{\gamma\delta} + \frac{1}{15}\hat{\Omega}^A_{\alpha\beta\gamma}\hat{\mu}^B_\delta) + \cdots, \end{aligned} \tag{2.1.11}$$

where the Einstein notation is used and $T_{\alpha\beta} = \nabla_\alpha\nabla_\beta R^{-1}$. Here, $\hat{\mu}^A_\alpha$ is the matrix element of the operator dipole moment acting on molecule A, $\hat{\Theta}^A_{\alpha\beta}$ is that of the quadrupole and $\hat{\Omega}^A_{\alpha\beta\gamma}$ is that of the octupole, so that 2.1.11 involves the dipole-dipole, dipole-quadrupole, dipole-octupole and the quadrupole-quadrupole interactions. Notice that all the terms of the multipolar expansion 2.1.11 depending on net charges, have been omitted for we have to deal with non-charged

molecules. In fact, this omission holds true also for charged molecules because excited states $|n\rangle$ and $|m\rangle$ are orthogonal to the ground state and the net charge q acts merely as a constant, so that all matrix elements depending on q are zero.

Since the perturbation H' is leaded by the dipole-dipole interaction, we could simplify the problem considering only the first term on the right-hand side of 2.1.11. Substituting it in 2.1.10 we obtain

$$\begin{aligned} U_{\text{disp}} =& -\sum_{m,n\neq 0} \frac{\langle 00|\hat{\mu}^A_\alpha T_{\alpha\beta}\hat{\mu}^B_\beta|mn\rangle\langle mn|\hat{\mu}^A_\gamma T_{\gamma\delta}\hat{\mu}^B_\delta|00\rangle}{E^A_m + E^B_n - E^A_0 + E^B_0} \\ =& -T_{\alpha\beta}T_{\gamma\delta}\sum_{m,n\neq 0}\frac{1}{W^A_{m0}+W^B_{n0}} \\ & \times \langle 0^A|\hat{\mu}^A_\alpha|m^A\rangle\langle m^A|\hat{\mu}^A_\gamma|0^A\rangle\langle 0^B|\hat{\mu}^A_\beta|n^B\rangle\langle n^B|\hat{\mu}^A_\delta|0^B\rangle, \end{aligned} \tag{2.1.12}$$

where $W^A_{m0} = E^A_m - E^A_0$ and we exploit the fact that the dipole moment operator $\hat{\mu}^A$ acts only on the electronic coordinates of A. Now, the matrix elements are factorized into terms referring to A and terms referring to B, but the denominator is not. To handle it, London [17] used the average-energy approximation [18]. First, the 2.1.12 is rewritten as

$$\begin{aligned} U_{\text{disp}} =& -T_{\alpha\beta}T_{\gamma\delta}\sum_{m,n\neq 0}\frac{W^A_{m0}W^B_{n0}}{W^A_{m0}+W^B_{n0}} \\ & \times \frac{\langle 0^A|\hat{\mu}^A_\alpha|m^A\rangle\langle m^A|\hat{\mu}^A_\gamma|0^A\rangle}{W^A_{m0}}\frac{\langle 0^B|\hat{\mu}^A_\beta|n^B\rangle\langle n^B|\hat{\mu}^A_\delta|0^B\rangle}{W^B_{n0}}. \end{aligned} \tag{2.1.13}$$

Then, the inconvenient factor $W^A_{m0}W^B_{n0}/(W^A_{m0}+W^B_{n0})$ is approximated using the average excitation energies U_A and U_B

$$\frac{W^A_{m0}W^B_{n0}}{W^A_{m0}+W^B_{n0}} \approx \frac{U_A U_B}{U_A+U_B}(1+\Delta_{mn}) \tag{2.1.14}$$

with

$$\Delta_{mn} = \frac{1/U_A - 1/W^A_{m0} + 1/U_B - 1/W^B_{n0}}{1/W^A_{m0} - 1/W^B_{n0}}. \tag{2.1.15}$$

For a proper choice of U_A and U_B, Δ_{mn} becomes negligible for all m and n and the dispersion energy become:

$$U_{\text{disp}} \approx -\frac{U_A U_B}{4(U_A+U_B)}T_{\alpha\beta}T_{\gamma\delta}\alpha^A_{\alpha\gamma}\alpha^B_{\beta\delta}, \tag{2.1.16}$$

where the sum-over-states expression for the matrix elements of the polarizability tensor α

$$\alpha_{\alpha\beta} = \sum_{n\neq 0} \frac{\langle 0|\hat{\mu}_\alpha|n\rangle\langle n|\hat{\mu}_\beta|0\rangle + \langle 0|\hat{\mu}_\beta|n\rangle\langle n|\hat{\mu}_\alpha|0\rangle}{W_n - W_0} \tag{2.1.17}$$

has been used. For atoms, where $\alpha_{\alpha\beta}$ reduces to $\overline{\alpha}\delta_{\alpha\beta}$, we obtain the London formula of dispersion energy:

$$U_{\text{disp}} = -\frac{C_6}{R_{AB}^6} \qquad \text{with} \qquad C_6 = -\frac{3U_A U_B}{2(U_A + U_B)}\overline{\alpha}^A\overline{\alpha}^B, \tag{2.1.18}$$

where the explicit expression for $T_{\alpha\beta}$ has been used. The same result can be applied to molecules when the dispersion energy is averaged over the relative orientations of the two molecules. It is worth to note that U_{disp} is always negative, i.e. it gives raise to attractive interactions between molecules. Moreover, dispersion energy are pairwise additive, this means that the total dispersion energy of a system composed by two or more molecules is just the sum of the dispersion energy between each pair of components $\sum_{i>j} U_{\text{disp}}^{ij}$.

For practical purposes, the evaluation of 2.1.18 requires suitable values of the average excitation energies U_A and U_B. It is common use to equals them the to the ionization energies, obtaining a rough approximation of C_6. Alternatively, using the lowest excitation energies of A and B, 2.1.18 gives an upper bound to the magnitude of dispersion. Slater and Kirkwood proposed a formula, in which U_A is approximated as $\sqrt{N_A/\alpha_A}$, where N_A is an effective number of valence electrons for molecule A.

2.2 Dispersion Forces in DFT

As shown in the previous chapter, dispersion interactions arise from the correlated motion of electrons and their proper treatment involves electronic excited states of the interacting chemical species. This could be achieved by the so-called post Hartree-Fock (post-HF) methods, such as Møller-Plesset perturbation theory at the second (MP2) or higher orders (MPx) and coupled

cluster approaches, see e.g. [5]. The 'chemical accuracy' of post-HF methods is unfortunately balanced by demanding computational burden, which becomes rapidly unpractical even for medium-size systems. On the contrary, DFT methods allows to handle chemical systems containing up to several hundreds of atoms. Although the exact density functional would be able to account for dispersion, commonly exploited local (LDA) and semi-local (GGA) functionals describes badly the physics of this kind of dynamical correlation [3]. Among several attempts made to include dispersion effects in density functional theory, some of them are mentioned in the follows.

Dion et al. [19] proposed a non-local density functional that accounts explicitly for dispersion by means of a non-local energy term

$$E_c^{\mathrm{NL}} = \int_0^\infty \frac{du}{2\pi} \,\mathrm{tr}\left[\ln\left(1 - V\tilde{\chi}\right) - \ln\epsilon\right], \tag{2.2.1}$$

where $\tilde{\chi}$ is the density response to the electric potential, neglecting spectator excitations, V is the interelectronic Coulomb interaction, ϵ is the (approximated) dielectric function and the integration runs over the imaginary frequency u.

Grimme [20], on the basis of the work done by Görling and Levy [21, 22], included dispersion in DFT by developing a so-called double-hybrid functional, containing some amount of correlation computed at the MP2 level

$$E_c^{\mathrm{MP2}} = \frac{1}{4}\sum_{ia}\sum_{jb} \frac{|\langle ia|r_{12}^{-1}|jb\rangle - \langle ib|r_{12}^{-1}|ja\rangle|^2}{\epsilon_i + \epsilon_j - \epsilon_a - \epsilon_b}, \tag{2.2.2}$$

besides the exact exchange 1.3.12. As for the latter, E_C^{MP2} is computed using KS orbitals.

It is worth to note that the group of Truhlar developed a suite of heavily parameterized hybrid meta-GGA functionals [23], which has been shown to model with good accuracy non covalent interactions.

Although these strategies allows to treat dispersion forces with good accuracy, their computational demand is fairly high, in particular when they are applied to the modeling of extended system such as crystalline polymers, organic-inorganic frameworks and self-assembled monolayers, where plane-wave basis

sets are commonly employed. Indeed, the efficiency of plane-wave algorithms drops dramatically when non-local potentials are involved. In order to include dispersion without affecting the computational effectiveness of DFT, a semi-empirical correction can be added to the exchange-correlation functional, in the form of a pairwise summation over the M atoms contained in the system

$$E_{\text{disp}} = -\sum_{i>j}^{M} f_{\text{damp}}(r_{ij}) \frac{C_{6ij}}{r_{ij}^6}, \tag{2.2.3}$$

where f_{damp} is the damping function

$$f_{\text{damp}}(r_{ij}) = \frac{s_6}{1 + \exp\left[-d\left(\frac{r_{ij}}{r_0} - 1\right)\right]}, \tag{2.2.4}$$

whose role is to prevent dispersion to take place at short distance, between directly bonded atoms. This method is known as dispersion-corrected Density Functional Theory (DFT-D). Here, s_6 represents a global-scaling parameter, whose value depends on the exchange-correlation functional actually used, C_{6ij} are obtained from tabulated values of atomic C_{6i} coefficients through a square root combination rule $C_{6ij} = \sqrt{C_{6i}C_{6j}}$ and r_0 is the sum of atomic Van der Waals radii, which are also tabulated. Although similar correction schemes were applied earlier even to Hartree-Fock calculations (see e.g. [24]), the approach developed by Grimme [8] is innovative since C_6 coefficients and Van der Waals radii are computed rather than fitted or taken from experiments. In principle this allows to provide dispersion parameters for the whole periodic table and not only for few atoms as happens in several implementations like this one. Dispersion coefficient of atomic species are computed as:

$$C_{6i} = 0.05 N_A I_i \alpha_i, \tag{2.2.5}$$

where N_A is an effective number of electrons assuming the values 2, 10, 18, 36 and 54 for elements belonging to rows 1-5 of the periodic table, I_i and α_i are the ionization potential and the static dipole polarizability computed by means of unrestricted DFT calculations carried out using the PBE0 density functional [25] with a QZPV basis set. Van der Waals radii are derived from

the radius of the 0.01 au contour of electron density of the atom in their ground state, computed at the HF level of theory using a TZV basis set, scaled by a factor 1.1.

Among the methods presented here, DFT-D is computationally cheap, gives good results for a broad range of compounds [8], can be used in conjunction with several flavors of Kohn-Sham energy functionals and its accuracy can be improved further by refining ad-hoc atomic C_6 parameters and Van der Waals radii for the system under study. Energy and gradients are easier to implement than those of other methods and can be straightforwardly extended to the periodic case, where also the stress tensor can be obtained analitically. It should be pointed out that an exact implementation of 2.2.3 would require the use of Ewald summation [26], however, since the dispersion energy decays as r^{-6}, it is absolutely convergent in crystals and the real-space summation 2.2.3 work fine. Indeed, in the prototypical case of graphite, the comparison of the two summation strategies results in a negligible differences ($< 0.3\%$) in the dispersion energy when the real-space summation is truncated at 200 au [27].

Bibliography

[1] R. G. Parr and W. Yang. *Density-Functional Theory of Atoms and Molecules*. Oxford University Press, 1989.

[2] W. Koch and M. C. Holthausen. *A Chemist's Guide to Density Functional Theory*. Wiley-VCH, 2001.

[3] S. Kristyán and P. Pulay. *Chem. Phys. Lett.*, **229**:175, 1994.

[4] E. C. Lee, D. Kim, P. Jurečka, P. Tarakeshwar, P. Hobza, and K. S. Kim. *J. Phys. Chem. A*, **111**:3446, 2007.

[5] A. Szabo and N. S. Ostlund. *Modern Quantum Chemistry: Introduction to Advanced Electronic Structure Theory*. Dover Publications, 1996.

[6] J. F. Dobson, J. Wang, B. P. Dinte, K. McLennan, and H. M. Le. *Int. J. Quantum Chem.*, **101**:579, 2005.

[7] T. Schwabe and S. Grimme. *Acc. Chem. Res.*, **41**:569, 2008.

[8] S. Grimme. *J. Comput. Chem.*, **27**:1787, 2006.

[9] M. Born and J. Oppenheimer. *Ann. Phys.*, **84**:457, 1927.

[10] P. Hohenberg and W. Kohn. *Phys. Rev.*, **136**:B864, 1964.

[11] T. L. Gilbert. *Phys. Rev. B*, **12**:2111, 1975.

[12] W. Kohn and L. J. Sham. *Phys. Rev.*, **140**:A1133, 1965.

[13] J. E. Harriman. *Phys. Rev. A*, **[3] 24**:680, 1981.

[14] S. H. Vosko, L. Wilk, and M. Nusair. *Can. J. Phys.*, **58**:1200, 1980.

[15] D. M. Ceperley and B. J. Alder. *Phys. Rev. Lett.*, **45**:566, 1980.

[16] A. J. Stone. *The Theory of Intermolecular Forces.* Oxford University Press, 2002.

[17] F. London. *Z. Physik*, **63**:245, 1930.

[18] A. Unsöld. *Z. Physik*, **43**:563, 1927.

[19] M. Dion, H. Rydberg, E. Schröder, D. C. Langreth, and B. I. Lundqvist. *Phys. Rev. Lett.*, **92**:246401, 2004.

[20] S. Grimme. *J. Chem. Phys*, **124**:34108, 2006.

[21] A. Görling and M. Levy. *Phys. Rev. B*, **47**:105, 1993.

[22] A. Görling and M. Levy. *Phys. Rev. A*, **50**:196, 1994.

[23] Y. Zhao and D. G. Truhlar. *Theor. Chem. Accounts*, **120**:215, 2008.

[24] J. Hepburn, G. Scoles, and R. Penco. *Chem. Phys. Lett.*, **36**:451, 1975.

[25] C. Adamo and V. Barone. *J. Chem. Phys.*, **110**:6158, 1999.

[26] T. Kerber, M. Sierka, and J. Sauer. *J. Comput. Chem.*, **29**:2088, 2009.

[27] T. Kerber. private communication.

List of Publications

1. M. Casarin, D. Forrer, T. Orzali, M. Petukhov, M. Sambi, E. Tondello and A. Vittadini. *"Strong Bonding of Single C_{60} Molecules to (1×2)-Pt(110): an STM/DFT Investigation"*. J. Phys. Chem. C, **111**:9365, 2007.

2. T. Orzali, D. Forrer, M. Sambi, A. Vittadini, M. Casarin, and E. Tondello. *"Temperature-Dependent Self-Assemblies of C_{60} on (1×2)-Pt(110): A STM/DFT Investigation"*. J. Phys. Chem. C, **112**:378, 2008.

3. M. Casarin, D. Forrer, F. Garau, L. Pandolfo, C. Pettinari and A. Vittadini. *"Density Functional Theory Study of the Binding Capability of Tris(pyrazol-1-yl)methane toward Cu(I) and Ag(I) Cations"*. J. Phys. Chem. A, **112**:6723, 2008.

4. M. Casarin, D. Forrer, F. Garau, L. Pandolfo, C. Pettinari and A. Vittadini. *"Tris(pyrazol-1-yl)borate and tris(pyrazol-1-yl)methane: A DFT study of their different binding capability toward Ag(I) and Cu(I) cations"*. Inorg. Chim. Acta, **362**:4358, 2009

5. V. Barone, M. Casarin, D. Forrer, M. Pavone, M. Sambi and A. Vittadini. *"Role and Effective Treatment of Dispersive Forces in Materials: Polyethylene and Graphite Crystals as Test Cases"*. J. Comput. Chem., **30**:934, 2009.

6. A. Bencini, M. Casarin, D. Forrer, L. Franco, F. Garau, N. Masciocchi, L. Pandolfo, C. Pettinari, M. Ruzzi and A. Vittadini. *"Magnetic Properties*

and Vapochromic Reversible Guest-Induced Transformation in a Bispyrazolato Copper(II) Polymer: an Experimental and Dispersion-Corrected Density Functional Theory Study". Inorg. Chem., **48**:4044, 2009.

7. M. Casarin, M. Di Marino, D. Forrer, M. Sambi, F. Sedona, E. Tondello, A. Vittadini, V. Barone and M. Pavone. *"Coverage-Dependent Architectures of Iron Phthalocyanine on Ag(110): a Comprehensive STM/DFT Study"*. J. Phys. Chem. C, to be published, 2010.

Strong Bonding of Single C_{60} Molecules to (1 × 2)-Pt(110): an STM/DFT Investigation

M. Casarin,[‡,§] D. Forrer,[‡] T. Orzali,[‡,§] M. Petukhov,[†,‡,⊥] M. Sambi,[*,‡,§] E. Tondello,[‡,§] and A. Vittadini[*,‡,§,||]

Dipartimento di Scienze Chimiche, Università di Padova, Consorzio INSTM, and ISTM-CNR, Via Marzolo 1, 35131 Padova, Italia, and LRRS, UMR 5613 CNRS-Université de Bourgogne, 9 av. A. Savary, BP 47870, 21078 Dijon Cedex, France

Received: March 5, 2007; In Final Form: April 24, 2007

The interaction of single C_{60} molecules with the (1 × 2)-Pt(110) surface has been studied by scanning tunneling microscopy and density functional theory (DFT) calculations on slab models. Molecules are observed to be frozen at room temperature and are found to be almost exclusively in the same configuration. Extensive DFT calculations show that this configuration is the global energy minimum, suggesting that adsorbed molecules have enough rototranslational freedom to escape from the numerous local minima. The adsorption energy (3.81 eV) is the strongest ever found for C_{60}, and it is roughly proportional to the number of the Pt and C atoms at contact distance. Analysis of DFT results shows that the surface−adsorbate interaction is covalent in nature. A minority fraction of C_{60} molecules appear to be adsorbed on surface defects. A careful investigation of their registry and height with respect to the regularly adsorbed units leads to an indirect structural characterization of the nanopits which act as their adsorption sites.

1. Introduction

A substantial amount of work has been devoted in recent years to the elucidation of the structural and electronic properties of fullerene molecules adsorbed on metal and semiconducting surfaces, with a particular emphasis on the production and characterization of ordered two-dimensional (2D) C_{60} islands. The interest is motivated in the first place by technologically relevant issues such as the exploitation of fullerenes, either alkali-doped or derivatized, in molecular electronic and nonlinear optical devices. To this end, a clear understanding of the modifications of molecular electronic and transport properties induced by bonding with the substrate is of critical importance. Initially, a rather simple picture of fullerene bonding to surfaces was expected,[1] essentially on the basis of weak Van der Waals (VdW) interactions. Even if we restrict our attention solely to transition metal substrates, by now it has become common knowledge that a great variety of bonding mechanisms (associated to different degrees of substrate/adsorbate charge transfer, ranging from predominantly ionic[2−4] to prevalently covalent interactions[5]) and a wide range of bonding strengths exist, with freely diffusing molecules at room temperature (RT) or below at one end,[6−9] and strongly bound and rotationally frozen species characterized by well-defined molecular orientations with respect to the surface at the other.[5,10] Frequently, the basic hexagonal close packed (hcp) structure of the fullerene overlayer can be distorted as a consequence of the complex interplay between horizontal intermolecular versus vertical overlayer-substrate interactions.[7,11,12] Substantial reconstructions of the substrate are frequently observed, whose driving force generally is the increase of fullerene−metal bonding through partial embedding of C_{60} molecules in the surface atomic layers of the substrate.[13−16]

Less attention has been devoted to the initial stages of growth of fullerene ad-islands on single-crystalline surfaces and in particular to the coordination of the just-landed, isolated monomer to the surface, with the works by Crommie et al. dealing with the elucidation of the C_{60} molecular orientation on Ag(100) held at 4 K being a notable exception.[17] However, when strong vertical interactions are concerned, the coordination of the single molecule to the surface can help in rationalizing the topology of compact 2D domains, since the intermolecular interactions in this case can be viewed as a higher order perturbation to the molecule−substrate bonding. In addition, the resolution of different monomer orientations and coordination sites can give valuable information about the molecular rototranslational degrees of freedom at the given deposition temperature, which obviously depend on the adsorption energy. The difficulties of an experimental investigation of the initial stages of C_{60} chemisorption on strongly interacting substrates are mainly related to the low coverage of the overlayer (producing low signals in surface-averaging techniques) and to the absence of well-developed translational order (which is obtained only with the annealing required to produce compact, ordered 2D islands). For these reasons, techniques which are best suited for the investigation of molecular orientation and interfacial structure of long-range ordered C_{60} overlayers, such as X-ray photoelectron diffraction (XPD)[15] and surface X-ray diffraction (SXRD),[14,18] are of little help in the present case. On the other hand, the local nature of scanning probe techniques, extensively used for the characterization of ordered fullerene islands, overcomes the above-mentioned difficulties and thereby proves to be even more valuable in the case of isolated monomers, if a sufficient degree of intramolecular fine structure is warranted by the experimental resolution. The locality of the probe is also crucial in giving detailed information about the minority species on the surface (such as defects), which is

* Corresponding authors. E-mail: mauro.sambi@unipd.it (M.S.). E-mail: andrea.vittadini@unipd.it. Fax: +39 049 827 5161 (A.V.).
† Permanent address: IGNP, RRC Kurchatov Institute, Kurchatov square, 123182 Moscow, Russia.
‡ Università di Padova.
§ Consorzio INSTM.
|| ISTM-CNR.
⊥ Université de Bourgogne.

10.1021/jp071783e CCC: $37.00
Published on Web 06/08/2007

filtered out to a large extent by techniques sensitive to the ordered fraction of the total population.

In this paper, we provide a detailed study of the initial stages of C_{60} chemisorption on (1×2)-Pt(110) by combining scanning tunneling microscopy (STM) with density functional theory (DFT) calculations. The substrate superstructure is given by a missing row reconstruction.[19] The surface is atomically smooth along the $[1\bar{1}0]$ close-packed direction, while it shows alternating ridges and troughs along the reconstructed [001] azimuth. The resulting highly anisotropic corrugation can be exploited as a template for organic and inorganic[20] film growth.

C_{60} is known to bind to platinum by means of strong covalent bonds[5] and to produce apparently disordered structures at RT. High-resolution STM measurements allow us to resolve the details of the molecular orientation on the as-deposited surface at RT, revealing a preferential bonding configuration, which is, however, not exclusive: metastable molecules trapped in local potential minima are also resolved and characterized. DFT calculations provide a rationale for the observed orientations and individuate the most stable chemisorption site for each orientation. Most importantly, STM reveals that a minority fraction of fullerene molecules decorates the substrate surface defects. A careful correlation of the in-plane registry and height difference of C_{60} residing in defects with respect to the majority molecules in their preferential bonding configuration leads to an indirect characterization of the defects structure.

2. Experimental and Computational Details

The experiments were performed with an Omicron scanning tunneling microscope (VT−STM) operating in ultrahigh vacuum at a base pressure of 5×10^{-11} mbar. The sample bias voltage (V_{bias}) is indicated for all STM images. The Pt(110) single crystal was prepared by repeated cycles of argon ion sputtering (kinetic energy, KE = 2 keV) and annealing at $T = 970$ K, followed by cooling in oxygen atmosphere ($p(O_2) = 5 \times 10^{-7}$ mbar) down to 700 K. The cleaning cycles were repeated until a well-ordered 1×2 reconstructed surface was obtained, as judged by low-energy electron diffraction (LEED). C_{60} (99% purity) was sublimed at ∼820 K from a tungsten crucible mounted on an Omicron EFM3 evaporator. The Pt specimen was kept at RT during sublimation. The crucible was outgassed for a long time to avoid impurities while depositing fullerenes onto the substrate. Coverages are given as fractions of a monolayer (ML), with 1 ML corresponding to a close-packed quasi-hexagonal arrangement of C_{60} units with a surface density of 0.125 molecules per unit cell of the unreconstructed substrate surface[21] and are of the order of one hundredth of a ML for all the reported images.

Density functional (DF) calculations were performed by using the Perdew−Burke−Ernzerhof[22] exchange-correlation functional. The wavefunctions were expanded in plane waves with a KE cutoff of 20 Ry, while the cutoff for the augmented electron density was 160 Ry. Vanderbilt ultrasoft pseudopotentials[23] were adopted for both C and Pt. The theoretical lattice constant (3.957 Å) was used for Pt. To represent the Pt(110)-(1×2) surface, models consisting of repeated slabs were adopted, including five Pt atomic layers. To keep the distance between the periodic images of C_{60} as large as possible, we adopted rhombic surface cells. Two supercells were used (see Figure 1): a smaller (hereafter, S1) one (12 atoms/layer, lattice vectors $a = b = 11.54$ Å), and a larger (hereafter, S2) one (20 atoms/layer, lattice vectors $a = b = 16.072$ Å). In both cases, the vertical supercell dimension was set to 23.07 Å, which allowed, even in the presence of adsorbed C_{60}, a minimum distance between atoms belonging to subsequent slabs of ∼10 Å. C_{60} was adsorbed on only one side of the slab. Geometry optimizations were performed by a quasi-Newton algorithm, keeping fixed the bottom two Pt atomic layers. Because of the number and size of the models to be considered, these runs were performed with a Γ-point Brillouin zone (BZ) sampling and with the S1 slab. We checked by increasing the computational accuracy (plane-wave cutoff, surface cell, slab thickness, BZ sampling) that the obtained adsorption energies are converged within 0.1 eV, which is sufficient for our purposes.

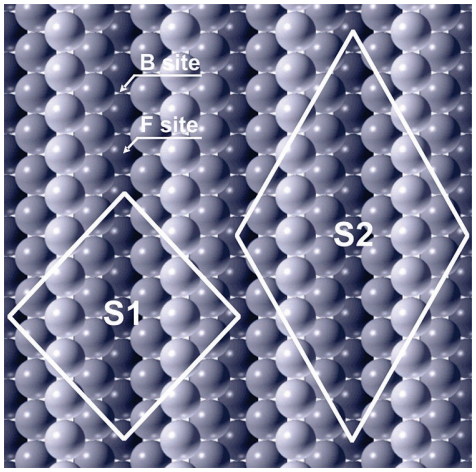

Figure 1. Top view of on (1×2)-Pt(110) surface showing the adopted supercells and adsorption sites for C_{60}. Darker spheres represent atoms deeper into the bulk.

Information on bonding was extracted from difference density ($\Delta\rho$) plots. These are obtained as the difference between the self-consistent (SC) electron density of a chemical system [$\rho(\mathbf{r})$] and an electron density relative to a noninteracting system. The latter is usually obtained from the superposition of the electron densities of free atoms [$\tilde{n}_i^0(\mathbf{r})$], placed in the same positions they have in the interacting system:

$$\Delta\tilde{n}_{atm}(\mathbf{r}) = \tilde{n}(\mathbf{r}) - \sum_{i}^{atoms} \tilde{n}_i^{\,0}(\mathbf{r}) \qquad (1)$$

where the "atm" label specifies that the noninteracting system consists of free atoms.

When analyzing coordination interactions, such as those involved in molecular adsorption, it is however more useful to adopt a different definition for $\Delta\rho$, where the noninteracting system is made by superposing the electron densities of two fragments, which are in this case the adsorbate and the substrate:

$$\Delta\rho(\mathbf{r}) = \rho(\mathbf{r}) - \rho^0_{C_{60}}(\mathbf{r}) - \rho^0_{surf}(\mathbf{r}) \qquad (2)$$

The ρ^0 densities are now relative to the SC densities of the noninteracting deformed fragments, computed using the geometry of the interacting system.

Whatever the definition of $\Delta\rho$, its spatial integration can be used to estimate charge transfers occurring in bond formations.

A fragment-based analysis has been also applied to adsorption energies (E_{ads}), which have been partitioned as:

$$E_{ads} = -[\Delta E_{prep}(C_{60}) + \Delta E_{prep}(surf) + \Delta E_{int}] \qquad (3)$$

where the "preparation" (ΔE_{prep}) terms represent the energy needed to modify the geometry of the noninteracting fragments, whereas the interaction (ΔE_{int}) term is the bonding energy

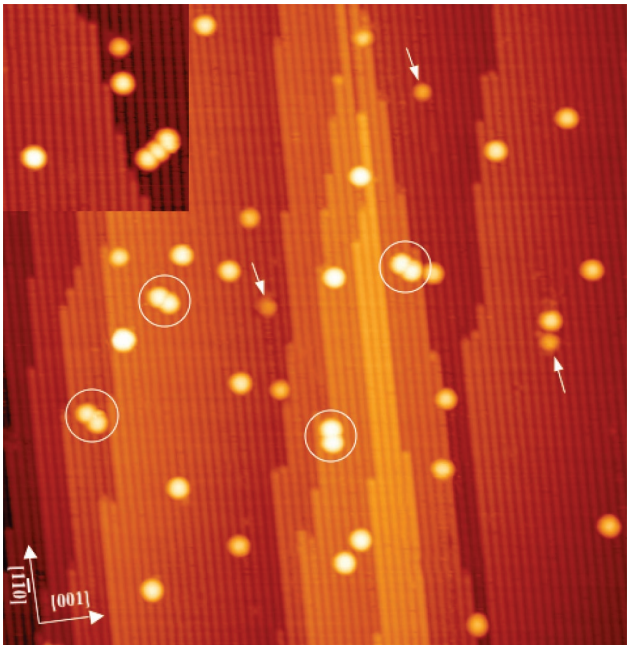

Figure 2. STM image of the (1 × 2)-Pt(110) reconstructed surface with ~0.02 ML of C_{60} deposited at RT (bias = 0.21 V; tunneling current (I_t) = 1.46 nA; 62 nm × 62 nm). White circles highlight apparent dimers; white arrows point to molecules adsorbed on surface defects (see text). Inset: STM image of the (1 × 2)-Pt(110) reconstructed surface with ~0.02 ML of C_{60} deposited at RT (bias = 0.21 V; I_t = 1.46 nA; 16.5 nm × 19 nm).

between the two deformed fragments. Because we have no tool to further decompose it, ΔE_{int} incorporates both the repulsive steric (the sum of the Pauli and electrostatic contributions) and the pure orbital interactions.

3. Results and Discussion

3.1. C_{60} Molecules at Regular Sites. *3.1.1. STM Experimental Data.* Figure 2 displays an STM topograph representative of the initial stages of adsorption of C_{60} molecules on the (1 × 2)-Pt(110) surface at RT. When a submonolayer coverage of fullerene is produced at the substrate surface, the majority molecular species invariably observed consists of isolated monomers sitting over the troughs between two neighboring Pt rows of the reconstructed surface. There is no preferential adsorption either at step edges or at kinks, and no nucleation of larger molecular clusters is observed, with the exception of a few apparent dimers (highlighted by white circles in Figure 2), which are discussed in more details below. The random distribution of molecules over the channels suggests that the most fundamental surface kinetic process, terrace diffusion, is frozen at RT. However, a limited degree of rototranslational motion immediately after landing on the surface should be allowed in order to optimize bonding to the substrate, since most molecules are found to adsorb equivalently and symmetrically between two adjacent Pt ridges. The average diameter of isolated C_{60} molecules measured with STM is equal to 17 Å as a consequence of a tip convolution effect, since the VdW diameter of the molecule equals 10.04 Å. The apparent height of imaged molecules, calibrated against a substrate step height (1.4 ± 0.1 Å) and measured with respect to the Pt ridges, is 5.5 ± 0.1 Å (the error bar is given as one standard deviation) at a bias voltage of 0.25 V. It is moderately dependent on the applied bias: it becomes 5.8 ± 0.1 Å at a bias voltage of 2.2 V. This value is considerably smaller than the molecule's VdW diameter and even smaller than the hard sphere diameter (7.3 Å). DFT calculations on C_{60} adsorption on (1 × 2)-Pt(110), extensively discussed below, give a physical height for the most stable molecular configuration of 7.4 Å. The smaller value observed in STM images can be attributed to local variations of the extraction potential on moving from the molecule to the bare metal substrate and to charge redistribution on the molecule because of bonding with the substrate, as confirmed by Tersoff−Hamann simulations of the adsorbed monomers, which fairly reproduce the experimentally observed corrugation (see section 3.1.4).

We turn now to consider the C_{60} dimers observed in Figure 2 (a trimer is reported in the left inset; we note that these features are 'apparent" rather than "true" dimers/trimers, since in the present case the two/three molecules in the unit are invariably at nonbonding distances[24,25]). Each molecule in a dimer is adsorbed on the same or (more frequently) on adjacent Pt troughs. Since molecular diameters exceed the channel spacing, molecules adsorbed on adjacent troughs are forced to form an angle smaller than 90° with the close-packed Pt rows running along the [1$\bar{1}$0] substrate azimuth. In fact, if two C_{60} molecules are put at an optimal VdW distance (10.04 Å) in adjacent troughs, simple trigonometry leads to an intermolecular axis tilted by 52.4° away from the [1$\bar{1}$0] direction. Angles close to this value (usually smaller by a few degrees) are indeed observed in Figure 2, though a more precisely measurable quantity, namely, the intermolecular distance in the dimer, is consistently higher than the VdW distance, with an average value of 11.4 ± 0.4 Å. What does prevent molecules from optimizing their lateral interactions across adjacent troughs? The answer lies in the strength of the vertical interaction with the substrate. If we suppose that there is a preferred adsorption site for C_{60} molecules on the chosen substrate and we also assume that vertical bonding interactions are stronger than intermolecular lateral interactions, then intermolecular nearest neighbor (NN) distances will mirror the separation between equivalent adsorption sites on the surface, at the expense of some loss in the effectiveness of in-plane interactions. Let us put a C_{60} molecule over a well-defined site in a trough of the (1 × 2)-Pt(110) surface. The nearest same-symmetry site in the nearby trough lies at one lattice parameter of the reconstructed surface along the [001] direction, that is, at 7.85 Å. However, this separation is too small to accommodate a second molecule without substantial repulsive intermolecular interactions (this is the reason why dimers are never found to align along the [001] main azimuth). The next same-symmetry sites are located at an integer multiple of the Pt lattice parameter along the [1$\bar{1}$0] direction, namely, at ±(n × 2.775) Å, with n being a positive integer. The first n values consistent with a physical separation between fullerene molecules are n = 2 and n = 3. For n = 2, we obtain an intermolecular distance of 9.6 Å, which still belongs to the repulsive region of the VdW potential.[24] For n = 3, the NN intermolecular separation is 11.4 Å, which perfectly corresponds to the experimentally determined value and which therefore confirms that both molecules in the dimer occupy the same adsorption site. The same intermolecular separation and hence the same-symmetry site occupancy is found also for the trimer reported as an inset to Figure 2.

This argument applied to the minority dimers aligned with the troughs (along the [1$\bar{1}$0] direction) would imply a mutual separation of 8.3 Å (for n = 3) or 11.1 Å (for n = 4). The experimental intermolecular distance is 10.9 ± 0.4 Å; that is close to but not equal to n = 4. As it will be shown below (see section 3.1.2, Figure 3 and section 3.2, Figure 14), molecules along the same trough can optimize their mutual interactions

by slightly tilting toward each other (thereby slightly reducing the mutual separation), while retaining the same adsorption site.

The same-site occupancy argument can be extended to monomers as well. It turns out that monomers symmetrically adsorbed over troughs are always separated by integer multiples of the Pt lattice parameter along the [1$\bar{1}$0] direction from each other and from C_{60} molecules belonging to dimers. This completes the proof that there is a strong preference for a single, well-defined adsorption site for C_{60} on (1 × 2)-Pt(110) at RT, though a negligible fraction of molecules may be found in less stable, local minima (see sections 3.1.2 and 3.1.4). Unfortunately, the exact nature of this site cannot be evinced directly from experimental data, since there is no atomic resolution along the [1$\bar{1}$0] Pt ridges at RT. This is the point where DFT calculations set in.

3.1.2. DFT Calculations. The potential energy hypersurface describing the interaction between C_{60} and the (1 × 2)-Pt(110) surface is rather complex. To explore it effectively at a reasonable computational cost, we performed a series of geometry optimizations which were started by placing the adsorbate in different positions and orientations. We selected eighteen starting geometries on the basis of three criteria, namely, the C_{60} geometry element (apex atom, 5:6 bond, 6:6 bond, six-membered ring, five-membered ring) closest to the surface, the orientation of the given geometry element with respect to the surface, and the surface adsorption site. Because STM shows that the center of mass (COM) of the adsorbate always lies at the center of the 1 × 2 troughs, two adsorption sites can be envisaged: the bridge site (B), where the COM is between two second layer Pt atoms, and the four-fold site (F), where the COM is among four second layer Pt atoms, that is, on top of a third layer atom (see Figure 1).

Our search yielded 16 potential energy local minima (see Figure 3). The most stable of these, hereafter indicated as M1 and M2 respectively, correspond to adsorption energies of 3.81 and 3.51 eV. In the M1 configuration, C_{60} places a (5:6) bond across a trough onto a bridge site, whereas in the M2 one, a six-membered ring is placed onto a four-fold site. Apparently, M1 and M2 can be easily interconverted into each other by a slight rototranslation of the molecule along the trough. In the most stable M1 configuration, the molecule is slightly tilted toward the lowermost hexagonal face along the [1$\bar{1}$0] direction with respect to an ideal (5:6) adsorption.

To understand factors governing the adsorption interaction, we first examined the dependency of E_{ads} on the number of fullerene−surface bonds for all of the found minima. As in ref 26, the number of bonds was determined from the close contacts between adsorbate and substrate atoms (here, we chose a Pt−C cutoff distance of 2.4 Å, but most bonds are in the 2.0−2.3 Å range) and confirmed by inspecting $\Delta\rho(\mathbf{r})$ maps. As expected, E_{ads} increases with the number of the Pt and C atoms involved in the bonds (see Figure 4); however, some irregularities are present, and minima with the same number of Pt−C bonds can differ in energy by as much as ∼1.5 eV. From fullerene chemistry, it is known that addition reactions to 6:6 bonds are favored over additions to 5:6 ones, because in the latter case a 5:6 double bond is created, which increases the C_{60} strain energy.[27] However, when analyzing E_{ads} on a fragment basis, we found that, though the adsorbate ΔE_{prep} term (which includes the strain energy of C_{60}) is large and ranges from 1.01 to 2.65 eV, the ΔE_{prep}(surf) term is of comparable importance and spans an even larger range (0.31−2.76 eV). Furthermore, the variations of the two terms are uncorrelated. Thus, criteria extracted from C_{60} chemistry are of little help in explaining the adsorption

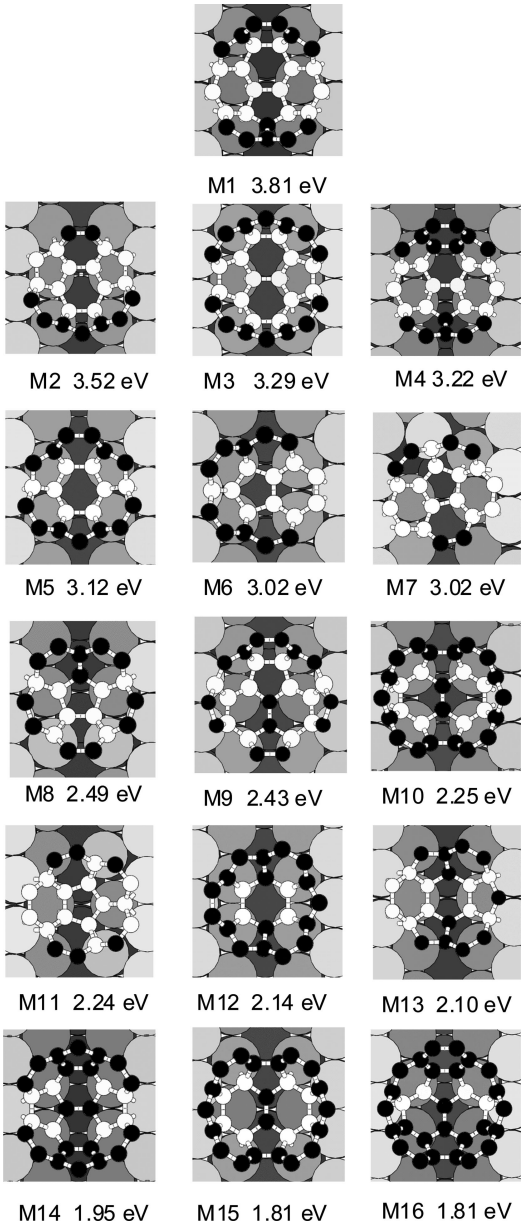

Figure 3. Top views of the relaxed structures of most stable potential energy minima, showing only the bottom part of C_{60}. Large and small circles represent Pt and C atoms, respectively. Darker Pt atoms are deeper into the surface. White (black) circles represent C atoms which are bonded (not bonded) to the surface. The adsorption energy for each configuration is reported.

energetics. We also found that, in the average, the sum of the two preparation terms is of the order of E_{ads}; that is, $-\Delta E_{int}$ is roughly twice E_{ads}.

This indicates that adsorption strongly modifies both the adsorbate and the surface and cannot be described as a simple physisorption. We finally compared the correlation between E_{ads} or ΔE_{int} with the number of interacting C and Pt atoms (see Figure 4). A fairly linear dependence for ΔE_{int} is obtained (in particular, when the number of interacting Pt atoms is taken as the independent variable), whereas the correlation for E_{ads} is poorer.

3.1.3. Nature of the C_{60}−Surface Interaction. We first point out that a 3.8 eV adsorption energy is, to our knowledge, the strongest ever computed for C_{60}[28] and explains its substantial immobility at RT: the adsorbate is "gulliverized" by a sum of

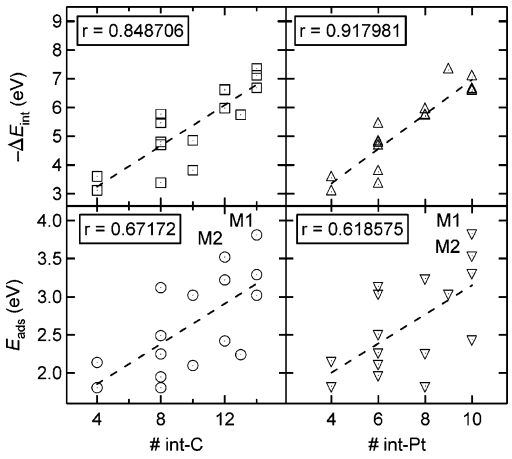

Figure 4. Surface C_{60} interaction energy of all of the found local minima plotted as a function of the number of the bonded C/Pt atoms (see text). The correlation coefficient r (Pearson's r) is reported for each fit.

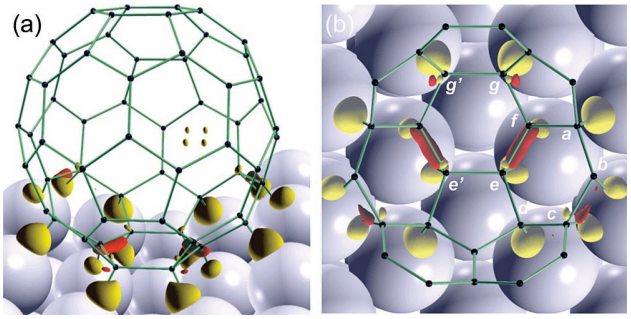

Figure 5. Difference density maps ($\Delta\rho$) for the most stable M1 configuration. Displayed isosurfaces are $\pm(8 \times 10^{-3})$ e/a_0^3. Yellow and red colors represents regions of increased and decreased density, respectively. (a) Perspective view and (b) top view showing only the bottom part of C_{60}.

several, individually weak bonds. An interesting issue however concerns the nature of these interactions, that is, whether they are prevalently ionic or covalent. In this regard, Lu et al.[17] carried out DFT calculations of C_{60} adsorption on Ag(100) and Au(111) and established the degree of ionicity of the C_{60}−surface interaction by integrating the difference density. As a boundary between the C_{60} and the surface, they chose a horizontal plane where the density vanishes, which is similar to a Bader analysis. This choice is not viable here, because of the corrugated shape of the (1 × 2)-Pt(110) surface. Thus, we adopted a Voronoi-type integration, as described in ref 29. Lu et al.[17] found that the electron transfer is substantially reduced on passing from Ag(100) to Au(111) (from −0.15 to −0.01 |e|, respectively) and attributed this effect to the variation of the work function (4.6 vs 5.3 eV). In fact, a lower work function means a relative stabilization of the C_{60} lowest unoccupied molecular orbital (LUMO), which favors an electron density flow from the surface to the adsorbate. Our results confirm this picture: actually, C_{60} is found to be positively charged by +0.07 |e|, in tune with the high work function of (1 × 2)-Pt(110) (5.84 eV[30]).

Nevertheless, the C_{60}−surface interaction is essentially covalent in nature, as it is revealed by the difference density map ($\Delta\rho$) reported in Figure 5. In fact, the electron density buildup (in yellow) due to the formation of C_{60}−surface covalent bonds[9,26,31] is well-evident. In addition, we note a substantial electron density decrease (in red) at the 6:6 C_{60} bonds involved in the adsorption (e−f and e′−f′).

TABLE 1. Internal C_{60} Bond Distance Changes (Å) for the M1 Configuration[a]

bond	type	Δr
a−b	6:6	+0.08
b−c	5:6	+0.02
c−d	6:6	+0.08
d−e	5:6	+0.05
e−f	6:6	+0.04
f−g	5:6	+0.06
e−e′	5:6	+0.03
g−g′	6:6	+0.14
a−f	5:6	+0.03
i−h	5:6	−0.01

[a] For free C_{60}, r(6:6) = 1.40, r(5:6) = 1.46. Atom codes as in Figure 6.

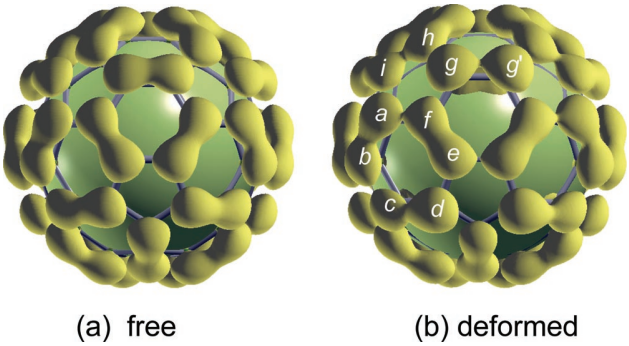

Figure 6. Charge density maps integrated in the HOMO energy range for (a) free C_{60} and (b) a non-interacting C_{60} molecule whose geometry has been deformed as in M1 (viewed from the bottom). To improve the figure readability, a sphere has been placed inside C_{60}. Displayed isosurfaces are 3×10^{-3} e/a_0^3.

One may wonder why a similar effect is not observed for the g−g′ bond. This can be explained if we consider that the $\rho^0_{C_{60}}(\mathbf{r})$ term of eq 2 is computed for a C_{60} that is *already* deformed. Because the e−f distance is only slightly elongated (see Table 1), its double bond character is still kept in the noninteracting, deformed C_{60} fragment. In contrast, the g−g′ elongation is so strong (0.14 Å) that the π bond density is removed *before* the interaction with the surface sets in. This can be realized by examining Figure 6, where the charge densities associated to the highest occupied molecular orbital (HOMO) in the undeformed and in the deformed free C_{60} are compared. A considerable reduction of the charge density in the g−g′ internuclear region is well-evident, which is not present in the f−e case. It is also interesting to note the incipient formation of a 5:6 bond connecting i and h atoms, which are not involved in surface−adsorbate bonds (see Table 1).

Further evidence confirming the occurrence of a covalent adsorption interaction can be inferred by the density of states (DOS) curves. In Figure 7, the partial density of states (PDOS)[32] of the M1 minimum is projected to C_{60}, and it is compared to the DOS curve of a free C_{60} molecule. Whereas the deep energy region of the DOS curve is practically unchanged upon adsorption, the region close to the Fermi level is strongly perturbed. In particular, broadenings and shifts of the HOMOs and LUMOs are apparent, and no energy gap is present, which suggests a strong mixing between substrate and adsorbate states.

In Figure 8, the C_{60} PDOS in the M1 configuration is projected to six sets of C atoms of increasing depth: the "1−10" curve represents the top C atoms, whereas the "51−60" curve represents the bottom C atoms. The PDOS of the bottom C atoms is rather flat for a wide energy region around the Fermi level, and prominent peaks are substantially absent, in contrast

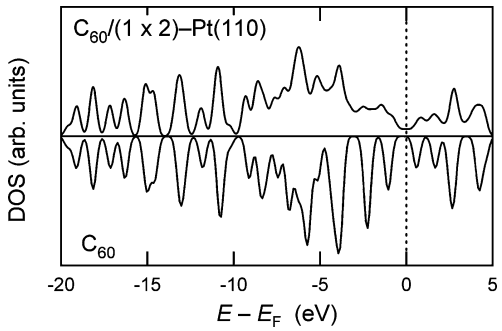

Figure 7. Top: PDOS projected to C_{60} in the M1 configuration. Bottom: DOS of free C_{60}. The origin of the free C_{60} DOS curve has been shifted to align the deepest peaks.

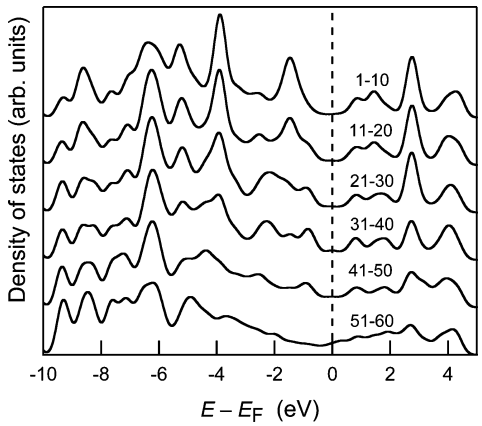

Figure 8. PDOS of C_{60} in the M1 configuration obtained by projecting the DOS onto increasingly deeper sets of C atoms (viz., the curve labeled "1−10" is relative to the topmost ten C atoms).

to what is observed for the topmost C atoms. This means that both the HOMOs and the LUMOs of C_{60} strongly interact with the surface states, but they are rehybridized yielding combinations localized on the bottom half and in the top half of C_{60}. The former interact with the surface, while the latter remains substantially unaffected.

The bonding picture outlined above implies that a clear distinction of bonding and antibonding levels is rather difficult. In Figure 9, we show several integrated local density of states (ILDOS) plots,[32] obtained by integrating the electron density in several regions close to the Fermi energy, which correspond to (a) the peak at ~ -3 eV, (b) the peak at ~ -2 eV, (c) the shoulder of the latter peak, and (d) the occupied states at the Fermi level (see Figure 8). Apparently, map "a" can be described as a surface−C_{60} bonding charge distribution, obtained by a HOMO polarized toward the bottom half of the adsorbate. Map "b" shows a nonbonding HOMO-like charge distribution mostly localized on the top half of the adsorbate. The interpretation of map "c" is not straightforward: it possibly corresponds to states with mixed bonding/antibonding character with respect to the adsorbate−substrate interaction and certainly includes the participation of LUMO states (see the presence of shared charge density in the 5:6 bonds at the bottom of C_{60}). For map "d", besides an increased metal participation, we note that the shape at the bottom of C_{60} is clearly LUMO-like and that an at least partial substrate−adsorbate bonding character is present.

3.1.4. Comparison between High-Resolution STM Images and DFT Simulated Images. Figure 10 displays high-resolution STM images of a monomer in the most stable M1 adsorption configuration on the (1 × 2)-Pt(110) surface at both positive and negative bias values (left and central colums). In addition,

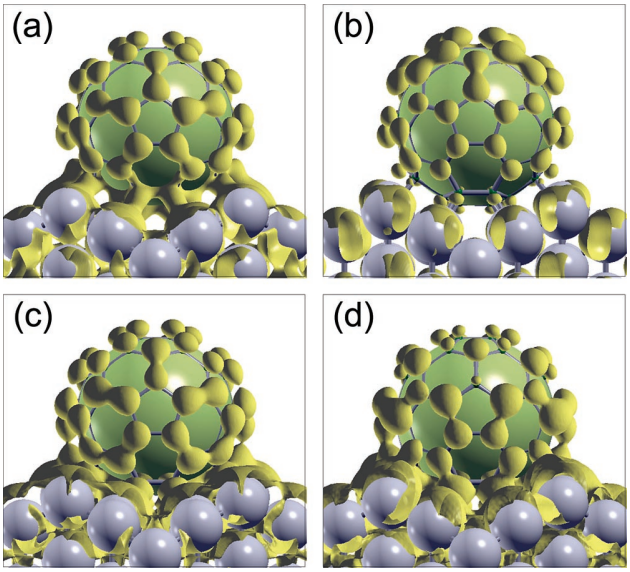

Figure 9. ILDOS for the M1 configuration obtained for the following energy ranges (wrt the Fermi level): (a) [(−2.91) − (−1.89)] eV (isosurface 5×10^{-3} e/a_0^3); (b) [(−1.85) − (−1.34)] eV (isosurface 5×10^{-3} e/a_0^3); (c) [(−1.34) − (−0.27)] eV (isosurface 1×10^{-3} e/a_0^3); and (d) [(−0.27) − (−0.00)] eV (isosurface 3×10^{-4} e/a_0^3).

a rarely observed molecule in the M2 adsorption configuration is reported at positive bias (right column). The rough images (first row) already show an exceptional degree of intramolecular fine structure for data measured at RT, which is further enhanced by convoluting the topographs with their current image (second row, ref 34). The figure definitely confirms that molecules are rotationally frozen and have a well defined orientation with respect to the surface. We obtained simulated STM images of monomers in the two most stable adsorption configurations, M1 and M2 (Figure 3), within the Tersoff−Hamann approach.[35] To improve the quality of the images, we followed the prescription of ref 36, mapping the height of an isodensity surface.

The resulting images reproduce very well the experimental maps, proving that the observed structures indeed correspond to the most stable theoretical minima.

The relative height of the C_{60} molecule with respect to the substrate has been measured as the difference between the maximum height of the chosen isodensity surface and its height on a Pt atom belonging to the [1$\bar{1}$0] ridge. The maximum values are found at −2.0 V for both M1 (6.85 Å) and M2 (6.89 Å); the minimum values are detected at −0.25 V for M1 (5.97 Å) and at 1.0 V for M2 (5.81 Å). There is a more pronounced dependence of the corrugation on the bias if compared with STM measurements (the maximum apparent height difference is about 1 Å in the simulations and 0.6 Å in the experiment), but considering the approximations in the adopted model and a certain degree of uncertainty in the choice of the isodensity surface, the comparison with the experimental values (5.5 ± 0.1 Å for M1 and 5.1 ± 0.1 Å for M2 at bias = 0.2 V; 5.8 ± 01 Å for M1 and 5.5 ± 0.1 for M2 at bias = 2.0 V) is fairly satisfactory.

3.2. C_{60} at Defect Sites. A further interesting feature in Figure 2 is the presence of several molecules (highlighted by white arrows) which are detected as apparently smaller than the others: their dimensions are 13.5 Å in diameter and 3.48 ± 0.11 Å in height, measured with respect to the Pt ridges. These molecules are adsorbed asymmetrically between a Pt ridge and a trough along the [001] direction. Distinct C_{60} molecular species characterized by different shapes and contrast have been

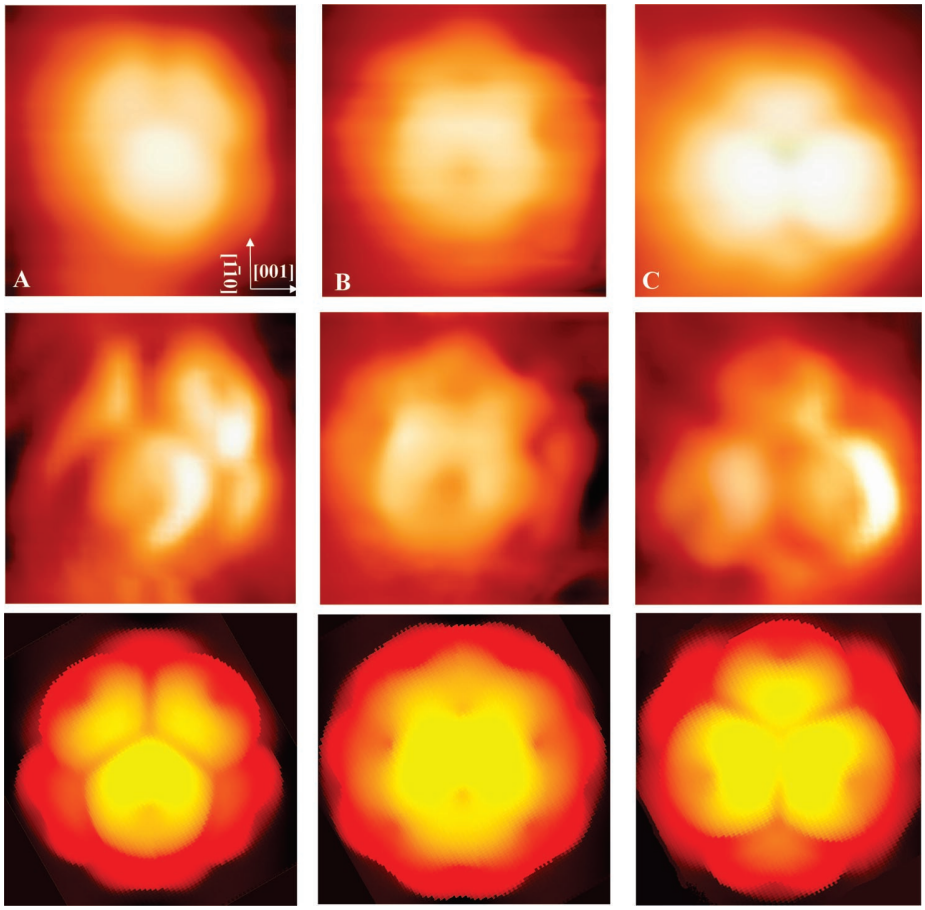

Figure 10. Top row: High-resolution STM images of C_{60} molecules in (a) M1 configuration, bias = +2.0 V; (b) M1 configuration, bias = −2.0 V; and (c) M2 configuration, bias = +2.0 V. Middle row: the same as in the top row, convoluted with the respective current images.[34] Bottom row: DFT simulations. The DFT images were obtained by mapping the vertical coordinate of an isodensity surface. Lighter colors correspond to regions at larger distance from the substrate. Molecules are oriented as in Figure 3.

previously observed on several substrates, like Pd(110),[15] Ni[110],[13] and Ag(100).[16] In this and other cases, the observed bright/dim contrast in STM topographs is too high to be accounted for by purely electronic effects, like in the case of Au(111).[3] Rather, substantial restructuring of the substrate through the formation of nanopits which accommodate the molecules at different physical levels (top layer adsorption, one layer deep pits, two layer deep pits, etc.) explains the observed contrast. The driving force for the restructuring is given by the increase in the C_{60}−metal lateral coordination upon embedding.

In the present case, simple adsorption at RT with no subsequent annealing does not supply enough thermal energy to overcome the kinetic barrier for substrate restructuring/molecular embedding. However, we observe a good correlation between the reduction of the density of defects such as vacancy islands already existing on the clean Pt substrate before C_{60} adsorption and the density of asymmetric and smaller fullerene molecules after deposition. Thus, a way of explaining the existence of "defective" C_{60} monomers on the Pt(110) surface considers their adsorption on the observed defects.

The nature of these defects can be elucidated by noting that (a) smaller molecules appear to be separated from symmetrically adsorbed molecules in monomers, dimers, or both by an integer number of lattice parameters along [1$\bar{1}$0]. In addition, as already noted above, (b) the adsorption site is asymmetric with respect to the ridge, and (c) the apparent height difference between larger and smaller molecules is 2.08 ± 0.14 Å. If we assume that bright molecules occupy bridge (B) sites on the second Pt

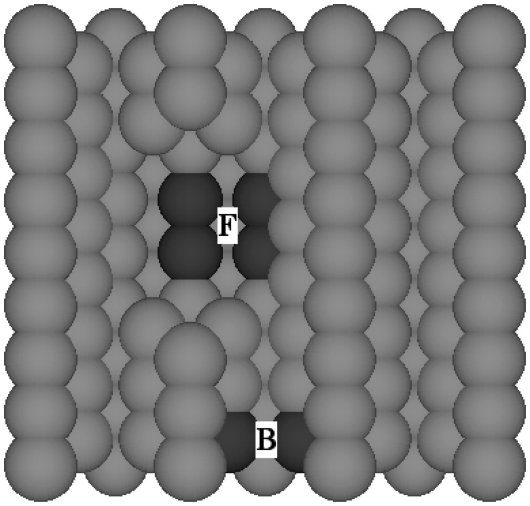

Figure 11. Bridge site (B) in the second Pt atomic layer in the (1 × 2) trough and four-fold hollow site (F) in a nanopit exposing the third layer Pt atoms.

atomic layer (see Figure 11) as determined by DFT calculations, we can explain the three observations reported above by assuming the adsorption of C_{60} in two layers deep nanopits, on four-fold (F) sites of the third Pt layer, as depicted in Figure 11. The pit is obtained by removing four Pt atoms on a ridge and three Pt atoms in the second layer on either side of the ridge. The reduced lateral coordination of the molecule on

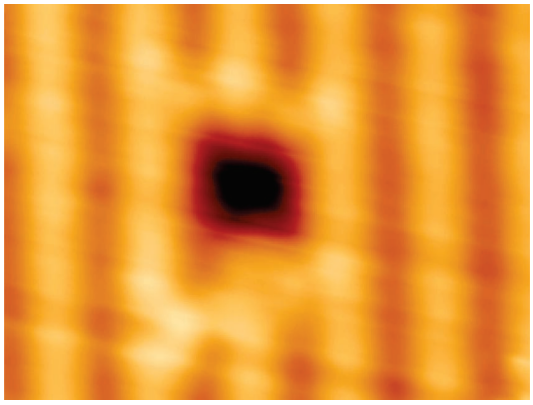

Figure 12. STM topograph (bias = 0.055 V; I_t = 1.37 nA; 4 nm × 5 nm) of a nanopit in the clean (1 × 2)-Pt(110) surface.

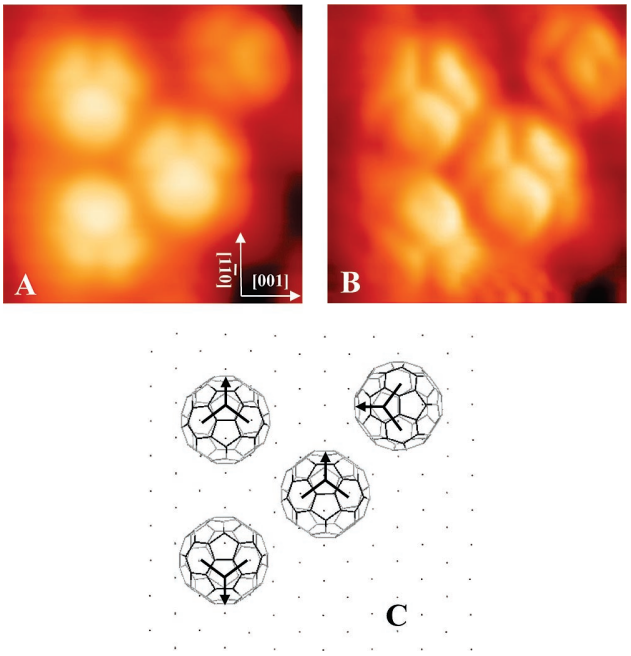

Figure 13. (a) Cluster of C_{60} molecules deposited on the Pt(110) surface at RT (bias = 2.1 V; I_t = 0.42 nA; 3.1 nm × 3.1 nm). (b) The same as in (a) but convoluted with the current image.[34] (c) Orientation of the LUMO nodes (lines) with respect to the molecular cage.

moving from the trough to the pit is partially compensated by the increased vertical coordination on going from a bridge to a four-fold hollow site. Figure 12 shows a close up of a typical pit detected on the clean (1 × 2)-Pt(110) surface prior to C_{60} dosing: its width along the ridge direction is 13.0 ± 0.2 Å which is consistent with the diameter of "small" molecules, while its apparent depth (1.1 ± 0.1 Å) is twice the apparent depth of the troughs with respect to the ridges (0.5 ± 0.1 Å) and hence consistent with a two layers deep well.

Figure 13 is a high-resolution STM image of a cluster of C_{60} molecules on the (1 × 2)-Pt(110) surface. By comparison with Figure 10, it is easily deduced that molecules in the trimer in the central part of Figure 13 face the substrate surface with a 5:6 bond parallel to the [001] direction, as shown in Figure 13c. A particularly interesting feature appears in the upper right corner of the figure: a molecule characterized by a lower apparent height with respect to the others and rotated by 90° with respect to the C_{60} units in the trimer. The latter is composed by a single molecule (right) over a trough and a couple of buckyballs aligned along the [1$\bar{1}$0] direction on the nearby trough of the (1 × 2) reconstruction of the substrate (left).

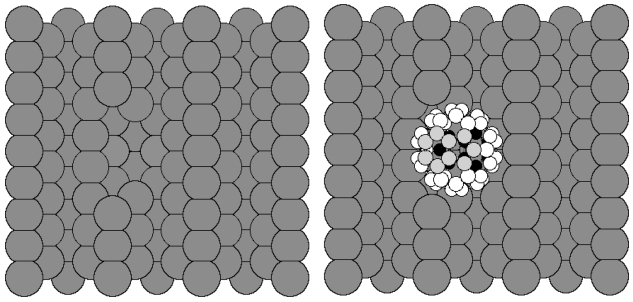

Figure 14. Nanopit accommodating the rotated C_{60} molecule of Figure 13 (left). Orientation of the C_{60} molecule within the pit (right). The lowermost (topmost) pentagon−hexagon C rings are reported in black (light gray). Other C atoms are depicted in white. Pt atoms are gray.

The separation along the [001] direction between the couple and the single molecule is twice the distance between the single molecule and the rotated molecule to the right; that is, the "defective" molecule is offset by half a lattice parameter of the × 2 reconstruction along [001] with respect to the symmetric adsorption site over the trough. However, at variance with the minority molecules discussed above, lying in nanopits as the one depicted in Figure 11, the distance of the defective molecule with respect to the regular ones (i.e., those lying symmetrically over the troughs) amounts to (n + 1/2) Pt lattice parameters along the [1$\bar{1}$0] direction. In addition, the difference in apparent height between the defective molecule and the trimer of regular molecules is only ∼1.0 Å.

The molecular configuration which is consistent with all of these observations is depicted in Figure 14. The adsorption site is a nanopit obtained by removing three Pt atoms from a ridge and two Pt atoms in the underlying second layer (see Figure 14, left). The molecule lies in the pit facing the surface with a 5:6 bond parallel to [1$\bar{1}$0] (Figure 14, right). In order to keep acceptable bond lengths, it is rotated by approximately 10° toward the vacancy on the ridge with respect to a pure 5:6 orientation. This means that the lowermost five-membered ring facing the substrate is almost parallel to the nominal (110) surface. (It is off the (110) plane by only 2−3°.)

4. Conclusion

A comprehensive experimental and theoretical investigation of the initial stages of C_{60} chemisorption on (1 × 2)-Pt(110) at RT has been performed by means of STM and DFT calculations.

The majority molecular species observed in STM experiments consists of isolated monomers sitting symmetrically over the troughs between two neighboring Pt rows of the (1 × 2) reconstructed substrate surface. Because of the strong C_{60}−(1 × 2)-Pt(110) interaction, the strongest ever calculated for fullerene chemisorption on metallic surfaces (E_{ads} = 3.81 eV), molecular diffusion on the substrate is frozen at RT. However, the observation of an almost unique molecular orientation with respect to the substrate in highly resolved STM images shows that a limited degree of rototranslational motion immediately after landing on the surface is allowed in order to optimize bonding to the Pt surface, thus avoiding the many local minima revealed by DFT optimizations. By combining STM and DFT calculations, it has been determined that C_{60} molecules are adsorbed in four-fold hollow sites of the second substrate layer and face the surface by means of a (5:6) C−C bond parallel to the [001] substrate direction. On this basis, experimental STM images displaying a high degree of intramolecular fine structure at RT have been reproduced by means of DFT calculations within the Tersoff−Hamann approach. Despite some indications

of a modest C_{60} electron density depletion, analyses of maps of charge density flows, ILDOS and DOS curves consistently converge on the picture of a covalent substrate−adsorbate interaction.

A minority fraction of molecules is shown to adsorb over substrate defects. By carefully determining the registry and the height of the latter with respect to the regularly adsorbed monomers, a detailed indirect characterization of surface defects has been shown to be viable.

The structure of C_{60} 2D ordered phases on (1 × 2)-Pt(110) will be discussed in a forthcoming paper.[21]

Acknowledgment. This work has been partially funded by MIUR through the FIRB research program *"Nano- and micro-spectroscopy by synchrotron radiation integrated with advanced STM/AFM systems to study manmade atomic scale functional materials"* (prot. N. RBNE0155X7) and by the University of Padua through Grant CPDA038285. Calculations have been performed by using the Quantum-ESPRESSO package[37] and run at CINECA (Bologna, Italy) and at LICC. We acknowledge a computer time grant from CINECA and INSTM (Firenze, Italy) under the "Super-Progetti di calcolo" program. Molecular graphics have been generated by XCrysDen.[38]

References and Notes

(1) Wilson, R. J.; Meijer, G.; Bethune, D. S.; Johnson, R. D.; Chambliss, D. D.; de Vries, M. S.; Hunziker, H. E.; Wendt, H. R. *Nature* **1990**, *348*, 621.

(2) Magnano, E.; Vandré, S.; Goldoni, A.; Laine, A. D.; Currò, G. M.; Santaniello, A.; Sancrotti, M. *Surf. Sci.* **1997**, *377*−*379*, 1066.

(3) Rogero, C.; Pascual, J. I.; Gómez-Herrero, J.; Baró, A. M. *J. Chem. Phys.* **2002**, *116*, 832.

(4) Rowe, J. E.; Rudolf, P.; Tjeng, L. H.; Malic, R. A.; Meigs, G.; Chen, C. T.; Chen, J.; Plummer, E. W. *Int. J. Mod. Phys. B* **1992**, *6*, 3909.

(5) Cepek, C.; Goldoni, A.; Modesti, S. *Phys. Rev. B* **1996**, *53*, 7466.

(6) Hashizume, T.; Motai, K.; Wang, X. D.; Shinohara, H.; Saito, Y.; Maruyama, Y.; Ohno, K.; Kawazoe, Y.; Nishina, Y.; Pickering, H. W.; Kuk, Y.; Sakurai, T. *Phys. Rev. Lett.* **1993**, *71*, 2959.

(7) Giudice, E.; Magnano, E.; Rusponi, S.; Boragno, C. Valbusa U. *Surf. Sci.* **1998**, *405*, L561.

(8) Guo, S.; Fogarty, D. P.; Nagel, P. M.; Kandel, S. A. *J. Phys. Chem. B* **2004**, *108*, 14074.

(9) Wang, L. T.; Cheng, H. P. *Phys. Rev. B* **2004**, *69*, 045404.

(10) He, H.; Swami, N.; Koel, B. E. *Thin Solid Films* **1999**, *348*, 30.

(11) Costantini, G.; Rusponi, S.; Giudice, E.; Boragno, C.; Valbusa, U. *Carbon* **1999**, *37*, 727.

(12) Kuk, Y.; Kim, D. K.; Suh, Y. D.; Park, K. H.; Noh, H. P.; Oh, S. J.; Kim, S. K. *Phys. Rev. Lett.* **1993**, *70*, 1948.

(13) Murray, P. W.; Pedersen, M. Ø.; Lægsgaard, E.; Stensgaard, I.; Besenbacher, F. *Phys. Rev. B* **1997**, *55*, 9360.

(14) Pedio, M.; Felici, R.; Torrelles, X.; Rudolf, P.; Capozi, M.; Rius, J.; Ferrer, S. *Phys. Rev. Lett.* **2000**, *85*, 1040.

(15) Weckesser, J.; Cepek, C.; Fasel, R.; Barth, J. V.; Baumberger, F.; Greber, T.; Kern, K. *J. Chem. Phys.* **2001**, *115*, 9001.

(16) Pai, W. W.; Hsu, C. L. *Phys. Rev. B* **2003**, *68*, 121403.

(17) Lu, X.; Grobis, M.; Khoo, K. H.; Louie, S. G.; Crommie, M. F. *Phys. Rev. B* **2004**, *70*, 115418.

(18) Felici, R.; Pedio, M.; Borgatti, F.; Iannotta, S.; Capozi, M.; Ciullo, G.; Stierle, A. *Nat. Mater.* **2005**, *4*, 688.

(19) Speller, S.; Kuntze, J.; Rauch, T.; Bömermann, J.; Huck, M.; Aschoff, M.; Heiland, W. *Surf. Sci.* **1996**, *366*, 251.

(20) Orzali, T.; Casarin, M.; Granozzi, G.; Sambi, M.; Vittadini, A. *Phys. Rev. Lett.* **2006**, *97*, 156101.

(21) Casarin, M.; Forrer, D.; Orzali, T.; Petukhov, M.; Sambi, M.; Tondello, E.; Vittadini, A.; *J. Phys. Chem. C*, to be submitted.

(22) Perdew, J. P.; Burke, K.; Ernzerhof, M. *Phys. Rev. Lett.* **1996**, *77*, 3865.

(23) Vanderbilt, D. *Phys. Rev. B* **1990**, *41*, 7892.

(24) Nakamura, J.; Nakayama, T.; Watanabe, S.; Aono, M. *Phys. Rev. Lett.* **2001**, *87*, 48301.

(25) Matsumoto, M.; Inukai, J.; Tsutsumi, E.; Yoshimoto, S.; Itaya, K.; Ito, O.; Fujiwara, K.; Murata, M.; Murata, Y.; Komatsu, K. *Langmuir* **2004**, *20*, 1245.

(26) Hobbs, C.; Kantorovich, L.; Gale, J. D. *Surf. Sci.* **2005**, *591*, 45.

(27) Hirsh, H. *J. Phys. Chem. Solids* **1997**, *58*, 1729.

(28) It should be noted that many calculations reported in literature adopted the local density functional, which overestimates the C_{60} surface interaction by ∼30% (see ref 26).

(29) Vittadini, A.; Selloni, A. *J. Chem. Phys.* **2002**, *117*, 353.

(30) Lide, D. R., Ed. *CRC Handbook of Chemistry and Physics*, 78th ed.; CRC Press: Boca Raton, FL, 1998.

(31) Stengel, M.; De Vita, A.; Baldereschi, A. *Phys. Rev. Lett.* **2003**, *91*, 166101.

(32) For details about the calculation of partial density of states and integrated local density of states, the reader is referred to ref 33.

(33) Kokalj, A.; Dal Corso, A.; de Gironcoli, S.; Baroni, S. *J. Phys. Chem. B* **2002**, *106*, 9839.

(34) Pascual, J. I.; Gómez-Herrero, J.; Rogero, C.; Baró, A. M.; Sánchez-Portal, D.; Artacho, E.; Ordejón, P.; Soler, J. M. *Chem. Phys. Lett.* **2000**, *321*, 78.

(35) Tersoff, J.; Hamann, D. R. *Phys. Rev. Lett.* **1983**, *50*, 1998.

(36) Lazzeri, M.; Selloni, A. *Phys. Rev. Lett.* **2001**, *87*, 266105.

(37) Baroni, S.; dal Corso, A.; de Gironcoli, S.; Giannozzi, P.; Cavazzoni, C.; Ballabio, G.; Scandolo, S.; Chiarotti, G.; Focher, P.; Pasquarello, A.; Laasonen, K.; Trave, A.; Car, R.; Marzari, N.; Kokalj, A. http://www.p-wscf.org (accessed May 28, 2007).

(38) Kokalj, A. *Comp. Mater. Sci.* **2003**, *28*, 155. Code available from http://www.xcrysden.org (accessed May 28, 2007).

Temperature-Dependent Self-Assemblies of C_{60} on (1 × 2)-Pt(110): A STM/DFT Investigation

T. Orzali,[†,‡] D. Forrer,[†,‡] M. Sambi,[*,†,‡] A. Vittadini,[†,‡,£] M. Casarin,[†,‡] and E. Tondello[†,‡]

Dipartimento di Scienze Chimiche, Università di Padova, Consorzio INSTM, and ISTM-CNR, Via Marzolo 1, 35131 Padova, Italia

Received: July 30, 2007; In Final Form: October 5, 2007

Thermal self-assembly of C_{60} on (1 × 2)-Pt(110) following room-temperature deposition has been studied by means of scanning tunneling microscopy (STM), low-energy electron diffraction (LEED), and density functional theory (DFT) calculations. Two distinct C_{60} chemisorption phases have been identified and characterized as a function of the annealing temperature. After a thermal treatment at 700 K, islands of a C_{60} quasi-hexagonal lattice form. These islands are characterized by the highest surface density so far reported for a two-dimensional surface-supported fullerene phase (the surface area per molecule is 87.0 Å^2), with intermolecular nearest-neighbor distances equal to 9.6 ± 0.1 Å. Embedded nanowires of fullerene dumbbell dimers (with an intermolecular distance equal to 9.2 ± 0.1 Å) occasionally nucleate within this high-density phase following a "molecular zip" mechanism. Highly site selective chemisorption driven by the particularly strong overlayer−substrate bonding is proposed to be responsible for the first reported example of surface-templated chemical bond formation between fullerene molecules. After annealing at 850 K, an oblique C_{60} chemisorption phase forms. This is characterized by a tetramolecular basis associated to each lattice point of the two-dimensional superstructure and by a peculiar bright−dim contrast in STM images acquired at positive sample bias values. The combination of high-resolution STM images with LEED data and DFT calculations leads to the conclusion that the (1 × 2) substrate reconstruction is lifted at the fullerene−platinum interface and also provides a detailed description of the molecular bonding sites and orientations found within the phase. It is proposed that the main factor ruling the interconversion of chemisorption phases is the variation of substrate atom mobility as a function of temperature.

1. Introduction

Since the discovery of C_{60} about two decades ago,[1,2] the deposition and ordering of fullerenes at single-crystal surfaces has rapidly grown into a substantial part of the scientific endeavors aimed at elucidating their structural, electronic, and functional properties. The interest is motivated in the first place by technologically relevant issues such as the exploitation of fullerenes, either alkali-doped or derivatized, in molecular electronic and nonlinear optical devices. To this end, a clear understanding of the modifications of molecular electronic and transport properties induced by bonding with the substrate is of critical importance. If a rather simple picture of fullerene bonding to surfaces was initially expected,[3] essentially based on weak van der Waals (VdW) interactions, it has subsequently become common knowledge that a great variety of bonding mechanisms (associated with different degrees of substrate−molecule charge transfer, leading from predominantly ionic to predominantly covalent bonding[4]) and a wide range of bonding strengths exist, with freely diffusing molecules at room temperature (RT) or below at one end[5−8] and strongly bound and rotationally frozen species characterized by well-defined molecular orientations with respect to the surface at the other.[9−11] Another issue concerns the effects of the interplay between intermolecular (lateral) and overlayer−substrate (vertical) interactions in determining the structural and electronic properties of ordered 2D fullerene arrays at surfaces, which are also influenced by the lattice matching with the substrate. If the latter is clearly a key factor, adsorbate-induced surface reconstructions are also rather common.[12−14]

As far as C_{60} deposited on metal single-crystal surfaces is concerned, a substantial amount of information has been gathered through the years, and a comprehensive picture of trends, similarities, and differences across the periodic table is beginning to develop. Particular attention has been devoted to group 10 and 11 metals used as substrates for fullerene self-assembling, and studies devoted to the structure and the bonding properties of C_{60} on Ni(110),[9,12] Ni(111),[15] Pd(110),[14,16] Pt(111),[4,9,10,17,18] Cu(100),[19] Cu(110),[12,19,20] Cu(111),[5,8,15,19,21] Ag(100),[6,22−24] Ag(110),[25−27] Ag(111),[21,28,29] Au(100),[30] Au(110),[13,31,32] and Au(111)[28,33−35] are now available in the literature. Fullerenes adsorbed at these and other surfaces generally tend to form hexagonal close-packed arrangements in order to optimize their lateral interactions. These are predominantly of the VdW type, with dipolar contributions arising from the uneven charge density distribution on single and double C−C bonds.[36,37] The resulting C_{60} nearest-neighbor (NN) distances are generally close to the 10.04 Å found in the fcc fullerite crystal. Distortions from perfect hcp fullerene layers are frequently observed; they arise when overlayer−substrate interactions are strong (leading to immobile adsorbates) and when there is a certain amount of lattice mismatch between the overlayer and the substrate. When these conditions are met,

* To whom correspondence should be addressed. E-mail: mauro.sambi@unipd.it. Fax: +39 049 827 5161.
† Università di Padova.
‡ Consorzio INSTM.
£ ISTM-CNR.

10.1021/jp076024a CCC: $40.75
Published on Web 12/21/2007

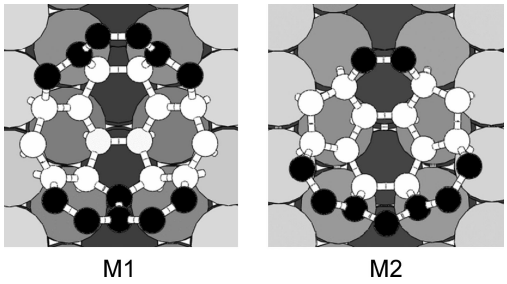

Figure 1. The two most stable chemisorption configurations of a single C_{60} molecule on (1 × 2)-Pt(110). Only the bottom part of C_{60} is shown. Large and small circles represent Pt and C atoms, respectively. Darker Pt atoms are deeper into the surface. White (black) circles represent C atoms which are bonded (not bonded) to the surface.[11]

$C_{60}-C_{60}$ NN distances may increase along certain directions and, to a minor extent, diminish along others. In these cases, the optimization of vertical overlayer−substrate bonding is clearly privileged with respect to intermolecular interactions. A particularly high NN distance anisotropy is found on Cu(110), where values ranging from 9.7 to 11.1 Å are found.[20] Similar expansions are found on other surfaces, while contractions are generally smaller due to the steepness of the repulsive region in the VdW potential.

It is often observed that strong vertical interactions are able to induce substantial reconstructions of the overlayer. In these cases, the driving force of the transformation is generally attributed to the increase of fullerene−metal bonding through partial embedding of C_{60} molecules in the surface atomic layers of the substrate. This may lead to varying degrees of reorganization of surface atoms, from the formation of ordered monatomic vacancies even on the lowest surface free-energy surfaces (Pt(111)[18]) to disordered (Ag(100)[24]) or ordered (Pd(110),[14] Au(110)[13]) polyatomic nanopits which accommodate the fullerene molecules, down to unusual missing row reconstructions, as on Ni(110).[12]

In a previous paper,[11] we investigated in detail the initial stages of C_{60} adsorption on the (1 × 2) reconstructed Pt(110) surface by means of scanning tunneling microscopy (STM) and density functional theory (DFT) calculations. Isolated molecules were found to bind to the surface with strong covalent bonds, leading to immobile adsorbates at room temperature. In the most stable adsorption configuration (M1 in Figure 1), the molecule approximately places a 5−6 bond (b56) on a bridge site of the second Pt layer, perpendicularly oriented with respect to the troughs of the (1 × 2) reconstruction. In the second most stable configuration (M2), the C_{60} molecule places a hexagonal ring (r6) approximately onto a fourfold site in the second Pt layer (see Figure 1). In both configurations, molecules undergo a slight polar tilt along the $[1\bar{1}0]$ direction with respect to pure b56 and r6 bonding.

In this paper, we describe the self-organization of C_{60} on (1 × 2)-Pt(110) into ordered islands upon thermal treatments, a missing tessera in the fascinating mosaics of fullerene chemisorption on transition-metal surfaces sketched above. C_{60} is known to bind strongly to the Pt(111) surface[18] leading to immobile adsorbates even at high temperatures. Ordered overlayers are eventually obtained by thermal annealing above 700 K. On the other hand, the missing row reconstruction of Pt(110), similar to that of the Au (110) case, produces a highly anisotropic surface corrugation of the substrate (with alternating ridges and troughs along the [001] direction, which in turn are atomically smooth along the $[1\bar{1}0]$ azimuth). This surface topology certainly poses strong constraints to molecular diffusion and assembling of ordered islands; in principle, the $[1\bar{1}0]$-oriented trenches may be easily identified as the privileged pathways for molecular migration. This scenario can be further complicated owing to possible adsorbate-induced de-reconstructions of the (1 × 2)-Pt(110) surface.[38] It is therefore interesting to study the interplay between molecular bonding to the substrate, lateral intermolecular interactions, substrate restructuring, and kinetic constraints to molecular motion in the presently studied system. These factors will be shown to ultimately lead to several unique features, such as the densest 2D C_{60} phase reported in the literature, the first reported example of surface-induced fullerene dimerization producing "molecular zips", that is, straight fullerene dimers, nanowires, and so forth. Though by no means exhaustive, this paper shows that the combination of high-resolution STM, low-energy electron diffraction (LEED), and DFT calculations gives definite answers to some of these issues while allowing us to make reasonable guesses about others.

2. Experimental and DFT Calculations

The experiments were performed with an Omicron scanning tunneling microscope (VT-STM) operating in ultrahigh vacuum at a base pressure of 5×10^{-11} mbar. The Pt(110) single crystal was prepared by repeated cycles of argon ion sputtering (kinetic energy, KE = 2 keV) and annealing at $T = 970$ K, followed by cooling in an oxygen atmosphere ($p(O_2) = 5 \times 10^{-7}$ mbar) down to 700 K. The cleaning cycles were repeated until a well-ordered (1 × 2) reconstructed surface was obtained, as judged by LEED. C_{60} (99% purity) was sublimed at ∼820 K from a tungsten crucible mounted on an Omicron EFM3 evaporator. The Pt specimen was kept at RT during sublimation. The crucible was outgassed for a long time to avoid impurities while depositing fullerenes onto the substrate. Coverages are given as fractions of a monolayer (ML), with 1 ML corresponding to a close-packed quasi-hexagonal arrangement of C_{60} units with a surface density of 0.125 molecules per unit cell of the unreconstructed substrate surface (see section 3.2). Self-organization of ordered fullerene islands was achieved by annealing the deposited C_{60} layers at 700 and 850 K for several minutes.

STM measurements suggest a substantial restructuring of the fullerene/platinum interface upon C_{60} thermal self-organization. For this reason, DFT calculations were performed as an aid in the determination of the most probable C_{60}/Pt interfacial structure. Calculations were run within the supercell method using a plane-wave basis set, Vanderbilt ultrasoft pseudopotentials,[38] and the Perdew−Burke−Ernzerhof[39] exchange−correlation functional, as described more extensively in our previous work.[11] A kinetic energy cutoff of 20 Ry was adopted for the wave functions, while 160 Ry was used for the augmentation charge. A total of 4 and 11 electrons were considered for C and Pt atoms, respectively. To represent the (1 × 2)-Pt(110) surface, models consisting of repeated slabs were adopted, each including five Pt atomic layers into a rhombic surface supercell containing 12 Pt atoms per layer (the one called "S1" in our previous paper). Fullerene chemisorption on several surface defects (as specified in section 3.3) involved only the top side of the slab, while the two bottommost Pt layers were kept frozen in their own bulk positions. Geometry optimizations were performed by a Broyden−Fletcher−Goldfarb−Shanno algorithm for the relevant molecular orientations. Because of the model size, these runs were performed with a Γ-point Brillouin zone sampling. We checked, by increasing the computational accuracy (plane-wave cutoff, surface cell, slab

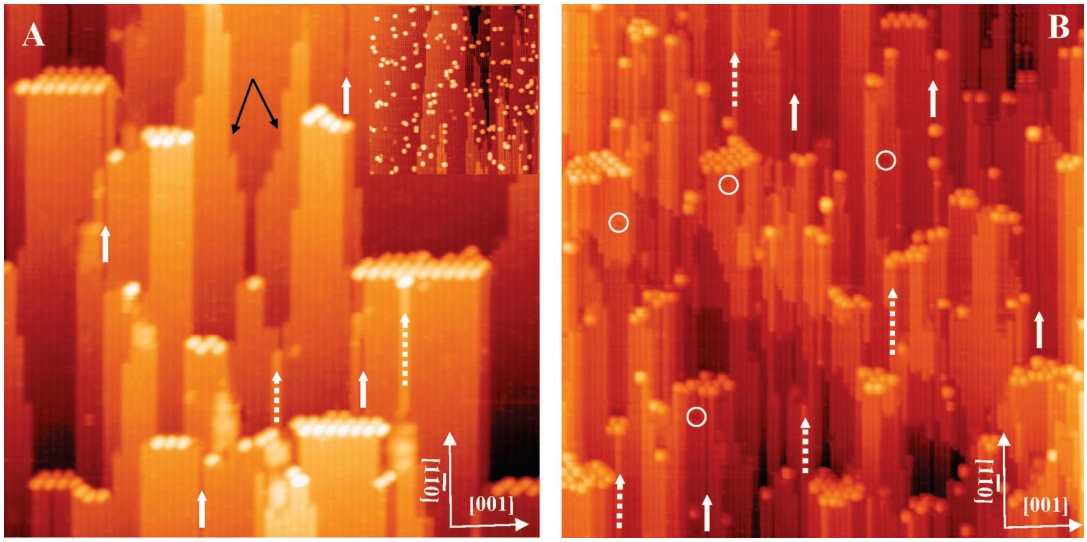

Figure 2. STM images of the (1 × 2)-Pt(110) reconstructed surface annealed at (A, left) 700 K and (B, right) 850 K. (A) coverage = 0.07 ML; bias = 0.29 V; I_T = 1.55 nA; 60 nm × 60 nm. Inset: STM image of the Pt surface before the annealing treatment (bias = 0.14 V; I_T = 1.50 nA; 76 nm × 78 nm). (B) coverage = 0.08 ML; bias = 0.2 V; I_T = 1.7 nA; 80 nm × 80 nm. White arrows indicate missing (full line) and added (dashed line) Pt atomic rows. Circles indicate pits in terraces. Black arrows point to residual fish-scale reconstructed steps.

thickness, BZ sampling), that the obtained adsorption energies converged within 0.1 eV, which is sufficient for our purposes. Simulated STM images were obtained within the Tersoff−Hamann approach.[40] To improve the quality of the images, we followed the prescription of ref 41, mapping the height of an isodensity surface.

3. Results and Discussion

3.1. The Effects of Annealing Treatments. Figure 2A shows the effect of an annealing treatment at 700 K followed by cooling back to 300 K on a submonolayer of C_{60} deposited on the (1 × 2)-Pt(110) surface. The inset represents the dosed surface at RT prior to annealing. Molecular migration toward kinks and step edges is observed, and small-island nucleation occurs, whose size depends on the fullerene dose. The temperature-induced increase of the diffusion coefficient allows nucleation exclusively at step edges since, at this temperature, the mobility of C_{60} molecules on Pt(110) is high enough for their mean free path to match the mean terrace width. Due to the anisotropy of the (1 × 2)-Pt(110) surface, diffusion paths along the [110] direction can be expected to be predominant. This is experimentally confirmed by the large population of single molecules bonded at corner sites and at step edges that are perpendicular to Pt rows, whereas steps parallel to Pt rows are never decorated. Fullerene islands appear to partly remove the typical fish-scale pattern[42,43] of the clean surface by stabilizing substrate steps parallel to the [001] direction, which give a rectangular shape to the Pt terraces. These features are never observed on the clean Pt substrate, where the fish-scale reconstruction arises from the greater stability of (111) facets (terminating steps parallel to[1$\bar{1}$0]) with respect to that of (100) facets (terminating steps parallel to [001]).[43,44] Figure 2A shows that the substrate surface has undergone a certain degree of restructuring, which implies substrate mass transport, upon annealing in the presence of C_{60}. Step profiles not decorated by fullerene molecules maintain the fish-scale pattern (see the central upper part of Figure 2A, indicated by black arrows), while fullerene clusters are elongated at newly formed step edges parallel to the [001] direction. Additional evidence of substrate mass transport upon C_{60} cluster nucleation during the annealing treatment is provided by the formation of added (white arrows, full line) and missing (white arrows, dashed lines) Pt atomic rows in/on the substrate terraces. However, the (1 × 2) periodicity of the substrate at this annealing temperature is substantially left intact at the terraces not covered by C_{60} clusters. In contrast, the surface morphology clearly changes if the annealing is performed at 850 K (Figure 2B); large and flat terraces are disrupted in favor of a highly corrugated substrate topography produced by a high surface density of missing rows, added rows, and polyatomic pits. Overall, this indicates that a substantial mass transport occurs in the substrate upon nucleation of fullerene ad-islands.

3.2. Annealing at 700 K. The Quasi-hexagonal Metastable Phase. Figure 3A shows an extended fullerene island nucleated upon annealing at 700 K at a kink in a (1 × 2) terrace. A domain boundary is clearly visible (red thick line) between molecules aligned with the troughs and molecules aligned with the ridges (marked by black hair lines) of the surrounding uncovered (1 × 2) terraces. Since it is known from our previous work that C_{60} on Pt(110) chemisorbs in the troughs of the (1 × 2) reconstruction, we indicate the lower left portion of the island reported in Figure 3A as the regular domain (RDo) and the upper left portion as the shifted domain (ShDo).

Because the height of both domains is the same, the C_{60} chemisorption in the ShDo must necessarily imply a reorganization of the underlying substrate surface; on-ridge chemisorption would place the molecules in the ShDo approximately 1.3 Å higher than the molecules in the RDo.

We can figure out several models to describe these observations. A first possibility is that each C_{60} unit in the ShDo resides in a Pt vacancy at the ridge of the (1 × 2) reconstruction, which should be at least biatomic (the length of the biatomic vacancy is 8.3 Å along [1$\bar{1}$0], i.e., comparable to the width of the trough along [001] (7.85 Å); see Figure 4). (We remind the reader that similar nanopits are produced by the adsorption of C_{60} on Pd(110).[14]) This hypothesis implies that the ridges of the (1 × 2) reconstruction, albeit defective, are preserved at the C_{60}/Pt interface in-line with the ridges of the surrounding (1 × 2) terraces. The biatomic pit on the ridge is a necessary and sufficient condition to achieve the same height of both domains; however, it is by no means a unique description of the along-ridge chemisorption site. In fact, different degrees of filling of

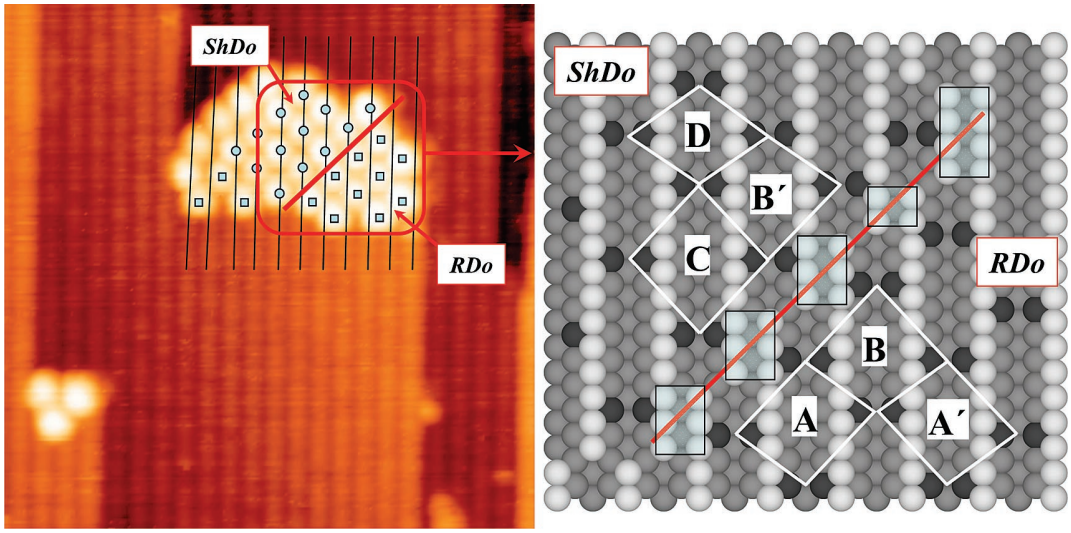

Figure 3. (A) (left): STM image of a fullerene island nucleated at a Pt step edge upon annealing at 700 K; bias = 1.1 V; I_T = 1.13 nA; 24 nm × 24 nm. Black lines correspond to ridges of the (1 × 2) substrate reconstruction of the clean Pt terraces surrounding the island. C_{60} molecules aligned with the troughs (the ridges) of the clean (1 × 2) reconstruction are marked with squares (circles). The phase boundary between the two types of molecules is marked by a thick line. (B) (right): Solid sphere model of the phase boundary. C_{60} molecules are not shown for clarity. C_{60} chemisorption sites (bridge sites in the II Pt layer) are marked as dark gray in the troughs of both the regular (RDo) and the shifted (ShDo) domain. (see text) Topmost Pt atoms are white. Different mutual arrangements of C_{60} molecules are highlighted by white lines and capital letters. Semitransparent rectangles indicate locally (1 × 1) reconstructed Pt patches.

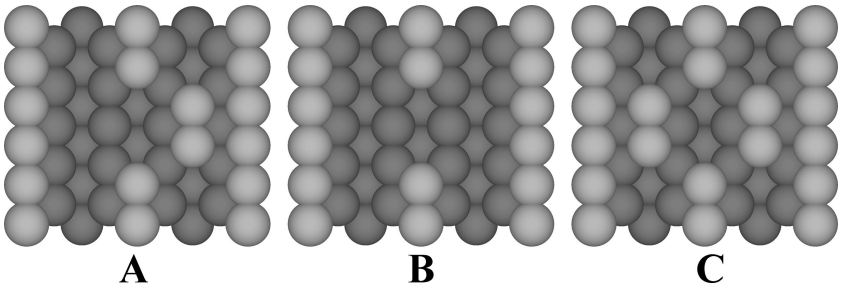

Figure 4. Models for "along-ridge" adsorption sites. Topmost Pt atoms are depicted in lighter gray.

the troughs neighboring the vacancy—with the same Pt atoms removed from the ridge (Figure 4A) and even with additional Pt atoms removed (Figure 4B) or supplied (Figure 4C) by the terrace diffusion field—are also compatible with same-height domains. Of course, other possibilities can be envisaged. However, all of these models can be argued for two reasons. First, they rely on the presence of a regular network of along-ridge Pt vacancies acting as chemisorption sites for C_{60} located exclusively in one domain (ShDo) and on the complete absence of such defects in the other one (RDo). Second, they imply a comparable formation energy for the two domains because these have a similar extension. This is at variance with DFT results for C_{60} chemisorption on sites as those depicted in Figure 4, which consistently yield total energies that are higher by 1.5–2.0 eV (less stable) than those for the in-trough adsorption (the M1 configuration of Figure 1 is assumed for reference).

An alternative and more satisfactory explanation for the occurrence of the ShDo is based on the mechanism for the adsorbate-induced (1 × 2) → (1 × 1) structural transformation of Pt(110) reported by Gritsch et al.,[37] who showed that above a threshold temperature (350 K for CO), adsorption induces a shift of entire ridge portions in the [001] direction by one lattice constant, which leads to the formation of small domains of the (1 × 1) phase.

This mechanism has been applied to the ShDo model in Figure 3B. Now, all C_{60} molecules, irrespective of the domain to which they belong, reside in-trough, thereby avoiding the vacancy network in the ShDo. The Pt ridge portions shifted along [001] in the latter cause the appearance of small (1 × 1) patches in the substrate at the domain boundary, highlighted by semitransparent rectangles in Figure 3B.

In this regard, we show in section 3.3 that annealing of the C_{60}/Pt(110) interface at a higher temperature (850 K) leads to the complete (1 × 2) → (1 × 1) de-reconstruction. Hence, the presence of the domain boundary between the ShDo and the RDo at 700 K can be seen as the onset of the removal of the (1 × 2) reconstruction at the C_{60}/Pt interface, which cannot proceed to completion at this temperature due to kinetic constraints.

If we assume this model for the interfacial structure, we can now reconstruct the registry of the two-domain island reported in Figure 3A by carefully measuring intermolecular distances and angles. As in the case of isolated fullerene molecules on the same substrate,[11] a strong site selection is at work here; all of the molecules within a domain are separated from each other by an integer number of lattice parameters along the [1$\bar{1}$0] direction, which amounts to saying that all of them occupy the same chemisorption site. If an M1-type configuration (see Figure 1) is assumed for in-trough adsorption,[11] the molecular arrangement with respect to the substrate in both domains can be easily worked out, as shown in Figure 3B. Note that the direction of the domain boundary is exactly reproduced. The intermolecular

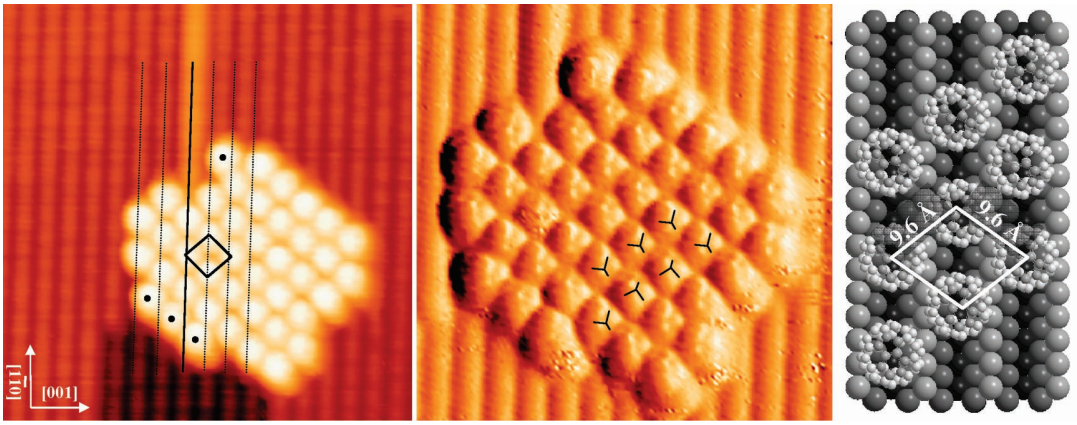

Figure 5. (A) (left): Fullerene island obtained after dosing 0.2 ML of C_{60} on the (1 × 2)-Pt(110) surface and annealing at 700 K; bias = 0.79 V; I_T = 1.13 nA; 17 nm × 17 nm. The solid line represents the phase boundary (coincident with an added row on the upper Pt terrace) between ShDo (left) and RDo (right) chemisorption. Dashed lines serve as a guide to the eye to highlight the molecular registry on either side of the boundary. The quasi-hexagonal unit cell is highlighted. Molecules which are defective with respect to the close-packed arrangement are indicated by black dots. (B) (center): Current image of the same island as that in (A); bias = 0.79 V; I_T = 1.13 nA; 12 nm × 12 nm. Nodes on the LUMO-based C_{60} features are highlighted on a few C_{60} molecules in order to evidence their orientation. (C) (right): Rigid spheres model of the quasi-hexagonal C_{60} arrangement as deduced from STM images. The topmost pentagon−hexagon rings of each molecule are highlighted in dark gray. The quasi-hexagonal unit cell is indicated.

NN distance across the boundary is 11.7 Å, as in the experimental image (Figure 3A).

In the RDo, molecules are invariably separated by 5 Pt lattice parameters along [1$\bar{1}$0] (13.9 Å). This leads to a certain degree of translational randomness within the domain since molecular "strings" in adjacent troughs are offset from each other by either 2/5 or 3/5 of an intermolecular NN distance along [1$\bar{1}$0], which ultimately results in the three different overlayer pseudounit cells shown in Figure 3B: A, its mirror analogue A′, and B. All of them are characterized by two long (11.4 Å) and two short (9.6 Å) intermolecular distances. Interestingly, the latter is shorter than the equilibrium VdW distance in a solid fullerene (10.05 Å), while it is considerably longer than the equilibrium distance in dumbbell fullerene dimers (9.1 ± 0.2 Å[45]). Hence, the vertical overlayer−substrate bonding dominates over lateral intermolecular interactions.

The ShDo shows an even higher degree of translational disorder. The intermolecular separation along [1$\bar{1}$0] varies from 4 (11.1 Å) to 6 (16.6 Å) Pt lattice parameters, which correspond to C and D pseudounit cells, respectively. The C local arrangement is particularly interesting since all four NN distances are equal to 9.6 Å.

The translational disorder found after annealing at 700 K in Figure 3 leads to local variations of the overlayer surface density and therefore does not represent the most effective packing strategy for the molecular monolayer. It is therefore interesting to see if more regularly stacked polymolecular clusters and extended islands can be found at the same annealing temperature.

Figure 5A shows a fullerene ad-island prepared at 700 K wherein a highly regular 2D close-packed arrangement is obtained, corresponding to the "D" mutual arrangement of Figure 3B, i.e., to a rhombic unit cell with 9.6 Å side length. The resulting matrix notation, defined with respect to the unreconstructed substrate surface, is

$$\begin{bmatrix} 2 & 2 \\ -2 & 2 \end{bmatrix}$$

This is the densest 2D fullerene surface phase reported in the literature to date; the surface density is 0.125 molecules per unreconstructed substrate unit cell, and the area per molecule is therefore 87.0 Å^2, that is, 0.5% smaller with respect to that of a perfectly hexagonal close-packed layer adopting C_{60} bulk NN distances. Molecules are aligned in close-packed rows along the [1$\bar{1}$± 2] substrate azimuths, which forms an angle of 54° with respect to the [1$\bar{1}$0] direction, that is, to the ridges of the (1 × 2) reconstruction. The NN intermolecular distance along these close-packed directions is 9.6 Å. Such a short distance, seldom observed on other substrates, is at the lower limit for VdW interactions (shorter distances imply the formation of intermolecular covalent bonds[46]) and is made possible by the very effective chemisorption site selection arising from strong overlayer−substrate bonding. In fact, fullerenes are separated by 11.1 Å along [1$\bar{1}$0], which corresponds to 4 Pt lattice parameters (a_{Pt} = 2.775 Å). This confirms that all of them occupy equivalent chemisorption sites within a domain. We note that in the only reported case of a C_{60} NN distance equal to 9.6 Å (found on Cu (110)[20]), this is limited to a couple of C_{60} molecules, while the next NN molecules in the quasi-hexagonal arrangement are placed at larger distances, thereby producing an overall reduced surface density with respect to that of a perfectly hexagonal close-packed layer adopting C_{60} bulk NN distances.

A careful inspection of Figure 5A reveals that two C_{60} domains coexist within the same island, separated by a boundary which coincides with the Pt added row on the upper substrate terrace, marked by a full line. Although the 2D quasi-hexagonal network is maintained across the boundary, molecules residing on the left of it line up along the ridges of the nearby bare (1 × 2) reconstruction, while those on the right are aligned with the troughs (see the dashed lines), giving rise to the ShDo and RDo, respectively, as in Figure 3. In addition, we point out that several molecules at the island borders (marked by black dots in Figure 5A) reside in sites at 11.7 Å from their NN; they represent the incipient formation of a domain boundary which is symmetry-equivalent to that reported in Figure 3.

Finally, the intramolecular resolution evidenced by Figure 5B allows us to resolve the details of molecular orientation within the close-packed layer. High-resolution images at positive bias values reveal that all of the molecules in the quasi-hexagonal arrangement have the same orientation, as highlighted by black segments, corresponding to LUMO nodal planes,

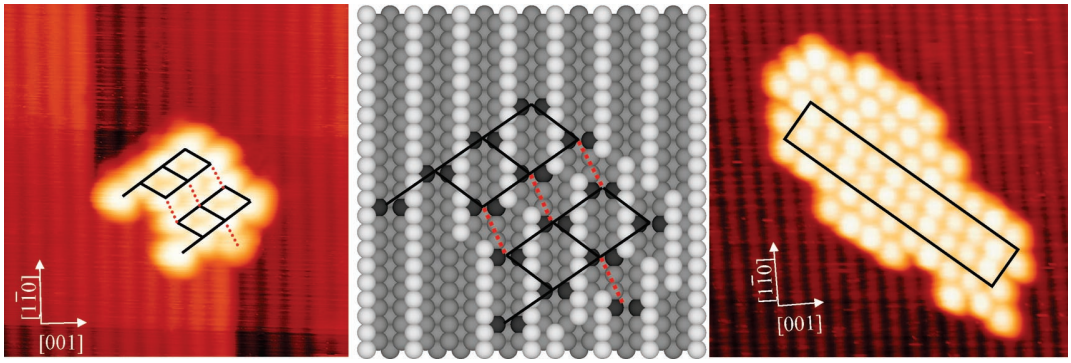

Figure 6. (A) (left): STM image of a fullerene island obtained after dosing 0.2 ML of C_{60} on the (1 × 2)-Pt(110) surface and annealing at 700 K; bias = 0.76 V; I_T = 0.66 nA; 15 nm × 15 nm. Red dashed lines connect sites belonging to different registry domains at a mutual separation of 9.2 Å. (B) (center): Solid sphere model of the phase boundary. C_{60} molecules are not shown for clarity. C_{60} chemisorption sites (M1 sites in the II Pt layer) are marked in dark gray. Topmost Pt atoms are white. (C) (right): STM image of another fullerene island obtained after dosing 0.2 ML of C_{60} on the (1 × 2)-Pt(110) surface and annealing at 700 K; bias = 0.26 V; I_T = 1.13 nA; 18 nm × 18 nm. The black rectangle highlights a nanowire of 10 C_{120} dumbbell dimers embedded in the quasi-hexagonal phase.

superimposed on some C_{60} units. Such nodes are associated with hexagonal rings, while intensity maxima between them correspond to pentagonal rings, as previously discussed.[11] Hence, the molecular adsorption is reminiscent of the M1 configuration reported in Figure 1, except for a marked ($\phi \sim 20°$) azimuthal rotation of each molecule around its vertical axis.

All of the information contained in the STM images of Figure 5A and B is summarized in the model reported in Figure 5C. The model shows that the azimuthal rotation of the C_{60} molecules allows them to face each other via hexagonal rings along the close-packed [1$\bar{1}$±2] directions. It is well-known that this optimizes the intermolecular VdW interactions between C_{60} units.[47] In fact, if all possible mutual orientations of a couple of C_{60} molecules are considered, the interaction energy varies by as much as 150 meV per couple at a distance of 9.5 Å.[48] Coupling through hexagonal or pentagonal rings is computed to be energetically favored, especially if the intermolecular distance is short with respect to the equilibrium distance in bulk fullerite.

A particularly interesting feature detected in several fullerene ad-islands grown by annealing the system at 700 K is displayed in Figure 6. Figure 6A shows a fullerene cluster nucleated at a kink of the (1 × 2) substrate reconstruction, in much the same way as that of the island reported in Figure 3. Also, in this case, a domain boundary between the RDo (upper left portion) and the ShDo (lower right portion) is observed. However (see the model reported in Figure 6B), NN molecules across the boundary (connected by red dashed lines in Figure 6A) are separated by only 3 Pt lattice parameters along the [1$\bar{1}$0] direction (instead of 4, as in the island of Figure 3).

This implies that the C_{60} molecules residing on sites connected by red lines in Figure 6 are only 9.2 ± 0.1 Å apart, that is, too close for VdW interactions. However, this separation fits the theoretical equilibrium distance of fullerene molecules bonded through a [2 + 2] cycloaddition reaction involving two 6−6 bonds very well.[46] As a matter of fact, the so-called C_{120} dumbbell dimers synthesized ex situ and deposited from solution on Au(111) were characterized by means of STM.[45] The observed features, a 9.1 ± 0.2 Å intermolecular distance and a low intensity at positive bias in the intermolecular region (the dimer looks like two closely spaced monomers), are in total agreement with our findings.

The reported measurements do not give access to the details of the dimers' dynamics of formation. Nevertheless, a few remarks can be put forward. In the first place, we note that a dimer is never found isolated within the island body as a single point defect in the 2D overlayer lattice; once a first dimer is formed, it is followed by a cascade of neighboring replicas along a straight line. In other words, it appears that occasionally formed dimers nucleate 1D growth along a definite direction. A rationale to this phenomenon can be given by considering the site-blocking effect exerted by the first dimer, formed by chance at the island growth front, on the possible chemisorption sites for the next C_{60} molecule coming from the terrace diffusion field. Figure 7 shows a close up of the boundary where dimer formation occurs. C_{60} chemisorption sites are highlighted by dark-gray Pt atoms. For clarity, molecules are sketched as gray circles. We first consider a molecule that nucleates an incipient domain boundary by chemisorbing on the Sh1 site. It forms a dimer with the molecule placed in R1, belonging to the already existing pseudohexagonal island. We now move to the neighboring trough to the left of R1.

The closest accessible adsorption sites for a further upcoming C_{60} molecule within this trough are highlighted by couples of green Pt atoms. The first one (Sh2a) is at 9.2 Å from its NN (R2) belonging to the RDo; the second one (Sh2b) is at 19.8 Å from R2. All of the intermediate sites between Sh2a and Sh2b are blocked by the presence of the molecule at Sh1. Hence, if close packing has to be maintained, the upcoming molecule is forced to adsorb on Sh2a, thereby forming a second dimer with the C_{60} molecule residing in R2. By recursion of this "molecular zip" packing scheme based on a site-blocking mechanism, the dimerized linear domain boundary can be explained.

Figure 6C displays an extended nanowire of dumbbell dimers embedded in an island prepared at 700 K. To our knowledge, this is the first observation of surface-templated coherent dimerization of fullerene molecules reported so far.

As to how a C_{60} unit can approach the island growth front at a NN distance of 9.2 Å, thereby overcoming the strong VdW repulsive interactions with its NN molecule, STM data do not provide a direct answer. Certainly, a complex interplay is at work here between the hopping frequency of diffusing molecules, the C_{60} cage distortion modes necessary to allow the intermolecular approach,[49] and the strong interaction with the substrate. It should also be considered that the cycloaddition process between two C−C bonds on adjacent molecules is not likely to occur at the annealing temperature because dumbbell dimers are only stable below 450 K[45] since they decompose to C_{60} monomers if heated above this temperature in an endothermic[49] reaction. Insofar as the formation of each dimer is spurred by that of the preceding one, the on-site residence time for a C_{60} molecule, which happens to initiate the dimer nanowire

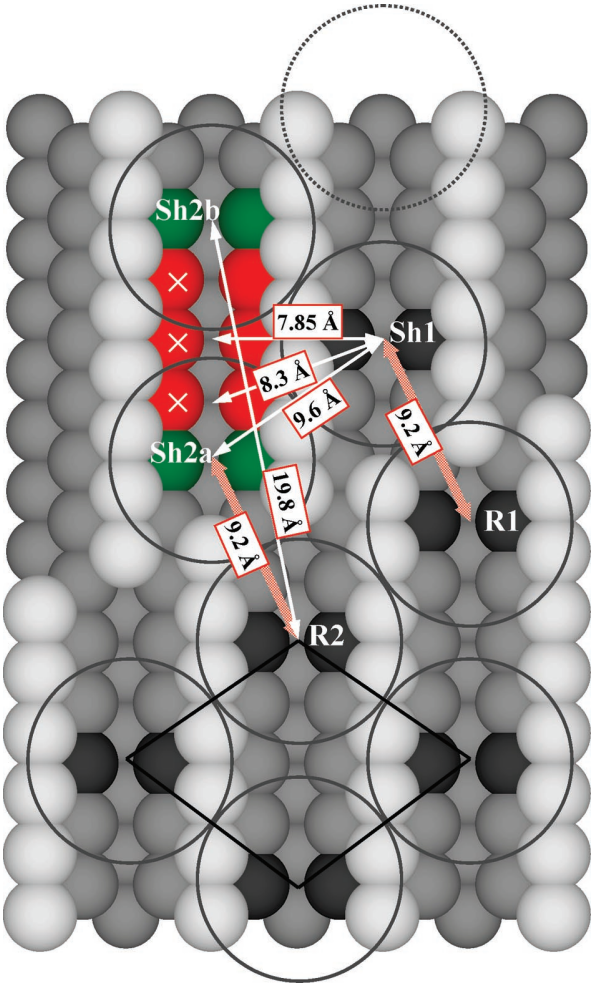

Figure 7. Close up of the boundary where the fullerene dumbbell dimer formation occurs. A regular pseudohexagonal domain (RDo) is marked by dark gray chemisorption sites in the lower part of the model. Occasionally, a molecule approaches the domain boundary at a distance of 9.2 Å (site Sh1) from the NN molecule (site R1) belonging to the RDo. Accessible sites for a C_{60} molecule approaching the already formed R1−Sh1 dimer are in green and marked Sh2a and Sh2b, while unaccessible sites are in red and marked by crosses. The relevant intersite distances are indicated.

by occupying site Sh1 in Figure 7, is suggested to be longer than the formation time of the neighboring R2−Sh2a couple. This is likely to be made possible by the strong bonding with the substrate, which limits the hopping frequency leading to the decay of the R1−Sh1 couple on the time scale of the R2−Sh2a couple formation, and/or by a further upcoming C_{60} molecule along the same Sh1-containing trough (the dashed circle in the upper right corner of Figure 7), which forbids the back-diffusion of the A2-adsorbed molecule. In addition, if the R2−Sh2a couple is able to form before the initial R1−Sh1 one dissociates, the site-blocking effect exerted by the latter on the former should further slow down their decay and therefore stabilize the phase boundary on the time scale of the annealing. In other words, the decay of a single C_{60} pair at dimer-like distance is a singular, uncorrelated event, while the decay of two or more adjacent pairs is a cooperative, correlated, and hence statistically less probable event—the more so, the higher the number of the aligned couples.

3.3. Annealing at 850 K. The Oblique Equilibrium Phase. Figure 8 shows the effect of annealing the (1 × 2)-Pt(110) surface predosed with ∼0.4 ML of C_{60} at 850 K. The inset evidences the random distribution of C_{60} molecules, mostly monomers, on the substrate surface at RT prior to annealing.[11] Upon the thermal treatment, C_{60} units self-organize in compact 2D islands whose structures are markedly different from the quasi-hexagonal phase obtained at 700 K; two domains are now clearly discernible, each one characterized by a single direction of alignment for the C_{60} molecular rows, marked by black arrows in Figure 8. These correspond to the $[5\bar{5}\pm8]$ substrate azimuths, at an angle of ±48° with the $[1\bar{1}0]$ substrate close-packed direction. Adjacent straight molecular rows in each domain are staggered from each other following a complex pattern which is rationalized below. Another important feature apparent in Figure 8 is the significant long-range mass transport undergone by the substrate.

The comparison of Figure 5A and Figure 6C with Figure 8 clearly indicates that in the former, the (1 × 2) substrate reconstruction remains largely unaltered on the Pt regions uncovered by fullerene islands, including the Pt areas in close proximity to the islands borders, whereas in the latter, a substantial increase of the substrate defectivity is observed. Frequent (1 × 3) and (1 × 4) locally reconstructed areas are detected (indicated in Figure 8 by full and dashed white arrows, respectively), along with atomically unresolved patches tentatively attributed to unreconstructed (1 × 1) Pt regions (they are coplanar with the ridges of the (1 × 2) reconstruction at any applied bias).

When measured at a negative sample bias value (see Figure 8), the apparent height of all of the molecules belonging to the ordered domains is the same within the experimental uncertainty (±0.1 Å). However, if the same phase is imaged at a +2.0 eV bias, a peculiar bright−dim (B−D) molecular contrast becomes evident, as shown in the high-resolution images reported in Figure 9. Now, the straight molecular rows along $[5\bar{5}\pm8]$ are further resolved in a succession of alternating B and D molecules (see the vertical white line in Figure 9A, corresponding to the reported line scan in the upper left inset). The B−D contrasted phase can be also perceived as a network of zigzag lines running through the B features, as highlighted by the black line in Figure 9A, acting as a guide to the eye. The apparent height difference between B and D molecules is 0.4 ± 0.1 Å in Figure 9, and it is bias-dependent, as already remarked in connection to Figure 8. The B−D contrast is commonly observed on a variety of substrates[12,14,16,31] and, when the contrast is strong and bias-independent, it is generally originated from differences in physical height between the adsorption sites of B and D molecules. A weaker and often bias-dependent contrast is due to different orientations of molecules adsorbed roughly at the same physical height, perhaps coupled to electronic effects caused by site-specific bonding. In the present case, the apparent height difference is too low with respect to a monatomic step height of the substrate (1.3 Å) and is also bias-dependent. Thus, it cannot be attributed to a substantial physical height difference between B and D molecules, as observed, for example, on Pd-(110)[14] and on Ag(100).[24] This makes it clear that the contrast is not related to the missing row reconstruction in the substrate, even more so if one considers the mutual separation between the molecules. In fact, if the (1 × 2) substrate reconstruction were preserved, both B and D molecules would be aligned along the ridges as well as along the troughs. Consider, for example, the B molecules indicated with “a” and “b” at the corners of the STM-derived unit cell reported in Figure 9B. Since they are spaced by a single Pt lattice parameter (3.9 ± 0.1 Å) along the [001] substrate direction, if “a” is supposed to sit on a ridge, than “b” would lie inside of a trough or vice versa, but this is

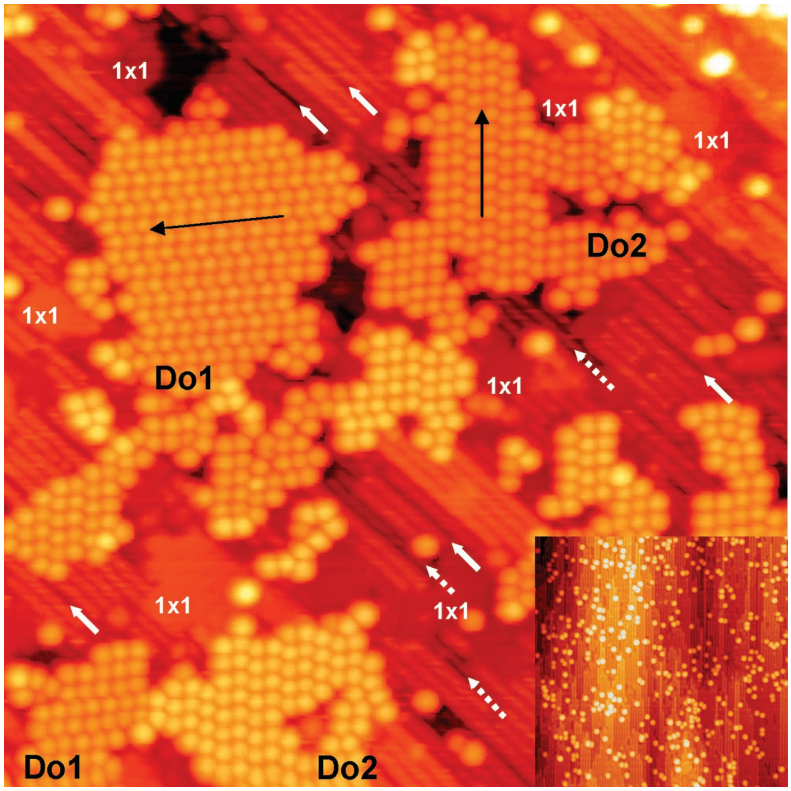

Figure 8. STM image of the (1 × 2)-Pt(110) surface covered by 0.42 ML of C_{60} after an annealing treatment at 850 K; bias = −1.5 V; I_T = 1.0 nA; 55 nm × 50 nm. Inset: The same surface before the annealing treatment; bias = 0.21 V; I_T = 3.1 nA; 87 nm × 87 nm. Black arrows indicate the alignment directions of fullerene close-packed rows in the two domains Do1 and Do2. Areas marked with "1 × 1" are interpreted as unreconstructed Pt islands. Full (dotted) white arrows aligned along the [1$\bar{1}$0] direction indicate 1 × 3 (1 × 4) locally reconstructed substrate areas.

contradicted by their identical apparent height. The same argument can be applied to D molecules. Hence, the (1 × 2) reconstruction is, at least partially, removed, in line with similar examples of adsorbate-induced de-reconstruction of the (1 × 2)-Pt(110) surface reported in the literature.[37,50] We now want to understand the extent of this de-reconstruction. As a matter of fact, "a" and "b" molecules, though having the same height, can still occupy different adsorption sites, reminiscent of the "in-trough" and "along-ridge" chemisorption. In other words, one cannot exclude that "a" is adsorbed at a partially filled trough and "b" at a vacancy on the ridge, as those depicted in Figure 4, depending on the extent of the Pt mass transport during the annealing treatment, as already discussed in connection with the quasi-hexagonal chemisorption phase in section 3.2. However, if "a" and "b" molecules had different chemisorption sites, the STM-derived unit cell would be only apparent since it would represent solely the periodicity of the overlayer rather than the full periodicity of the selvedge. Thus, in order to connect fully equivalent molecules from the point of view of the translational symmetry, the true superstructure unit vectors should be twice the ones deduced from Figure 9.

In order to check if this is the case, one needs to sample the periodicity of the whole three-dimensional selvedge. For this reason, the LEED pattern of the equilibrium oblique phase has been measured, and it is reported in Figure 10.

The LEED pattern corresponds to the surface topography imaged in Figure 9A, with the oblique C_{60} chemisorption phase coexisting with bare, still largely (1 × 2) reconstructed substrate areas, the latter giving rise to the clearly detectable fractional spots of the (1 × 2) reconstruction, highlighted by white squares in Figure 10 (left). The rather faint features induced by the fullerene-induced reconstruction are reproduced by assuming a superstructure unit cell which quantitatively matches the STM-derived one and whose matrix notation is

$$\begin{bmatrix} 8 & \pm 1 \\ -5 & \pm 4 \end{bmatrix}$$

Hence, "a" and "b" molecules in Figure 9B are adsorbed on equivalent substrate sites, which amounts to saying that the removal of the (1 × 2) reconstruction underneath of the C_{60} islands is complete. In other words, the distinction between "in-trough" and "along-ridge" chemisorption sites does not hold; all B molecules have identical chemisorption sites, as do D ones. However, there are two ways to configure the interface in accordance with the periodicity revealed by STM and LEED; molecules could either be adsorbed on a network of nanopits of monatomic depth, as depicted in Figure 9D (left), where some of them are shown without the overlying molecule, or on a perfectly flat (1 × 1)-Pt(110) terrace, as in Figure 9D (right).

Before addressing this important question, we point out that different molecular orientations coexist within the equilibrium phase, as shown by the rich intramolecular fine structure of Figure 9B and C. Interestingly, both B and D molecules can be further split into two subsets (B_1−D_1 and B_2−D_2 in Figure 9C); B1 (D1) is related to B2 (D2) by an azimuthal rotation (i.e., a rotation with respect to an axis perpendicular to the surface and passing through the molecular center of mass) of approximately 180°. In summary, there is a tetramolecular basis associated with each point of the oblique Bravais lattice.

The intramolecular fine structure for both B and D molecules is reminiscent of the single-molecule orientation in the M1 configuration on (1 × 2)-Pt(110), reported in Figure 1:[11] one major and two symmetric minor lobes separated by an ap-

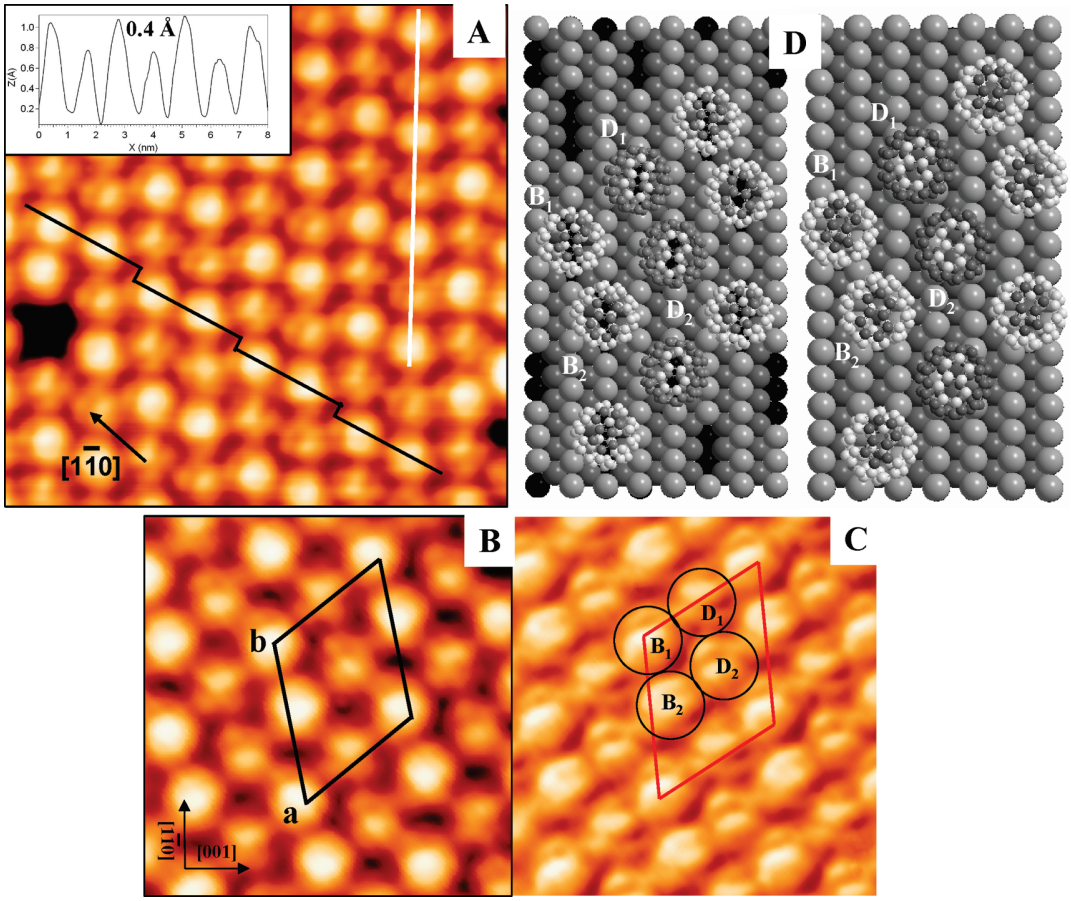

Figure 9. (A) High-resolution STM image of the equilibrium oblique C_{60} chemisorption phase on (1 × 2)-Pt(110), obtained after annealing at 850 K; bias = 2.1 V; I_T = 1.28 nA; 11 nm × 11 nm. The inset shows the linear section through the vertical white line, indicating the apparent height difference between the bright (B) and dim (D) C_{60} molecules in a row aligned along [5$\bar{5}$8]. The black line evidences the peculiar zigzag pattern of the B−D-contrasted phase at the chosen positive bias. (B) Close up of the same phase (6 nm × 6 nm), with the indication of the STM-derived superstructure unit cell. (C) the same as that in (B), convoluted with the current image. Two different orientations for both B and D molecules (B_1, B_2 and D_1, D_2, respectively) are detected. (D) Possible models for the C_{60}/Pt(110) interface in the oblique phase (see text): molecules adsorbed on a network of bi- and triatomic nanopits on the unreconstructed substrate surface (left) and molecules adsorbed on the unreconstructed Pt(110) surface (right). B (D) molecules are represented with light (dark) gray C atoms with dark (light) topmost pentagon−hexagon rings. Pt atoms are the larger gray spheres. Darker Pt atoms are deeper into the surface.

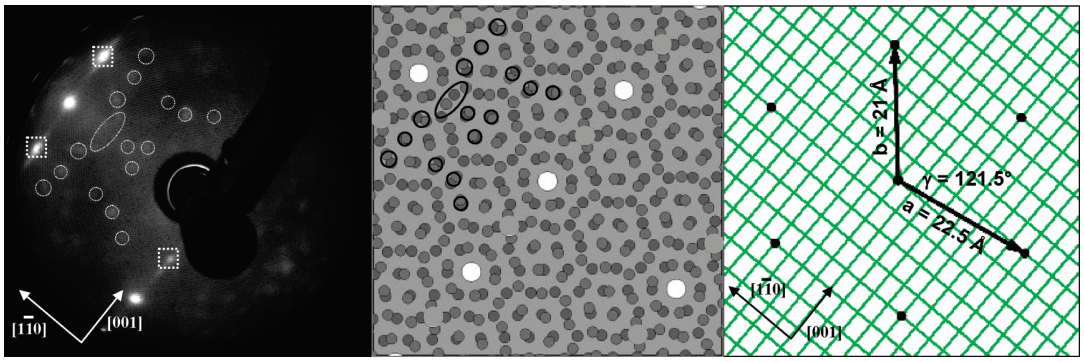

Figure 10. LEED pattern (E = 46 eV) of the oblique C_{60}/Pt(110) phase (left); kinematic simulation of the LEED pattern (center), corresponding to the superstructure reported in the right panel. The most prominent fractional diffraction spots due to the superstructure are highlighted by white (black) circles and ellipses in the experiment (simulation). The fractional spots of the substrate, indicated by white squares in the experimental image, are due to uncovered, (1 × 2) reconstructed substrate areas.

proximately threefold nodal feature, as evidenced in Figure 11 (center), which corresponds to a somewhat tilted b56 bonding to the substrate, as already remarked in connection to Figure 1. We also note in Figure 11 that the relative intensity of the major lobe with respect to the two minor ones changes (increases) upon going from D to B molecules; we can envisage a different degree of polar tilt for roughly iso-oriented molecules.

Let us now turn to the Pt vacancy network model for the fullerene/platinum interface. A reasonable choice for the chemisorption site of either the B or D subset is a biatomic surface vacancy (see the central top part of the model in Figure 8D, left), which is similar to the most stable M1 adsorption configuration where the trough of the (1 × 2) reconstruction has been completely filled by Pt atoms, except for the chemi-

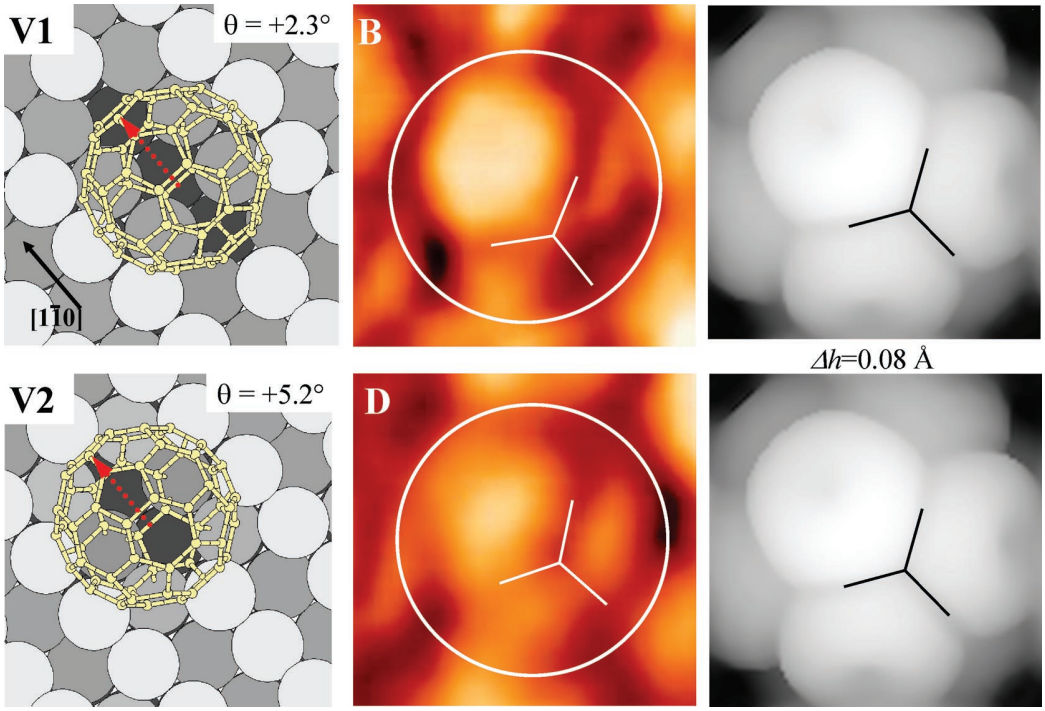

Figure 11. Left: Chemisorption configurations for C_{60} on a triatomic (V1) and a biatomic (V2) vacancy on (1 × 1)-Pt(110), as deduced by DFT calculations. The polar tilt θ is indicated in the top right corner. The direction of polar tilt is highlighted by means of red arrows. Center: Experimental STM images (bias = +2.0 V; I_T = 1.28 nA;1.8 nm × *1.8 nm)* of a B (top) and of a D (bottom) molecule within the oblique chemisorption phase. The white circle highlights the single-molecule boundary. The nodal feature separating the three main lobes of the charge density distribution is highlighted by three white segments. Right: Simulations of the STM images within the Tersoff−Hamann approximation for the V1 (top) and V2 (bottom) chemisorption configurations; Δh is the apparent height difference between the two bonding configurations at the given bias value deduced from the simulated STM images.

sorption site. If, as in Figure 9D (left), biatomic vacancies are occupied by D molecules, intermolecular distances and angles require that B molecules sit at the center of linear three-atomic vacancies, as that in the model shown in the upper left part of the model. Chemisorption of C_{60} at triatomic vacancy sites is incidentally observed on Pd(110).[14] Conversely, if B molecules are assigned to biatomic vacancies, D molecules would sit in three-atomic nanopits.

Chemisorption of C_{60} has been modeled by means of DFT calculations on both bi- and triatomic vacancies on the (1 × 1)-Pt(110) substrate. The resulting optimized chemisorption geometries, along with the corresponding STM simulations within the Tersoff−Hamann approximation, are reported in Figure 11.

The molecular orientation on both the triatomic (V1) and the biatomic vacancy (V2) is reminiscent of the M1 configuration for C_{60} adsorption on (1 × 2)-Pt(110)[11] reported in Figure 1; in both cases, the molecule adsorbs symmetrically over the vacancy with the lowermost b56 C−C bond pointing toward the surface and aligned with the [001] substrate direction.[51] In an ideal b56 bonding configuration, the molecular axis bisecting the lowermost and the topmost b56 bonds would be perpendicular to the substrate surface (the two bonds crossed by the red dashed arrow in Figure 11 (left) would superimpose in a top view such as those reported in the figure). It can be seen from Figure 11 that in both cases, the C_{60} molecule undergoes a slight polar tilt along the [1$\bar{1}$0] substrate direction with respect to the ideal case. The polar tilt, indicated by red dashed arrows is taken as positive (negative) if it is in the same (opposite) direction as the substrate [1$\bar{1}$0] azimuth, as oriented in Figure 11 (top left). Given this choice, the V1 molecule is tilted by $\theta = +2.3°$, while V2 is tilted by $\theta = +5.2°$. The tilt difference $\Delta\theta$ between the two configurations therefore amounts to only 2.9°, which is too small of a value to be detected from the simulated images reported in Figure 11 (right). In fact, the two simulations are almost indistinguishable, at variance with the clearly detectable tilt difference seen in the experimental STM images of B and D molecules (Figure 11, center). In addition, the apparent height difference (Δh) at the bias value of +2.0 V for the simulated images amounts to just 0.08 Å, too small to account for the experimentally determined B−D contrast. In conclusion, the vacancy network model is incompatible both with the B−D contrast and with the details of the intramolecular fine structure.

As already remarked on the basis of STM and LEED measurements, the last possible option for the interfacial matching of the oblique C_{60} phase is the unreconstructed (1 × 1)-Pt(110) surface. (Figure 9D, right). Two high-symmetry chemisorption configurations have been identified by means of DFT simulations and are reported in Figure 12 (left) as N1 and N2; the former corresponds to b56 adsorption over a substrate fourfold site, with b56 parallel to the [001] substrate direction, while the latter is characterized by b56 adsorption over a substrate bridge site, again with b56 parallel to Pt[001].

Molecules adsorbed on both sites are still tilted along the [1$\bar{1}$0] substrate direction but by larger amounts with respect to the vacancy network hypothesis and in opposite directions with respect to each other. In fact, N1 is tilted by $\theta = -5.6°$, while N2 is tilted by $\theta = +7.6°$. $\Delta\theta$ between the two configurations therefore amounts to 13.0°. This substantial difference in polar tilt is clearly reflected in the simulated STM images of the two bonding configurations, reported in Figure 12 (right), which show different intensity ratios between the main (most intense) and the two secondary intramolecular features. A remarkable similarity with the experimental STM data (Figure 12, center) is found if the N1 adsorption configuration is associated with B molecules and the N2 configuration to D ones. In addition,

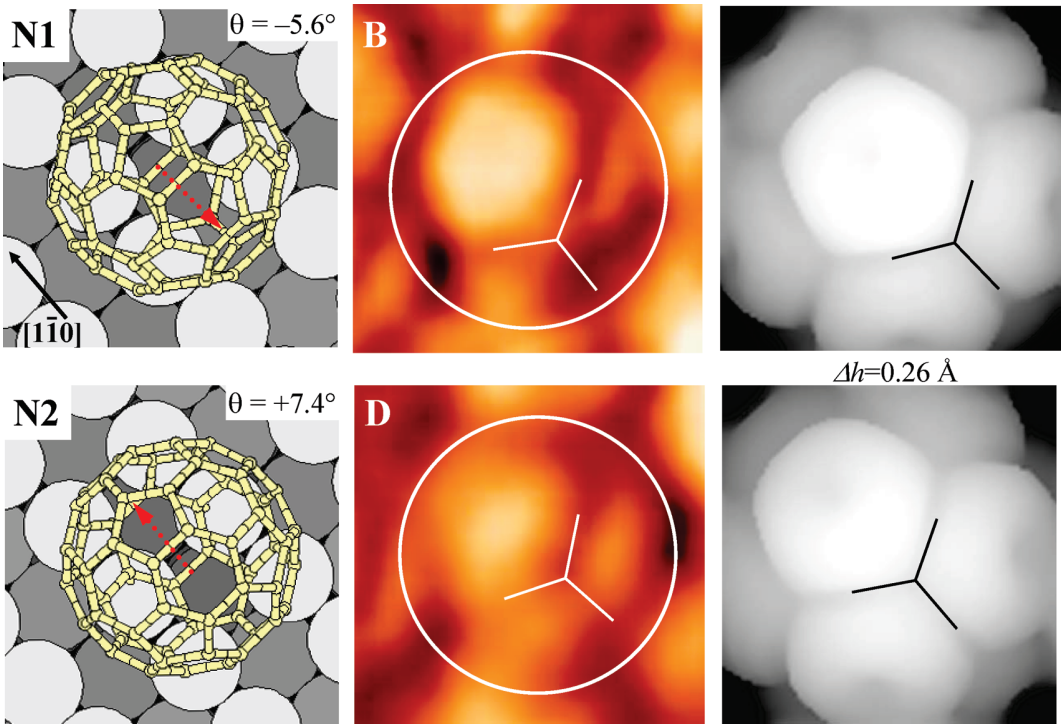

Figure 12. Left: Chemisorption configurations for C_{60} on (1 × 1)-Pt(110) as deduced by DFT calculations. The polar tilt θ is indicated in the top right corner. The direction of polar tilt is highlighted by means of red dashed arrows. Center: As that in Figure 11. Right: Simulations of the STM images within the Tersoff−Hamann approximation for the N1 (top) and N2 (bottom) chemisorption configurations.

the calculated apparent height difference between N1 and N2 at a sample bias of +2.0 V is 0.26 Å, to be compared to the experimental difference of 0.4 ± 0.1 Å between B and D molecules.

In summary, N1−N2 adsorption on unreconstructed (1 × 1)-Pt(110) is the only interface model for the oblique C_{60} phase on Pt(110) that correctly reproduces both the differences in intramolecular fine structure and the apparent height difference between B and D molecules at positive sample bias values.

The DFT calculation results reported in Figures 11 and 12 refer to simplified models where "isolated" molecules are considered, that is, in-plane intermolecular interactions are not taken into account. It is known that these interactions account for approximately 1.30 eV/molecule for a 2D C_{60} hexagonal layer with NN molecules at the equilibrium VdW distance (10.05 Å),[46] thus representing a nonnegligible fraction of the total energy. A careful look at the STM data reported in Figure 9A−C (and at the derived structural models reported in Figure 9D) reveals that all C_{60} units (both B and D) are azimuthally rotated by the same amount, $\phi = 6° \pm 1°$, with respect to the symmetric b56 adsorption configuration reported in Figure 12. This azimuthal rotation is driven by intermolecular interactions. In fact, the four C_{60} units belonging to the molecular basis associated with each Bravais lattice point turn out to face each other exactly through hexagonal rings, which, as already remarked, maximizes their mutual VdW interactions.[47,48] The joint effect of polar/azimuthal tilts experienced by both sets of C_{60} molecules on their respective chemisorption sites ultimately leads the C_{60} NN distance to match (10.0 ± 0.1 Å) the value found in bulk-like fullerite and in C_{60} ultrathin films grown on less strongly interacting surfaces. The next-NN distance (the separation between two B or two D molecules along the [1$\bar{1}$0] substrate direction; see Figure 9 D) amounts to 13.2 Å. The resulting surface density for this phase (0.11 molecules per unreconstructed substrate unit cell, corresponding to an area per molecule of 98.9 Å^2) is thus considerably lower than that for the quasi-hexagonal phase (0.125 molecules per unreconstructed substrate unit cell; 87.1 Å^2 per molecule).

Finally, the average C_{60} islands height with respect to the ridges of the (1 × 2) reconstructed bare surface areas is either 4.4 ± 0.1 or 3.1 ± 0.1 Å from STM topographs at a −2.0 V sample bias, depending on the actual Pt terrace taken as a reference for the height measurement. In fact, it appears from both Figure 2B and Figure 8 that Pt terraces of different heights coexist in close proximity to the C_{60} islands. Since C_{60} adsorbed on the troughs of the (1 × 2) reconstruction in the M1 configuration has an apparent height of approximately 5.7 ± 0.1 Å at comparable bias values,[11] the 1.3 ± 0.1 Å height difference is consistent with a monatomic step of the substrate surface. We therefore conclude that the whole C_{60} island in the oblique phase is embedded in at least one/two atomic layers of the (1 × 2) reconstructed areas; it appears that the removal of the (1 × 2) substrate reconstruction underneath of the fullerene islands is attained by removing the Pt ridges rather than by filling the troughs by upcoming Pt atoms from the surface diffusion field. This is consistent with the observation of the atomically flat and unresolved patches in close proximity to the C_{60} islands (see Figure 8), which we have tentatively assigned to (1 × 1)-Pt(110); in the suggested dynamics of interface formation, these areas would be the sink of the Pt atoms removed at the C_{60}/Pt boundary.

4. Conclusions

The self-assembling properties of C_{60} on (1 × 2)-Pt(110) have been studied as a function of the preparation temperature by means of STM, LEED, and DFT calculations. Two distinct ordered phases have been detected and characterized, a metastable quasi-hexagonal phase obtained upon annealing the fullerene-dosed platinum surface at 700 K and a stable oblique

phase which is produced if the system is annealed at 850 K. The two chemisorption phases differ profoundly from each other as far as the surface density, the molecular bonding configurations, and the interfacial structure are concerned. The discriminating factor between the two arrangements appears to be the degree of surface mobility of Pt atoms at the developing interface as a function of temperature. The formation of the lower-temperature (700 K) quasi-hexagonal phase is accompanied by a limited, albeit clearly detectable, Pt mass transport. While it is evident that fullerene island nucleation at Pt step edges involves a restructuring of the substrate steps' orientation (thus removing the typical fish-scale pattern of clean (1 × 2)-Pt(110)) and a certain degree of local restructuring at the C_{60}/Pt interface (which can be interpreted as the onset of the (1 × 2) → (1 × 1) de-reconstruction), the (1 × 2) superstructure typical of clean Pt(110) is largely preserved, even in close proximity to the C_{60} island borders. The tight constraint posed by the large surface corrugation coupled to the particularly strong covalent bonding of the molecules to the substrate (the strongest ever computed for a fullerene on any metal surface[11]), with a definite preference for a single chemisorption site, leads to a close-packed structure. The C_{60} NN distances mirror the short (9.6 Å) separation between the underlying Pt sites and lead to interadsorbate VdW repulsions. In other words, vertical interactions dominate over lateral ones on a still rather "stiff" substrate surface reconstruction. The overall outcome is the highest surface density phase reported in the literature so far for surface-supported 2D fullerene structures.

The quasi-hexagonal phase occasionally nucleates a most interesting 1D defect, which is proposed to consist of a linear array of C_{120} dumbbell dimers embedded in the close-packed islands and formed through [2 + 2] cycloaddition between two 6−6 bonds belonging to adjacent C_{60} molecules. The formation of these "molecular zips" can be qualitatively explained by a recursive mechanism whose main ingredients are the strong molecule−substrate bonding and the site-blocking effect exerted by the already formed dimer on the next one in the line. To our knowledge, this is the first example of surface-templated chemical bond formation between fullerene molecules reported in the literature without the aid of either high pressure[49] or STM high-voltage pulses.[52] Further work should be devoted in the future to a more detailed understanding of the kinetics of formation of the dimer nanowires and to the elucidation of the factors which govern their occurrence and their relative abundance, such as the effects of residual carbon contamination at the surface, of hydrogen or oxygen predosing of the substrate, and so forth.

If the system is annealed at a higher temperature (850 K), a less dense oblique phase is formed, characterized by a complex mutual arrangement of four C_{60} units within the unit cell. Subtle differences in site geometry and adsorbate orientation give rise to a peculiar bright−dim contrast in STM topographs acquired at positive sample bias values. The enhanced mobility of surface Pt atoms at the higher annealing temperature accounts for the most striking feature of the oblique phase, namely, the complete removal of the (1 × 2) reconstruction at the C_{60}/Pt interface. In fact, an integrated use of STM, LEED, and DFT results allows us to conclude that the oblique phase consists of C_{60} islands residing on (1 × 1)-Pt(110) areas and to give a detailed description of molecular chemisorption sites. At submonolayer coverage, the C_{60} islands as a whole are additionally embedded in the first few atomic layers of the substrate.

Acknowledgment. This work has been partially funded by MIUR through the FIRB research program "Nano- and microspectroscopy by synchrotron radiation integrated with advanced STM/AFM systems to study manmade atomic scale functional materials" (Prot. N. RBNE0155X7) and by the University of Padua through the Grant CPDA038285. Calculations have been performed by using the Quantum-ESPRESSO package.[53] Computational resources and assistance were provided by the "Laboratorio Interdipartimentale di Chimica Computazionale" (LICC) at the Department of Chemistry of the University of Padova. and by CINECA (Bologna, Italy). We acknowledge a computer time grant from CINECA and INSTM (Firenze, Italy) under the "Super-Progetti di calcolo" program. Molecular graphics has been generated by XCrysDen.[54]

References and Notes

(1) Kroto, H. W.; Health, J. R.; O'Brien, S. C.; Curl, R. F.; Smalley, R. E. *Nature* **1985**, *318*, 162.
(2) Kratschmer, W.; Lamb, L. D.; Fostiropulos, K.; Huffman, D. R. *Nature* **1990**, *347*, 354.
(3) Wilson, R. J.; Meijer, G.; Bethune, D. S.; Johnson, R. D.; Chambliss, D. D.; de Vries, M. S.; Hunziker, H. E.; Wendt, H. R. *Nature* **1990**, *348*, 621.
(4) Pedio, M.; Hevesi, K.; Zema, N.; Capozi, M.; Perfetti, P.; Gouttebaron, R.; Pireaux, J.; Caudano, R.; Rudolf, P. *Surf. Sci.* **1999**, *437*, 249.
(5) Hashizume, T.; Motai, K.; Wang, X. D.; Shinohara, H.; Saito, Y.; Maruyama, Y.; Ohno, K.; Kawazoe, Y.; Nishina, Y.; Pickering, H. W.; Kuk, Y.; Sakurai, T. *Phys. Rev. Lett.* **1993**, *71*, 2959.
(6) Giudice, E.; Magnano, E.; Rusponi, S.; Boragno, C.; Valbusa, U. *Surf. Sci.* **1998**, *405*, L561.
(7) Guo, S.; Fogarty, D. P.; Nagel, P. M.; Kandel, S. A. *J. Phys. Chem. B* **2004**, *108*, 14074.
(8) Wang, L. T.; Cheng, H. P. *Phys. Rev. B* **2004**, *69*, 045404.
(9) Cepek, C.; Goldoni, A.; Modesti, S. *Phys. Rev. B* **1996**, *53*, 7466.
(10) He, H.; Swami, N.; Koel, B. E. *Thin Solid Films* **1999**, *348*, 30.
(11) Casarin, M.; Forrer, D.; Orzali, T.; Petukhov, M.; Sambi, M.; Tondello, E.; Vittadini, A. *J. Phys. Chem. C* **2007**, *111*, 9365.
(12) Murray, P. W.; Pedersen, M. Ø.; Lægsgaard, E.; Stensgaard, I.; Besenbacher, F. *Phys. Rev. B* **1997**, *55*, 9360.
(13) Pedio, M.; Felici, R.; Torrelles, X.; Rudolf, P.; Capozi, M.; Rius, J.; Ferrer, S. *Phys. Rev. Lett.* **2000**, *85*, 1040.
(14) Weckesser, J.; Cepek, C.; Fasel, R.; Barth, J. V.; Baumberger, F.; Greber, T.; Kern, K. *J. Chem. Phys.* **2001**, *115*, 9001.
(15) Kiguchi, M.; Iizumi, K.; Saiki, K.; Koma, A. *Appl. Surf. Sci.* **2003**, *212*−*213*, 101.
(16) Weckesser, J.; Barth, J. V.; Kern, K. *Phys. Rev. B* **2001**, *64*, 161403.
(17) Giovannelli, L.; Cepek, C.; Floreano, L.; Magnano, E.; Sancrotti, M.; Gotter, R.; Morgante, A.; Verdini, A.; Pesci, A.; Ferrari, L.; Pedio, M. *Appl. Surf. Sci.* **2003**, *212*−*213*, 57.
(18) Felici, R.; Pedio, M.; Borgatti, F.; Iannotta, S.; Capozi, M.; Ciullo, G.; Stierle, A. *Nat. Mater.* **2005**, *4*, 688.
(19) Rowe, J. E.; Rudolf, P.; Tjeng, L. H.; Malic, R. A.; Meigs, G.; Chen, C. T.; Chen, J.; Plummer, E. W. *Int. J. Mod. Phys. B* **1992**, *6*, 3909.
(20) Fasel, R.; Agostino, R. G.; Aebi, P.; Schlapbach, L. *Phys. Rev. B* **1999**, *60*, 4517.
(21) Sakurai, T.; Wang, X. D.; Hashizume, T.; Yurov, V.; Shinohara, H.; Pickering, H. W. *Appl. Surf. Sci.* **1995**, *87*−*88*, 405.
(22) Costantini, G.; Rusponi, S.; Giudice, E.; Boragno, C.; Valbusa, U. *Carbon* **1999**, *37*, 727.
(23) Cepek, C.; Fasel, R.; Sancrotti, M.; Greber, T.; Osterwalder, J. *Phys. Rev. B* **2001**, *63*, 125406.
(24) Pai, W. W.; Hsu, C. L. *Phys. Rev. B* **2003**, *68*, 121403.
(25) David, T.; Gimzewski, J. K.; Purdie, D.; Reihl, B.; Schlitter, R. R. *Phys. Rev. B* **1994**, *50*, 5810.
(26) Kovac, J.; Scarel, G.; Sakho, O.; Sancrotti, M. *J. Electron Spectrosc. Relat. Phenom.* **1995**, *72*, 71.
(27) Magnano, E.; Vandré, S.; Goldoni, A.; Laine, A. D.; Currò, G. M.; Santaniello, A.; Sancrotti, M. *Surf. Sci.* **1997**, *377*−*379*, 1066.
(28) Altman, E. I.; Colton, R. J. *Phys. Rev. B* **1993**, *48*, 18244.
(29) Yoshida, Y.; Tanigaki, N.; Yase, K. *Thin Solid Films* **1996**, *281*−*282*, 80.
(30) Kuk, Y.; Kim, D. K.; Suh, Y. D.; Park, K. H.; Noh, H. P.; Oh, S. J.; Kim, S. K. *Phys. Rev. Lett.* **1993**, *70*, 1948.
(31) Gimzewski, J. K.; Modesti, S.; Schlitter, R. R. *Phys. Rev. Lett.* **1994**, *72*, 1036.
(32) Hunt, M. R. C.; Rudolf, P.; Modesti, S. *Phys. Rev. B* **1997**, *55*, 7882.

(33) Tzeng, C.-T.; Lo, W.-S.; Yuh, J.-Y.; Chu, R.-J.; Tsuei, K.-D. *Phys. Rev. B* **2000**, *61*, 2263.
(34) Rogero, C.; Pascual, J. I.; Gómez-Herrero, J.; Baró, A. M. *J. Chem. Phys.* **2002**, *116*, 832.
(35) Guo, S.; Fogarty, D. P.; Nagel, P. M.; Kandel, S. A. *J. Phys. Chem. B* **2004**, *108*, 14074.
(36) Hou, J. G.; Jinlong, Y.; Haiqian, W.; Qunxiang, L.; Changgan, Z.; Langfeng, Y.; Bing, W.; Chen, D. M.; Qinshi, Z. *Nature* **2001**, *409*, 304.
(37) Gritsch, T.; Coulman, D.; Behm, R. J.; Ertl, G. *Phys. Rev. Lett.* **1989**, *63*, 1086.
(38) Vanderbilt, D. *Phys. Rev. B* **1990**, *41*, 7892.
(39) Perdew, J. P.; Burke, K.; Ernzerhof, M. *Phys. Rev. Lett.* **1996**, *77*, 3865.
(40) Tersoff, J.; Hamann, D. R. *Phys. Rev. Lett.* **1983**, *50*, 1998.
(41) Lazzeri, M.; Selloni, A. *Phys. Rev. Lett.* **2001**, *87*, 266105.
(42) Gritsch, T.; Coulman, D.; Behm, R. J.; Ertl, G. *Surf. Sci.* **1991**, *257*, 297.
(43) Speller, S.; Kuntze, J.; Rauch, T.; Bömermann, J.; Huck, M.; Aschoff, M.; Heiland, W. *Surf. Sci.* **1996**, *366*, 251.
(44) Vilfan, I. *Surf. Sci.* **1996**, *350*, 329.
(45) Matsumoto, M.; Inukai, J.; Tsutsumi, E.; Yoshimoto, S.; Itaya, K.; Ito, O.; Fujiwara, K.; Murata, M.; Murata, Y.; Komatsu, K. *Langmuir* **2004**, *20*, 1245.
(46) Nakamura, J.; Nakayama, T.; Watanabe, S.; Aono, M. *Phys. Rev. Lett.* **2001**, *87*, 048301.
(47) Hsu, C. L.; Pai, W. W. *Phys. Rev. B* **2003**, *68*, 245414.
(48) Girifalco, L. A. *J. Phys. Chem.* **1991**, *95*, 5370.
(49) Ozaki, T.; Iwasa, Y.; Mitani, T. *Chem. Phys. Lett.* **1998**, *285*, 289.
(50) Bittner, A. M.; Wintterlin, J.; Ertl, G. *J. Electroanal. Chem.* **1995**, *388*, 225.
(51) In particular, V2 is almost identical to M1, provided that the trough of the (1 × 2) reconstruction has been filled by Pt atoms, except for the site occupied by the C_{60} molecule.
(52) Nakamura, Y.; Kagawa, F.; Kasai, K.; Mera, Y.; Maeda, K. *Appl. Phys. Lett.* **2004**, *85*, 5242.
(53) Baroni, S.; dal Corso, A.; de Gironcoli, S.; Giannozzi, P.; Cavazzoni, C.; Ballabio, G.; Scandolo, S.; Chiarotti, G.; Focher, P.; Pasquarello, A.; Laasonen, K.; Trave, A.; Car, R.; Marzari, N.; Kokalj, A. Plane-Wave Self-Consistent Field. http://www.pwscf.org/.
(54) Kokalj, A. *Comput. Mater. Sci.* **2003**, *28*, 155. Code available from http://www.xcrysden.org/.

Density Functional Theory Study of the Binding Capability of Tris(pyrazol-1-yl)methane toward Cu(I) and Ag(I) Cations

Maurizio Casarin,*,†,‡,§ Daniel Forrer,†,§ Federica Garau,† Luciano Pandolfo,†,§ Claudio Pettinari,|| and Andrea Vittadini‡,§

Dipartimento di Scienze Chimiche, Università degli Studi di Padova, Padova 35131, Italy, Dipartimento di Scienze Chimiche, Università degli Studi di Camerino, Camerino (MC) 62032, Italy, Istituto di Scienze Molecolari del CNR, Padova 35131, Italy, and Consorzio Interuniversitario di Scienza e Tecnologia dei Materiali, Firenze 50121, Italy

Received: March 4, 2008; Revised Manuscript Received: April 28, 2008

Density functional theory (DFT) has been used to look into the electronic structure of $[M(tpm)]^+$ molecular ion conformers (M = Cu, Ag; tpm = tris(pyrazol-1-yl)methane) and to study the energetics of their interconversion. Theoretical data pertaining to the free tpm state the intrinsic instability of its κ^3-like conformation, thus indicating that, even though frequently observed, the κ^3-tripodal coordinative mode is unlikely to be directly achieved through the interaction of M(I) with the κ^3-like tpm conformer. It is also found that the energy barrier for the κ^2-$[M(tpm)]^+ \rightarrow \kappa^3$-$[M(tpm)]^+$ conversion is negligible. As far as the bonding scheme is concerned, the tpm $\rightarrow$ M(I) donation, both σ and π in character, is the main source of the M(I)−tpm bonding, whereas back-donation from completely occupied M(I) d orbitals into tpm-based π^* levels plays a negligible role.

1. Introduction

Tris(pyrazol-1-yl)borate (hereafter, tp) and tris(pyrazol-1-yl) methane (hereafter, tpm) are considered among the most useful ligands in modern coordination chemistry.[1] Substituted and unsubstituted tp and tpm supply in fact a significant steric shielding of the metal center serving, at the same time, as reliable spectator ligands. These peculiarities make them useful for the synthesis of complexes with virtually all metals in the periodic table, having thus applications in diverse and important fields ranging from catalysis to biomedicine, from metal extraction to biomimetic inorganic chemistry.[1f,g,h,i] In general, tp and tpm behave as tripodal κ^3-ligands through the lone pairs of the nitrogen heteroatoms [N(•)] of the three pyrazolyl fragments (see Figure 1d).[2] In this regard, these ligands are often labeled as scorpionates, a consequence of an oneiric description of their bonding capabilities where, like the pincers of a scorpion, the N(•) of two pyrazolyl moieties attached to B (tp) or C (tpm) bind a metal, and the third pyrazolyl attached to the central atom rotates forward like the scorpion's tail to "sting" the metal. Although such a picture is certainly attractive, crystallographic data pertaining to the free tp[3a] and tpm,[4] i.e., the simplest members of the scorpionate family, suggest alternative bonding mechanisms. In fact, both tp and tpm solid state structures are characterized by a single pyrazolyl group with N(•) in trans with respect to the H atom of the B−H (tp)/C−H (tpm) fragments (see Figure 1b).[5]

Theoretical work so far devoted to the study of tp and tpm ligands with metal ions is very limited. De Bari and Zimmer[7] carried out a study of the conformational flexibility of tp and tpm behaving as κ^3-tripodal ligands showing, through the use of molecular mechanics and database analysis, that "tripodal scorpionate ligands can accommodate a variety of metal sizes by opening up the ligand".

In this paper we present and discuss the results of a series of first-principle numerical experiments devoted to the study of the electronic structure of κ^1-monodentate, κ^2-chelating, and κ^3-tripodal $[M(tpm)]^+$ molecular ions (M = Cu, Ag) as well as to the energetics of their interconversion.[8] The first section of the contribution is dedicated to the theoretical analysis of the free pyrazole molecule (hereafter, Hpz)[9] and its hypothetical $[M(Hpz)]^+$ σ and π complexes with the aim of gaining quantitative information about the nature and the strength of the M(I)−Hpz interaction. The second part deals with the conformation flexibility of the free tpm ligand, leaving aside any problem concerning optical isomerism, and the third one is focused on binding energies and electronic properties of the $[M(tpm)]^+$ molecular ions.

2. Computational Details

All the numerical experiments have been carried out by using the Amsterdam Density Functional (ADF) package[12] and adopting the scalar relativistic zeroth-order regular approximation (ZORA).[13] Optimized geometries for ground and transition states (GS and TS, respectively) were obtained by employing generalized gradient (GGA) corrections self-consistently included through the Becke−Perdew formula,[14] and without imposing any symmetry. All TS's have been estimated through the following procedure: (i) a linear transit (LT) calculation has been run by varying a dihedral angle[15] (vide infra); (ii) from the TS guess provided by step (i), a stationary point on the energy surface has been searched; (iii) the adequacy of the TS estimate has been then checked by computing vibrational frequencies at the corresponding geometry and verifying that one of them is imaginary; (iv) the Hessian computed in the third step is employed for the final TS optimization.

TZP ZORA basis sets were adopted for all the atoms;[16] inner cores of Cu (1s2s2p3s3p), Ag (1s2s2p3s3p3d), C (1s), and N

† Università degli Studi di Padova.
|| Università degli Studi di Camerino.
‡ Istituto di Scienze Molecolari del CNR.
§ Consorzio Interuniversitario di Scienza e Tecnologia dei Materiali.

10.1021/jp801902c CCC: $40.75
Published on Web 07/01/2008

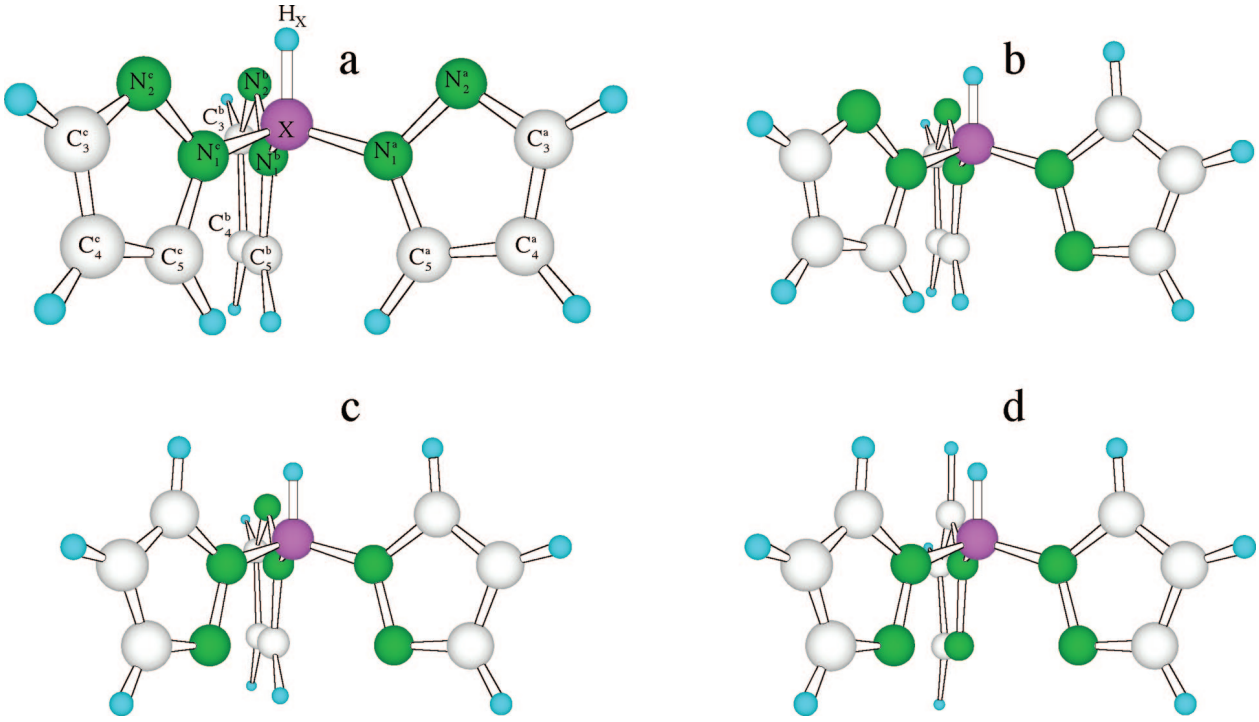

Figure 1. Schematic representation of possible relative arrangements of pyrazolyl fragments in tp (X = B) and tpm (X = C).

(1s) atoms were kept frozen throughout the calculations. Binding energies (BEs) were analyzed in terms of fragment molecular orbitals (FMO's) by applying the Ziegler's extended transition state method (ETS).[17] According to the ETS scheme,

$$\mathrm{BE} = \Delta E_{\mathrm{es}} + \Delta E_{\mathrm{Pauli}} + \Delta E_{\mathrm{int}} + \Delta E_{\mathrm{prep}} \qquad (1)$$

where ΔE_{es} is the pure electrostatic interaction, $\Delta E_{\mathrm{Pauli}}$ is the destabilizing two-orbital-four-electron interaction between the occupied orbitals of the interacting fragments (($\Delta E_{\mathrm{es}} + \Delta E_{\mathrm{Pauli}}$) corresponds to the so called steric interaction (ΔE_{st}) contribution), ΔE_{int} derives from the stabilizing interaction between occupied and empty orbitals of the interacting fragments, and ΔE_{prep} provides information about the energy required to relax the structure of the free fragments to the geometry they assume in the final system. BE's were further corrected by taking into account the basis set superposition error (BSSE) which was estimated by making use of reference energies calculated with "ghost" fragments.[18]

Rather than displaying discrete eigenvalues along an energy axis, we preferred to plot the density of states (hereafter, DOS) as a function of energy by using a 0.25 eV Lorentzian broadening factor. These plots, based on Mulliken's prescription for partitioning the overlap density,[19] have the advantage of providing insights into the atomic composition of MO's over a broad range of energy. Finally, information about the localization and the bonding/antibonding character of selected MO's was obtained by using crystal orbital overlap populations (COOP's)[20] computed by weighting one-electron energy levels by their basis orbital percentage.

3. Results and Discussion

As above mentioned, tpm is a potentially tripodal, neutral ligand characterized by the presence of three pyrazolyl moieties bonded to a central methine carbon atom (see Figure 1). Now, Hpz is planar, fully conjugated, and isoelectronic with the cyclopentadienyl anion, but the higher electronegativity of nitrogen (3.04)[21] compared to that of carbon (2.55)[21] determines a higher electronic charge density on N atoms both in the molecular plane and out of it. In consequence of that, each tpm pyrazolyl group may be involved in two competitive metal−ligand bonding mechanisms: a σ-binding implying the N(•) lone pair (hereafter, n_{N}) and a π-binding involving the π electron density of the aromatic ring. An intimate comprehension of the tpm coordination capabilities necessarily passes through a deep understanding of the σ/π $[\mathrm{M(Hpz)}]^+$ bonding scheme.

3.1. Hpz and σ/π $[\mathrm{M(Hpz)}]^+$ Complexes. Optimized coordinates of Hpz are reported in Table S1, and selected geometrical parameters and Mulliken[19] and Hirshfeld[22] gross atomic charges are collected in Tables 1 and 2, respectively. The agreement with data obtained by accurate ab initio calculations (CBS-APNO QCISD/6-311G(d,p))[23] is remarkable; moreover, theoretical estimates of the Hpz dipole moment (μ), lowest ionization energies (IEs)[24] and VUV-absorption bands agree very well with experiment.[27]

The Hpz valence manifold includes five π-like and the n_{N} MO's. Among them, the π_1, π_2, and π_3 ones (the 8a, 12a, and 13a levels, respectively) and n_{N} (the 11a MO) are occupied, whereas π_4 and π_5 (the 14a and 16a MO's, respectively) are empty; moreover, π_3 and π_4 correspond to the Hpz HOMO and LUMO, respectively. 3D-contour plots of the whole Hpz valence manifold are displayed in Figure 2.

The contemporary presence of the aromatic π system and of the n_{N} allows two competitive bonding mechanisms in $[\mathrm{M(Hpz)}]^+$. With reference to the Hpz → M(I) donation, a simple electron count coupled to symmetry arguments and overlap considerations indicate that (i) n_{N} will limit its involvement to the M(I)−Hpz σ bonding; (ii) the Hpz π system may contribute to both σ and π interactions; (iii) M(I) will participate with its s and p virtual atomic orbitals (AO's). As far as the M(I) → Hpz back-donation is concerned, the charge transfer is possible between the fulfilled M(I) d AO's and the Hpz-based π_4 and π_5 virtual MO's.

A schematic representation of the optimized structure of σ/π $[\mathrm{M(Hpz)}]^+$ complexes is displayed in Figure 3 (corresponding

TABLE 1: Selected Geometrical Parameters of the Free Hpz and σ/π $[M(Hpz)]^+$ Complexes[a]

		$[Cu(Hpz)]^+$		$[Ag(Hpz)]^+$	
	Hpz	σ	π	σ	π
M−N(1)			3.205		3.412
M−N(2)		1.856	3.271	2.129	3.256
M−C(3)			2.593		2.548
M−C(4)			1.975		2.279
M−C(5)			2.565		2.972
N(1)−N(2)	1.356	1.366	1.369	1.363	1.358
N(2)−C(3)	1.340	1.353	1.322	1.351	1.335
C(3)−C(4)	1.415	1.398	1.459	1.400	1.454
C(4)−C(5)	1.386	1.389	1.435	1.387	1.414
C(5)−N(1)	1.361	1.350	1.335	1.352	1.342
N(1)N(2)C(3)	103.8	106.0	104.7	105.6	104.3
N(2)C(3)C(4)	112.0	110.0	111.9	110.4	111.4
C(3)C(4)C(5)	104.6	105.7	102.8	105.4	103.5
C(4)C(5)N(1)	106.0	107.5	106.0	107.3	106.0
C(5)N(1)N(2)	113.4	110.9	114.6	111.3	114.8

[a] Bond lengths and bond angles in Å and deg, respectively.

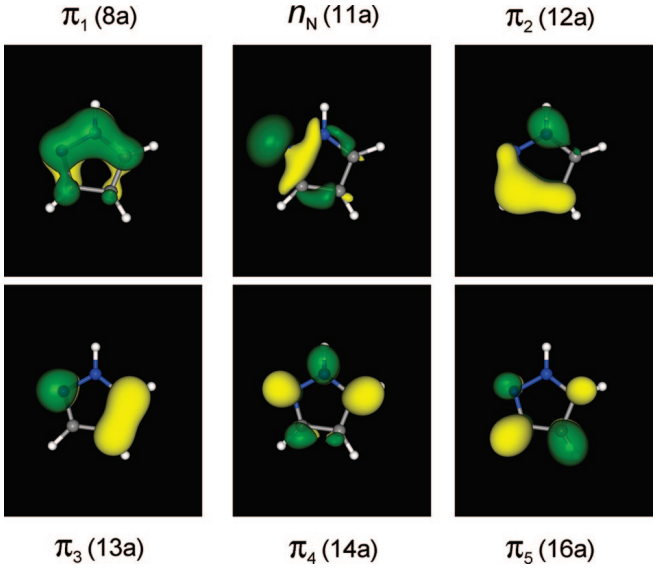

Figure 2. 3D contour plots of the Hpz $\pi_1-\pi_5$ MO's. The 3D plot of the n_N is also included. Yellow (green) surfaces correspond to a constant positive (negative) value of 0.06 $e^{1/2}/Å^{3/2}$.

optimized coordinates are reported in Tables S2−S5), and selected geometrical parameters, Mulliken/Hirshfeld gross atomic charges and ETS contributions to the metal-ligand BE's are collected in Tables 1, 2 and 3, respectively. Structural perturbations undergone by the C_3N_2 pyrazole ring are rather similar for the two coordinative modes, except for the significant rehybridization of C(4) in π-$[M(Hpz)]^+$ (see Figure 3).[29] The analysis of COOP curves in Figure 4, and of gross atomic charge variations at C(4) on passing from the free ligand to the coordinated one (see Table 2) testifies that the C(4) rehybridization in π-$[M(Hpz)]^+$ has to be ultimately traced back to the concomitant Hpz $\pi_3 \rightarrow$ M(I) sp donation and M(I) d $\rightarrow \pi_5$ back-donation, with the former much stronger than the latter.[30] According to that, a lengthening of the C(4)−C(5) and C(3)−C(4) bond distances is computed on passing from the free to the coordinated Hpz.

A further point to be emphasized concerns the relevance of π contributions to the metal-ligand bond in σ-$[M(Hpz)]^+$ complexes. More specifically, the inspection of Figure 5 testifies that, besides the $n_M \rightarrow {}^N$(sp) donation, high lying Hpz π orbitals strongly localized on N(•) (π_3 and π_4 MO's, see Figure 2) significantly participate to the metal-ligand interaction.

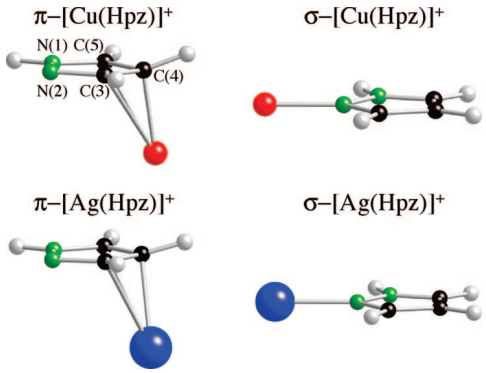

Figure 3. Schematic representations of the optimized structure of σ/π-$[M(Hpz)]^+$ complexes.

As far as BE values are concerned, the examination of data reported in Table 3 is particularly intriguing. In fact, despite BE's of σ complexes being larger than those corresponding to the π ones and $[Cu(Hpz)]^+$ BE's being larger than the $[Ag(Hpz)]^+$ ones, ΔE_{int} contributions show an opposite trend, thus indicating that each BE value is the result of a subtle balance of different contributions, with ΔE_{st} playing a very important role.

3.2. tpm Conformational Flexibility. The tpm X-ray crystal structure is characterized by a single pyrazolyl group with N(•) (N_2^a in Figure 1b) in trans with respect to the hydrogen of the C−H fragment. This conformer has been labeled tpm-1,[31] and those corresponding to the κ^2-chelating (Figure 1c) and κ^3-tripodal (Figure 1d) coordinative modes have been tagged as tpm-2 and tpm-3, respectively. The tpm-0 conformer (see Figure 1a) is obviously the one with the three N(•) in cis with respect the methine fragment. Relative BE′s corresponding to tpm-0, tpm-1, and tpm-2 GS′s as well as to relevant saddle points are displayed in Figure 6 where sketches of the corresponding optimized molecular structures are also reported.[31,33] The tpm-3 conformer is not reported because it was found to be unstable.

Before going on, it deserves to be mentioned that the tpm-0 optimized structure is characterized by the presence of a C_3 axis with pyrazolyl fragments adopting a propeller-like orientation.[34] Such a result allowed us to label the linear combinations of Hpz-based frontier orbitals according to the a + e irreducible representations of the C_3 point group (see Figure 7). Interestingly, even though BE(tpm-0) and BE(tpm-1) are very close ($\Delta BE_{0,1}$ = BE(tpm-0) − BE(tpm-1) = 0.88 kcal/mol), tpm-1 corresponds to the absolute minimum not only in the solid state but also in the isolated molecule, thus confirming early semiempirical MNDO results of Claramunt et al.[36,37] This rather small difference is the balance of opposite effects involving ΔE_{st} (positive) and ΔE_{int} (negative) contributions in eq 1: ΔE_{st}(tpm-0) is actually smaller than ΔE_{st}(tpm-1) by 18.88 kcal/mol, and ΔE_{int}(tpm-0) exceeds ΔE_{int}(tpm-1) by 19.76 kcal/mol. Furthermore, consistently with the free rotation around H_CC-N bonds proved by NMR measurements at room temperature,[38] the energy barrier associated to the tpm-0 → tpm-1 saddle point (TS1) is predicted very low (less than 2.5 kcal/mol).[40] We remark that, with the obvious exception of the LT parameter, all tpm internal coordinates are substantially unaffected by the tpm-0 → tpm-1 conversion (see Figure 8).

For the tpm-1 → tpm-2 conversion, two parameters can be chosen for the TS search, i.e., the rotations around either the $H_CC-N_1^b$ bond (TS2b) or the $H_CC-N_1^c$ one (TS2c, see Figure 1). The inspection of Figures 6 and 8 testifies that (i) TS2b and TS2c BE's are very similar and close to the TS1 one; (ii) $\Delta BE_{2,1} > \Delta BE_{0,1}$; and (iii) similarly to the tpm-0 → tpm-1 conversion,

TABLE 2: Mulliken (Q^M) and Hirshfeld (Q^H) Charges of Selected Atoms of the Free Hpz and σ/π $[M(Hpz)]^+$ Complexes

	Hpz	$[Cu(Hpz)]^+$		$[Ag(Hpz)]^+$	
		σ	π	σ	π
Q^M_M (Q^H_M)		0.79 (0.54)	0.51 (0.53)	0.83 (0.60)	0.63 (0.60)
$Q^M_{N(1)}$ ($Q^H_{N(1)}$)	0.14 (−0.02)	0.18 (0.02)	0.17 (0.04)	0.17 (0.01)	0.17 (0.03)
$Q^M_{N(2)}$ ($Q^H_{N(2)}$)	−0.28 (−0.15)	−0.45 (−0.07)	−0.20 (−0.07)	−0.42 (−0.08)	−0.20 (−0.09)
$Q^M_{C(3)}$ ($Q^H_{C(3)}$)	0.28 (−0.03)	0.36 (0.03)	0.43 (0.03)	0.34 (0.02)	0.33 (0.01)
$Q^M_{C(4)}$ ($Q^H_{C(4)}$)	0.10 (−0.09)	0.18 (−0.03)	−0.08 (−0.07)	0.17 (−0.04)	−0.02 (−0.06)
$Q^M_{C(5)}$ ($Q^H_{C(5)}$)	0.25 (−0.02)	0.33 (0.05)	0.41 (0.05)	0.32 (0.04)	0.37 (0.04)

TABLE 3: Binding Energy Contributions in kcal/mol for σ/π $[M(Hpz)]^+$ Complexes

	$[Cu(Hpz)]^+$		$[Ag(Hpz)]^+$	
	σ	π	σ	π
ΔE_{st}	−15.3	−1.2	26.1	43.2
ΔE_{int}	−59.5	−65.1	−79.4	−88.2
ΔE_{prep}	1.1	5.9	0.8	3.2
BSSE	1.2	1.7	0.3	0.4
BE	−72.5	−58.7	−52.2	−41.3

the tpm-1 → tpm-2 one negligibly affects tpm internal coordinates (see Figure 8).

The ΔE_{int}(tpm-1) and ΔE_{int}(tpm-2) contributions are very similar (the latter is 0.25 kcal/mol larger than the former), whereas ΔE_{st}(tpm-2) exceeds ΔE_{st}(tpm-1) by 2.75 kcal/mol. Such a result ultimately indicates that the lower stability of tpm-2 compared to tpm-1 has to be traced back to the repulsive

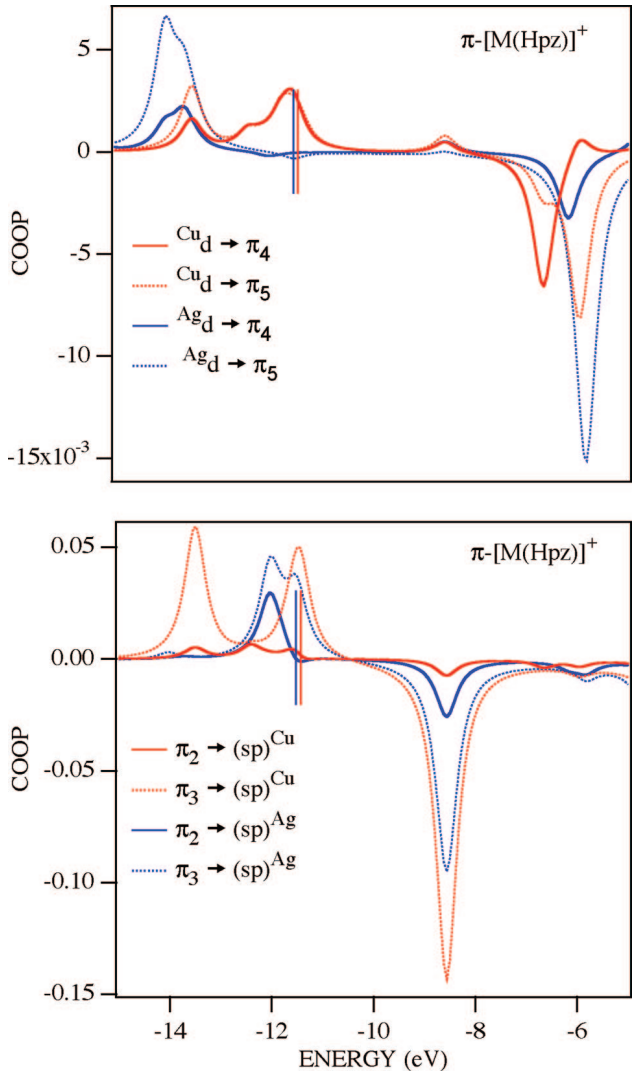

Figure 4. M(I) d → π^* Hpz (up) and Hpz π → sp M(I) (down) COOP's in π-$[M(Hpz)]^+$ complexes. Bonding (antibonding) states correspond to positive (negative) peaks. Vertical bars represent the HOMO energies.

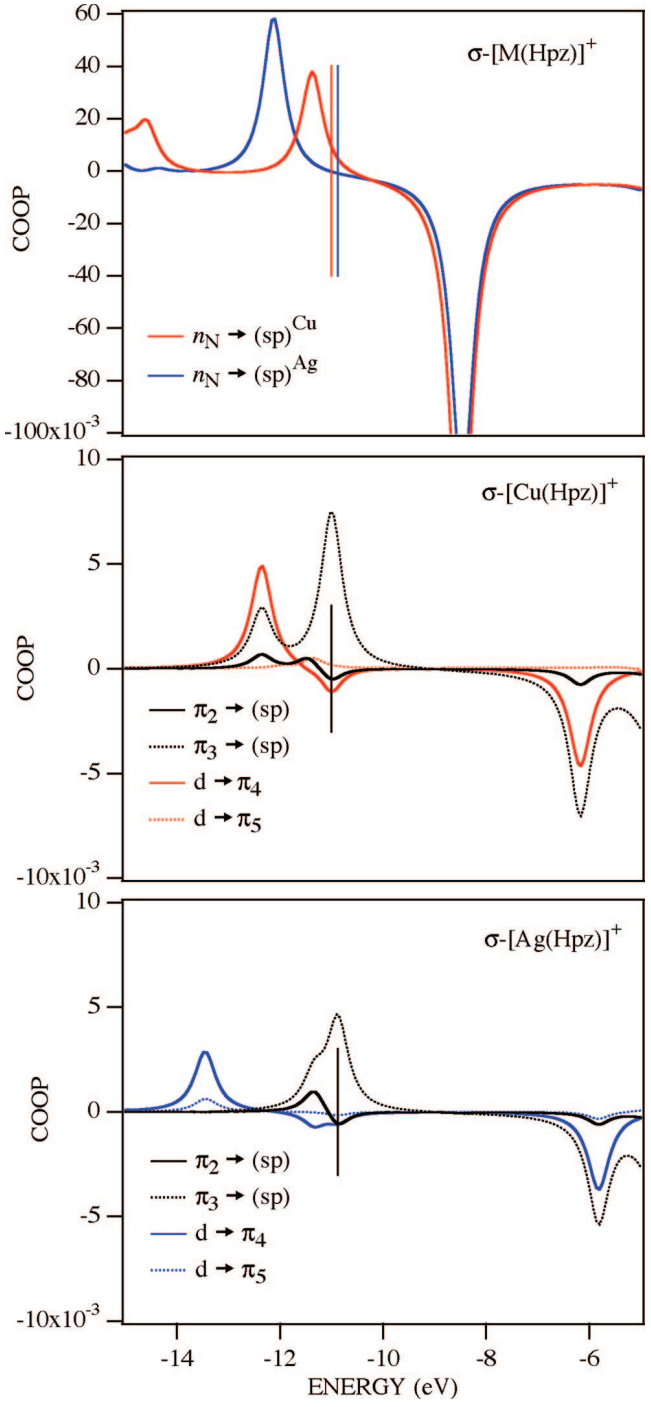

Figure 5. Hpz n_N → sp M(I) (up) and [Hpz π → sp M(I)]/[M(I) d → π^* Hpz] (middle and down) COOP's in σ-$[M(Hpz)]^+$ complexes.

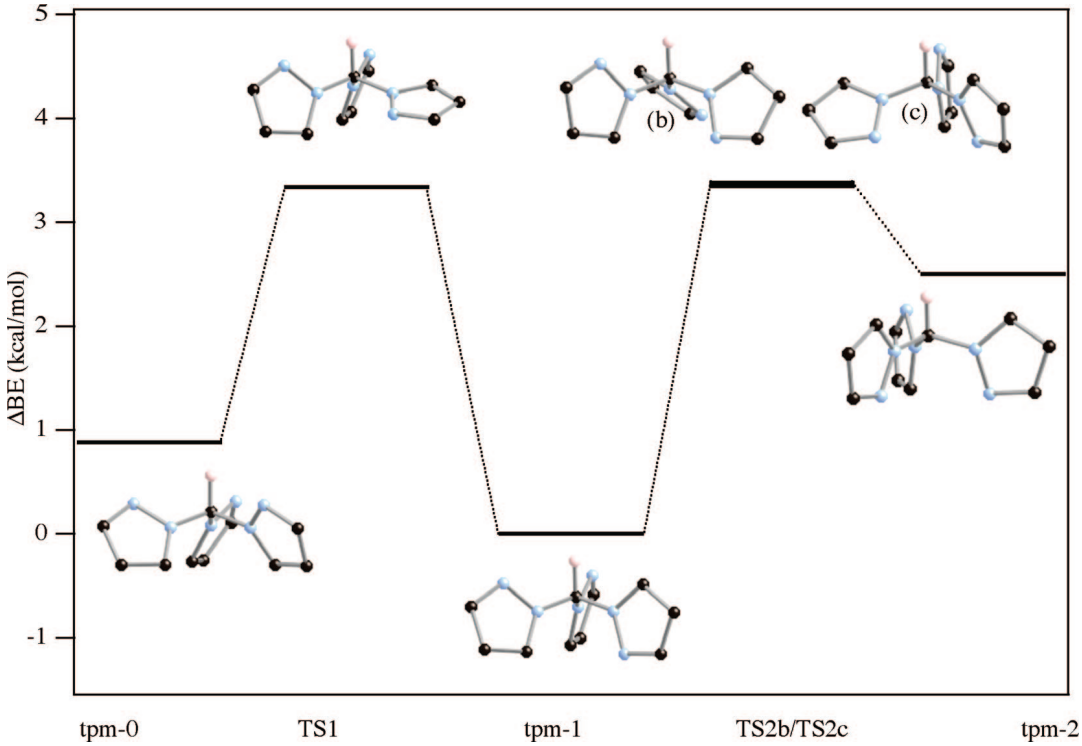

Figure 6. Relative BE values of tpm-0, TS1, tpm-1, TS2b/TS2c, tpm-2. The zero energy value corresponds to the tpm-1 BE. Schematic representations of the corresponding optimized structure are also displayed.

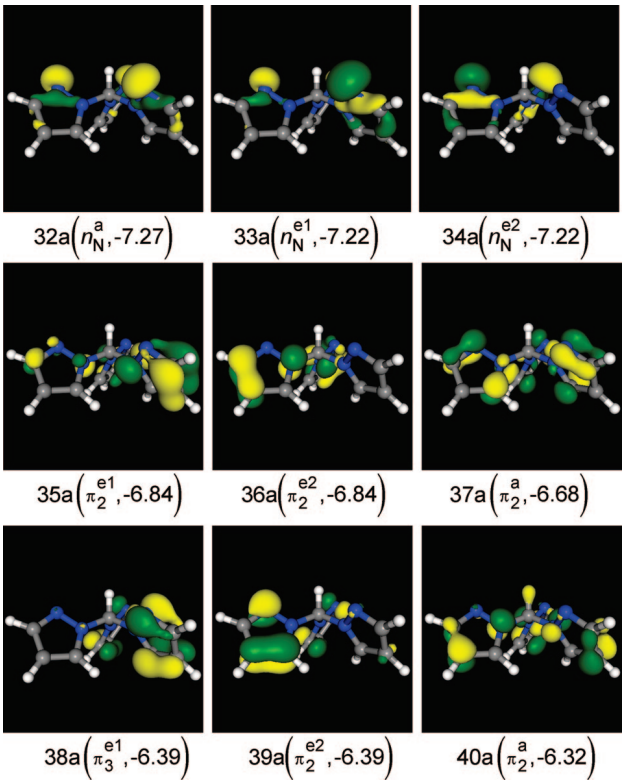

Figure 7. 3D contour plots of tpm-0 outermost occupied MO's. In parentheses is reported the energy in electronvolt of each level and its parenthood with the Hpz-based orbitals. Contour plot parameters are the same of Figure 2.

interaction between the two N(•) n_N in trans to the H_CC fragment (ΔE_{Pauli}(tpm-1) and ΔE_{Pauli}(tpm-2) differ by 3.18 kcal/mol).

As a whole, the above described theoretical results outline that, though common, the tpm κ^3-tripodal coordinative mode is unlikely to be achieved through the direct interaction of M(I) with tpm having a tpm-3 arrangement.

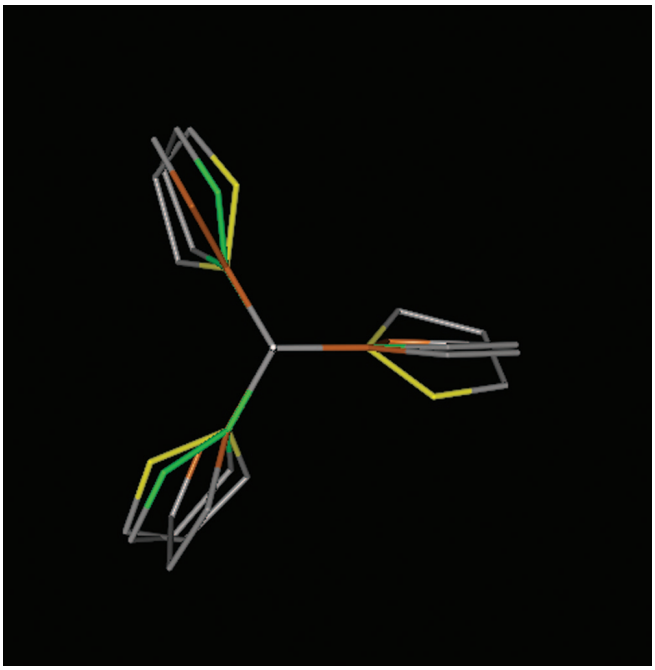

Figure 8. Superimposed licorice representation of tpm-0 (N atoms in yellow), tpm-1 (N atoms in light green), and tpm-2 (N atoms in orange) optimized structures. The view is along the C−H_C bond. Hydrogen atoms of pyrazolyl fragments are not displayed for the sake of clarity.

3.3. $[Cu(tpm)]^+$ and $[Ag(tpm)]^+$ Complexes. Reger and coworkers first reported the synthesis and characterization of cationic [tris(pyrazol-1-yl)methane]M(I) (M = Cu,[41a] Ag[41b]) complexes about ten years ago, and although a lot of chemistry has been published on this subject since then,[42] not only are theoretical investigations devoted to tpm metal complexes very few in number,[6e,32,43] but none of them has been specifically dedicated to the analysis of the metal−ligand bonding scheme.

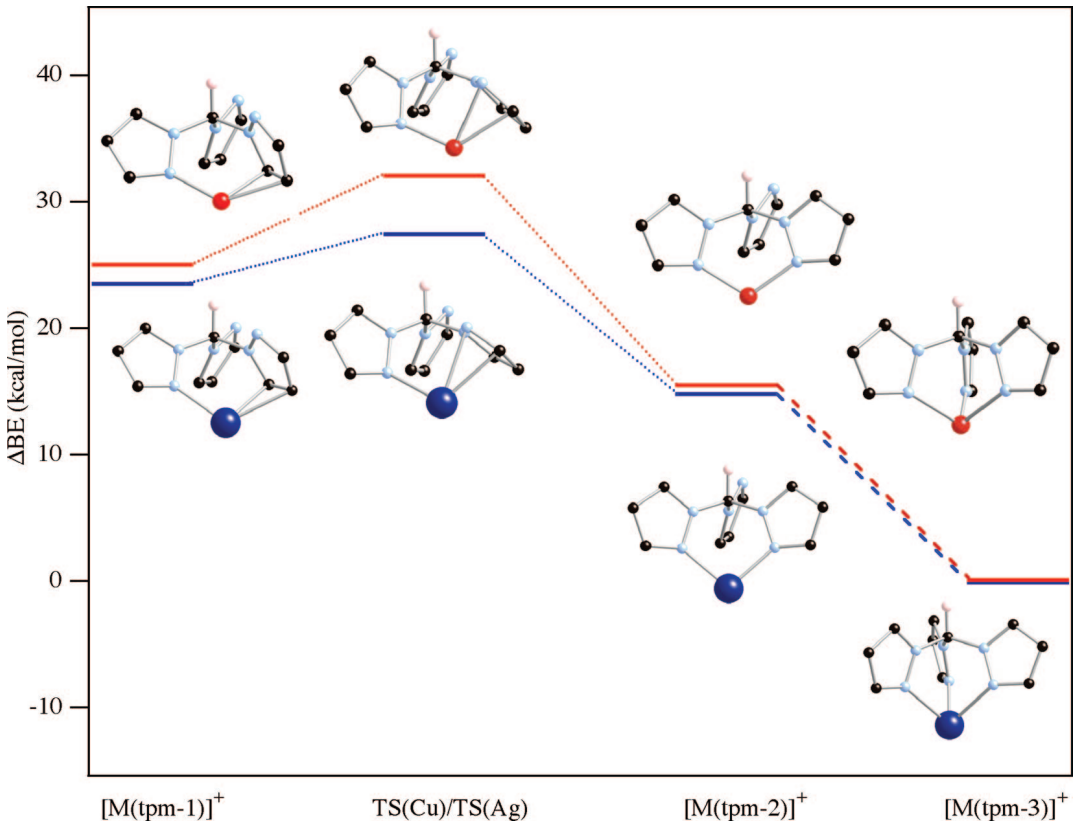

Figure 9. Relative BE values of $[M(tpm\text{-}1)]^+$, TS(M), $[M(tpm\text{-}2)]^+$, and $[M(tpm\text{-}3)]^+$. The zero energy value corresponds to the $[M(tpm\text{-}3)]^+$ BE. Schematic representations of the corresponding optimized structure are also displayed. Red and blue spheres correspond to copper and Silver atoms, respectively.

TABLE 4: Binding Energy Contributions in kcal/mol for $[M(tpm)]^+$ Complexes

	$[M(tpm\text{-}1)]^+$	TS(M)	$M(tpm\text{-}2)]^+$	$M(tpm\text{-}3)]^+$
$^{Cu}\Delta E_{st}$	−0.87	−4.97	−14.13	−30.14
$^{Cu}\Delta E_{int}$	−97.18	−86.05	−93.47	−92.95
$^{Cu}\Delta E_{prep}$	6.92		4.67	
^{Cu}BSSE	2.79		2.46	
^{Cu}BE	−88.34		−100.47	
$^{Ag}\Delta E_{st}$	64.76	51.51	50.27	43.92
$^{Ag}\Delta E_{int}$	−132.66	−115.46	−126.87	−135.32
$^{Ag}\Delta E_{prep}$	4.50		3.91	
^{Ag}BSSE	0.66		0.52	
^{Ag}BE	−62.74		−72.17	

The strength and the nature of the M(I)−tpm bond in $[M(tpm\text{-}n)]^+$ (n = 1, 2, and 3) have been obtained through the ETS scheme by considering M(I) and tpm as interacting fragments.[12] Optimized coordinates of $[M(tpm\text{-}n)]^+$ species and of TS(Cu) and TS(Ag) saddle points corresponding to the $[M(tpm\text{-}1)]^+ \rightarrow [M(tpm\text{-}2)]^+$ conversions are collected in Tables S12−S19. Relative BE's are displayed in Figure 9 where sketches of the corresponding optimized molecular structures are also displayed.

The comparison between data of Figure 9 and Figure 6 reveals that, as a consequence of the M(I)−tpm interaction, the $[M(tpm\text{-}2)]^+$ molecular ion is more stable than the $[M(tpm\text{-}1)]^+$ one, reversing the energy order found for the free ligand. Quite unexpectedly, this is not due to covalent but to steric effects (see Table 4). In this regard, theoretical results pertaining to $[M(tpm\text{-}n)]^+$ molecular ions substantially mirror those already discussed for the σ/π-$[M(Hpz)]^+$ species: despite the Ag(I)−ligand interaction being stronger than the Cu(I)−ligand one, ΔE_{st} contributions play a crucial role in determining final BE's values.

Interestingly, even though $[Cu(tpm\text{-}2)]^+$ and $[Ag(tpm\text{-}2)]^+$ correspond to local minima, we were unable to find the saddle point corresponding to the $[M(tpm\text{-}2)]^+ \rightarrow [M(tpm\text{-}3)]^+$ conversion because of the flatness of the potential energy surface in that region. This indicates that, when the κ^2-complex is formed, either from the interaction of M(I) with tpm-2 or through the $[M(tpm\text{-}1)]^+ \rightarrow [M(tpm\text{-}2)]^+$ conversion, the κ^3-tripodal species will be readily formed. However, the $[M(tpm\text{-}2)]^+ \rightarrow [M(tpm\text{-}3)]^+$ conversion could be hampered by several reasons such as (i) the coordinative saturation of the metal center by concurrent ligands; (ii) the coordination of the N(•) of the third pyrazolyl group to a different metal center; (iii) steric factors determined by bulky substituents of tpm.[44] In this regard, it has to be noted that, despite the M(I) coordinative unsaturation, the optimized geometrical parameters of $[Ag(tpm\text{-}2)]^+$, $[Cu(tpm\text{-}3)]^+$, and $[Ag(tpm\text{-}3)]^+$ agree satisfactorily with those experimentally determined for Ag(I) κ^2-[44i,l] and M(I) κ^3-complexes.[41,44i,l,45] No X-ray data pertaining to Cu(I) κ^2-complexes are available for comparison to our knowledge.

Further insights into to the M(I)-tpm bonding scheme can be gained by referring to Figures 10 and 11 where $[M(tpm\text{-}n)]^+$ PDOS and COOP curves are displayed. The inspection of the two figures[46] testifies to (i) the leading role played by the tpm → M(I) donation, mainly σ in character, (ii) the stronger involvement of the M(I) s AO compared to the one of the M(I) p AO's, and (iii) the negligible contribution provided by the M(I) → tpm back-donation.

4. Concluding Remarks

In this contribution we have presented and discussed the results of a series of first-principle numerical experiments

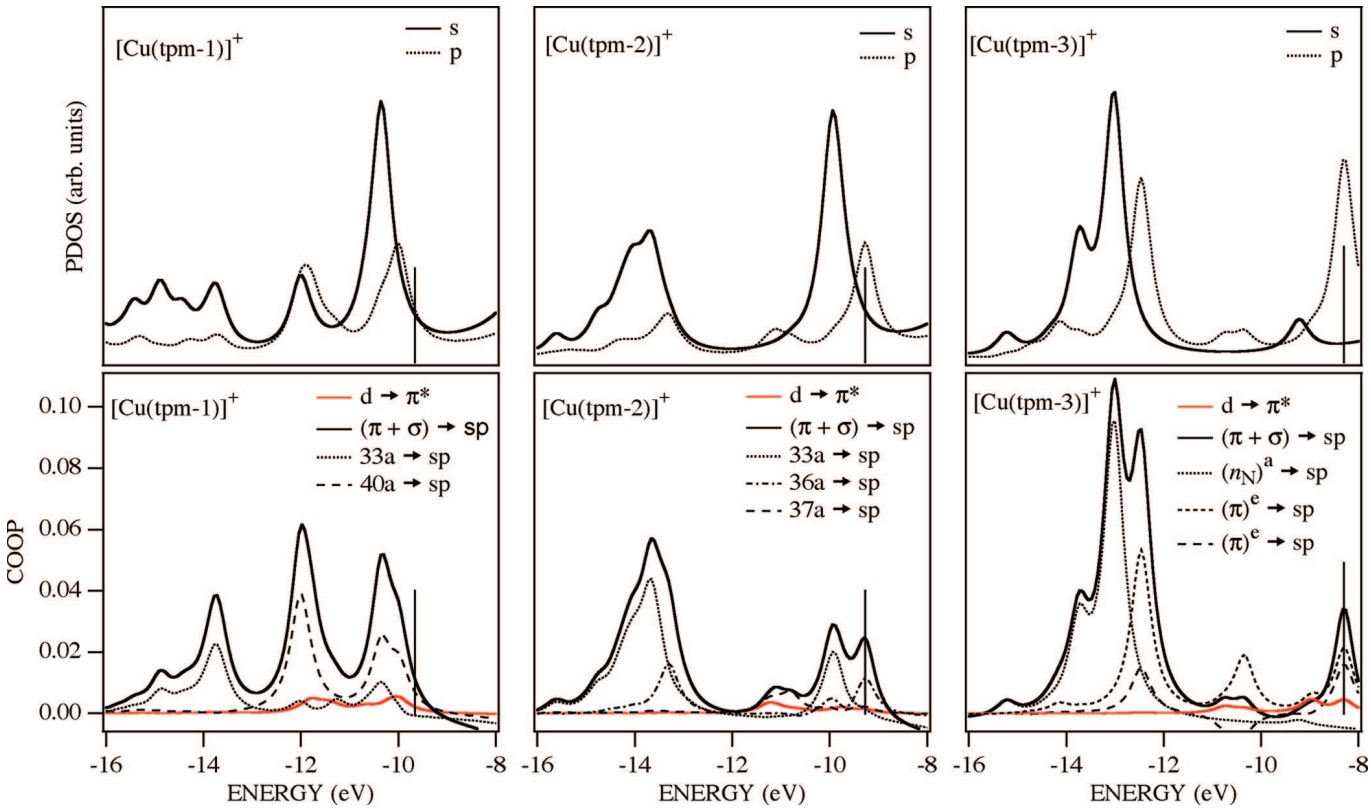

Figure 10. s and p PDOS (up) and major components of tpm $\sigma \rightarrow$ sp Cu(I), tpm $\pi \rightarrow$ sp Cu(I), and Cu(I) d $\rightarrow \pi^*$ tpm (down) for $[Cu(tpm\text{-}n)]^+$ (n = 1, 2, and 3).

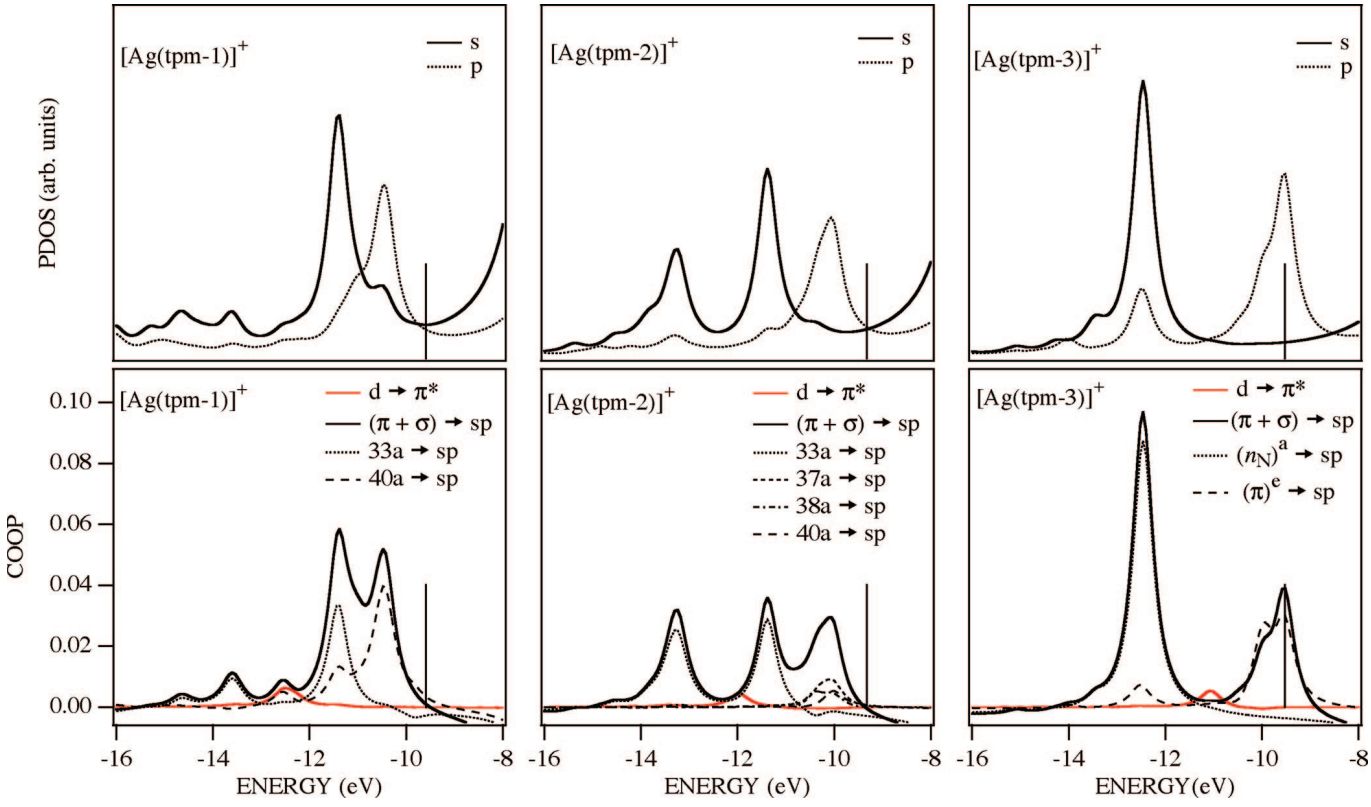

Figure 11. s and p PDOS (up) and major components of tpm $\sigma \rightarrow$ sp Ag(I), tpm $\pi \rightarrow$ sp Ag(I), and Ag(I) d $\rightarrow \pi^*$ tpm (down) for $[Ag(tpm\text{-}n)]^+$ (n = 1, 2, and 3).

carried out on the free Hpz and tpm ligands, as well as on their Cu(I) and Ag(I) complexes. We gave detailed information about the energetics of interconversions among conformers, both for the free and for the coordinated ligands. Finally, we analyzed the M−ligand interaction showing that, independently of the coordinative mode, this is dominated by the ligand → M(I) σ donation with negligible contribution from back-donation.

Acknowledgment. This work was partially supported by the Italian PRIN founding n. 2006038447. The "Laboratorio Interdipartimentale di Chimica Computazionale" (LICC) at the Department of Chemistry of the University of Padova is acknowledged for support of the computer facilities.

Supporting Information Available: Optimized coordinates of Hpz, π-[Cu(Hpz)]$^+$, σ-[Cu(Hpz)]$^+$, π-[Ag(Hpz)]$^+$, σ-[Ag(Hpz)]$^+$, tpm-0, tpm-1, tpm-2, TS1, TS2b, TS2c, [Cu(tpm-1)]$^+$, TS(Cu), [Cu(tpm-2)]$^+$, [Cu(tpm-3)]$^+$, [Ag(tpm-1)]$^+$, TS(Ag), [Ag(tpm-2)]$^+$, and [Ag(tpm-3)]$^+$ are reported in Tables S1−S19, respectively. The comparison between the Hpz VUV-absorption spectrum and TD-DFT results is displayed in Figure S1. This material is available free of charge via the Internet at http://pubs.acs.org.

References and Notes

(1) (a) Pettinari, C.; Pettinari, R. *Coord. Chem. Rev.* **2005**, *249*, 525, and references therein reported. (b) Pettinari, C.; Santini, C. *Compr. Coord. Chem. II* **2004**, *1*, 159. (c) Trofimenko, S. *Scorpionates, The coordination Chemistry of Polypyrazolylborate Ligands*; Imperial College Press: London, 1999. (d) Pettinari, C. *Scorpionates II: Chelating borate ligands*; World Scientific Publishing: New York, 2008. (e) Trofimenko, S. J. *Chem. Educ.* **2005**, *82*, 1715. (f) Murtuza, S.; Casagrande, O. L., Jr.; Jordan, R. F. *Polym. Mater. Sci. Eng.* **2001**, *84*, 109. (g) Santos, I.; Paulo, A.; Correia, J. D. *Top. Curr. Chem.* **2005**, *252*, 45. (h) Kitano, T.; Wada, H.; Mukai, H.; Ueda, K.; Sohrin, Y. *Anal. Sci.* **2001**, *17*, i1113. (i) de la Lande, A.; Gérard, H.; Moliner, V.; Izzet, G.; Reinaud, O.; Parisel, O. J. *Biol. Inorg. Chem.* **2006**, *11*, 593.

(2) tp and tpm may also act as κ^2-ligands bonded to a single metal (κ^2-chelating), as κ^1-κ^2-ligands bridging two metals or, hardly ever, as κ^1-ligands depending on the steric congestion around the metal center and the number of donor substituents on the central atom X, which may be P and Ga other than B and C (see refs 1 and 3).

(3) (a) Paneque, M.; Sirol, S.; Trujillo, M.; Gutiérrez-Puebla, E.; Monge, M. A.; Carmona, E. *Angew. Chem. Int. Ed.* **2000**, *39*, 218. (b) Ellis, D. D.; Jeffery, J. C.; Jelliss, P. A.; Kautz, J. A.; Stone, F. G. A. *Inorg. Chem.* **2001**, *40*, 2041.

(4) McLauchlan, C. C.; Varda, A. N.; Giles, J. R. *Acta Crystallogr, Sect. E: Struct. Rep. Online* **2004**, *60*, o1419.

(5) The relative position of pyrazolyl fragments in substituted and unsubstituted tp and tpm is strongly influenced by the steric hindrance of substituents possibly present on the ring carbon atoms.[6]

(6) (a) Dias, H. V. R.; Jin, W.; Kim, H.-J.; Lu, H.-L. *Inorg. Chem.* **1996**, *35*, 2317. (b) Reger, D. L.; Semeniuc, R. F.; Smith, M. D. *Eur. J. Inorg. Chem.* **2003**, 3480. (c) Declercq, J. P.; van Meerssche, M. *Acta Crystallogr., Sect. C: Cryst. Struct. Commun.* **1984**, *40*, 1098. (d) Ochando, L. E.; Rius, J.; Louer, D.; Claramunt, R. M.; Lopez, C.; Elguero, J.; Amigo, J. M. *Acta Crystallogr., Sect. B: Struct. Sci.* **1997**, *53*, 939. (e) Fujisawa, K.; Ono, T.; Ishikawa, Y.; Amir, N.; Miyashita, Y.; Okamoto, K.; Lehnert, N. *Inorg. Chem.* **2006**, *45*, 1698. (f) Hammes, B. S.; Luo, X.; Carrano, M. W.; Carrano, C. J. *Angew. Chem. Int. Ed.* **2002**, *41*, 3259.

(7) De Bari, H.; Zimmer, M. *Inorg. Chem.* **2004**, *43*, 3344 Database searches and analyses carried out by the authors were done by using the Conquest and Vista programs associated with Cambridge Structural Database13 (CSD) v5.24.

(8) Here the negatively charged tp ligand is not taken into account to avoid the use of extended basis sets.

(9) We are perfectly aware that Hpz electronic properties have been the subject of several theoretical[10] and experimental[11] investigations, but we decided to extend our study to this molecule to compare homogeneous theoretical data.

(10) (a) Kuznetsov, M. L.; Dementiev, A. I.; Krasnoshchoikov, S. V. *J. Mol. Struct. (THEOCHEM)* **1998**, *453*, 17. (b) da Silva, G.; Moore, E. E.; Bozzelli, J. W. *J. Phys. Chem. A* **2006**, *110*, 13979. (c) El-Azhary, A. A. *Spectrochim. Acta A* **2003**, *59*, 2009.

(11) Walker, I. C.; Palmer, M. H.; Hubin-Franskin, M. -J.; Delwiche, J. *Chem. Phys. Lett.* **2003**, *367*, 517.

(12) Amsterdam Density Functional (ADF) version 2007.01. http://www.scm.com.

(13) (a) van Lenthe, E.; Baerends, E. J.; Snijders, J. G. *J. Chem. Phys.* **1993**, *99*, 4597. (b) van Lenthe, E.; Baerends, E. J.; Snijders, J. G. *J. Chem. Phys.* **1994**, *101*, 9783. (c) van Lenthe, E.; Ehlers, A. W.; Baerends, E. J.; Snijders, J. G. *J. Chem. Phys.* **1999**, *110*, 8543.

(14) (a) Becke, A. D. *Phys Rev A* **1988**, *38*, 3098. (b) Perdew, J. P. *Phys. Rev. B* **1986**, *33*, 8822.

(15) A LT calculation implies a linear change of a selected LT parameter from its initial to its final value through a specified number of equidistant steps.

(16) van Lenthe, E.; Baerends, E. J. *J. Comput. Chem.* **2003**, *24*, 1142.

(17) Ziegler, T.; Rauk, A. *Theor. Chim. Acta* **1977**, *46*, 1.

(18) Rosa, A.; Ehlers, A. W.; Baerends, E. J.; Snijders, J. G.; te Velde, G. *J. Phys. Chem.* **1996**, *100*, 5690.

(19) Mulliken, R. S. *J. Chem. Phys.* **1955**, *23*, 1833.

(20) Hoffmann, R. *Solids and Surfaces: A Chemist's View of Bonding in Extended Structures*; VCH: New York, 1988.

(21) Pauling electronegativity for most of the elements are reported in the following website http://www.webelements.com/.

(22) Hirshfeld, F. L. *Theor. Chim. Acta* **1977**, *44*, 129.

(23) Da Silva, G.; Moore, E. E.; Bozzelli, J. W. *J. Phys. Chem. A* **2006**, *110*, 13979.

(24) IE's have been evaluated by using the Slater transition state procedure,[25] and lowest lying excitation energies and corresponding oscillator strengths were evaluated by employing the time dependent DFT (TD-DFT) approach.[26]

(25) Slater, J. C. *Quantum Theory of Molecules and Solids. The Self-Consistent Field For Molecules and Solids*; McGraw-Hill: New York, 1974, Vol. 4.

(26) Gross, E. K. U.; Dobson, J. F.; Petersilka, M. In *Density Functional Theory*; Nalewajski, R. F., Ed.; Springer, Heidelberg, 1996.

(27) The theoretical (experimental)[28] μ_{Hpz} value is 2.282 (2.214 ± 0.015) D, theoretical (experimental)[11] IEs of n_N, π_2, and π_3 frontier MO′s are 10.68 (10.65), 9.74 (9.88), and 9.48 (9.15) eV, respectively. The comparison between theoretical and experimental[11] absorption spectrum in the 5−9 eV energy range is reported as Supporting Information.

(28) Kirchhoff, W. H. *J. Am. Chem. Soc.* **1967**, *89*, 1312.

(29) In the [Cu(Hpz)]$^+$ ([Ag(Hpz)]$^+$) π-complex the N(1)N(2)C(3)C(4) and N(2)N(1)C(5)C(4) dihedral angles are 1.5° (1.3°) and 0.1° (0.0°), respectively, and the N(2)C(3)C(4)$H_{C(4)}$ and N(1)C(5)C(4)$H_{C(4)}$ ones are 152.5° and 152.6° (both 160.9°), respectively. Moreover, the CuC(4)$H_{C(4)}$ (AgC(4)$H_{C(4)}$) bond angle corresponds to 102.4° (99.7°).

(30) Both π_3 and π_5 MO′s are strongly localized on the C(4) atom (see Figure 2).

(31) The tpm-1 conformer has not been associated to the κ^1-mode because, to our knowledge, the only structurally ascertained compound with a scorpionate ligand truly κ^1-monodentate is the Rh(I) complex reported by Paneque et al.,[3a] where the metal ion and the H atom of the B−H fragment of the hydrotris(3,5-dimethylpyrazolyl)borato are in a cis arrangement. Even if Reger et al.[32] recently revealed an unprecedented coordination mode of a tpm analogue in {[Ph_2(O)$POCH_2$C(pz)$_3$Ag]$_2$(THF)$_2$}(BF_4)$_2$.

(32) Reger, D. L.; Semeniuc, R. F.; Captain, B.; Smith, M. D. *Inorg. Chem.* **2005**, *44*, 2995.

(33) Optimized coordinates of tpm-0, tpm-1, tpm-2, TS1, and TS2 are reported in Tables S6−S11.

(34) The propeller-like configuration is the same obtained, through molecular mechanics calculations, for the global minimum of free tp by Sohrin et al.[35]

(35) Sohrin, Y.; Kokusen, H.; Matsd, M. *Inorg. Chem.* **1995**, *34*, 3928.

(36) Claramunt, R. M.; Elguero, J.; Fabre, M. J.; Foces-Foces, C.; Cano, F. H.; Fuentes, I. H.; Jaime, C.; López, C. *Tetrahedron* **1989**, *45*, 7805.

(37) Even though MNDO calculations of Claramunt et al.[36] succeeded in foreseen a tpm-1-like arrangement as the most stable conformation of the free ligand, they computed a $\Delta BE_{0,1}$ (2.62 kcal/mol) value significantly higher than that herein reported (0.88 kcal/mol).

(38) The ^{1}H NMR spectrum of tpm at room temperature shows a singlet for the CH methyne proton and two pseudodoublet and one pseudotriplet for the heterocyclic ring protons.[39ab] The three pyrazolyl fragments are all equivalent likely as a consequence of the rapid rotation around the H−C axis. In this regard, Reger suggested that within each tpm unit, the orientation of the three pyrazolyl moieties has a propeller arrangement.[39c]

(39) (a) Elguero, J.; Claramunt, R. M.; Garcerán, R.; Julià, S.; Avila, L.; del Mazo, J. M. *Magn. Reson. Chem.* **1987**, *25*, 260. (b) Otting, G.; Messerle, B. A.; Soler, L. P. *J. Am. Chem. Soc.* **1996**, *118*, 5096. (c) Reger, D. L.; Grattan, T. C. *Synthesis* **2003**, *3*, 350.

(40) The tpm-0 → tpm-1 conversion has been evaluated by starting from tpm-0 and specifying, as single LT parameter, the rotation angle around a H_CC−N bond.

(41) (a) Reger, D. L.; Collins, J. E.; Rheingold, A. L.; Liable-Sands, L. M. *Organometallics* **1996**, *15*, 2029. (b) Reger, D. L.; Collins, J. E.; Rheingold, A. L.; Liable-Sands, L. M.; Yap, G. P. A. *Organometallcs* **1997**, *16*, 349.

(42) (a) Reger, D. L.; Watson, R. P.; Smith, M. D. *Inorg. Chem.* **2006**, *45*, 10077, and references therein reported. (b) Reger, D. L.; Semeniuc, R. F.; Gardinier, J. R.; O'Neal, J.; Reinecke, B.; Smith, M. D. *Inorg. Chem.* **2006**, *45*, 4337, and references therein reported.

(43) (a) Chu, H. S.; Xu, Z.; Ng, S. M.; Lau, C. P.; Lin, Z. *Eur. J. Inorg. Chem.* **2000**, 993. (b) Lehnert, N.; Cornelissen, U.; Neese, F.; Ono, T.; Noguchi, Y.; Okamoto, K.; Fujisawa, K. *Inorg. Chem.* **2007**, *46*, 3916.

(44) (a) Canty, A. J.; Minchin, N. J.; Patrick, J. M.; Healy, P. C.; White, A. H. *J. Chem. Soc., Dalton Trans.* **1982**, 1795. (b) Canty, A. J.; Minchin, N. J.; Patrick, J. M.; White, A. H. *J. Chem. Soc., Dalton Trans.* **1983**, 1253. (c) Canty, A. J.; Minchin, N. J.; Engelhardt, L. M.; Skelton, B. W. *J. Chem. Soc., Dalton Trans.* **1986**, 645. (d) Adams, C. J.; Connelly, N. G.; Emslie, D. J. H.; Hayward, O. D.; Manson, T.; Orpen, A. G.; Rieger, P. H. *Dalton Trans.* **2003**, 2835. (e) Bhambri, S.; Tocher, D. A. *J. Chem. Soc., Dalton Trans.* **1997**, 3367. (f) Iengo, E.; Zangrando, E.; Baiutti, E.; Munini, F.; Alessio, E. *Eur. J. Inorg. Chem.* **2005**, 1019. (g) Bellachioma, G.; Cardaci, G.; Gramlich, V.; Ruegger, H.; Terenzi, S.; Venanzi, L. M. *Organometallics* **1997**, *16*, 2139. (h) Titze, C.; Hermann, J.; Vahrenkamp, H. *Chem. Ber.* **1995**, *128*, 1095. (i) Reger, D. L.; Semeniuc, R. F.; Smith, M. D. *Eur. J. Inorg. Chem.* **2003**, 3480. (j) Reger, D. L.; Semeniuc, R. F.; Captain, B.; Smith, M. D. *Inorg. Chem.* **2005**, *44*, 2995. (k) Reger, D. L.; Semeniuc, R. F.; Little, C. A.; Smith, M. D. *Inorg. Chem.* **2006**, *45*, 7758. (l) Cingolani, A.; Effendy; Martini, D.; Pellei, M.; Pettinari, C.; Skelton, B. W.; White, A. H. *Inorg. Chim. Acta* **2002**, *328*, 87.

(45) (a) Cvetkovic, M.; Batten, S. R.; Moubaraki, B.; Murray, K. S.; Spiccia, L. *Inorg. Chim. Acta* **2001**, *324*, 131. (b) Reger, D. L.; Semeniuc, R. F.; Smith, M. D. *Rev. Roum. Chim.* **2002**, *47*, 1037. (c) Choi, I. Y.; Ahn, S.; Seo, J.; Park, K.-M. *Bull. Korean Chem. Soc.* **2004**, *25*, 1065. (d) Fujisawa, K.; Ono, T.; Ishikawa, Y.; Amir, N.; Miyashita, Y.; Okamoto, K.; Lehnert, N. *Inorg. Chem.* **2006**, *45*, 1698. (e) Kaim, W.; Titze, C.; Schurr, T.; Sieger, M.; Lawson, M.; Jordanov, J.; Rojas, D.; Garcia, A. M.; Manzur, J. Z. *Anorg. Allg. Chem.* **2005**, *631*, 2568.

(46) The absence of any local symmetry in $[M(tpm\text{-}1)]^+$ and $[M(tpm\text{-}2)]^+$ allows a quite extensive mixing among highest occupied tpm based MO′s (n_N and π_2/π_3 linear combinations). MO′s have been then labeled in Figures 10 and 11 by simply referring to their energy order in the free tpm fragment.

JP801902C

Inorganica Chimica Acta 362 (2009) 4358–4364

Contents lists available at ScienceDirect

Inorganica Chimica Acta

journal homepage: www.elsevier.com/locate/ica

Tris(pyrazol-1-yl)borate and tris(pyrazol-1-yl)methane: A DFT study of their different binding capability toward Ag(I) and Cu(I) cations

Maurizio Casarin [a,c,d,*], Daniel Forrer [a,d], Federica Garau [a], Luciano Pandolfo [a,d], Claudio Pettinari [b], Andrea Vittadini [c,d]

[a] Dipartimento di Scienze Chimiche, Università degli Studi di Padova, Via Marzolo 1, 35131 Padova, Italy
[b] Dipartimento di Scienze Chimiche, Camerino, Italy
[c] Istituto di Scienze Molecolari del CNR, Padova, Italy
[d] Consorzio Interuniversitario di Scienza e Tecnologia dei Materiali, Firenze, Italy

ARTICLE INFO

Article history:
Received 1 November 2008
Accepted 5 February 2009
Available online 15 February 2009

Dedicated to the memory of Swiatoslaw ("Jerry") Trofimenko

Keywords:
Density functional theory
Scorpionates
Cu(I) and Ag(I) metal complexes

ABSTRACT

Density functional theory has been used to study the electronic structure of [M(tp)] and $[M(tpm)]^+$ conformers (M = Cu, Ag; tp = tris(pyrazol-1-yl)borate anion, tpm = tris(pyrazol-1-yl)methane) and the energetics of their interconversions. Results for the free tp ligand are similar to those of tpm [M. Casarin, D. Forrer, F. Garau, L. Pandolfo, C. Pettinari, A. Vittadini, J. Phys. Chem. A 112 (2008) 6723], indicating an intrinsic instability of the tripodal conformation (κ^3-like). This points out that, though frequently observed, the κ^3-coordinative mode is unlikely to be directly achieved through the interaction of M(I) with the κ^3-like tp/tpm conformer. Analogously to the $[M(tpm)]^+$ molecular ions, the energy barrier for the κ^2-[M(tp)] → κ^3-[M(tp)] conversion is computed to be negligible. Though κ^n-[M(tp)] and κ^n-$[M(tpm)]^+$ (n = 1, 2, 3) have similar metal–ligand covalent interactions, the negative charge associated to the tp ligand makes the M-tp bonding stronger.

1. Introduction

Tris(pyrazol-1-yl)borate anion (hereafter, tp) and tris(pyrazol-1-yl)methane (hereafter, tpm) ligands play a leading role in modern coordination chemistry [1]. In fact, they are able, both in the substituted and unsubstituted forms, to supply an important steric shielding of the metal center serving, at the same time, as reliable spectator ligands. Complexes of the tp-based ligands are known for most of the metals in the periodic table and have applications in diverse and important fields ranging from catalysis to biomedicine, from metal extraction to biomimetic inorganic chemistry [1]. The common coordination geometry for both tp and tpm is the tripodal one[1] (κ^3-) where the lone pairs of the nitrogen heteroatoms [N(•)] of two pyrazolyl fragments attached to B (tp) or C (tpm) act like the pincers of a scorpion binding the metal centre, while the third pyrazolyl attached to the central atom rotates forward like a scorpion's tail to "sting" the metal. The family of ligands with this coordination capability, whose simplest members are tp and tpm, is know as "scorpionates". However, we recently showed [3] that crystal data for both "uncoordinated" tp [2a,b] and free tpm [4] ligands suggest alternative and less evocative coordination modes. In fact, both tp and tpm are characterized by the presence of a single pyrazolyl group with N(•) in *trans* with respect to the B–H (tp)/C–H (tpm) fragments.[2]

Theoretical work so far devoted to the study of the interaction of tp and tpm ligands with metal ions is rather limited. A few years ago, De Bari and Zimmer [6] carried out a conformational study based on molecular mechanics and structural database analysis of tp and tpm behaving as κ^3-tripodal ligands. They concluded that "tripodal scorpionate ligands can accommodate a variety of metal sizes by opening up the ligand". More recently, we employed the density functional theory (DFT) to study the electronic structure of $[M(tpm)]^+$ molecular ion conformers (M = Cu, Ag) as well as the energetics of their interconversion [3].

In this paper we study the κ^1-monodentate, κ^2-chelating, and κ^3-tripodal conformers of [M(tp)] (M = Cu, Ag). Our aim is to investigate the electronic properties and the energetics of the interconversion of the conformers, and to make a comparison with the results previously obtained with the analogous $[M(tpm)]^+$

* Corresponding author. Address: Dipartimento di Scienze Chimiche, Università degli Studi di Padova, Via Marzolo 1, 35131 Padova, Italy.
E-mail address: maurizio.casarin@unipd.it (M. Casarin).

[1] tp and tpm may also act as κ^2-ligands bonded to a single metal (κ^2-chelating), as κ^1–κ^2-ligands bridging two metals or, hardly ever, as κ^1-ligands likely depending on the steric congestion around the metal center and the number of donor substituents on the central atom X, which may be P and Ga other than B and C (see Refs. [1,2]). tp may also have a "κ^0" denticity as shown by the Carmona group in Rh(I) and Rh(III) complexes [2a,b].

[2] The relative position of pyrazolyl fragments in substituted and unsubstituted tp and tpm is strongly influenced by the steric hindrance of substituents possibly present on the ring carbon atoms [5].

0020-1693/$ - see front matter © 2009 Elsevier B.V. All rights reserved.
doi:10.1016/j.ica.2009.02.004

complexes [3]. The first section of this contribution is dedicated to the assessment of the conformational properties of the free tp ligand leaving aside any problem concerning optical isomerism, while in the second part we focus on the binding energies and electronic properties of the [M(tp)] conformers, and we finally make a comparison between the $[M(tpm)]^+$ and [M(tp)] bonding schemes.

2. Computational details

All the presented results are based on DFT, and have been obtained by running the Amsterdam Density Functional (ADF) package [7] and adopting the scalar relativistic zeroth-order regular approximation (ZORA) [8]. Generalized gradient corrections have been self-consistently included through the Becke–Perdew formula [9], TZP ZORA basis sets have been adopted for all the atoms [10]; inner cores of Cu (1s2s2p3s3p), Ag (1s2s2p3s3p3d), B (1s), C (1s), and N (1s) atoms were kept frozen throughout the calculations. Geometries for ground- and transition-states (GS and TS, respectively) have been optimized without imposing any symmetry. All TS's have been estimated through the following procedure: (i) a linear transit (LT) calculation has been run by varying a dihedral angle;[3] (ii) from the TS guess provided by step (i), a stationary point on the energy surface has been searched; (iii) the adequacy of the TS estimate has been then checked by computing vibrational frequencies at the corresponding geometry and verifying that one of them is imaginary; (iv) the Hessian computed in the third step is employed for the final TS optimization. Binding energies (*BE*) were analyzed in terms of fragment molecular orbitals (FMO) by applying the Ziegler's extended transition state method (ETS) [11]. According to the ETS scheme,

$$BE = \Delta E_{es} + \Delta E_{Pauli} + \Delta E_{int} + \Delta E_{prep} \quad (1)$$

where ΔE_{es} is the pure electrostatic interaction, ΔE_{Pauli} is the destabilizing two-orbital-four-electron interaction between the occupied orbitals of the interacting fragments ((ΔE_{es} + ΔE_{Pauli}) corresponds to the so called steric interaction (ΔE_{st}) contribution), ΔE_{int} derives from the stabilizing interaction between occupied and empty orbitals of the interacting fragments, and ΔE_{prep} is the energy required to relax the structure of the free fragments to the geometry they assume in the final system. *BE*s were further corrected by taking into account the basis set superposition error (*BSSE*) which was estimated by making use of reference energies calculated with "ghost" fragments [12].

One-electron levels are displayed as density of states (hereafter, DOS) by using a 0.25 eV Lorentzian broadening factor. These plots, based on Mulliken's prescription for partitioning the overlap density [13], have the advantage of providing insights into the atomic composition of MOs over a broad range of energy. Finally, information about the localization and the bonding/antibonding character of selected MOs was obtained by using crystal orbital overlap populations (COOP) [14] computed by weighting one-electron energy levels by their basis orbital percentage.

3. Results and discussion

Tp and tpm are potentially tripodal ligands characterized by the presence of three pyrazolyl moieties bonded to a central B and C atom, respectively. The MO structure of both the Hpz free molecule and the $[M(Hpz)]^+$ complexes have been recently described by our group [3], We briefly resume the main findings in the following. Hpz is planar, fully conjugated, and isoelectronic with the cyclopentadienyl anion, though characterized by a high electronic charge density on N atoms both in the molecular plane and out of it. Its valence manifold includes five π-like MOs and the N(•) lone pair (hereafter, n_N). Among them, the π_1, π_2, π_3 ones and n_N are occupied, whereas the π_4 and π_5 MOs are empty. Moreover, π_3 and π_4 correspond to the Hpz HOMO and LUMO, respectively. As a consequence of these peculiarities, each tp/tpm pyrazolyl group may be involved in two competitive metal–ligand bonding mechanisms: a σ-binding implying n_N and a π-binding entailing the π states of the aromatic ring. The DFT results pertaining to σ/π $[M(Hpz)]^+$ complexes revealed the importance of π contributions to the metal–ligand bond in σ-$[M(Hpz)]^+$ molecular ions and the leading role played by the ΔE_{st} term of Eq. (1) in determing the final *BE* value of σ/π-$[M(Hpz)]^+$ complexes.

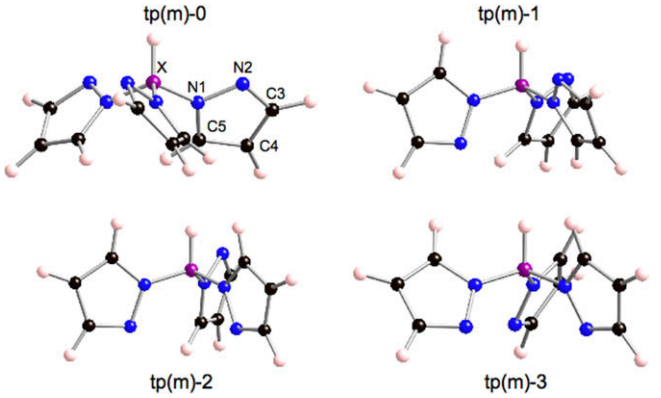

Fig. 1. Schematic representation of possible relative arrangements of the three pyrazolyl fragments in tp (X = B) and tpm (X = C).

Table 1
Relative binding energy contributions (kcal/mol) for tp and tpm free ligands.

	tp-0(tpm-0)	tp-1/(tpm-1)	tp-2/(tpm-2)	tp-3/(tpm-3)
$\Delta(\Delta E_{Pauli})$	−7.86 (−17.51)	–(–)	3.29 (3.18)	6.14 (−1.17)
$\Delta(\Delta E_{el})$	−2.25 (−1.37)	–(–)	−0.87 (−0.42)	−4.99 (−3.76)
$\Delta(\Delta E_{st})$	−10.10 (−18.88)	–(–)	2.42 (2.75)	1.15 (−4.93)
$\Delta(\Delta E_{int})$	10.38 (19.76)	–(–)	−0.89 (−0.25)	5.35 (13.32)

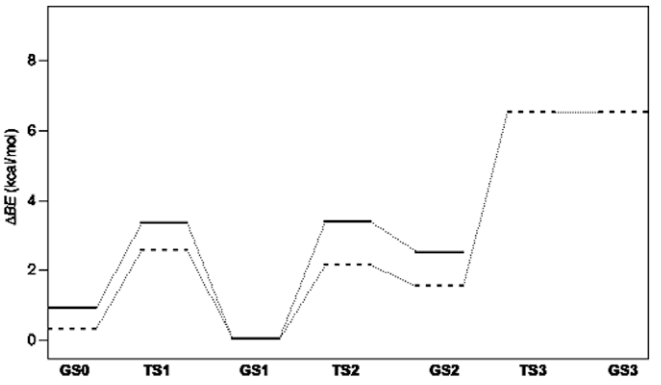

Fig. 2. Relative *BE* values of GS0, TS1, GS1, TS2, and GS2 for tp (dashed lines) and tpm (solid lines); TS3 and GS3 are limited to tp (see text). The zero energy value corresponds to the GS1 *BE*.

3.1. tp conformational properties

Because of its charged nature, the free ligand cannot be characterized by X-ray diffraction. However, it is noteworthy that about 10 years ago Carmona and coworkers [2a,b] synthesized and structurally characterized what they called an isolated

[3] A LT calculation implies a linear change of a selected LT parameter from its initial to its final value through a specified number of equidistant steps.

Table 2
Binding energy contributions in kcal/mol for the [M(tp-*n*)] and [M(tpm-*n*)]$^+$ conformers.

	[M(tp-1)] ([M(tpm-1)]$^+$)	TS(M)	[M(tp-2)] ([M(tpm-2)]$^+$)	[M(tp-3)] ([M(tpm-3)]$^+$)
$^{Cu}\Delta E_{Pauli}$	142.49 (129.59)	122.77	160.37 (143.80)	142.47 (131.68)
$^{Cu}\Delta E_{el}$	−232.29 (−130.46)	−213.24	−261.15 (−157.93)	−262.69 (−161.82)
$^{Cu}\Delta E_{st}$	−89.80 (−0.87)	−90.47	−100.78 (−14.13)	−120.22 (−30.14)
$^{Cu}E_{int}$	−103.72 (−97.18)	−95.67	−103.06 (−93.47)	−98.92 (−92.95)
$^{Cu}\Delta E_{prep}$	8.24 (6.92)		4.55 (4.67)	3.96
$^{Cu}BSSE$	2.84 (2.79)		2.42 (2.46)	2.71
^{Cu}BE	−182.44 (−88.34)		−196.87 (−100.47)	−212.47
$^{Ag}\Delta E_{Pauli}$	184.73 (152.24)	152.28	184.57 (160.19)	191.54 (160.37)
$^{Ag}\Delta E_{el}$	−191.63 (−87.48)	−172.44	−210.22 (−109.92)	−220.52 (−116.45)
$^{Ag}\Delta E_{st}$	−6.90 (64.76)	−20.16	−25.65 (50.27)	−28.98 (43.92)
$^{Ag}\Delta E_{int}$	−153.39 (−132.66)	−134.22	−144.32 (−126.87)	−154.67 (−135.32)
$^{Ag}\Delta E_{prep}$	6.01 (4.50)		4.09 (3.91)	2.14
$^{Ag}BSSE$	0.66 (0.66)		0.53 (0.52)	0.58
^{Ag}BE	−153.62 (−62.74)		−165.35 (−72.17)	−180.93

hydrotris(pyrazolyl)borate anions having a "κ^0" coordinative mode. Interestingly, the structure of this κ^0 unsubstituted tp is characterized by a single pyrazolyl group with N(•) in *trans* with respect to the hydrogen of the B–H fragment, similarly to the structural arrangement of the free tpm [5].[4] In agreement with the labeling scheme adopted in Ref. [3], this conformer has been tagged tp-1, while those corresponding to the κ^2-chelating and κ^3-tripodal coordinative modes have been labeled as tp-2 and tp-3, respectively (see Fig. 1). Obviously, the tp-0 conformer is the one with the three N(•) in *cis* with respect the B–H moiety. Optimized coordinates of tp-0, tp-1, tp-2, tp-3, TS1, TS2, TS3 are reported in Tables S0–S6 of the Supplementary material.

Analogously to tpm-0, the pyrazolyl fragments of the tp-0 optimized structure are symmetry related by a C_3 axis, and assume a propeller-like arrangement. Relative *BE*s corresponding to tp-*n* GS as well as to relevant saddle points are reported in Table 1 and displayed in Fig. 2 together *BE*'s of akin tpm conformers. The relative stability order of tp-*n* conformers (n = 0–3) is the same we found for the tpm ones [3], but the energy barriers associated to these interconversion paths (TS1, TS2, and TS3) are systematically lower than those evaluated for tpm (see Fig. 2). This is consistent with NMR data collected at room temperature by the Carmona group for the κ^0 hydrotris(pyrazolyl)borate anions [2a] which indicate a substantial free rotation around the B–N bonds.

A further point worth of note concerns the H–B vibrational frequencies (ν_{BH}) computed for the optimized tp-0, tp-1, and tp-2 structures (2517, 2513, and 2482 cm^{-1}, respectively). These values are all in reasonable agreement with the experimental κ^0 tp ν_{BH} value reporded by Paneque et al. [2a] (2474 cm^{-1}). At variance to that, the calculated tp-3 ν_{BH} lies at a significantly lower frequency (2388 cm^{-1}). In this regard, it can be useful to remark that the optimized tp-1 bond lengths and bond angles agree well with structural data reported by Paneque et al. [2a], tp-0, tp-1, and tp-2 H–B bond lengths are very similar (1.201, 1.202, and 1.206 Å, respectively), while the tp-3 H–B internuclear distance (1.218 Å) is longer than that corresponding to the other tp conformers.

In general, theoretical results pertaining to tp-*n* reproduce those recently published for tpm-*n* [3]: though common, the κ^3-tripodal coordinative mode is unlikely to be achieved through a direct interaction of a metal center with the ligand having a tp-3/tpm-3 arrangement. However, at variance to the tpm case, we were able to locate the tp GS3 energy minimum. Consistently with a very flat potential energy surface in this region, the energy difference between tp TS3 and GS3 is negligible (see Fig. 2).[5]

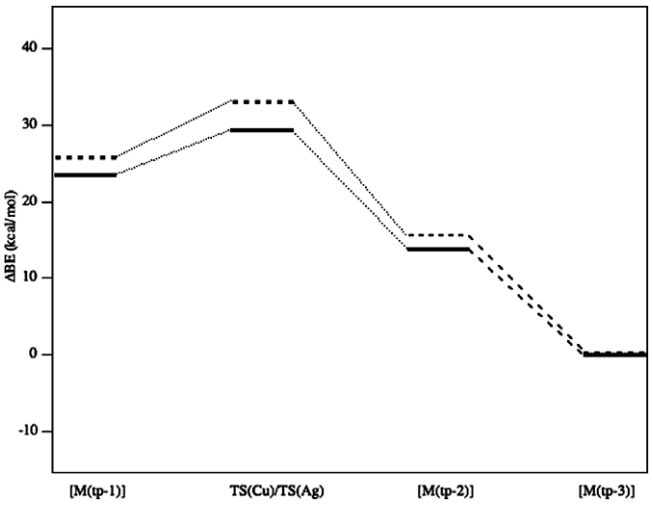

Fig. 3. Relative *BE* values of [M(tp-1)], TS(M), [M(tp-2)], and [M(tp-3)] (M = Cu (dashed lines) and Ag (solid lines)). The zero *BE* value corresponds to the [M(tp-3)] *BE*. Between [M(tp-2)] and [M(tp-3)] no TS has been found.

3.2. [Cu(tp)] and [Ag(tp)] complexes

The structural and electronic properties of tp metal complexes have been the subject of several experimental contributions [1,2,5,6,15]. From these works, it was established that N_3 tripodal ligands such as hydrotris (pyrazolyl)borate anionic ligands or tris(pyrazolyl)methane neutral ligands behave as biomimetic systems. This suggested their use as a modeling tool to investigate the catalytic activity of metal centers in biological systems. However, no study has been so far specifically dedicated to the analysis of the interplay between the metal–ligand interaction and the ligand hapticity.

The strength and the nature of the M(I)–tp bond in [M(tp-*n*)] (n = 1, 2, and 3) have been obtained through the ETS scheme by considering M(I) and tp as interacting fragments [11]. Optimized coordinates of [M(tp-*n*)] species and of TS(Cu) and TS(Ag) saddle points corresponding to the [M(tp-1)] → [M(tp-2)] conversions

[4] Despite isolated hydrotris(pyrazolyl)borate derivatives may have different conformations, it has to be pointed out that, in these cases [5a,5e], the specific structural arrangement is ruled by steric factors.

[5] Vibrational frequencies have been evaluated for both TS3 and GS3 verifying that: (i) one of them is imaginary in the former case; and (ii) they are all positive in the latter one.

are collected in Tables S7–S14. Relative *BE*s are reported in Table 2 and displayed in Fig. 3.

As far as the relative stability of these species is concerned, a comparison between Figs. 3 and 2 reveals that, as previously found for $[M(tpm\text{-}n)]^+$ molecular ions [3], [M(tp-1)] is more stable than [M(tp-2)], i.e. the order is reversed with respect to the free ligand. It is also remarkable that, despite both [Cu(tp-2)] and [Ag(tp-2)] correspond to local minima, they are so shallow that we were unable to find the saddle point corresponding to the [M(tp-2)] → [M(tp-3)] conversion. This indicates that, in tune with our previous calculations on $[M(tpm\text{-}n)]^+$ conformers, once the κ^2-complex is formed, either from the interaction of M(I) with tp-2 or through the [M(tp-1)] → [M(tp-2)] conversion, the κ^3-tripodal species may be readily formed. However, the [M(tp-2)] → [M(tp-3)] conversion could be hampered by several reasons such as: (i) the coordinative saturation of the metal center by concurrent ligands; (ii) the coordination of the N(•) of the third pyrazolyl group to a different metal center; (iii) steric factors determined by bulky substituents on tp; (iv) electronic factors favoring specific arrangements [2,16].

Concerning the nature of the metal–ligand interaction, the ETS analysis (see Table 2) indicates that, independently of the coordi-

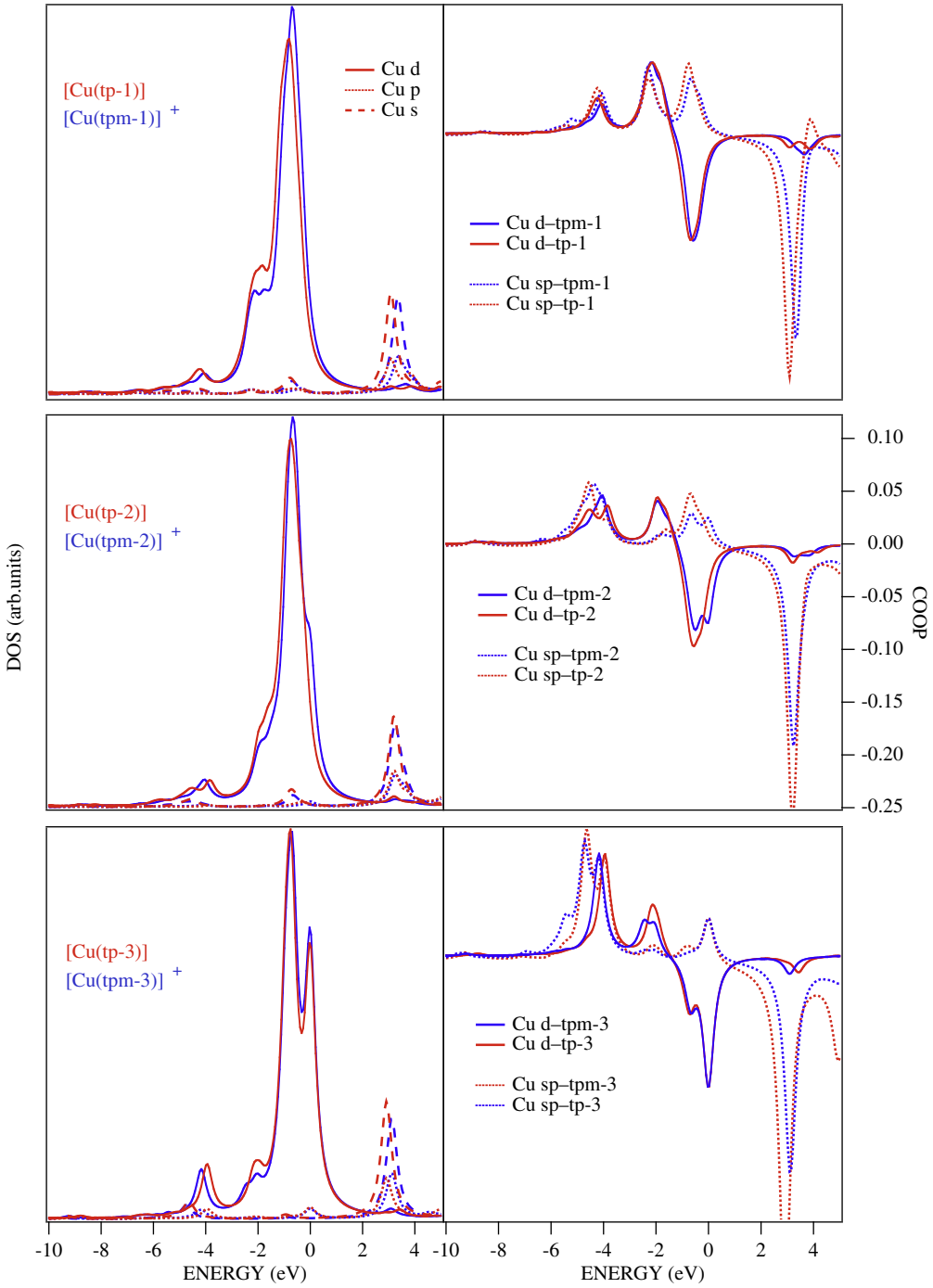

Fig. 4. (Left) d, s and p Cu PDOS of $[Cu(tp\text{-}n)]$ and $[Cu(tpm\text{-}n)]^+$; (right) Cu–(tp-*n*) and Cu–(tpm-*n*) COOP, bonding (antibonding) states correspond to positive (negative) peaks. The zero energy matches the HOMO energy of each species.

native mode, the covalent component of the metal–ligand interaction is quite similar in [M(tp)] and [M(tpm)]$^+$, while the electrostatic interaction between M(I) and the negatively charged tp significantly strengthens the metal–ligand bond on passing from [M(tpm)]$^+$ to [M(tp)]. Further insights can be obtained from the inspection of M(I) PDOS and M(I)–ligand COOP curves (see Figs. 4 and 5) coupled to the analysis of the M(I)/ligand Hirshfeld charges [17] (Q^H) in [M(tp-*n*)] and [M(tpm-*n*)]$^+$ (Table 3). Though the overall interaction between the M(I) and tp charged fragments is definitely stronger than that between M(I) and the neutral tpm, Figs. 4, 5 and data reported in Table 3 reveal: (i) the close similarity of metal-based s, p, and d PDOS on passing from [M(tp-*n*)] to [M(tpm-*n*)]$^+$; (ii) the negligible contribution provided by the M(I) → tp/tpm backdonation to the metal–ligand interaction; (iii) the leading role played by the tp/tpm → M(I) donation in the metal–ligand bonding.

Structural and electronic differences of a series of κ^3-[Cu(tp)] and κ^3-[Cu(tpm)]$^+$ complexes have been recently investigated by Fujisawa et al. [5e] through experimental and DFT studies. One of their main conclusions was that since κ^3-tpm is a weaker donor than κ^3-tp, the Cu(I) ion in the κ^3-tpm complex is electron-poorer, and in consequence less involved in back-donation. In contrast to

Table 3
Q^H values of M, tp, and tpm fragments in [M(tp-*n*)] and [M(tpm-*n*)]$^+$ species.

	[M(tp-1)] ([M(tpm-1)]$^+$)	[M(tp-2)] ([M(tpm-2)]$^+$)	[M(tp-3)] ([M(tpm-3)]$^+$)
Q^H_{Cu}	0.75 (0.79)	0.76 (0.78)	0.79 (0.81)
$Q^H_{tp}\left(Q^H_{tpm}\right)$	−0.75 (0.21)	−0.76 (0.22)	−0.79 (0.19)
Q^H_{Ag}	0.71 (0.75)	0.77 (0.76)	0.74 (0.77)
$Q^H_{tp}\left(Q^H_{tpm}\right)$	−0.71 (0.25)	−0.77 (0.24)	−0.74 (0.23)

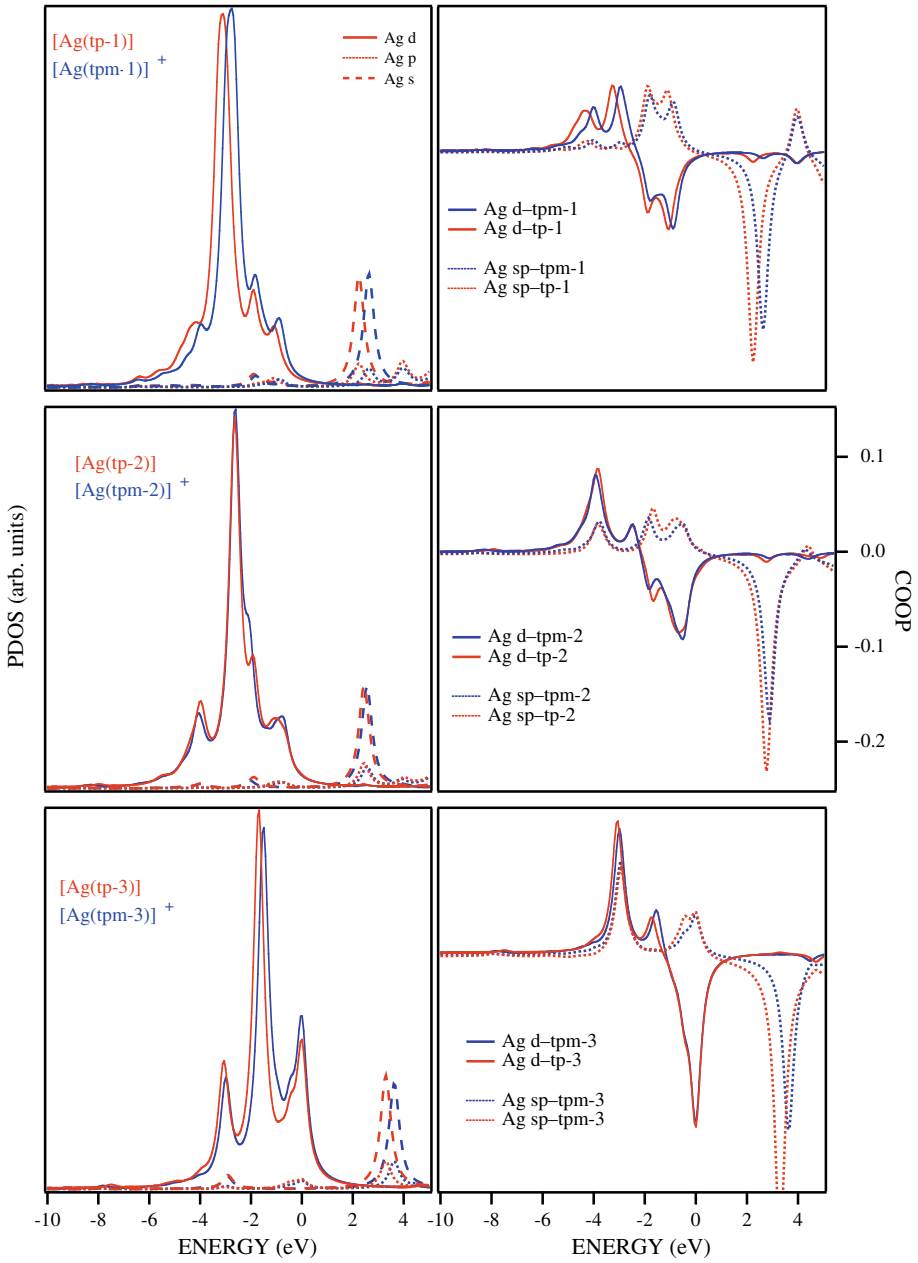

Fig. 5. (Left) d, s and p Ag PDOS of [Ag(tp-*n*)] and [Ag(tpm-*n*)]$^+$; (right) Ag–(tp-*n*) and Ag–(tpm-*n*) COOP, bonding (antibonding) states correspond to positive (negative) peaks. The zero energy matches the HOMO energy of each species.

Table 4
Binding energy contributions (kcal/mol) to the interaction between M(L) and CO fragment (M = Cu,Ag; L=tp-3, tpm-3).

	M(tp-3)–CO	M(tpm-3)–CO
$^{Cu}\Delta E_{Pauli}$	127.44	109.34
$^{Cu}\Delta E_{el}$	−101.97	−92.23
$^{Cu}\Delta E_{st}$	25.46	17.11
$^{Cu}\Delta E_{int}$	−64.49	−56.14
$^{Cu}\Delta E_{prep}$	3.02	2.64
$^{Cu}BSSE$	0.81	0.96
^{Cu}BE	−35.20	−35.43
$Q^{H}_{M(Ligand)}$	0.15	1.10
Q^{H}_{CO}	−0.15	−0.10
$^{Ag}\Delta E_{Pauli}$	131.18	112.94
$^{Ag}\Delta E_{el}$	−101.53	−90.52
$^{Ag}\Delta E_{st}$	29.65	22.42
$^{Ag}\Delta E_{int}$	−58.35	−50.46
$^{Ag}\Delta E_{prep}$	0.42	0.01
$^{Ag}BSSE$	0.77	0.70
^{Ag}BE	−27.51	−27.33
$Q^{H}_{M(Ligand)}$	0.11	1.05
Q^{H}_{CO}	−0.11	−0.05

this conclusion, data reported in Table 3 indicate that the difference between the free tp and tpm charge (−1 and 0, respectively) has negligible effects on the final Q^{H}_{M} values, consistently with the rather close $^{Cu}\Delta E_{int}$(tp-3) and $^{Cu}\Delta E_{int}$(tpm-3) values. To clarify this discrepancy, we have carried out calculations also for the [M(tp-3)(CO)] and [M(tpm-3)(CO)]$^{+}$ model complexes. We analyzed the results on the basis of the ETS scheme, considering as interacting fragments [M(tp-3)] and [CO] in one case, and [M(tpm-3)]$^{+}$ and [CO] in the other one. Optimized coordinates of [Cu(tp-3)(CO)] (hereafter, ^{tp}**I**), [Cu(tpm-3)(CO)]$^{+}$ (^{tpm}**I**), [Ag(tp-3)(CO)] (^{tp}**II**), and [Ag(tpm-3)(CO)]$^{+}$ (^{tpm}**II**) are reported in Tables S15–S18, respectively, while interacting fragments Q^{H} and corresponding binding energies are collected in Table 4.

As far as the optimized structural parameters are concerned (see Tables S15–S18), both the Cu–CO (1.810 and 1.825 Å in ^{tp}**I** and ^{tpm}**I**, respectively) and C–O (1.153 and 1.146 Å in ^{tp}**I** and ^{tpm}**I**, respectively) bond lengths (BLs) are in reasonable agreement with experimental and theoretical data reported by Fujisawa et al. [5e]. The same holds for the ^{tp}**II** Ag–CO and C–O BLs (1.964 and 1.150 Å, respectively) which are quite similar to those experimentally determined by Dias and Jin [18] for the [Ag{HB(3,5-$(CF_3)_2Pz_3$}(CO)] complex. No comparison with the ^{tp}**II** Ag–CO and C–O BLs (1.991 and 1.142 Å, respectively) is possible as crystallographic data pertaining to κ^3-[Ag(tpm)(CO)]$^{+}$-like species are unavailable.

The inspection of Table 4 results particularly useful to understand the [M(tp-3)]/[M(tpm-3)]–[CO] bonding interaction. In particular, we point out that carbon monoxide always carries a negative charge, i.e. it is a net electron acceptor; moreover, the absolute value of the charge is larger in the tp-based complexes than in the tpm-based ones. According to that, ν_{CO} (2039, 2090, 2049, 2105 cm^{-1} in ^{tp}**I**, ^{tpm}**I**, ^{tp}**II**, and ^{tpm}**II**, respectively)[6] is systematically red shifted with respect the harmonic theoretical value computed for the free CO (2113 cm^{-1}). Remarkably, the (^{tpm}**I** − ^{tp}**I**) $\Delta\nu_{CO}$ (51 cm^{-1}) exactly reproduces the experimental value reported by Fujisawa et al. [5e]. As a whole, these results confirm the conclusions reported on Ref. [5e]; however, taking advantage of the ETS analysis [11], we find that, despite the [Cu(tpm-3)]$^{+}$ and [Ag(tpm-3)]$^{+}$ positive fragments are weaker electron donor than the neutral [Cu(tp-3)] and [Ag(tp-3)] ones, the ΔBEs between [Cu(tpm-3)(CO)]$^{+}$ and [Cu(tp-3)(CO)] as well as between [Ag(tpm-3)}(CO)]$^{+}$ and [Ag(tp-3)(CO)] are negligible. The reason is that the more negative $^{M}\Delta E_{int}$ term in the neutral adducts is compensated by the less positive $^{M}\Delta E_{st}$ contribution in the charged species.

[6] Experimental ν_{CO} values reported by Fujisawa et al. [5d] for [Cu{HB(3,5-$iPr_2pz)_3$}(CO)] and [Cu{HC(3,5-$iPr_2pz)_3$}(CO)](PF_6) are 2056 and 2107 cm^{-1}, respectively. The blue shifted value reported by Dias and Jin [18] for [AgHB(3,5-$(CF_3)_2Pz_3$(CO)] (2162 cm^{-1}) is most probably due to the presence of CF_3 substituents on the pz rings.

4. Concluding remarks

In this contribution we have presented and discussed the results of a series of first-principle calculations carried out on the free tp ligand and its Cu(I) and Ag(I) complexes. The energetics of conformational transitions has been studied for the free ligand and for its complexes. Moreover, we analyzed the metal–ligand bonding showing that, independently of the coordinative mode, the covalent components are rather similar in M-tp and (M-tpm)$^{+}$. However, the electrostatic interaction between M(I) and the negatively charged tp significantly strengthens the metal–ligand bond on passing from (M-tpm)$^{+}$ to (M-tp). We have also considered the electronic and molecular properties of the adducts [Cu(tp-3)(CO)], [Cu(tpm-3)(CO)]$^{+}$, [Ag(tp-3)(CO)], and [Ag(tpm-3)(CO)]$^{+}$ showing that: (i) CO always behaves as an electron donor; (ii) the charged species [Cu(tpm-3)]$^{+}$ and [Ag(tpm-3)]$^{+}$ are weaker donor than the neutral ones; (iii) [M(tpm-3)}(CO)]$^{+}$ and [M(tp-3)(CO)] have, for each metal, the same binding energy.

Acknowledgments

This work was partially supported by the Italian PRIN founding n. 2006038447. The "Laboratorio Interdipartimentale di Chimica Computazionale" (LICC) at the Department of Chemistry of the University of Padova is acknowledged for support of the computer facilities.

Appendix A. Supplementary material

Supplementary data associated with this article can be found, in the online version, at doi:10.1016/j.ica.2009.02.004.

References

[1] (a) C. Pettinari, R. Pettinari, Coord. Chem. Rev. 249 (2005) 525. and references therein reported;
(b) C. Pettinari, C. Santini, Compr. Coord. Chem. II 1 (2004) 159;
(c) S. Trofimenko, Scorpionates, The Coordination Chemistry of Polypyrazolylborate Ligands, Imperial College Press, 1999;
(d) C. Pettinari, Scorpionates II: Chelating Borate Ligands, World Scientific Publishing, New York, 2008;
(e) S. Trofimenko, J. Chem. Ed. 82 (2005) 1715;
(f) S. Murtuza, O.L. Casagrande Jr., R.F. Jordan, Polym. Mater. Sci. Eng. 84 (2001) 109;
(g) I. Santos, A. Paulo, J.D. Correia, Top. Curr. Chem. 252 (2005) 45;
(h) T. Kitano, H. Wada, H. Mukai, K. Ueda, Y. Sohrin, Anal. Sci. 17 (2001) i1113;
(i) A. de la Lande, H. Gérard, V. Moliner, G. Izzet, O. Reinaud, O. Parisel, J. Biol. Inorg. Chem. 11 (2006) 593.
[2] (a) M. Paneque, S. Sirol, M. Trujillo, E. Gutiérrez-Puebla, M.A. Monge, E. Carmona, Angew. Chem., Int. Ed. 39 (2000) 218;
(b) M. Paneque, S. Sirol, M. Trujillo, E. Carmona, E. Gutiérrez-Puebla, M.A. Monge, C. Ruiz, F. Malbosc, C. Serra-Le Berre, P. Kalck, M. Etienne, J.C. Daran, Chem. Eur. J. 7 (2001) 3868;
(c) D.D. Ellis, J.C. Jeffery, P.A. Jelliss, J.A. Kautz, F.G.A. Stone, Inorg. Chem. 40 (2001) 2041.
[3] M. Casarin, D. Forrer, F. Garau, L. Pandolfo, C. Pettinari, A. Vittadini, J. Phys. Chem. A 112 (2008) 6723.
[4] C.C. McLauchlan, A.N. Varda, J.R. Giles, Acta Crystallogr., Sect. E: Struct. Rep. 60 (2004) o1419.
[5] (a) H.V.R. Dias, W. Jin, H.-J. Kim, H.-L. Lu, Inorg. Chem. 35 (1996) 2317;
(b) D.L. Reger, R.F. Semeniuc, M.D. Smith, Eur. J. Inorg. Chem. (2003) 3480;
(c) J.P. Declercq, M. van Meerssche, Acta Crystallogr., Sect. C: Cryst. Struct. Commun. 40 (1984) 40;
(d) L.E. Ochando, J. Rius, D. Louer, R.M. Claramunt, C. Lopez, J. Elguero, J.M. Amigo, Acta Crystallogr., Sect. B: Struct. Sci. 53 (1997) 939;
(e) K. Fujisawa, T. Ono, Y. Ishikawa, N. Amir, Y. Miyashita, K. Okamoto, N. Lehnert, Inorg. Chem. 45 (2006) 1698;
(f) B.S. Hammes, X. Luo, M.W. Carrano, C.J. Carrano, Angew. Chem., Int. Ed. 41 (2002) 3259.

[6] H. De Bari, M. Zimmer, Inorg. Chem. 43 (2004) 3344. Database searches and analyses carried out by the authors were done by using the Conquest and Vista programs associated with Cambridge Structural Database13 (CSD) v5.24.
[7] Amsterdam Density Functional (ADF) version 2007.01 <http://www.scm.com>.
[8] (a) E. van Lenthe, E.J. Baerends, J.G. Snijders, J. Chem. Phys. 99 (1993) 4597;
(b) E. van Lenthe, E.J. Baerends, J.G. Snijders, J. Chem. Phys. 101 (1994) 9783;
(c) E. van Lenthe, A.W. Ehlers, E.J. Baerends, J.G. Snijders, J. Chem. Phys. 110 (1999) 8543.
[9] (a) A.D. Becke, Phys. Rev. A 38 (1988) 3098;
(b) J.P. Perdew, Phys. Rev. B 33 (1986) 8822.
[10] E. van Lenthe, E.J. Baerends, J. Comput. Chem. 24 (2003) 1142.
[11] T. Ziegler, A. Rauk, Theor. Chim. Acta 46 (1977) 1.
[12] A. Rosa, A.W. Ehlers, E.J. Baerends, J.G. Snijders, G. te Velde, J. Phys. Chem. 100 (1996) 5690.
[13] R.S. Mulliken, J. Chem. Phys. 23 (1955) 1833.
[14] R. Hoffmann, Solids and Surfaces: A Chemist's View of Bonding in Extended Structures, VCH, New York, 1988.
[15] (a) L.M. Mirica, X. Ottenwaelder, T.D.P. Stack, Chem. Rev. 104 (2004) 1013. and references therein reported;
(b) E.A. Lewis, W.B. Tolman, Chem. Rev. 194 (2004) 1047;
(c) N. Lehnert, U. Cornelissen, F. Neese, T. Ono, Y. Noguchi, K. Okamoto, K. Fujisawa, Inorg. Chem. 46 (2007) 3916.
[16] (a) D.L. Reger, Y. Ding, Polyhedron 13 (1994) 869;
(b) C. Gemel, R. John, C. Slugovc, K. Mereiter, R. Schmid, K. Kirchner, J. Chem. Soc., Dalton Trans. (2000) 2607;
(c) J.S. Thompson, R.L. Harlow, J.F. Whitney, J. Am. Chem. Soc. 105 (1983) 3522;
(d) J.S. Thompson, J.F. Whitney, Acta Crystallogr., Sect. C: Cryst. Struct. Commun. 40 (1984) 756;
(e) Z. Hu, R.D. Williams, D. Tran, T.G. Spiro, S.M. Gorun, J. Am. Chem. Soc. 122 (2000) 3556;
(f) E.R. Humphrey, Z. Reeves, J.C. Jeffery, J.A. McCleverty, M.D. Ward, Polyhedron 18 (1999) 1335;
(g) M. Kujime, S. Hikichi, M. Akita, Dalton Trans. (2003) 3506;
(h) A.J. Canty, N.J. Minchin, L.M. Engelhardt, B.W. Skelton, A.H. White, J. Chem. Soc., Dalton Trans. (1986) 645;
(i) A.L. Rheingold, L.M. Liable-Sands, C.L. Incarvito, S. Trofimenko, J. Chem. Soc., Dalton Trans. (2002) 2297;
(j) A.J. Canty, J.L. Hoare, B.W. Skelton, A.H. White, G. van Koten, J. Organomet. Chem. 552 (1998) 23;
(k) J. Campora, P. Palma, D. del Rio, J.A. Lopez, E. Alvarez, N.G. Connelly, Organometallics 24 (2005) 3624;
(l) M. Akita, T. Miyaji, S. Hikichi, Y. Moro-oka, Chem. Commun. (1998) 1005;
(m) T. Miyaji, M. Kujime, S. Hikichi, Y. Moro-oka, M. Akita, Inorg. Chem. 41 (2002) 5286;
(n) J.-M. Valk, F. Maassarani, P. van der Sluis, A.L. Spek, J. Boersma, G. van Koten, Organometallics 13 (1994) 2320;
(o) M. Akita, T. Miyaji, N. Muroga, C. Mock-Knoblauch, W. Adam, S. Hikichi, Y. Moro-oka, Inorg. Chem. 39 (2000) 2096;
(p) M. Kujime, S. Hikichi, M. Akita, Organometallics 20 (2001) 4049;
(q) W. Klaui, B. Turkowski, H. Wunderlich, Z. Anorg. Allg. Chem. 627 (2001) 2397;
(r) M. Akita, T. Miyaji, S. Hikichi, Y. Moro-oka, Chem. Lett. (1999) 813;
(s) A.J. Canty, H. Jin, A.S. Roberts, P.R. Traill, B.W. Skelton, A.H. White, J. Organomet. Chem. 489 (1995) 153;
(t) P.E. Rush, J.D. Oliver, Chem. Commun. (1974) 996;
(u) J.D. Oliver, N.C. Rice, Inorg. Chem. 15 (1976) 2741;
(v) D.D. Wick, K.I. Goldberg, J. Am. Chem. Soc. 119 (1997) 10235;
(w) S. Reinartz, P.S. White, M. Brookhart, J.L. Templeton, J. Am. Chem. Soc. 123 (2001) 12724;
(x) S. Reinartz, P.S. White, M. Brookhart, J.L. Templeton, Organometallics 19 (2000) 3854;
(y) D.L. Reger, J.C. Baxter, L. Lebioda, Inorg. Chim. Acta 165 (1989) 201.
[17] F.L. Hirshfeld, Theor. Chim. Acta 44 (1977) 129.
[18] H.V.R. Dias, W. Jin, J. Am. Chem. Soc. 117 (1995) 11381.

Role and Effective Treatment of Dispersive Forces in Materials: Polyethylene and Graphite Crystals as Test Cases

VINCENZO BARONE,[1,2] MAURIZIO CASARIN,[3,5] DANIEL FORRER,[3] MICHELE PAVONE,[2,5] MAURO SAMBI,[3,5] ANDREA VITTADINI[3,5]

[1]*Istituto per i Processi Chimico-Fisici, CNR, Area della Ricerca del CNR Via Moruzzi 1, 56124 Pisa, Italy*

[2]*CR-INSTM "Village," Complesso Universitario Monte Sant'Angelo, Via Cintia, 80126 Napoli, Italy*

[3]*Dipartimento di Scienze Chimiche, Universitàdi Padova, CR-INSTM "Village," Via Marzolo 1, 35131 Padova, Italy*

[4]*ISTM-CNR, Via Marzolo 1, 35131 Padova, Italy*

[5]*Dipartimento di Chimica "Paolo Corradini," Universitàdi Napoli "Federico II," Complesso Universitario Monte Sant'Angelo, Via Cintia, 80126 Napoli, Italy*

Received 12 June 2008; Revised 23 July 2008; Accepted 24 July 2008
DOI 10.1002/jcc.21112
Published online 10 September 2008 in Wiley InterScience (www.interscience.wiley.com).

Abstract: A semiempirical addition of dispersive forces to conventional density functionals (DFT-D) has been implemented into a pseudopotential plane-wave code. Test calculations on the benzene dimer reproduced the results obtained by using localized basis set, provided that the latter are corrected for the basis set superposition error. By applying the DFT-D/plane-wave approach a substantial agreement with experiments is found for the structure and energetics of polyethylene and graphite, two typical solids that are badly described by standard local and semilocal density functionals.

 J Comput Chem 30: 934–939, 2009

Key words: DFT-D; graphite; polyethylene; dispersion

Introduction

The development of effective and accurate computational tools provides invaluable benefits to the quest for new materials. Indeed, the ability to describe at the atomistic scale the quantum mechanical behavior of interacting nuclei and electrons gives to material scientists the chance of validating ambiguous data from *in vitro* experiments, and it could also drive the design of new systems with tailored functions. Therefore, at the forefront of current research in theoretical and computational chemistry there is a great effort to increase the accuracy and reliability of available methods. In this respect, a considerable success has been achieved in the last decades by implementations of the density functional theory (DFT).[1] However, the exact form of the electron density functional is still unknown, and there are many cases where the physics of the investigated system is badly described by currently available approximated density functionals. Van der Waals (VdW) interactions, also referred to as dispersion forces, represent an important case of failure of commonly exploited local and semilocal density functionals.[2] VdW forces between two atoms or two molecules arise from the interaction of instant induced dipole moments, because of fluctuation of the electron densities. Despite being usually referred to as "weak force," dispersion plays a pivotal role in the assembly of nanostructured materials as well as in the folding of biological macromolecules and in many other very relevant physicochemical processes.[3] Thus, the correct accounting of such interactions is crucial for an accurate theoretical description of complex systems. However, VdW forces are nonclassical and nonlocal interactions that need a proper treatment of electronic dynamic correlation.[2,4] This could be achieved by the so-called post Hartree–Fock (post-HF) methods, in particular by the many-body perturbation theory and coupled cluster approaches.[5] The "chemical accuracy" of post-HF methods is unfortunately balanced by demanding computational burden, which practically limits their use to small molecular systems.[6] On this basis, it would be extremely convenient to include an effective description of dispersion forces within the framework of DFT. Indeed,

Correspondence to: D. Forrer or M. Pavone; e-mail: daniel.forrer@unipd.it or mipavone@unina.it

this goal is currently being pursued by many groups working in the research field of VdW complexes, see refs. 7 and 8 for recent reviews of the proposed solutions. A particularly effective and computationally convenient scheme to include dispersion has been achieved by adding a semiempirical correction term to the Kohn–Sham energy functional.[9] Following the London formula,[4] this correction models the long-range attractive potential of dispersive forces in terms of a pairwise atomic potential proportional to C_6R^{-6}, where R is the interatomic distance and C_6 is a semiempirical parameter which is proportional to atomic polarizabilities and first ionization energies.[10] The results are further improved by including a scaling parameter in order to fit the contribution of dispersion with the exchange-repulsion behavior of the Kohn–Sham term, and by applying a damping function to shut off the correction at short internuclear distances (e.g., for atoms involved in a covalent bond), thus avoiding definition of any monomer or fragments.[11] Dispersion-corrected DFT (DFT-D) has been successfully applied to a wide range of VdW molecular systems for energy and structure calculations,[10,12] vibrational frequencies, and *ab initio* molecular dynamics.[13] Although the DFT-D method has been recently tested on extended systems like graphene sheets,[14] graphite,[15] and molecular crystals,[16] there is still some lack of confidence about the reliability of DFT-D for bulk materials, in particular when the cohesive forces are mainly due to dispersion. In this work, we address this issue by applying the DFT-D correction to semilocal gradient-corrected density functionals (GGAs) in the case of periodic systems, which are conveniently studied by the plane-wave (PW) pseudopotential formalism. Within this context, it is worth noting that an alternative approach to DFT-D has been recently developed by exploiting the nonunique definition of core pseudopotentials in order to generate a library of dispersion-corrected atom-centered potentials (DCACPs).[17,18] Briefly, each DCACP is built by tuning few pseudopotential parameters against high-level post-HF data on a single-reference system. Despite the encouraging results obtained by using DCACPs,[19] we focused on the DFT-D scheme as recently proposed by Grimme,[10] first, because the available parameters have been tested on a large benchmark set of molecular complexes, and, second, because it does not require the presence of core potentials, thus allowing the chance of directly comparing results obtained by full-electron DFT calculations.

Here, we report the implementation of the periodic dispersion correction term within the PWscf code, which is part of the Quantum-ESPRESSO package.[20] The systems we investigated are the benzene dimer, and the polyethylene (PE) and graphite crystals. The relevance of carbon based compounds in material science is evident; moreover, because of the ubiquitous presence of carbon in chemistry it is quite hard to select some prototypical systems able to represent the whole range of its properties. Here, we first focused on the well-known case of the benzene dimer in order to test the implementation and to validate the accuracy of DFT-D parameters with pseudopotentials and PW basis set. As a matter of fact, recent works[10,21,22] pointed out the effects of finite-size basis sets, and their corresponding basis set superposition error (BSSE), on the choice of dispersion parameters and consequently on DFT-D results. The benzene dimers provide us the opportunity to compare BSSE-free PW/DFT-D results with those obtained by exploiting very large basis set based on Gaussian type orbitals (GTOs).[23] Once validated, we applied the DFT-D method to bulk solids, PE, and graphite, discussing the importance of dispersive forces in determining the structural and energetic features of these materials. Remarkably, our approach provided results in fair agreement with experimental data, in particular concerning those observables for which commonly exploited GGA density functionals provide a qualitatively wrong picture, thus highlighting the effectiveness of the DFT-D scheme also for delocalized systems.

Methods and Computational Details

Following the DFT-D approach ($E_{\mathrm{DFT\text{-}D}} = E_{\mathrm{DFT}} + E_{\mathrm{disp}}$), we implemented the dispersion energy term and its analytic gradient in a locally modified version of the PWscf code, including periodic boundary conditions by means of a real space summation scheme:

$$E_{\mathrm{disp}} = -\frac{1}{2}\sum_{i,j} C_{6ij}\left[\sum_{\vec{R}} \left|\vec{r}_{ij}+\vec{R}\right|^{-6} f_{\mathrm{damp}}\left(\left|\vec{r}_{ij}+\vec{R}\right|\right)\right] \tag{1a}$$

$$f_{\mathrm{damp}}\left(\left|\vec{r}_{ij}+\vec{R}\right|\right) = s_6 \cdot \left\{1+\exp\left[-d\cdot\left(\frac{\left|\vec{r}_{ij}+\vec{R}\right|}{r_0}-1\right)\right]\right\}^{-1} \tag{1b}$$

where $\vec{r}_{ij} = (\vec{r}_j - \vec{r}_i)$ is the atom–atom distance vector, $\vec{R}(= l\vec{a} + m\vec{b} + n\vec{c})$ are lattice vectors, s_6 is functional-dependent scaling parameter, and d is a parameter that tunes the steepness of the damping function ($d = 20$, $s_6 = 0.75$ for PBE, see later). The C_{6ij} coefficients are computed for each atom pair by the geometric mean of atomic terms ($C_{6ij} = \sqrt{C_{6i}\cdot C_{6j}}$), and r_0 terms are computed by the simple sum of VdW radii of the atom pairs ($r_0 = r_{0i} + r_{0j}$). In this work, we adopted the DFT-D parameters (C_{6i} and r_{0i}) proposed by Grimme.[10] The external summation in eq. (1a) runs over the atoms in the crystal unit cell, while the inner summation runs over the lattice parameters until the distance $|\vec{r}_{ij}+\vec{R}|$ become larger than 100 Å; with this choice we ensure that E_{disp} is converged better than 10^{-6} Ry. We exploited the well-known GGA density functional of Perdew, Burke, and Ernzerhof (PBE),[24] in its original form, and corrected by the dispersion term (PBE-D). Ion cores of both C and H atoms were replaced by ultrasoft pseudopotentials.[25] The electronic wave functions were expanded in PWs up to a kinetic energy cutoff of 32 Ry, while the cutoff for the augmented electron density was set to 200 Ry. These thresholds provided converged energies for all the reported systems and were used throughout the whole work.

Results

Benzene Dimers

The benzene dimer (see Fig. 1) was placed in a large cubic supercell of 40 au size, and only the Γ-point was included in the

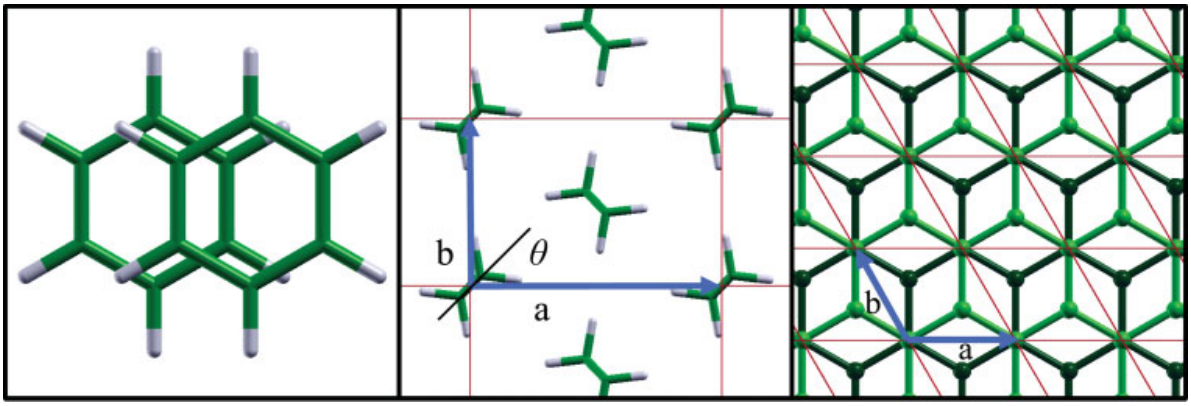

Figure 1. From left to right: benzene dimer parallel displaced (B2D) configuration; orthorhombic polyethylene (the polyethylene chain is directed along the crystalline axis *c*, i.e. perpendicular to the paper sheet); and hexagonal graphite.

Brillouin zone (BZ) summation. The adequacy of pseudopotentials, cutoff energies, and supercell dimension was checked by comparison with all-electron calculations carried out with a local version of the Gaussian package.[26] Gaussian calculations were performed with the same PBE and PBE-D functionals, by using the quite large augmented correlation consistent triple-ζ GTO basis set (Aug-cc-pVTZ)[27]; single-point energies and optimizations were carried out using tight convergence criteria. The geometry of a single benzene molecule was optimized with the PBE functional, using both PW and GTO basis sets: PW calculations provided C—C and C—H bond lengths of 1.399 and 1.092 Å, respectively, whereas the corresponding values optimized with the GTO basis set are 1.399 and 1.091 Å, respectively. The remarkable match in these structural parameters provides a proof of reliability for the exploited pseudopotentials. Table 1 lists the interaction energies of benzene dimers as computed within both plane wave and GTO approaches. Single-point energy calculations were carried out on benchmark structures of the parallel sandwich (B2P), the parallel displaced (B2D), and the T-shaped (B2T) isomers, as optimized at the CCSD(T) level of theory.[28] PWscf and Gaussian calculations agree quite well, provided that the latter are corrected for the BSSE via the counterpoise scheme[29]: the energy difference amounts to ~4 meV in the least favorable case. Moreover, the last row of Table 1 shows that periodic PW and the nonperiodic GTO results are consistent, and that the differences between the two sets of results change by ~0.1 meV on passing from the PBE to the PBE-D functional. This last finding proves the adequacy of the adopted real-space pairwise summation scheme. Figure 2 shows the interaction energy as a function of the distance h between the centers of mass computed using both basis sets; in this calculation the monomer structures were kept fixed at the reference geometry.[28] The energy minimum of the B2P dimer was found at h_{B2P} = 3.9 Å and for the B2T dimer at h_{B2T} = 4.9 Å, which is in excellent agreement with the most accurate post-HF data (h_{B2P} = 3.9 Å and h_{B2T} = 5.0 Å) reported in recent literature.[28] The B2D dimer is characterized not only by the distance h_{B2D} between the molecular planes but also by the displacement coordinate d_{B2D}, i.e. the distance between the centers of mass, projected onto the molecular plane of the benzene monomer. The minimum-energy geometrical parameters of the B2D isomer (h_{B2D} = 3.4 Å and d_{B2D} = 1.7 Å), as obtained by interaction energy scans, were found to be in fair agreement with the post-HF reference data (h_{B2D} = 3.6 Å, d_{B2D} = 1.6 Å).[28]

Polyethylene

The PE crystal cell (see Fig. 1) presents a "hard" coordinate (c) along the polymer chain, related to the intrachain covalent bonding structure, and the "soft" coordinates (a and b) that are ruled by nonbonding interactions between the polymer chains. Because of its insulating properties and also its well-defined band gap, PE seems to be an ideal candidate to test the performance of DFT-D for bulk materials. The hard coordinate was optimized by minimizing the isotropic stress of the unit cell. The resulting value (2.55 Å) is in close agreement with the experimental one,[30] as reported in Table 2. A scan of the potential energy surface (PES) was carried out by varying independently both a and b parameters over a broad range of values, as

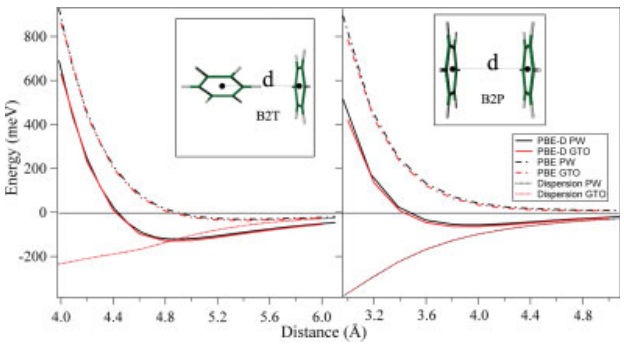

Figure 2. C_6H_6—C_6H_6 interaction energy as a function of the distance between centers of mass: red (black) lines refer to Gaussian (PWscf) calculations. GTO results were not corrected for BSSE.

Table 1. Interaction Energy (meV) of Benzene Dimers Computed with PW and GTO Basis Sets on Reference Geometries, Optimized at the CCSD(T) Level of Theory [28].

	B2P		B2D		B2T	
	PBE	PBE-D	PBE	PBE-D	PBE	PBE-D
PW	55.56	−57.01	39.54	−98.27	−14.76	−119.09
GTO_{CP} (BSSE)	52.80 (5.77)	−59.65	35.51 (6.73)	−102.22	−17.69 (5.29)	−121.92
ΔE $(E_{(PW)} - E_{(GTO_{CP})})$	2.76	2.64	4.03	3.95	2.93	2.83

Reported GTO energies are corrected for the BSSE (in parentheses) via the counterpoise correction (CP).

depicted in Figure 3. For each pair of these values, the atomic coordinates were allowed to relax. Because of the weakness of interchain interactions, particular care has to be taken to achieve a smooth PES. Thus, a $10 \times 6 \times 4$ mesh was adopted in the BZ integration, while geometry optimizations were carried out until the total energy and the total force were converged better than of 10^{-6} Ry and 10^{-4} Ry $bohr^{-1}$, respectively.

PBE calculations led to repulsive PE interchain interactions along the whole investigated range of soft cell parameters, as clearly depicted by Figure 3. In other words, the PE chains are predicted to be unbound by pure GGA density functional, and thus the crystal to be unstable. In contrast to that, by providing a proper accounting of dispersive forces, we found a quite flat energy minimum corresponding to cell parameter values, a = 6.67 Å and b = 4.55 Å, in satisfactory agreement with the experiment (Table 2). Although the DFT-D approach leads to a compression of about 7% along both a and b lattice vectors, it provides a substantial improvement with respect to the standard PBE functional, which is unable to predict, even qualitatively, the energetics of crystalline polymeric materials. Moreover, it should be realized that when dealing with flat PES, small errors in energy correspond to significant deviations of lattice cell parameters. In fact, energies corresponding to the optimized and to the experimental cell parameters differ by only ~10 meV per CH_2— group. This does not strike down the relevance of our findings, also because the agreement could be further improved by acting on the semiempirical parameters.

Graphene and Graphite

PW calculations of graphite were carried out using the previously described computational setup, and the BZ integration required 1152 k-points organized in a dense $12 \times 12 \times 8$ grid. Moreover, a cold smearing[33] of 0.02 Ry was applied to the orbital population function. Structural and energetic features of bulk graphite computed for the PBE and PBE-D functionals are listed in Table 3. A large portion of the PES was explored via single-point total-energy calculations performed by varying the in-plane lattice parameter a_0 and the "soft" lattice parameter c_0, with the latter ruling the distance between graphene sheets. The results are displayed in Figure 4: PBE calculations provided an unreliable bound state at the large distance of 9.6 Å, while the inclusion of dispersion forces provided a well-defined minimum-energy well of ~54 meV at 6.4 Å. The bulk modulus B was computed using a Birch equation of state,[42] assuming that a hydrostatic pressure acting on the graphite crystal could only lead to an uniaxial compression along the c_0 "soft" direction. In other words, we neglected the effects of hydrostatic pressure on the structural parameters of the graphene sheets. This approximation is supported by the evidence that the a_0 compressibility is two orders of magnitude larger than the c_0 one[43]: the resulting B value, 46.5 GPa, is in very good agreement with the experimental value, 41 GPa.

The exfoliation energy of graphite was determined as the difference between the energy of the bulk material and the energy of the graphene sheets, with the latter computed at the limit of large c_0 values. Only three *indirect* experimental estimates are available for the graphite exfoliation energy. These were extracted respectively from heat of wetting experiments[39] (43 meV/atom), from collapsed carbon-nanotube structure[40] (35 meV/atom), and from thermal desorption experiments of polyaromatic hydrocarbons[41] (52 ± 5 meV/atom). Our result (54 meV/atom) is in excellent agreement with the most recent experiment. Not surprisingly, we also found a fair agreement with the exfoliation energy recently computed by Grimme et al.[14] using a small number of finite-size graphene sheets. As in the case of PE, PBE-D calculations provide a c_0 lattice parameter (6.43 Å) smaller than the experimental value (6.656 Å) by about the 3%, confirming the overbinding tendency of the adopted parameter set for the investigated systems. Nevertheless, the PBE-D functional represents once again a dramatic improvement over the original PBE density functional, which is unable to provide an acceptable description of the graphite bulk.

Table 2. Structural Properties and Cohesive Energy of PE Compared with Experimental and Theoretical Literature Data.

	a (Å)	b (Å)	c (Å)	θ (°)	E_{int} (meV)
PBE-D[a]	6.67 (−6.3%)	4.55 (−6.2%)	2.55	43	102
BLYP+D[b]	7.4	4.9	2.53	–	110
VdW-DF[c]	7.30	5.22	2.57	44	105
Exp.[d]	7.121	4.851	2.548	41	–

[a]Present work.
[b]Dispersion-corrected BLYP calculations (BLYP+D) using *ad hoc* parametrization of the C_6R^{-6} term, from ref. [31].
[c]VdW density functional (VdW-DF) from ref. [32].
[d]Neutron scattering experiment at low temperature from ref. [30].

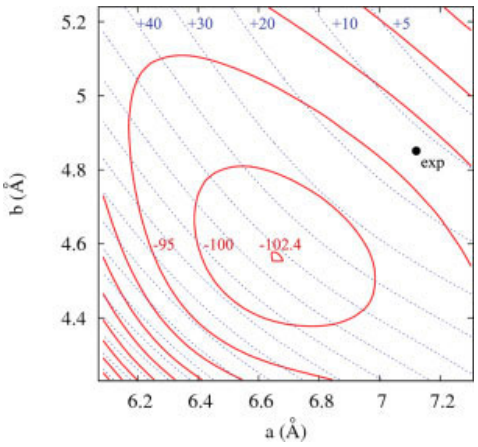

Figure 3. Interchain interaction energy (meV) per CH_2— group as a function of lattice parameters, computed at the PBE-D (red, solid line) and PBE (blue, dashed line) levels of theory.

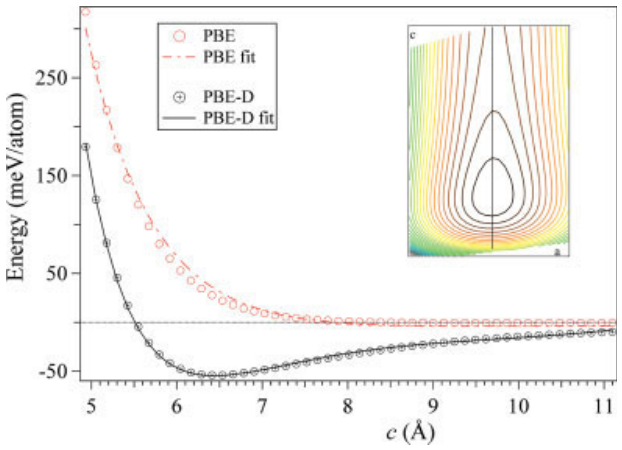

Figure 4. Graphene sheet–sheet interaction energy (meV per carbon atom) as a function of the c lattice parameter. Computed values were fitted to a second-order Birch equation of state. The inset shows a map of the PES in the a, c space. The vertical black line indicates the section shown in the main plot.

Conclusions

In this article, we report the results of a theoretical investigation on the role of dispersive forces in tuning the structural and energetic features of carbon-based materials. We focused our attention on PE and graphite because they are solid systems of great technological relevance, and also because they both represent prototypical cases where the crystal cohesion is mainly due to dispersive forces. In fact, commonly exploited semilocal density functionals are not able to provide a reliable picture of these materials: PE intrachain parameters and single sheets of graphene could be safely and accurately described by conventional GGA approximations, but in both cases the whole crystal has been predicted to be unstable, in striking contrast to experiments. Under such circumstances, the addition of a semiempirical term accounting for dispersion, within the DFT-D scheme, provided bulk properties in fair agreement with available experimental data. Our results represent a convincing validation of the DFT-D approach for pseudopotential PW calculations. The parameters we exploited were proven to be transferable from quantum chemistry calculations based on GTO to periodic calculations based on the pseudopotential PW formalism, as we found in the prototypical case of benzene dimer. The slight overbinding found for the PE and graphite crystal structures is a minor drawback, when compared with the remarkable and substantial improvements over bare GGA results. Moreover, further refining of DFT-D parameters could overcome such tendency. In particular, a simple and viable route could be the reduction of the scaling parameter (s_6) for minimizing the overattractive potential arising from the dispersion term, as recently proposed by Civalleri et al. for hydrogen-bonded molecular crystals.[16] In conclusion, this work paves the route toward a successful application of the DFT-D method for an accurate modelling of nanoscale materials, such as self-assembled monolayer of hydrocarbons, by the effective use of periodic boundary conditions and state-of-the-art electronic structure methods.

Table 3. Structural Properties and Cohesive Energy of Graphite Compared with Experimental and Theoretical Literature Data.

	a_0 (Å)	c_0 (Å)	B (GPa)	E_{ex} (meV)
PBE-D[a]	2.466	6.43 (−3.4%)	46.5	54.1
PBE[a]	2.466	9.62	0.8	0.6
PW91+D[b]	2.455	6.69	–	83.5
VdW-DF[c]	2.47	7.52	12	24
Exp.	2.462[d]	6.656[e]/6.707[d]	41[f]	43[g], 35[h], 52 ± 5[i]

[a]Present work.
[b]Dispersion-corrected PW91 calculations based on *ad hoc* parameterization of the C_6R^{-6} term [15].
[c]VdW density functional from ref. [34].
[d]Ref. [35] at room temperature.
[e]Ref. [36], as reported by Ref. [37], at low temperature.
[f]Ref. [38].
[g]Ref. [39].
[h]Ref. [40].
[i]Ref. [41].

Acknowledgments

The large-scale computer facilities of the CR-INSTM "Village" network (http://village.unina.it) are kindly acknowledged.

References

1. Koch, W.; Holthausen, M. C. A Chemist's Guide to Density Functional Theory; Wiley-VCH: Weinheim, 2002.
2. Kristyán, S.; Pulay, P. Chem Phys Lett 1994, 229, 175.
3. Lee, E. C.; Kim, D.; Jurečka, P.; Tarakeshwar, P.; Hobza, P.; Kim, K. S. J Chem Phys A 2007, 111, 3446.
4. London, F. Z Phys 1930, 63, 245.

5. Szabo, A.; Ostlund, N. S. Modern Quantum Chemistry; Dover: New York, 1999
6. Janowski, T.; Pulay, P. Chem Phys Lett 2007, 447, 27.
7. Dobson, J. F.; Wang, J.; Dinte, B. P.; McLennan, K.; Le, H. M. Int J Quantum Chem 2005, 101, 579.
8. Schwabe, T.; Grimme, S. Acc Chem Res 2008, 41, 569.
9. Wu, X.; Vargas, M. C.; Nayak, S.; Lotrich, V.; Scoles, G. J Chem Phys 2001, 115, 8748.
10. Grimme, S. J Comput Chem 2006, 27, 1787.
11. Wu, Q.; Yang, W. J Chem Phys 2002, 116, 515.
12. Riley, K. E.; Hobza, P. J Phys Chem B 2008, 112, 3157.
13. Pavone, M.; Rega, N.; Barone, V. Chem Phys Lett 2008, 452, 333.
14. Grimme, S.; Mück-Lichtenfeld, C.; Antony, J. J Phys Chem C 2007, 111, 11199.
15. Ortmann, F.; Bechstedt, F.; Schmidt, W. G. Phys Rev B 2006, 73, 205101.
16. Civalleri, B.; Zicovich-Wilson, C. M.; Valenzano, L.; Ugliengo, P. CrystEngComm 2008, 10, 405.
17. von Lilienfeld, O. A.; Tavernelli, I.; Rothlisberger, U. Phys Rev Lett 2004, 93, 153004.
18. Lin, I.-C.; Coutinho-Neto, M. C.; Felsenheimer, C.; von Lilienfeld, O. A.; Tavernelli, I.; Rothlisberger, U. Phys Rev B 2007, 75, 205131.
19. Lin, I.-C.; von Lilienfeld, O. A.; Coutinho-Neto, M. C.; Tavernelli, I.; Rothlisberger, U. J Phys Chem B 2007, 111, 14346.
20. Baroni, S.; dal Corso, A.; de Gironcoli, S.; Giannozzi, P.; Cavazzoni, C.; Ballabio, G.; Scandolo, S.; Chiarotti, G.; Focher, P.; Pasquarello, A.; Laasonen, K.; Trave, A.; Car, R.; Marzari, N.; Kokalj, A. Plane-wave self-consistent field. http://www.pwscf.org/.
21. Dulcéré, J.-M.; Cavallo, L. J Phys Chem B 2007, 111, 13124.
22. Jurečka, P.; Černý, J.; Hobza, P.; Salahub, D. R. J Comput Chem 2007, 28, 555.
23. Ditchfield, R.; Hehre, W. J.; Pople, J. A. J Chem Phys 1971, 54, 724.
24. Perdew, J. P.; Burke, K.; Ernzerhof, M. Phys Rev Lett 1996, 77, 3865.
25. Vanderbilt, D. Phys Rev B 1990, 41, 7892.
26. Frisch, M. J.; Trucks, G. W.; Schlegel, H. B.; Scuseria, G. E.; Robb, M. A.; Cheeseman, J. R.; Montgomery, Jr., J. A.; Vreven, T.; Kudin, K. N.; Burant, J. C.; Millam, J. M.; Iyengar, S. S.; Tomasi, J.; Barone, V.; Mennucci, B.; Cossi, M.; Scalmani, G.; Rega, N.; Petersson, G. A.; Nakatsuji, H.; Hada, M.; Ehara, M.; Toyota, K.; Fukuda, R.; Hasegawa, J.; Ishida, M.; Nakajima, T.; Honda, Y.; Kitao, O.; Nakai, H.; Klene, M.; Li, X.; Knox, J. E.; Hratchian, H. P.; Cross, J. B.; Bakken, V.; Adamo, C.; Jaramillo, J.; Gomperts, R.; Stratmann, R. E.; Yazyev, O.; Austin, A. J.; Cammi, R.; Pomelli, C.; Ochterski, J. W.; Ayala, P. Y.; Morokuma, K.; Voth, G. A.; Salvador, P.; Dannenberg, J. J.; Zakrzewski, V. G.; Dapprich, S.; Daniels, A. D.; Strain, M. C.; Farkas, O.; Malick, D. K.; Rabuck, A. D.; Raghavachari, K.; Foresman, J. B.; Ortiz, J. V.; Cui, Q.; Baboul, A. G.; Clifford, S.; Cioslowski, J.; Stefanov, B. B.; Liu, G.; Liashenko, A.; Piskorz, P.; Komaromi, I.; Martin, R. L.; Fox, D. J.; Keith, T.; Al-Laham, M. A.; Peng, C. Y.; Nanayakkara, A.; Challacombe, M.; Gill, P. M. W.; Johnson, B.; Chen, W.; Wong, M. W.; Gonzalez, C.; and Pople, J. A. Gaussian 03, Revision C.02; Gaussian, Inc.: Wallingford, CT, 2004.
27. Kendall, R. A.; Dunning, T. H., Jr.; Harrison, R. J. J Chem Phys 1992, 96, 6796.
28. DiStasio, R. A., Jr.; von Helden, G.; Steele, R. P.; Head-Gordon, M. Chem Phys Lett 2007, 437, 277.
29. Boys, S. F.; Bernardi, F. Mol Phys 1970, 19, 553.
30. Avitabile, G.; Napolitano, R.; Pirozzi, B.; Rouse, K. D.; Thomas, M. W.; Willis, B. T. M. J Polym Sci Polym Lett Ed 1975, 13, 351.
31. Serra, S.; Iarlori, S.; Tosatti, E.; Scandolo, S.; Santoro, G. Chem Phys Lett 2000, 331, 339.
32. Kleis, J.; Lundqvist, B. I.; Langreth, D. C.; Schröder, E. Phys Rev B 2007, 76, 100201.
33. Marzari, N.; Vanderbilt, D.; De Vita, A.; Payne, M. C. Phys Rev Lett 1999, 82, 3296.
34. Rydberg, H.; Dion, M.; Jacobson, N.; Schroeder, E.; Hyldgaard, P.; Simak, S. I.; Langreth, D. C.; Lundqvist B. I. Phys Rev Lett 2003, 91, 126402.
35. Zhao, Y. X.; Spain, I. L. Phys Rev B 1989, 40, 993.
36. Ludsteck, A. Acta Cryst 1972, A28, 59.
37. Jansen, H. J. F.; Freeman, A. J Phys Rev B 1987, 35, 8207.
38. Gauster, W. B.; Fritz, I. J. J Appl Phys 1974, 45, 3309.
39. Girifalco, L. A.; Lad, R. A. J Chem Phys 1956, 25, 693.
40. Benedict, L. X.; Chopra, N. G.; Cohen, M. L.; Zettl, A.; Louie, S. G.; Crespi, V. H. Chem Phys Lett 1998, 286, 490.
41. Zacharia, R.; Ulbricht, H.; Hertel, T. Phys Rev B 2004, 69, 155406.
42. Birch, F. Phys Rev 1947, 71, 809.
43. Hanfland, M.; Beister, H.; Syassen, K. Phys Rev B 1989, 39, 12598.

Inorg. Chem. **2009**, *48*, 4044−4051

Magnetic Properties and Vapochromic Reversible Guest-Induced Transformation in a Bispyrazolato Copper(II) Polymer: an Experimental and Dispersion-Corrected Density Functional Theory Study

Alessandro Bencini,[†] Maurizio Casarin,[‡,§] Daniel Forrer,[‡] Lorenzo Franco,[‡] Federica Garau,[‡] Norberto Masciocchi,[||] Luciano Pandolfo,[*,‡] Claudio Pettinari,[⊥] Marco Ruzzi,[‡] and Andrea Vittadini[*,‡,§]

Dipartimento di Chimica, Università di Firenze, via della Lastruccia 3, I-50019 Firenze, Italy, Dipartimento di Scienze Chimiche, Università di Padova, via Marzolo 1, I-35131 Padova, Italy, Istituto di Scienze e Tecnologie Molecolari del CNR (ISTM-CNR), via Marzolo 1, I-35131 Padova, Italy, Dipartimento di Scienze Chimiche e Ambientali, Università dell'Insubria, via Valleggio 11, I-22100 Como, Italy, and Dipartimento di Scienze Chimiche, Università di Camerino, via S.Agostino 1, I-62032 Camerino(MC), Italy

Received October 10, 2008

Dispersion-corrected density functional theory (DFT-D) calculations, Electron Spin Resonance spectroscopy (EPR), and variable temperature magnetic moment measurements were used to investigate the structure and the electronic/magnetic properties of bispyrazolato-copper(II) coordination polymer and of its hydration product. The Cu(II) ions are antiferromagnetically coupled through the σ system of the pyrazolate rings in both compounds. Theoretical electron density maps reveal that water molecules interact simultaneously and to a comparable extent with two Cu(II) centers (through the electronegative O end) and two pyrazolate rings (through the partly positively charged H atoms), which is compatible with the observed internuclear distances. DFT-D calculations indicate that low kinetic barriers are involved in the rearrangement of the host structure.

Introduction

The increasing demand for better materials for gas sensing and gas storage applications has stimulated the design of new porous materials based on molecular frameworks. This crystal engineering process is, however, hampered by the natural tendency of molecular systems to pack as close as possible, intrinsically limiting the number of porous compounds.[1] In this context, a promising class of materials is represented by systems which are able to reversibly change their crystal structure in the presence of guest molecules in such a way as to create otherwise absent pores or to modify their shapes, dimensions, and/or functional properties.[2]

In a recent communication,[2a] some of us reported on the synthesis of a novel polymorph (the "β" phase) of copper(II) pyrazolate, β-$[Cu(pz)_2]_n$, a one-dimensional (1D) coordination polymer obtained by reacting Cu(II) carboxylates with pyrazole (Hpz) in MeCN. Remarkably, this compound is able, in the solid state, to absorb/desorb water and several other small guest molecules (viz. NH_3, $MeNH_2$, CH_3CN, pyridine, MeOH, and EtOH) through a reversible change of the mutual arrangement of the polymer chains, accompanied by significant color modifications. The crystal structure of the anhydrous and of the hydrated polymers were determined by X-ray powder diffraction (XRPD) methods: β-$[Cu(pz)_2]_n$, crystallizes in the monoclinic system ($P2_1/m$ space group; $a = 9.055$ Å, $b = 7.401$ Å, $c = 5.597$ Å, $\beta = 99.48°$, see Figure 1a), whereas the hydrated phase $[Cu(pz)_2 \cdot (H_2O)]_n$, is orthorhombic (*Cmcm* space group; $a = 16.960$ Å, $b = 6.236$ Å, $c = 7.283$ Å, see Figure 1c).

In our preliminary communication,[2a] the presence of a magnetic interaction coupling the Cu(II) ions was noted. In this work, we address in more detail these magnetic interactions from an experimental and computational point of view, and we obtain more detailed information on the bonding between the host and the guest water molecules, for which an approximate location was experimentally

* To whom correspondence should be addressed. E-mail: andrea.vittadini@unipd.it.
[†] Università di Firenze.
[‡] Università di Padova.
[§] Istituto di Scienze e Tecnologie Molecolari del CNR.
[||] Università dell'Insubria.
[⊥] Università di Camerino.

10.1021/ic801928b CCC: $40.75
Published on Web 04/06/2009

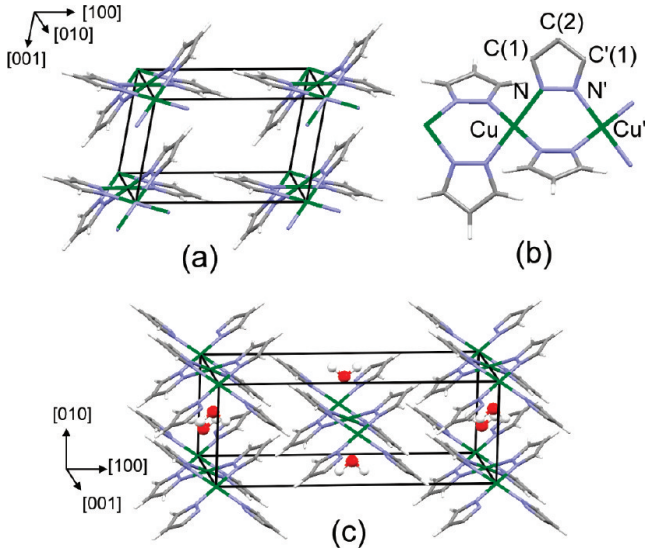

Figure 1. (a) Schematic drawings of: (a) β-$[Cu(pz)_2]_n$; (b) a portion of the $Cu(pz)_2$ chain running along [010]; (c) the unit cell of $[Cu(pz)_2 \cdot (H_2O)]_n$. The H_2O molecules, shown in a ball-and-stick representation, are in the equilibrium configuration as determined by the DFT calculations.

determined by XRPD. Furthermore, we investigate the mechanism of the structure transformations involved in the water sorption/desorption processes. Finally, we report also a new and more efficient synthetic procedure for the obtaining of β-$[Cu(pz)_2]_n$, that has also made possible its embedding into pumice sheets.

Material and Methods

Synthesis and Sample Manipulation. If not otherwise stated, reactions and manipulations were carried out in the air. Reagents (Aldrich) were used without further purification. Elemental analyses (C, H, N) were performed with a Fisons Instruments 1108 CHNS-O Elemental Analyzer. IR spectra were recorded from 4000 to 400 cm^{-1} with a Perkin-Elmer 983 instrument. UV−vis spectra were recorded from 200 to 800 nm with a Varian Cary 5E instrument.

$[Cu(pz)_2 \cdot (NH_3)]_n$, **1**.

This species was obtained by slightly modifying a procedure reported by Inoue et al.[3]

A solution of $Cu(NO_3)_2 \cdot 2.5H_2O$ (1.823 g, 7.83 mmol) in 40 mL of 28% aqueous ammonia was added at room temperature (r.t.) under vigorous stirring to a solution of 1.088 g of Hpz (15.98 mmol) in 40 mL of 28% aqueous ammonia. The obtained dark-blue suspension was stirred for 20 min obtaining a blue precipitate that was filtered, washed with 28% aqueous ammonia, and dried under vacuum (0.1 mmHg) at r.t., obtaining 1.31 g of a blue solid (Yield 78%). Similar results were obtained by using copper(II) sulfate and copper(II) chloride.

1. Elem. Anal. Calcd for $C_6H_9N_5Cu$: C, 33.56; H, 4.22; N, 32.62. Found: C, 33.98; H, 3.91; N, 31.99.

Mp. At about 120 °C compound **1** turns into a light-brown solid (β-$[Cu(pz)_2]_n$, **2**, vide infra), stable up to about 300 °C, where decomposition begins.

β-$[Cu(pz)_2]_n$, **2**.

$[Cu(pz)_2 \cdot (NH_3)]_n$, **1**, (266.8 mg, 1.24 mmol) was heated (90 °C) under dynamic vacuum (0.1 mmHg) for 15 min observing a weight loss of 20.9 mg, corresponding to the elimination of 1.23 mmol of NH_3, and the simultaneous color change into beige.

2. Elem. Anal. Calcd for $C_6H_6N_4Cu$: C, 36.45; H, 3.06; N, 28.34. Found: C, 36.09; H, 3.30; N, 28.25.

$[Cu(pz)_2 \cdot (H_2O)]_n$, **3**.

Compound **2** at 25 °C easily absorbs water vapors from the air or from solvate moist environments and rapidly yields the pale-pink derivative $[Cu(pz)_2 \cdot (H_2O)]_n$, **3**.

3. Elem. Anal. Calcd for $C_6H_8N_4OCu$: C, 33.41; H, 3.74; N, 25.97. Found: C, 33.12; H, 3.85; N, 25.67.

The identity of **1**, **2**, and **3** was confirmed by their IR, UV−vis, and XRPD spectra that resulted identical to those previously reported.[2a] Moreover, **2** adsorbs reversibly NH_3, H_2O, $MeNH_2$, and so forth, yielding the corresponding solvated derivatives previously reported.[2a] Cycles of sorption/desorption of water and NH_3 were repeated on compound **2** 10 times without observing any degradation.

Embedding of 1, 2, and 3 into Pumice Sheets. Sheets of pumice (ca. 10 × 20 × 1 mm) were obtained by cutting a commercial pumice block obtained from a local hardware store. Subsequently. the sheets were accurately washed with water, maintained in *aqua regia* for 1 h, washed with running tap water for 2 h, with running deionized water for 1 h, put into 28% NH_3 aqueous solution for 2 h, rinsed with running deionized water for 20 min, and then dried by vacuum pumping (0.1 mmHg) for 8 h at r.t. The cleaned sheets of pumice were soaked for 2 h into a solution of Hpz (0.388 g, 5.7 mmol) in a 28% NH_3 aqueous solution and then dipped into a stirred solution of $Cu(NO_3)_2 \cdot 2.5H_2O$ (0.676 g, 2.9 mmol) in 10 mL of 28% NH_3 aqueous solution and here maintained overnight. Deep-blue colored sheets formed, which were washed with running deionized water for 20 min and finally dried under vacuum (0.1 mmHg) at rt, the blue color being practically unchanged. Upon heating (ca. 90 °C) under dynamic vacuum (0.1 mmHg) for 20 min, the blue sheets turned beige, indicating that the transformation of embedded **1** in **2** occurred. Moreover the beige sheets, changed color (pale pink) when put in contact with H_2O vapors (indicating the formation of embedded **3**) and became blue in the presence of NH_3, reversibly forming **1**, analogously to what was previously reported for pure bulk species.[2a] The sorption/desorption cycles of water and NH_3 were repeated 10 times also on these sheets, obtaining analogous results with respect to pure compounds.

Electron Paramagnetic Resonance (EPR) Measurements. The EPR spectra were recorded on about 10 mg of powdered samples put into 4 mm diameter quartz tubes, using a Bruker ER200D X-band spectrometer equipped with a nitrogen-flow variable temperature system for measurements in the temperature range 100−400 K. Typical acquisition parameters were: microwave power 10 mW, modulation amplitude 5 G, sweep time 3 min. For g-factor determination, the microwave frequency was measured using a HP5342 frequency counter, and the magnetic field was calibrated using a DPPH standard.

Magnetic Susceptibility Measurements. The temperature dependence of the magnetic susceptibility of all the compounds was measured using a Cryogenic S600 SQUID magnetometer. The measurements were performed on polycrystalline powder samples

(1) Barbour, L. J. *Chem. Commun.* **2006**, 1163.
(2) (a) Cingolani, A.; Galli, S.; Masciocchi, N.; Pandolfo, L.; Pettinari, C.; Sironi, A. *J. Am. Chem. Soc.* **2005**, *127*, 6144. (b) Yamada, K.; Tanaka, H.; Yagishita, S.; Adachi, K.; Uemura, T.; Kitagawa, S.; Kawata, S. *Inorg. Chem.* **2006**, *45*, 4322. (c) Takamizawa, S.; Kojima, K.; Akatsuka, T. *Inorg. Chem.* **2006**, *45*, 4580. (d) Supriya, S.; Das, S. K. *J. Am. Chem. Soc.* **2007**, *129*, 3464. (e) Dobrzan′ska, L.; Gareth, O.; Lloyd, G. O.; Esterhuysen, C.; Barbour, L. J. *Angew. Chem., Int. Ed.* **2006**, *45*, 5856. (f) Nagarathinam, M.; Vittal, J. J. *Angew. Chem., Int. Ed.* **2006**, *45*, 4337. (g) Serre, C.; Millange, F.; Thouvenot, C.; Noguès, M.; Marsolier, G.; Louer, D.; Férey, G. *J. Am. Chem. Soc.* **2002**, *124*, 13519. (h) Serre, C.; Mellot-Draznieks, C.; Surblé, S.; Audebrand, N.; Filinchuk, Y.; Férey, G. *Science* **2007**, *315*, 1828.
(3) Inoue, M.; Kishita, M.; Kubo, M. *Inorg. Chem.* **1965**, *4*, 626.

in an external magnetic field of 0.1 T varying the temperature between 2 and 300 K. β-$[Cu(pz)_2]_n$ was kept in an oven at 80 °C under vacuum for 24 h and weighed in a glovebox. All the data were corrected for diamagnetism.[4]

Density Functional Calculations. Density functional (DF) calculations were performed using the Perdew−Burke−Ernzerhof exchange-correlation functional[5] and Vanderbilt[6] pseudopotentials. Because the polymer chains interact through dispersion forces, the dispersion-corrected DFT-D method by Grimme,[7] recently implemented by some of us[8] in the Quantum-ESPRESSO package,[9] was adopted. A total of 11, 6, 5, 4, and 1 valence electrons were explicitly considered for Cu, O, N, C, and H, respectively. The smooth part of the wave function was expanded in plane waves, with a kinetic energy cutoff of 30 Ry, while the cutoff for the augmented electron density charge was 250 Ry. Plane wave calculations have been shown to be adequate for describing magnetic interactions in Cu(II) complexes.[10] The Brillouin zone integration was performed using the Monkhorst−Pack scheme,[11] with $2 \times 4 \times 2$ and a $1 \times 2 \times 4$ meshes for β-$[Cu(pz)_2]_n$, **2** and $[Cu(pz)_2 \cdot (H_2O)]_n$, **3**, respectively. Both lattice constants and internal parameters were fully optimized with a BFGS algorithm. Finite-basis set effects were corrected following the procedure by Bernasconi et al.[12] with $A = 40$ Ry, $E_0 = 30$ Ry, and $\sigma = 4$ Ry. Calculations were performed for both the ferromagnetic (FM) and the antiferromagnetic (AFM) states. The energy difference was used to estimate the exchange coupling J by fitting to an Ising model.

Results and Discussion

In 1965 Inoue et al.[3] in a study on the magnetic properties of a variety of copper(II) complexes with nitrogen heterocyclic ligands reported, inter alia, obtaining purple microcrystals of "bis(pyrazolato)copper(II) hemiammonia hemihydrate, $Cu(C_3H_3N_2)_2 \cdot 0.5NH_3 \cdot 0.5H_2O$" by reacting copper(II) sulfate with pyrazole in concentrated aqueous ammonia. They also observed that, on heating, the compound eliminated ammonia and water and the purple microcrystals turned brown, but this latter compound was not characterized further. Recently, we reported the synthesis and characterization of the β polymorph, β-$[Cu(pz)_2]_n$, **2**,[2a] which is pale-brown and changes color on sorption of water and ammonia, giving $[Cu(pz)_2 \cdot (H_2O)]_n$, **3**, (pale pink) and $[Cu(pz)_2 \cdot (NH_3)]_n$, **1**, (blue), respectively. Suspecting that the brown compound observed by Inoue et al.[3] was **2**, we repeated their procedures in slightly different conditions (see Materials and Methods section) and succeeded in obtaining $[Cu(pz)_2 \cdot (NH_3)]_n$, **1**, in about 78% yield, somewhat lower with respect to the almost quantitative yield of our previous synthesis.[2a] On the other hand, this drawback is balanced by the possibility to use practically any copper(II) salt, and not only the more expensive carboxylates and, most important, to avoid the use of the organic solvents like MeCN. In this procedure MeCN is replaced by aqueous concentrated ammonia that acts also as deprotonating agent of Hpz, a role originally played by the carboxylate ions.[2a] Thus, the deprotonated pyrazoles coordinated to cuproammoniacal species formed by Cu(II) salts are dissolved in aqueous ammonia yielding **1**. The accessibility of the cavities and the diffusion of the reactants within the pores of the bulk pumice make it possible to prepare solid, resistant sheets where **1** is permanently adsorbed.

Scheme 1

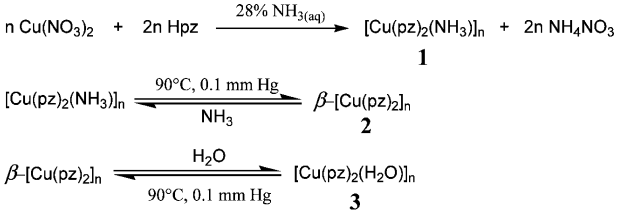

Pure crystalline powders of **1** or even **1** adsorbed into pumice sheets show the reversible sorption/desorption behavior discussed in ref 2a, and schematically sumarized in Scheme 1. This can be easily appreciated from Figure 2, where the different materials are collectively shown. This demonstrates that when suitably supported, the polymer could be in principle used to detect water or other small molecules.

Magnetic Susceptibilty Results. The temperature dependence of χ of **2** and **3** is typical of an antiferromagnetic linear chain of $S = 1/2$ spins[13,14] containing low amounts of paramagnetic impurities (Figure 3). Although much theoretical work has been done on low-dimensional magnetic systems in the last decades, there is still no exact closed-form equation for the temperature dependence of the magnetic susceptibility of a regular 1D chain of 1/2 spins described by the Heisenberg isotropic exchange Hamiltonian, $H = -J\sum_i \mathbf{S}_i \cdot \mathbf{S}_{i+1}$ (J is the isotropic exchange coupling constants), which are valid for the whole temperature range. The magnetic susceptibility of these systems was originally solved by Bonner and Fisher,[13,15] who computed the magnetic susceptibilities of ring chains of increasing size (up to 11 magnetic centers), and proposed an extrapolation for the infinite ring. Close equations exist for the low temperature limit[15] when $J < 0$ (antiferromagnetic interaction), and for the high temperature region for both positive and negative J.[16] An efficient way of measuring J is to use equations derived by fitting Bonner−Fisher's numerical

(4) O'Connor, C. J. *Prog. Inorg. Chem.* **1982**, *29*, 203.
(5) Perdew, J. P.; Burke, K.; Ernzerhof, M. *Phys. Rev. Lett.* **1996**, *77*, 3865.
(6) Vanderbilt, D. *Phys. Rev. B* **1990**, *41*, 7892.
(7) Grimme, S. *J. Comput. Chem.* **2006**, *27*, 1787.
(8) Barone, V.; Casarin, M.; Forrer, D.; Pavone, M.; Sambi, M.; Vittadini, A. *J. Comput. Chem.* **2009**, *30*, 934.
(9) Baroni, S.; dal Corso, A.; de Gironcoli, S.; Giannozzi, P.; Cavazzoni, C.; Ballabio, G.; Scandolo, S.; Chiarotti, G.; Focher, P.; Pasquarello, A.; Laasonen, K.; Trave, A.; Car, R.; Marzari, N.; Kokalj, A. http://www.pwscf.org.
(10) Massobrio, C.; Ruiz, E. *Monatsh. Chem.* **2003**, *134*, 317.
(11) Monkhorst, H.; Pack, J. *Phys. Rev. B* **1976**, *13*, 5188.
(12) Bernasconi, M.; Chiarotti, G. L.; Focher, P.; Scandolo, S.; Tosatti, E.; Parrinello, M. *J. Phys. Chem. Solids* **1995**, *56*, 501.
(13) Kahn, O. *Molecular Magnetism*; VCH Publishers: New York, 1993.
(14) Jotham, R. W. *J. Chem. Soc., Dalton Trans.* **1977**, 266.
(15) Bonner, J. C.; Fisher, M. E. *Phys. Rev. A* **1964**, *135*, 640.
(16) (a) Baker, G. A.; Rushbrooke, G. S.; Gilbert, H. E. *Phys. Rev.* **1964**, *135*, A1272. (b) Baker, G. A.; Rushbrooke, G. S.; Gilbert, H. E. *Phys. Rev.* **1967**, *164*, 800.

Figure 2. Pumice sheets embedding anhydrous β-$[Cu(pz)_2]_n$, **2**, (left), hydrated $[Cu(pz)_2 \cdot (H_2O)]_n$, **3**, (center), and ammonia complex $[Cu(pz)_2 \cdot (NH_3)]_n$, **1**, (right) together with corresponding microcrystalline powdered compounds.

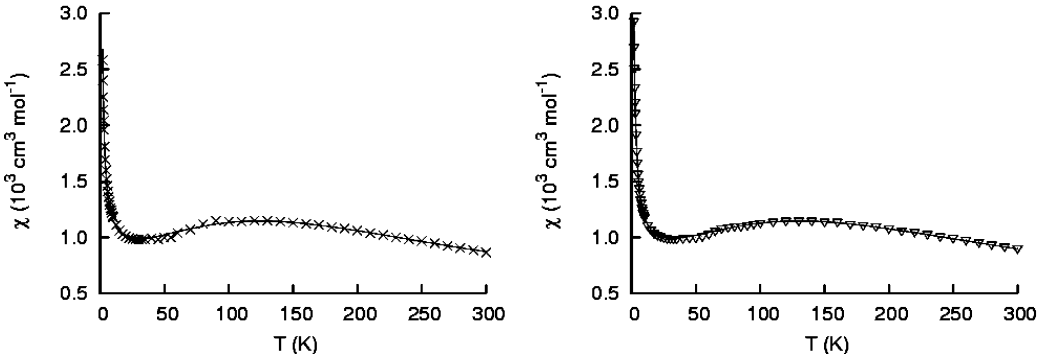

Figure 3. Temperature dependence of χ for $[Cu(pz)_2]_n$ (left) and $[Cu(pz)_2 \cdot (H_2O)]_n$ (right). Solid lines are the best fit curves (see text).

results with polynomial expressions by Jotham[14,15] and Hall.[17]

We used here the Hall equation:

$$\chi_{BF}(T) = \frac{Ng^2\mu_B^2}{kT}\frac{0.25 + 0.074975x + 0.075235x^2}{1.0 + 0.9931x + 0.172135x^2 + 0.757825x^3} \quad (1)$$

where $x = |J|/kT$.

Including in eq 1 the effect of a paramagnetic impurity, we obtain the working equation expressing the magnetic susceptibility, χ_c, to be compared with the experimental values:

$$\chi_c(T) = \chi_{BF}(T)(1 - \rho) + \frac{Ng^2\mu_B^2}{3kT}\rho \quad (2)$$

where ρ is the molar fraction of the impurity assumed to have the same g of the Cu(II) ions in the chain. The magnetic data, $\chi_o(T_i)$, were fit using the MINUIT[18] routine keeping J and ρ as free parameters. Since g and J were found to be strongly correlated, g was kept fixed at 2.07 (the value obtained from EPR spectra, vide infra). The experimental results are compared to the computed ones in Figure 3. The best fit curve (solid lines) were obtained with the parameters $J = -141.8(7)$ cm^{-1}, $\rho = 0.91(7)\%$ for β-$[Cu(pz)_2]_n$ and $J = -145.5(3)$ cm^{-1}, $\rho = 0.97(6)\%$ for $[Cu(pz)_2 \cdot (H_2O)]_n$. The agreement factors were $R = 1.5\%$ and $R = 0.5\%$ in the two cases, respectively.

Antiferromagnetic interactions are commonly observed in bis-pirazolato bridged dimers. Originally we reported a "weak exchange interaction" on the basis of preliminary results. On repeating and better analysing the experiments, more accurate values of J (reported above) were determined, which can be considered rather high and in the range usually observed in dinuclear copper(II) complexes,[19] and compare well with those of the α-$[Cu(pz)_2]_n$ phase ($J = -156$ cm^{-1}).[16,20] Unexpectedly, these values indicate a scarce sensitivity on the stereochemical parameters. As a matter of fact, magneto-structural correlations, within the orbital model of the exchange interactions, showed that deviation from co-planarity of the two pyrazolato ligands could affect even the sign of the exchange coupling constant, apparently counter balanced by the non-co-planarity of the Cu(II) coordination planes.[20,21]

EPR Results. EPR spectra of both β-$[Cu(pz)_2]_n$, **2**, and the hydrated compound $[Cu(pz)_2 \cdot (H_2O)]_n$, **3** at r.t., show a single isotropic resonance at $g = 2.07 \pm 0.01$. As a representative example, the polycrystalline EPR powder spectrum of β-$[Cu(pz)_2]_n$ is shown in Figure 4. The line shape is almost purely Lorentzian and the peak-to-peak line width is 230 G for **2** and 250 G for **3**.

The Lorentzian line shape, maintained throughout the investigated temperature range (100−350 K), is due to the relatively strong spin exchange interaction between copper atoms, which averages out all the anisotropies from the g-factor and hyperfine interactions. Likely, this occurs because magnetic exchange overcomes other relaxation mechanisms, like spin−lattice relaxation.[22] In the temperature

(17) (a) Hall, J. W. Ph.D. Dissertation, University of North Carolina, 1977. (b) Estes, W. E.; Gavel, D. P.; Hatfield, W. E.; Hodgson, D. *Inorg. Chem.* **1978**, *17*, 1415. (c) Estes, W. E.; Hatfield, W. E.; van Ooijen, J. A. C.; Reedijk, J. *J. Chem. Soc., Dalton Trans.* **1980**, 2121.
(18) James, F. *MINUIT*, version 96.03; CERN program library: Geneva.
(19) Tanase, S.; Koval, I. A.; Bouwman, E.; de Gelder, R.; Reedijk, J. *Inorg. Chem.* **2005**, *44*, 7860.
(20) Ehlert, M. K.; Retting, S. J.; Storr, A.; Thompson, R. C.; Trotter, J. *Can. J. Chem.* **1989**, *67*, 1970.
(21) Ajò, D.; Bencini, A.; Mani, F. *Inorg. Chem.* **1988**, *27*, 2437.

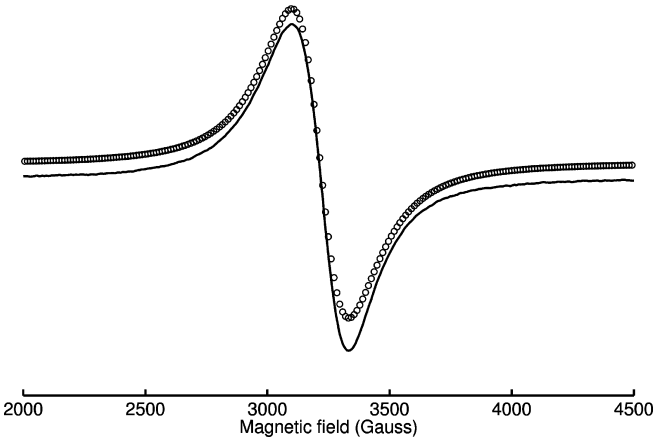

Figure 4. Room temperature polycrystalline powder EPR spectrum of β-$[Cu(pz)_2]_n$. Solid line: experimental spectrum. Circles: best fit Lorentzian line.

range 100−350 K, the doubly integrated EPR intensities show a maximum at about 160 K for **2** and at slightly higher temperature for **3** (data not shown).

The intensity of an EPR spectrum, when exchange interactions are dominating the relaxation mechanisms, is proportional to the magnetic susceptibility of the sample.[19] Therefore an estimate of J can be obtained by fitting the EPR intensities with the polynomial expression of eq 2. The best fit values are $J = -168$ cm^{-1} for **2** and -190 cm^{-1} for **3**. Considering the larger uncertainties of the EPR results, these values are in fair agreement with magnetic susceptibility data.

Summarizing, magnetism and EPR measurements indicate that the presence of water molecules in the hydrated polymer is slightly increasing the superexchange interaction between the copper ions. This effect is, however, weak as a consequence of the relatively long Cu−OH_2 distance (as discussed below).

Theoretical Calculations. We first point out that this is, to our knowledge, the first application of the DFT-D method to coordination polymer systems. The DFT-D method allowed us to fully optimize the lattice structures, even though the polymer chains interact only through dispersion forces. The optimized cell constants are $a = 8.76$ Å (−3.2%), $b = 7.52$ Å (+1.6%), $c = 5.20$ Å (−7.1%), $\beta = 101°$ β-$[Cu(pz)_2]_n$, **2**, and $a = 15.94$ Å (−6.0%), $b = 6.08$ Å (−2.6%), $c = 7.37$ Å (+1.3%) for $[Cu(pz)_2 \cdot (H_2O)]_n$, **3**. The underestimation of the lattice constants corresponding to the "soft" directions is similar to the one reported for DFT-D calculations on polyethilene.[8] In this work, the aims of the theoretical calculations are the following: (*i*) understanding the mechanism of the Cu(II)−Cu(II) antiferromagnetic coupling; (*ii*) evaluating the water-host bonding interaction; (*iii*) obtaining insight into the mechanism of pore formation by water sorption. Whereas the inclusion of dispersion forces was found to be unimportant for the determination of the electronic and magnetic properties, significant improvements were found in the estimate of the water sorption energy, and, most important, in the study of the energetics of the lattice transformation.

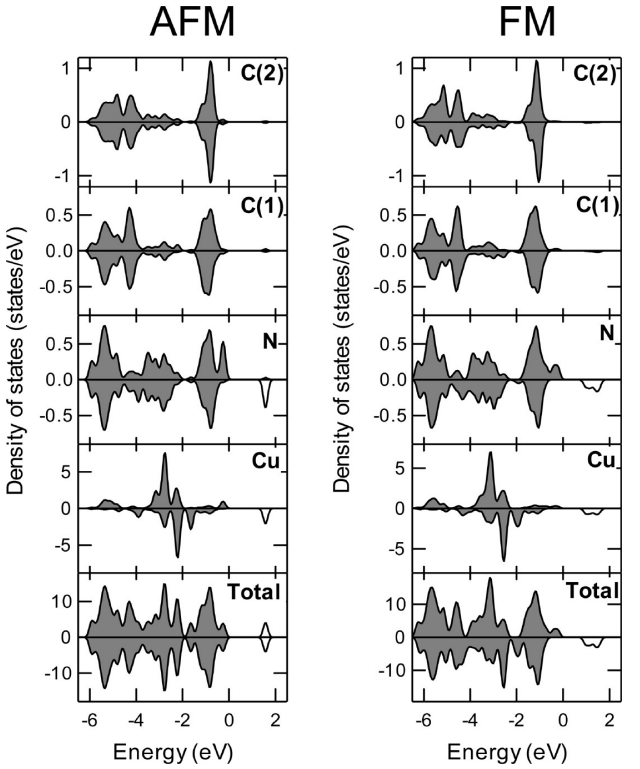

Figure 5. Spin-resolved density of states for β-$[Cu(pz)_2]_n$, **2**. Left: antiferromagnetic order; right: ferromagnetic order. Positive/negative values indicate spin up/down density of states. Filled areas indicate occupied states. Partial density of states are referred to single atoms. Atomic labels as indicated in Figure 1b.

We start from the analysis of the magnetic interactions in β-$[Cu(pz)_2]_n$, **2**. Both the FM and the AFM phases were found to be insulating, with a large band gap (see Figure 5), the AFM system being more stable by 0.051 eV/cell. The superexchange coupling constant J can be evaluated from the total energies of the ferromagnetic, E^{FM}, and antiferromagnetic, E^{AFM}, phases through the formula:

$$E^{AFM} - E^{FM} = \frac{2zS^2J}{K} \qquad (3)$$

where the z indicates the number of couplings per unit cell (2, in this case[23]), and $K = 8065.6$ is the conversion factor from eV to cm^{-1}. This allows us to estimate that $J = -415$ cm^{-1}. As found in similar calculations based on "pure" density functionals,[24] the coupling constant is significantly overestimated because of the excessively delocalized spin density.

More interesting is the information gained from local magnetic moments (M), which are obtained by projecting the wave functions into atomic functions (see Table 1), and from spin density maps (see Figure 6). As it clearly appears

(22) (a) Abragam, A.; Bleaney, B. *Electron Paramagnetic Resonance of Transition Ions*; Clarendon Press: Oxford, 1970. (b) Bencini, A.; Gatteschi, D. *Electron Paramagnetic Resonance of Exchange Coupled Systems*; Springer-Verlag: Berlin, 1990.

(23) In the case of $[Cu(pz)_2 \cdot H_2O]_n$ the factor 2 should be replaced by a factor 4 to account for the presence of 4 chain interactions in the unit cell (see Figure 1c).

(24) (a) Ruiz, E.; Llunell, M.; Alemany, P. *J. Solid State Chem.* **2003**, *176*, 400. (b) Doll, K.; Wolter, A. U. B.; Klauss, H.-H. *Phys Rev. B* **2007**, *75*, 184433.

Table 1. Local Magnetic Moments (μ_B) Computed for Anhydrous and Hydrated Polymers in the AFM and FM States[a]

	β-$[Cu(pz)_2]_n$, **2**		$[Cu(pz)_2\cdot(H_2O)]_n$, **3**	
	AFM	FM	AFM	FM
Cu/Cu′	0.556/−0.556	0.574	0.573/−0.573	0.590
N/N′	0.090/−0.090	0.098	0.092/−0.092	0.096
C(1)/C′(1)	−0.005/0.005	−0.002	−0.006/0.006	−0.002
C(2)	0.000	0.007	0.000	0.006
O			0.000/0.000	−0.001

[a] Atoms are labeled as in Figure 1b.

from Figure 6, the Cu magnetic orbital is the d(x^2-y^2) one, while the superexchange interaction is mediated by the σ pyrazolate system. The spin density is largely carried by Cu and N atoms, only minor fractions of it being localized at the C(1) and C(2) sites (see Table 1). Local magnetic moments at the Cu ions are similar to those previously computed for other antiferromagnetic Cu polymers, Cu(thiazole)$_2X_2$, X =Cl, Br.[25]

Turning now to $[Cu(pz)_2\cdot(H_2O)]_n$, **3**, we first want to focus on the polymer-sorbate interaction. The equilibrium positions of water molecules were determined by performing several optimization runs, each started from different initial molecule orientations. In the most stable configuration, water molecules are oriented with the H atoms pointing toward the closest pyrazolate rings, as shown in Figure 7.

Optimized distances (in Å) are 0.98 (O−H); 2.85 (Cu···O); 3.34 (π···O); and bond angles (in degrees) are 104.3 (H−O−H); 80.7 (Cu−O−Cu). The computed Cu−O distances fairly agree with the experiment (ca. 2.91 Å) and are rather long even for a weakly bound species as a μ-H_2O, being the usual Cu−O distance for a water molecule bridging Cu(II) ions below 2.4 Å.[26] This may be indicative that another species is competing in the interaction with the water molecules, as it occurs, for a lesser amount, for example, in the binuclear complex μ-acetato- μ-aqua- μ-hydroxo-bis[(1,4-dimethyl-1,4,7-triazacyclononane-κ *N*-3)-copper(II)] diperchlorate, where the electrostatic interaction between the μ-aquo ligand and the counteranions lengthens the Cu−OH_2 distance to 2.737 Å.[27] In the present case, the competing interaction may be the O−H···π one, occurring between the water hydrogens and the pyrazolate rings of the nearest polymer chain. Interestingly, the computed O···π distance is typical for OH···π interactions for phenyl rings in neutral organometallic compounds.[28] Because, in contrast to that, the Cu−OH_2 bonds are unusually elongated, we infer that the water-pyrazolate interaction is stronger than, or at least comparable to, the water-copper(II) one. This interpretation is supported by the electron difference density plots reported in Figure 8, which are obtained by computing the difference between the electron density of the *interacting* polymer−water system and that of a *non-interacting* system. The latter is obtained by summing the electron densities of the separated polymer and water moieties, each taken with the structure it assumes in the *interacting* system (i.e., the atomic positions are the same in both systems). These maps are useful to pinpoint the electron density rearrangements due to the formation of bonds and are particularly effective when dealing with molecular fragments. Looking at Figure 8, we can easily appreciate a considerable charge rearrangement in the Cu−O direction which is typical of weak electrostatic interactions:[29] the oxygen lone pairs are polarized toward the positive charged Cu atoms (see Figure 8b). In complete agreement with the previous discussion based on the simple inspection of interactomic distances, a *similar* and *comparable* charge rearrangement also occurs along the H···C directions (see Figure 8a). This similarity stems from the fact that also O−H···π interactions are electrostatic in nature. On the other hand, the comparability of the charge rearrangements further confirms that the water-pyrazolate interactions are at least as strong as the water−Cu ones. Inter alia, this computational evidence may allow the comprehension of the "phase change" of **2** during water absorption (from a monoclinic to a orthorhombic lattice), likely driven by the formation of many (cooperative) OH···π interactions in the lattice of **3**.

As far as the sorption energy is concerned, this can be straightforwardly computed from the total energies through the formula:

$$E_{sorpt}(H_2O) = E\{[Cu(pz)_2(H_2O)]\} - E\{\beta\text{-}[Cu(pz)_2]\} - E\{H_2O\}$$

while the water/host interaction energy (E_{int}) can be computed by using an analogous formula where the β-$[Cu(pz)_2]$ phase is replaced by an hypothetical relaxed "waterless" $[Cu(pz)_2\cdot(H_2O)]$ phase. The low (0.56 eV, 54 kJ/mol) computed E_{sorpt} value explains the facile dehydration of the compound, while the E_{int} value (0.71 eV, 69 kJ/mol) is well in tune with the electrostatic nature of the water-polymer interaction discussed above. Finally, magnetic moments (see Table 1) are scarcely affected by water sorption. Even lower is the effect on the relative energy of the FM and AFM phases (computed to be 0.050 eV/cell in favor of the latter), and, consequently, on J (computed to be -404 cm^{-1}).

We now turn our attention to the mechanism of the structural rearrangement occurring during the water sorption/desorption process. As pointed out in the Introduction, the β-$[Cu(pz)_2]_n$, **2**, → $[Cu(pz)_2\cdot(H_2O)]_n$, **3**, transformation (as well as $[Cu(pz)_2\cdot(NH_3)]_n$, **1** → β-$[Cu(pz)_2]_n$, **2**) is characterized by reversibility and easiness. Because a first-principle simulation of the transformation is obviously not feasible,

(25) Zhou, L.; Yao, K. L.; Liu, Z. L. *J. Phys.: Condens. Matter* **2006**, *18*, 3325.
(26) (a) Chaudhuri, P.; Ventur, D.; Wieghardt, K.; Peters, E.-M.; Peters, K.; Simon, A. *Angew. Chem., Int. Ed. Engl.* **1985**, *24*, 57. (b) Christou, G.; Perples, S. P.; Libby, E.; Folting, K.; Huffman, J. C.; Webb, R.; Hendrickson, D. N. *Inorg. Chem.* **1990**, *29*, 3657. (c) Youngme, S.; van Albada, G. A.; Roubeau, O.; Pakawatchai, C.; Chaichit, N.; Reedijk, J. *Inorg. Chim. Acta* **2003**, *342*, 48. (d) He, H.-Y.; Zhou, Y.-L.; Zhu, L.-G. *Acta Crystallogr. C* **2004**, *60*, m569. (e) Barquin, M.; Gonzalez Garmendia, M. J.; Larrinaga, L.; Pinilla, E.; Torres, M. R. *Z. Anorg. Allg. Chem.* **2005**, *631*, 2151. (f) Gautier-Luneau, I.; Phanon, D.; Duboc, C.; Luneau, D.; Pierre, J.-L. *Dalton Trans.* **2005**, 3795. (g) Chailuecha, C.; Youngme, S.; Pakawatchai, C.; Chaichit, N.; van Albada, G. A.; Reedijk, J. *Inorg. Chim. Acta* **2006**, *359*, 4168.
(27) Elliot, D. J.; Martin, L. L.; Taylor, M. R. *Acta Crystallogr. C* **1998**, *54*, 1259.
(28) Braga, D.; Grepioni, F.; Tedesco, E. *Organometallics* **1998**, *17*, 2669.
(29) Casarin, M.; Maccato, C.; Vittadini, A. *J. Phys. Chem. B* **1998**, *102*, 10745.

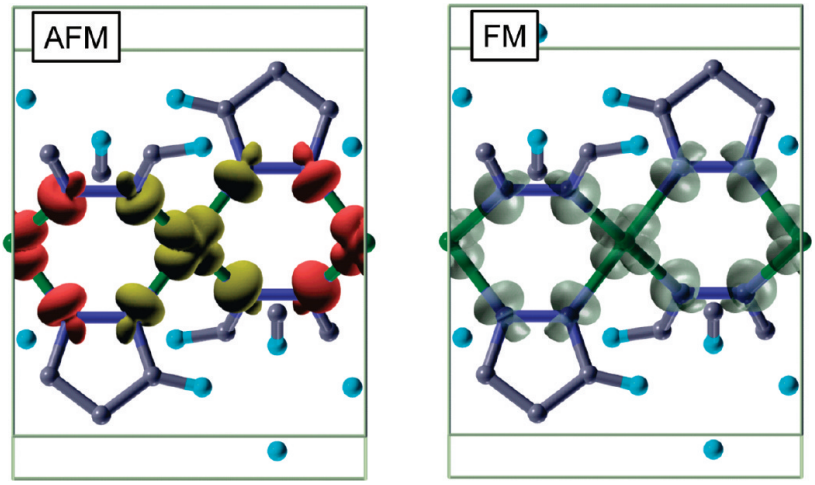

Figure 6. Three dimensional spin density maps for the AFM- (left) and the FM- (right) ordered phases β-$[Cu(pz)_2]_n$, **2** polymers. Displayed isosurfaces are $\pm$ 0.005 e/a_0^3. For the AFM order, yellow/red color surfaces have been used to show regions with positive/negative spin density. For the FM phase, where negative spin density is negligible, a semitransparent surface has been adopted.

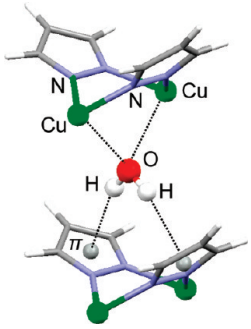

Figure 7. Local coordination of a water molecule to fragments of the nearest polymer chains in the AFM phase. Centroids of pyrazolate rings are displayed as gray balls and are marked by the π symbol.

we focus on an idealized model process where only the rearrangement of the host structure is considered, as described in the following. In Figure 9, where **2** and **3** are viewed down the (010) and the (001) planes, respectively, the close metric relationship between the two structures is evident. If we now consider for **3** the smaller oblique cell (indicated by the solid lines) instead of the more symmetric rectangular one, it turns out that the **2** $\rightarrow$ **3** transformation can be approximately described as a lowering of the monoclinic β angle from $\sim$100° (the value of the anhydrous β phase) to $\sim$70° (the angle corresponding to the hydrated phase). This can be easily done by shifting, in the horizontal direction, adjacent rows of 1D chains, and passing from a dense structure to a porous one, favored by new OH$\cdots\pi$ interactions with the guest molecules. Accordingly, this structure modification is somehow triggered by water molecules initially adsorbed at the surface of the polymer, and finds its driving force in the water sorption enthalpy. Considering that the latter has been computed to be rather small, the energy barrier for changing the polymer structure is probably low. To estimate this barrier, we performed "linear transit" (LT) calculations where the β parameter of the monoclinic structure of **2** was progressively lowered from 105° to 65° in 5° steps. Given the idealized nature of the investigated transformation, and the approximate nature of the LT approach, we avoided time-consuming variable cell calculations carrying out *two* sets of runs, where the cell constants were kept fixed at the theoretical values of **2** and **3**, respectively (see Figure 10).

The total energy curve obtained for the denser structures corresponding to the β-$[Cu(pz)_2]_n$ constants (Figure 10, squares) is characterized by a single, deep minimum at $\beta \sim 100°$, characteristic of the dehydrated compound, and by an inflection point at $\beta \sim 85°$. In contrast to that, two almost equivalent minima are found for the host structure when the constants of the more expanded $[Cu(pz)_2\cdot(H_2O)]_n$ phase are taken. The second minimum is found at $\beta \sim 75°$, which is quite close to the value of the monoclinic cell of $[Cu(pz)_2\cdot(H_2O)]_n$ phase. An estimate of the activation energy involved in the pore opening transformation (100° $\rightarrow$ 75°) is given by the energy of the crossing point between the two curves. The low resulting value (18 kJ/mol) explains the easiness of the water sorption process. On the other hand, the almost vanishing barrier for the backward (75° $\rightarrow$100°) transformation indicates that the solvent-free porous structure is unlikely to be obtained. Overall, our approximated potential energy curve is quite well compatible with the reversibility of the water absorption/desorption process.

Conclusions

Solid microcrystalline coordination polymer β-$[Cu(pz)_2]_n$, **2**, can adsorb, reversibly, one molecule of water generating the hydrated species $[Cu(pz)_2\cdot(H_2O)]_n$, **3**. In this solid state process, the monoclinic structure of **2** changes to the orthorhombic **3** and, being that the structure of **2** is compact, without pores or channels, water accommodates in voids that are "generated" in the adsorption process, a particular case of porosity "without pores".[1] In the present paper we report, besides a new, more profitable synthetic procedure to obtain **2**, an experimental and theoretical study on the magnetic properties of **2** and of the hydrated phase **3**, carried out by magnetic susceptibility measurements, EPR spectroscopy, and DFT-D calculations.

Both theoretical and experimental evidence show that Cu(II) ions are antiferromagnetically coupled with a relatively strong exchange interaction. The additional water molecule in the hydrated phase slightly increases the interaction between copper ions. Inspection of the theoretical spin

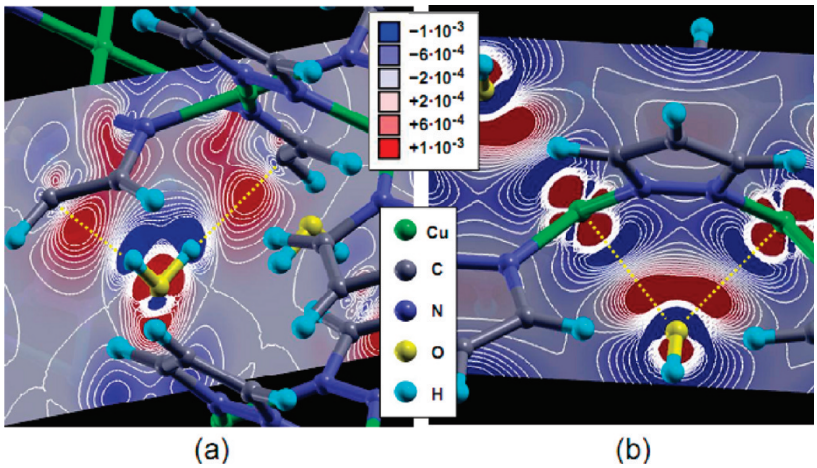

Figure 8. Electron difference density plots referring to the $H_2O-Cu(pz)_2$ interaction (see text). Displayed sections are as follows: (a) a (100) plane bisecting two pyrazolate rings which bridge the same Cu atoms; (b) a (001) plane passing through the Cu atoms of a polymer chain.

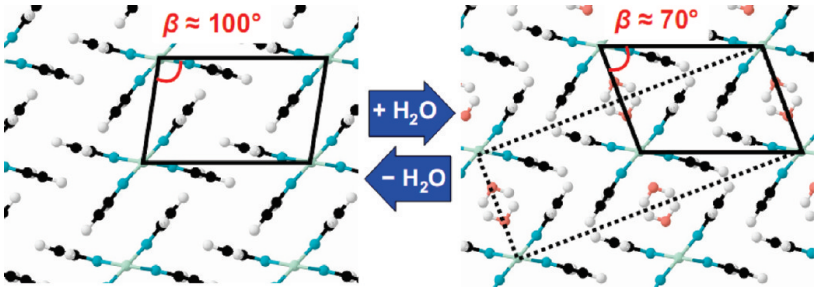

Figure 9. Left: view of the lattice structures of β-$[Cu(pz)_2]_n$, **2**, down the (010) plane. Right: view of the lattice structure of $[Cu(pz)_2 \cdot (H_2O)]_n$, **3**, down the (001) plane. Solid lines show the monoclinic cells. The dashed line on the $[Cu(pz)_2 \cdot (H_2O)]_n$, **3** structure indicates the orthorhombic cell.

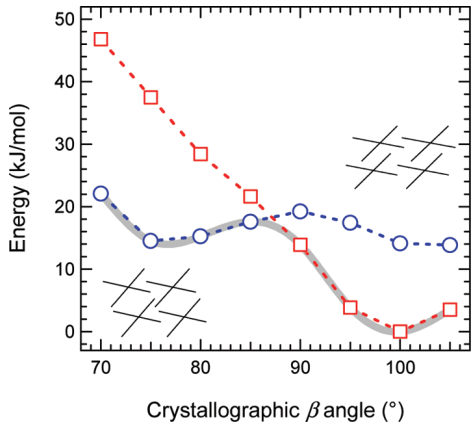

Figure 10. Total energy curves obtained by scanning the monoclinic β angle of the dehydrated phase over a 5°-spaced grid. The cell edges are kept fixed at the theoretical values corresponding to β-$[Cu(pz)_2]_n$, **2** (squares) and to $[Cu(pz)_2 \cdot (H_2O)]_n$, **3**, (circles) experimental structures. Energies are referred to 1 mol of $Cu(pz)_2$. The gray curve indicates the (approximate) path followed by the lattice transformation, schematically shown in the insets.

densities show that the dominant magnetic interactions involve the σ orbitals of the pyrazolate ligands. Furthermore, calculations show that the long $H_2O-Cu(II)$ distances are due to the concurrent interaction between the water protons and the pyrazolate rings of the neighboring chains. The energetics of the pore opening mechanism has also been studied, finding that the energy barriers for the pore formation are indeed low.

Acknowledgment. This work was supported by the Italian PRIN (n. 2006038447) and by FIRB 2003 (n. RBNE033KMA) funds. Computational resources and assistance were provided by the Laboratorio Interdipartimentale di Chimica Computazionale (LICC) at the Department of Chemistry of the University of Padova. Density functional calculations have been performed by using the Quantum-ESPRESSO package.[9] Molecular graphics have been generated by XcrysDen[30] and Mercury.[31]

IC801928B

(30) Kokalj, A. *Comput. Mater. Sci.* **2003**, *28*, 155; Code available from http://www.xcrysden.org/.
(31) Bruno, I. J.; Cole, J. C.; Edgington, P. R.; Kessler, M.; Macrae, C. F.; McCabe, P.; Pearson, J.; Taylor, R. *Acta Crystallogr. B* **2002**, *58*, 389; Available from http://www.ccdc.cam.ac.uk.

Coverage-Dependent Architectures of Iron Phthalocyanine on Ag(110): a Comprehensive STM/DFT Study

M. Casarin,[†,‡,§] M. Di Marino,[†] D. Forrer,[†] M. Sambi,[*,†] F. Sedona,[†] E. Tondello,[†] A. Vittadini,[†,‡,§] V. Barone,[§,∥] and M. Pavone[§,⊥]

Dipartimento di Scienze Chimiche, Università di Padova and CNR-ISTM, Via Marzolo 1, 35131 Padova, Italy, Scuola Normale Superiore di Pisa, Piazza dei Cavalieri 7, 56126, Pisa, Italy, Dipartimento di Chimica "Paolo Corradini", Università di Napoli "Federico II", Via Cintia, 80126 Napoli, Italy, and CR-INSTM "VILLAGE"

Received: May 7, 2009; Revised Manuscript Received: December 23, 2009

Iron(II) phthalocyanine (FePc) self-assembly on Ag(110) has been studied in ultrahigh-vacuum conditions at room temperature by means of scanning tunneling microscopy (STM) and density functional theory (DFT) calculations.

For submonolayer to monolayer coverage, FePc molecules lie parallel to the Ag(110) surface, arranged in rows running along the [001] direction. Two similar yet distinct ordered phases are formed, the c(10 × 4) and p(10 × 4) superstructures. The latter is characterized by two equivalent equilibrium configurations of the constituent FePc units, that interconvert by means of a concerted transformation wherein molecules belonging to adjacent rows collectively rotate in opposite directions around the molecular axis perpendicular to the surface. The FePc adsorption site for both superstructures and the transition mechanism between the two configurations in the p(10 × 4) phase have been inferred from high resolution STM images and rationalized by means of DFT calculations. In the case of multilayer films a (1 ± 4, 4 ∓3) phase is observed, whose stacking geometry has been revealed by STM analysis. The p(10 × 4)/c(10 × 4) → (1 ± 4, 4 ∓3) coverage-dependent transformation is analyzed by DFT calculations, and shown to be driven by the overlayer−substrate interaction. The inclusion of the dispersion contribution to this interaction is found to be essential to correctly reproduce the observed phenomenon.

1. Introduction

The reliable production of highly ordered, self-assembled phthalocyanine (Pc) superstructures on a large variety of solid surfaces represents a major progress toward the fabrication of nanometer-sized electronic devices such as thin-film transistors, solar cells, nonlinear optical devices, and sensors.[1,2] Pcs have been intensively studied in the past because of their interesting electrical and optical properties. The electronic structure of these molecules (e.g., HOMO−LUMO gap, redox potential) can be tuned through the appropriate choice of the coordinated central metal ion and/or by the functionalization of the molecular rim by peripheral substituents,[3−6] thus allowing great versatility in controlling molecular properties. Moreover, the tendency of Pcs to self-organize when deposited on most surfaces makes them especially attractive for all applications that require dense packing and/or highly ordered patterns. For instance, the possibility of obtaining electron donor−acceptor systems that couple macrocyclic dyes with C_{60} is currently explored with the aim of obtaining highly efficient photovoltaic devices and artificial light harvesting systems.[7,8] Almost all of the applications mentioned above require a certain degree of molecular ordering at an interface, and therefore a detailed understanding of the interface formation and of its electronic properties at the molecular level is required.

In this context, iron phthalocyanine (FePc) is particularly fascinating, because on one hand it is known to catalyze the four-electron oxygen reduction reaction to form H_2O from O_2,[9] and is thereby an interesting candidate for a high-performance electrocatalyst in low temperature fuel cell devices alternative to the more expensive platinum-based catalytic routines; on the other hand this molecular system is closely related to the oxygen-binding active center of hemoglobin. In recent years FePc adsorption geometry, self-assembly patterns, electronic and/or magnetic properties have been studied on Au (111),[10,11] on Au(001)-(5 × 20),[12] on TiO_2(110),[13] on InAs(100) and InSb(100),[14] on Cu (111) and NaCl/Cu(111),[15] on Ag(111)[16] and on graphite.[10,17] A recent article reported a low energy electron diffraction (LEED) and X-ray photoelectron spectroscopy (XPS) exploration of the superstructures FePc generates on the Ag(110) surface,[18] although the structural models and surface densities proposed therein should be thoroughly reconsidered on the basis of the STM data discussed in this article.

Here we combine the experimental results of scanning tunneling microscopy (STM) on FePc deposited on Ag(110) in ultrahigh-vacuum (UHV) conditions at room temperature (RT), with a density functional theory (DFT) based analysis of the adsorption geometry, energetics, and self-assembly properties of FePc on the chosen substrate. Two different FePc phases were identified for submonolayer to monolayer (ML) coverages, where all FePc molecules lie flat and directly connected to the substrate, whereas another phase has been observed for multilayer films. The FePc adsorption sites in the sub-ML coverage range on the Ag surface were inferred from high resolution STM images and rationalized by means of DFT calculations. STM also revealed the FePc stacking in multilayer films. The

* Corresponding author. E-mail: mauro.sambi@unipd.it. Fax: +39 049 827 5161.
† Università di Padova.
‡ CNR-ISTM.
§ CR-INSTM "Village".
∥ Scuola Normale Superiore di Pisa.
⊥ Università di Napoli "Federico II".

10.1021/jp904260p

overlayer structural phase transition that is observed at the completion of the first ML is once again explained by DFT results.

2. Experimental Section and Calculations

The experiments were performed by using an Omicron variable temperature (VT) STM system. The instrument consists of an UHV preparation chamber with a base pressure of 2×10^{-10} mbar containing equipment for sample sputtering, thermal annealing, FePc deposition, XPS and LEED, connected to a chamber equipped with the STM stage.

A Ag(110) single crystal (MaTeck GmbH, Germany) was used as the substrate. It was cleaned by repeated cycles of 1 keV Ar^+ sputtering and annealing at 820 K until a clean surface with sufficiently large terraces was obtained, as confirmed by STM imaging.

A few mg of FePc (Alfa Aesar GmbH, 95% purity) were loaded into a PBN crucible connected to the preparation chamber. The FePc sample was carefully degassed while monitoring the UHV system base pressure. The crucible temperature was raised to 540 K in approximately 30 h, held at 540 K for 25 h and increased to 560−570 K for additional 6 h. Depositions were performed with the crucible temperature held at 550 K. The Ag substrate was held at RT throughout the experiments.

One ML of FePc is defined as corresponding to the sample fully covered by a close-packed molecular film displaying a c(10 × 4) superstructure (see below). The resulting surface coverage (θ) corresponds to 1 molecule per $10\sqrt{2}a^2 = 2.38$ nm^2, where a is the Ag lattice parameter along the [001] main azimuth (0.41 nm).

The STM measurements were carried out at RT in constant current mode, using a Pt−Ir tip obtained by electrochemical etching in aqueous solution. STM images were analyzed with the WSxM software.[19] Sample bias values are reported throughout the article.

Density functional theory (DFT) calculations were performed using the Quantum-espresso (QE) package.[20] Wave functions were expanded in a plane-wave basis set and the interaction of valence electrons with ion cores was modeled by ultrasoft pseudopotentials.[21] A kinetic energy cutoff of 27 Ry and a cutoff of 250 Ry on the augmentation charge were adopted. Spin-polarized calculations were run, using the Perdew−Burke−Ernzerhof (PBE) exchange-correlation functional.[22] In geometry optimizations, the convergence thresholds on total energy and residual forces were set to 10^{-4} Ry and 10^{-3} Ry a_0^{-1}, respectively. Because of the large dimension of the examined slab models, Brillouin zones were sampled only at Γ, while a cold smearing[23] was applied to the population functions.

Since van der Waals interactions play a non-negligible role in self-assembled organic structures, we adopted the semiempirical dispersion-corrected DFT (DFT-D) method proposed by Grimme,[24] and recently implemented in the QE package.[25] In principle, the C_6 expansion cannot reproduce the theoretically correct behavior of dispersion forces at metal surfaces.[26] Caciuc et al.[27] recently examined the adsorption energetics of thymine on Cu(110), comparing the DFT-D approach and the more sophisticated nonlocal vdW-DF scheme developed by Dion et al.[28] The two methods were found to be in qualitative, and in most cases quantitative agreement. This prompted us to perform calculations of the adsorbed phases both with the DFT and with the DFT-D approaches. In addition, another set of calculations (hereafter indicated as DFT-D′) was also carried out where the dispersion corrections were introduced only within the molecular overlayer by setting C_6 coefficients of Ag atoms to zero.

The theoretical ($a = 0.414$ nm) lattice constant of Ag was used to build the surface models.

3. Results and Discussion

In the following sections, the results of STM experiments and DFT calculations are presented and discussed. We start with a detailed characterization of the c(10 × 4) and p(10 × 4) superstructures, as observed in STM experiments at the sub-ML regime. Here, the physical origin of STM intermolecular bright features at the Ag surface and the noninterconvertibility of the observed phases are discussed on the basis of computational results. Subsequently, the ordered multilayer phase is described and the transition mechanism from the ML to the multilayer is explored by means of DFT calculations.

3.1. Ordered ML Phases. The large scale STM images reported in Figure 1 show that FePc molecules lie parallel to the surface, as previously reported in many studies of the deposition of metal-free and metal phthalocyanines.[10−17] In particular, two different phases were observed at $\theta < 1$ ML: a c(10 × 4), 2.90 × 1.64 nm^2 superstructure, where all FePc molecules are oriented alike, with the molecular axes bisecting the phenyl rings forming a 45° angle with respect to the [1$\bar{1}$0] direction of the Ag substrate (see Figure 1a−c), and a p(10 × 4), 2.90 × 1.64 nm^2 superstructure that differs from the previous one for the arrangement of FePcs in an alternated sequence of "A" and "B" linear arrays, both aligned along the [001] direction of the Ag substrate. The A and B arrays differ because the FePc molecular axes are rotated with respect to the [1$\bar{1}$0] direction by (30 ± 2)° and (−30 ± 2)° angles, respectively (see Figure 1d−f). The two phases are observed after depositing at RT and persist after extensive annealing (∼2 h) at 473 K. This proves that their adsorption energy is similar, i.e. there is no kinetic stabilization of a metastable phase at RT.

The corresponding LEED pattern (not reported) shows only a c(10 × 4) superstructure. This is attributed to the fact that the A and B arrays in the p(10 × 4) switch into each other (see below), coupled to the fact that the LEED pattern is mainly determined by electron scattering from the heavy Fe atoms, that form a c(10 × 4) subnet in both superstructures.

The registry of FePc molecules with respect to the Ag surface lattice was determined by analyzing several STM images (the one reported in Figure 1c being a typical example) of the sub-ML samples, where the Ag substrate is only partially covered by FePc islands. The Ag surface shows alternating monatomic rows and troughs aligned along the [1$\bar{1}$0] direction. The central Fe atoms belonging to FePc molecules in both sub-ML phases are on top of Ag rows. However, since atomic resolution along the [1$\bar{1}$0] close packed direction of the Ag substrate is lacking, the adsorption site of Fe atoms along the rows cannot be determined from STM images. The apparent height of the central Fe atom relative to the Ag substrate topmost atoms (belonging to the close-packed ridges) is 0.5 ± 0.1 Å in the c(10 × 4) arrangement. Interestingly, STM measurements at the domain boundary between the two superstructures show that the apparent height of Fe atoms is 0.12 ± 0.03 Å lower in the p(10 × 4) phase.

As is clearly visible in the high resolution STM images reported in Figure 1, panels a and d, regular circular bright tunneling features are identifiable among FePc units. These features, as well as the other details of the low coverage phases, are described in the following.

3.1.1. c(10 × 4) Phase. In order to assess the chemisorption site and to understand the nature of the intermolecular tunneling

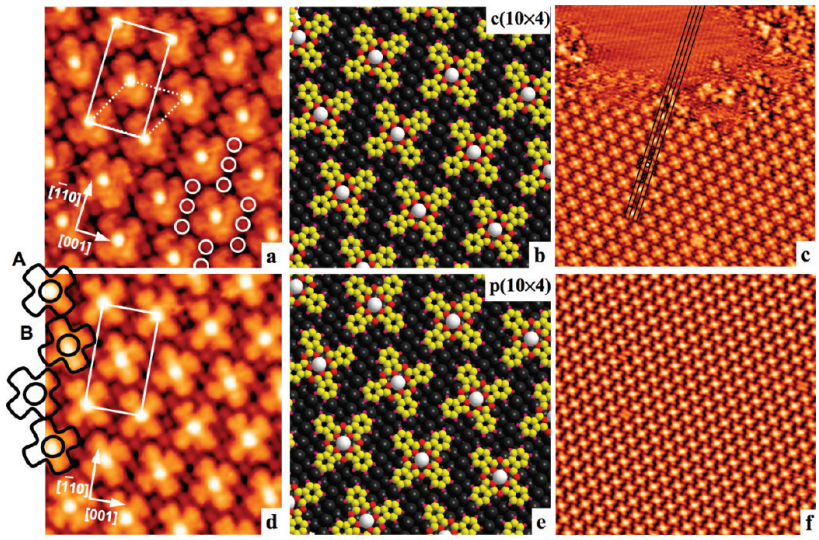

Figure 1. STM images (a. 6.8 × 7.4 nm^2, V_{sample} = +0.037 V, I = 0.05 nA; c. 30 × 30 nm^2, V_{sample} = 0.36 V, I = 0.2 nA; d. 6.8 × 7.4 nm^2, V_{sample} = +0.4 V, I = 0.7 nA; f. 35 × 35 nm^2, V_{sample} = −0.6 V, I = 0.1 nA) of samples with FePc coverage ≤1 ML. Main crystallographic axes and overlayer unit cells are shown. Schemes indicating the alternating rows (A and B) with two different molecular orientations are shown in panel d. Atomic models of the c(10 × 4) and p(10 × 4) phases are shown in panels b and e, respectively. The Ag rows are clearly visible in the upper part of panel c, that is not covered by FePc molecules. The registry between FePc-related STM features and the Ag substrate is evidenced: black lines correspond to the troughs between adjacent Ag close-packed rows aligned with the [1$\bar{1}$0] substrate direction. In panel a, white circles highlight several intermolecular tunneling features.

TABLE 1: Computational Results on the c(10 × 4) 1 ML Phase for the On-Top and Short-Bridge Minima[a]

		DFT	DFT-D′	DFT-D
on top	h_{Fe}	0.285	0.285	0.250
	E_{ads}	–0.86	–0.93	–6.09
short bridge	h_{Fe}	0.288	0.288	0.260
	E_{ads}	–0.68	–0.75	–5.91
	ΔE_{ads}	–0.18	–0.18	–0.18

[a] Adsorption energies (E_{ads}) are given in eV/molecule. Fe atom heights (h_{Fe}) are in nm. ΔE_{ads} = E_{ads} (On Top) - E_{ads} (Short Bridge). Energies are in eV, distances in nm.

features, DFT-D calculations were performed on a model of the c(10 × 4) phase (Figures 1a−c). The metal surface was represented by a periodic slab of 5 atomic layers (Figure 1a, dotted). In tune with previous work,[26] FePc molecules are found to have a triplet ground state. Whereas the magnetization of the FePc molecule is not significantly affected by the intrafilm interactions, it turns out to be approximately halved (from M = 2.0 μ_B to M = 0.9 μ_B) when the film is placed on the support surface.

For each set of calculations, geometry optimizations were carried out by keeping the two bottom layers of the Ag slab frozen to their bulk positions. FePc molecular centers were placed either at on top (OT) or short-bridge (SB) sites. For each configuration the adsorption energy (E_{ads}) was computed as follows:

$$E_{ads} = (E^{tot}_{phase} - E^{tot}_{clean} - nE^{tot}_{FePc})/n$$

where E^{tot}_{clean}, E^{tot}_{FePc}, and E^{tot}_{phase} are the total energies of the clean Ag(110) surface, of the free FePc molecule, and of the supported metal/organic phase, while n indicates the number of FePc molecules in the model (n = 1 in the present case). $E^{tot}_{FePc}$was computed by placing the molecule in a large tetragonal supercell (a = b = 4.5 nm, c = 2.3 nm). The results of the calculations (see Table 1) indicate that the OT site is favored. The relative height h_{Fe} of the Fe atom with respect to the top layer Ag atoms is computed to be 0.285 nm.

As far as the effects of the dispersion corrections are concerned, we find that passing from the DFT to the DFT-D′ approach yields only a limited increase in the adsorption energies, with negligible effects on the geometries. Instead, significant differences are found on passing from the DFT-D′ to the full DFT-D level: the Fe−Ag distance decreases to 0.250 nm, while the adsorption energy increases by 1 order of magnitude. However, in spite of such changes, the energy difference between the two adsorption configurations remains unchanged (Table 1). This suggests that, although the Ag dispersion term largely affects adsorption energies, van der Waals forces play a negligible role in defining the diffusion barriers experienced by the molecule moving on the metal surface. In fact, in a physisorbed state diffusion barriers are expected to be related to purely repulsive interactions between the electron densities of the adsorbate and of the substrate. On the other hand, dispersion interactions at a metal/organic interface can be ascribed to the coupling of density fluctuations in molecules with the metal surface plasmon.[27] Since the latter is a collective phenomenon occurring at the surface, the van der Waals interaction will be fairly independent of the actual adsorption site of the molecule. This behavior seems to be reproduced by the semiempirical dispersion correction term.

Simulated STM images of the on-top configuration, obtained within the Tersoff−Hamann[30] approximation (Figure 2), reproduce fairly well all the features of the experimental images. The Fe atom appears brighter than the Pc ligand, while small bright features can be recognized on the metal regions that are not covered by the molecular overlayer. However, the relative brightness of the features of the Fe atom, of the organic ligand, and of the surface are not well reproduced. This discrepancy can be attributed to the inadequacy of the Tersoff−Hamann approximation and, in particular, to the lack of two ingredients: the tip wave function (the STM tip being simply represented by an s-type orbital) and the conduction rate at the organic−metal interface. In particular, it is known that the TH approximation is able to give qualitatively correct results, but it does not

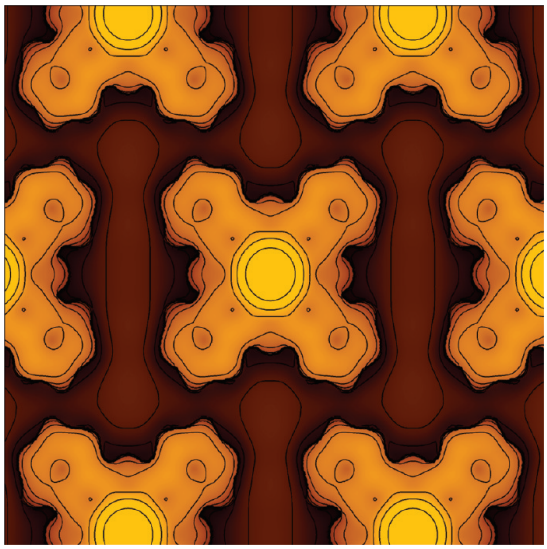

Figure 2. Simulated STM image (3.1 × 3.1 nm^2, $V_{sample} = 0.4$ V) of the c(10 × 4) ML phase of FePc/Ag(110) assuming the on-top adsorption site (see text), obtained within the Tersoff-Hamann approximation on the DFT-D′ optimized superstructure. The contour increment is 0.04 nm.

reproduce quantitatively the corrugation of the surface because of the scarce reliability of the tip model (see, e.g., ref 31 for a review).

The physical origin of the bright intermolecular features at the Ag surface can be inferred by studying the changes in the electronic density of the subsystems as they are put together. Electron density difference ($\Delta\rho$) plots of the equilibrium configurations, shown in Figure 3, reveal that the adsorption of FePc molecules produces a large charge build-up on the metal surface, whose maxima are localized at the bare surface patches between the adsorbates. This evidence can be explained by the so-called "cushion effect",[32] which is a consequence of the Pauli repulsion between the electronic clouds of the metal surface and those of the molecules. This pushes extra electron density at free surface sites, and leads to the shining of the metal surface free area at least for negative biases, where the tunneling current is directed from the surface to the tip. Actually, STM images of the intermolecular patches consist of discrete spots, whereas continuous streaks are apparent in Figure 3, a discrepancy that can be traced back to the already mentioned limits of the TH approximation.

3.1.2. p(10 × 4) Phase. As pointed out above, molecules in the first ML lie flat on the surface. Concerning the molecular orientation, STM images show that the FePc axes bisecting the phenyl rings can be oriented to form an angle of either 45° (c(10 × 4) phase) or ±30° (p(10 × 4) phase) with the [1$\bar{1}$0] direction. As already remarked, the p(10 × 4) phase consists of an alternated sequence of linear arrays made of differently oriented FePcs (labeled "A" and "B" in Figure 1d). Moreover, FePcs in the p(10 × 4) phase can switch between the two orientations: Figure 4 shows a series of time-lapsed STM images of the p(10 × 4) phase, where the FePc molecules change twice their orientation by a collective rotation. On passing from panel a to panel b in Figure 4, "A" rows switch to "B" orientation, whereas in Figure panel c the system turns back to the initial configuration. This kind of collective rotation appears in several images, and seems to be promoted by the presence of point defects in the superstructure. Defects are likely to trigger the rotation of one or more neighboring FePc molecules, that in turn propagate the orientation change to their nearest neighbors, with a domino effect, until the process is finally interrupted by other defects. Interestingly, the intermediate c(10 × 4) arrangement was never observed during the switching process; that is, the two ML phases do not interconvert into each other.

In order to get further insight into the overlayer ordering, calculations on the p(10 × 4) phase were performed. As for the c(10 × 4) phase, the metal surface was modeled by a 5 Ag atomic layer slab where molecules were adsorbed on the top side. A 1.66 nm × 2.93 nm rectangular surface cell was adopted and repeated images along the Z axis were separated by a vacuum space thicker than 1 nm. In order to handle this very large cell, containing 200 Ag atoms as well as two FePc units and a total number of 2600 valence electrons, geometry optimizations were run spin-unpolarized with a kinetic energy cutoff decreased to 24 Ry. Total energies were then recomputed with spin-polarized single point calculations on the previously relaxed geometries with the usual 27 Ry kinetic energy cutoff. No pure DFT calculations were performed for the p(10 × 4) phase.

In agreement with experiments, DFT-D′ calculations predict phenyl rings to form an angle of ±30° with the [1$\bar{1}$0] direction of the Ag surface. Remarkably, the p(10 × 4) and the c(10 × 4) phases are found to differ not only in the molecular orientations, but also in the adsorption site. In fact, for the p(10 × 4) phase, the SB ($E_{ads} = -0.90$ eV/molecule) configuration was found to be favored over the OT site ($E_{ads} = -0.66$ eV/molecule). This explains why, although the stability of the p(10 × 4) and c(10 × 4) arrangements are quite similar, the two phases do not interconvert easily. A further point of agreement with the experiment is that the relative height of Fe in the p(10 × 4) model is $h_{Fe} = 0.254$ nm, i.e., 0.31 Å lower than in the OT-c(10 × 4) model.

The SB-p(10 × 4) model was studied also by means of the full DFT-D scheme. As in DFT-D′ calculations, the relative height of Fe atoms ($h_{Fe} = 0.230$ Å) was found to be lower than in the OT-c(10 × 4) model, whereas the adsorption energy was found to be $E_{ads} = -6.44$ eV per molecule, i.e., 0.34 eV more stable than the c(10 × 4) phase. Such an energy difference would imply the exclusive presence of the p(10 × 4) phase in thermodynamic equilibrium conditions. However, this is in conflict with the experiments, that show that the p(10 × 4) and c(10 × 4) phases coexist even after extensive annealing at 473 K. This failure of the full DFT-D scheme can be attributed to an overestimation of dispersions at the metal surface. Qualitatively, it can be thought to be caused by an overbinding between the ridge Ag atoms and the peripheral phenyl rings of FePc units. In fact, by looking carefully at the OT-c(10 × 4) adsorption geometry, it can be recognized that only one C−C bond per phenyl ring is on-top of an Ag surface atom, even though all phenyls are adsorbed on the surface ridges. In the SB-p(10 × 4) case, only two of the four phenyls are adsorbed on the surface trenches, but the number of Ag-π interactions increases from 4 to 6: one for each phenyl on the trenches and two for each one on the ridges. Since the interaction between phenyl rings and the metal surface is mostly dispersive in nature, the overestimation of the Ag-π interaction is likely to lead to the observed overstabilization of the SB-p(10 × 4) configuration.

So far, we have considered only the experimentally observed phases. We now want to give more insight into the properties of the ML by exploring its potential energy surface (PES). To this end, the (unsupported) overlayer was modeled by a 1.64 nm × 2.9 nm × 1.2 nm orthorhombic model slab containing two FePc units whose molecular planes were placed at the same z coordinate, while the centers of mass were fixed at the (0, 0,

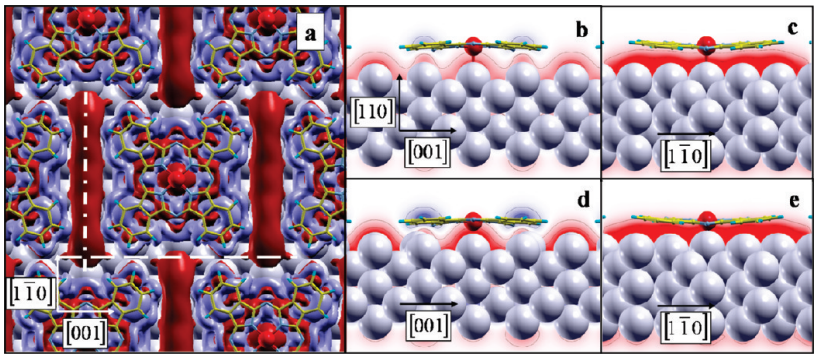

Figure 3. Electron density difference ($\Delta\rho$) plots of the on-top equilibrium configuration (see text). Red/blue isosurfaces indicate regions of charge accumulation/depletion. In panel a, the displayed isosurfaces are $\pm 6.7 \times 10^{-4}$ e/a_0^3. In the side views, $\Delta\rho$ is sectioned as shown by the dashed and dotted-dashed lines in the top view in panel a. Panels a−c refer to the DFT-D′ calculation, whereas panels d and e show the full DFT-D results.

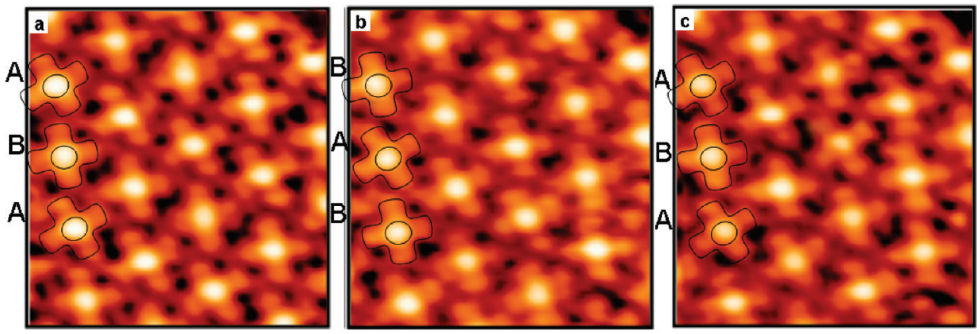

Figure 4. Time-lapsed imaging sequence ($\Delta t \approx 2$ min) of the p(10 × 4) phase (7.7 × 8.4 nm^2, $V_{sample} = -0.40$ V, $I = 0.03$ nA). Black bordered shapes represent FePc molecules and highlight their rotation and the consequent A/B rows switching.

z/*c*) and (0.5, 0.5, *z*/*c*) fractional coordinates, respectively. The slab size corresponds to a p(10 × 4) Ag(110) supercell built on the basis of the experimental Ag fcc lattice constant (0.41 nm), and to a 1.2 nm vacuum space to separate the images repeated along *z*. Since the ground state of the isolated molecule has $S = 1$, the total spin of the system can be either $S = 0$ or 2. Spin interactions are however expected to be small, because the molecular spin density is strongly localized on the Fe atom. Accordingly, tests performed on selected configurations show that total energies computed for the two states differ by less than 1 meV. Thus, only the antiferromagnetic state ($S = 0$) was considered.

The PES exploration was limited to the two-dimensional subspace spanned by the rotations of the rigid molecules around their (vertical) C_4 symmetry axes. The angular coordinates of these rotations are indicated as α and β for the molecules whose centers are fixed at (0, 0) and (0.5, 0.5), respectively. The PES was sampled on a uniform ($\Delta\alpha = \Delta\beta = 5°$) grid of points. Given the symmetry of the system, only the ($0° < \alpha < 45°$, $\alpha < \beta < 90° - \alpha$) subspace was explicitly sampled. For each pair of (α, β) the interaction energy $\Delta E(\alpha,\beta)$ was evaluated from the $E^{tot}_{film}(\alpha,\beta)$ total energy as:

$$\Delta E(\alpha,\beta) = [E^{tot}_{film}(\alpha,\beta) - 2E^{tot}_{FePc}]/2$$

A large portion of the PES ($0° < \alpha, \beta < 90°$) is shown in Figure 5. The PES is rather flat, except for some high-energy configurations, where strong repulsions occur because of the proximity of the phenyl rings belonging to adjacent molecules. We also note the presence of two broad minimum-energy regions (dark blue in Figure 5) covering a large portion of the PES, that are connected by a narrow trough. The experimentally observed rotated conformations lie at these minima. The two configurations are connected by an almost barrierless path (Figure 5, top).

In order to assess the role of the interactions with the support in the switching between the two equilibrium positions of the p(10 × 4) phase, we studied the rotation of a single FePc molecule placed in an orthorhombic supercell with lateral dimensions corresponding to a p(6 × 4) cell. This is computationally more manageable than the true p(10 × 4) cell, yet allowing a sufficiently large intermolecular spacing. In fact, the shortest C−C distance between phenyl rings belonging to adjacent molecules is larger than 6 Å. In practice, we performed a series of constrained optimizations, where the molecule was rotated by steps of 5° and then fully optimized, except for the (*x*, *y*) coordinates of the Fe and one of the N-bridge atoms. The adsorption energies were then computed as the sum of two contributions: the vertical Ag-FePc adhesion energy, computed using the smaller cell, and the intermolecular interactions occurring in the overlayer, that was taken from the PES calculation described above. Given the symmetry of the model, only one-half of the path was actually computed. DFT-D′ calculations predicts an energy barrier $E_b = 0.25$ eV to switch from the (30°, 60°) to the equivalent (60°, 30°) orientation (see Figure 5, top), whereas a 0.62 eV barrier is computed with DFT-D calculations. The larger value computed when dispersions are allowed on Ag can be traced back to the already proposed overestimation of the Ag - phenyl interactions, that are largest in the p(10 × 4) arrangement. A quantitative estimate of the switch frequency starting from the computed single-molecule barrier values has a questionable physical meaning, because the actual process involves the correlated motion of an ensemble of molecules (Figure 4). However, irrespective of the actual barrier height, calculations unquestionably show that (a)

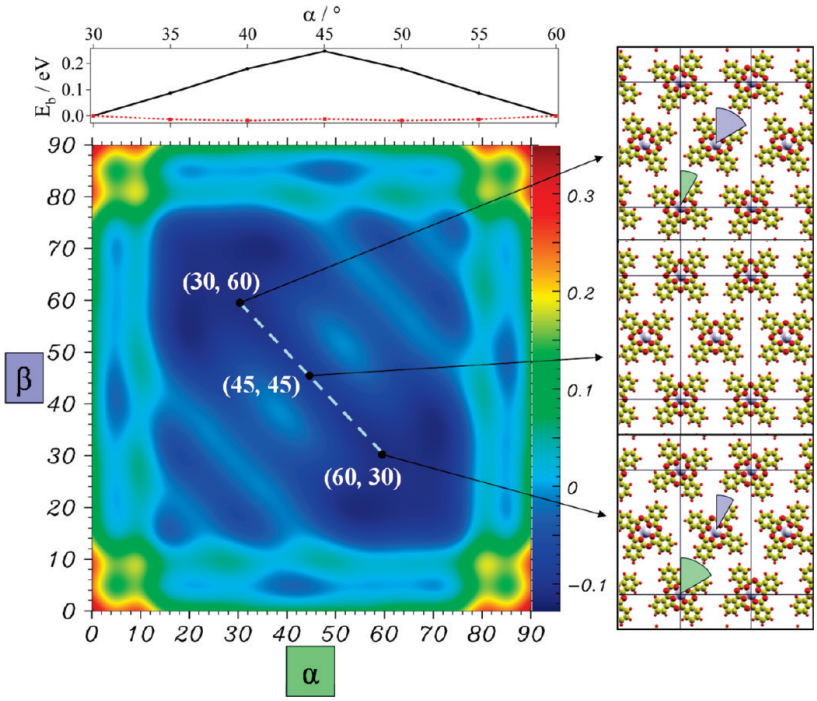

Figure 5. Potential energy surface for the unsupported ML. Energies are in eV/molecule. The dashed line shows the minimum energy path for the transition between the two configurations of the p(10 × 4) phase. The upper panel shows the energy barrier E_b along the path for the unsupported ML (red dashed line) and for the Ag-supported ML in the DFT-D′ framework (black full line), respectively. The geometries of some relevant configurations are sketched in the panels on the right, where also the meaning of the angles α and β is shown. Angles are in degrees.

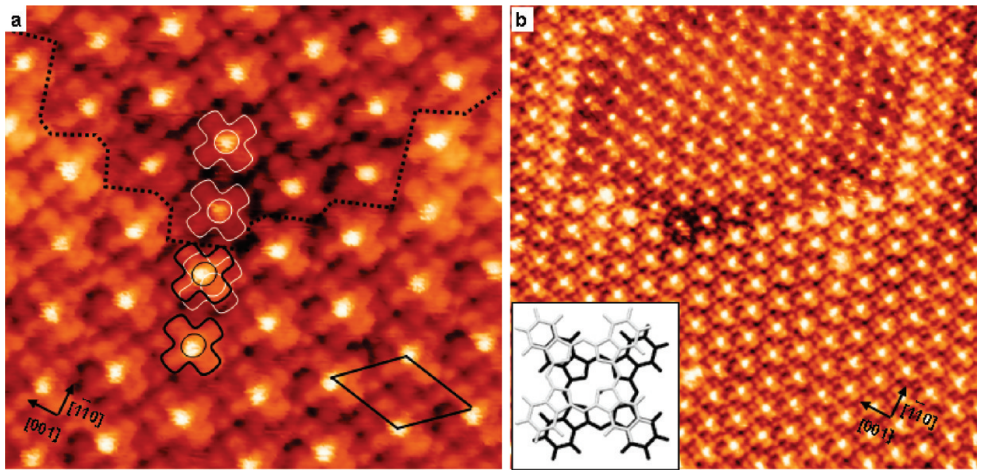

Figure 6. (a) High resolution (12 × 12 nm^2, $V_{sample} = 0.040$ V, $I = 18$ nA) and (b) large scale (30 × 30 nm^2, $V_{sample} = -0.050$ V, $I = 18$ nA) STM images of the (1 4, 4 −3) phase obtained after the deposition of 4 ML of FePc on Ag(110). In panel a, the STM features have been evidenced with black lines for the topmost layer and with white lines for the underlying layer. The (1 4, 4 −3) superstructure unit cell is indicated in panel a. The inset in panel b shows the stacking of FePc units in the multilayer phase.

switching between the two configurations is an activated process, (b) the barrier is set by the vertical overlayer−substrate interactions, and (c) the intermediate position at (45°, 45°), i.e., a c(10 × 4) superstructure where the adsorbate molecules sit at SB sites, corresponds to a saddle point. This last finding explains why the c(10 × 4) pattern is never observed in time-lapsed imaging sequences as the one reported in Figure 4.

3.2. Ordered Multilayer Phase. For θ ranging between 1 and 4 ML, the LEED patterns (not shown) and the STM images (Figure 6) show a (1 ± 4, 4 ∓3) superstructure, whose cell parameters are $a = 1.66$, $b = 1.68$ nm and $\gamma = 127°$. This phase consists of closely spaced molecular wires running along the [5$\bar{5}$ ± 2] azimuths, at an angle α = ± 16° relative to the 1$\bar{1}$0 low index direction of the Ag surface. Only one of the two equivalent domains is shown in Figure 6 and referred to in the following discussion.

In order to determine the stacking of FePc molecules in the multilayer film, the sample was eroded by scanning the STM tip at a high set-point current. The result of the erosion process is shown in Figure 6. It is evident that the underlying layers show the same pattern of the topmost layer. A close-up STM image of the region at the crater's edge (black dotted line) is shown in Figure 6a: molecules belonging to the topmost and to the underlying layer are marked by black and white lines, respectively.

It appears that the FePc molecules lying in two successive layers are not exactly superimposed. This is not surprising, because in their crystals phthalocyanine molecules are usually arranged in columnar stacks whose main alignment direction is not normal to the molecular plane. The angle between the molecular plane and the stacking direction is called the "setting angle". Reducing the setting angle from 90° to smaller values

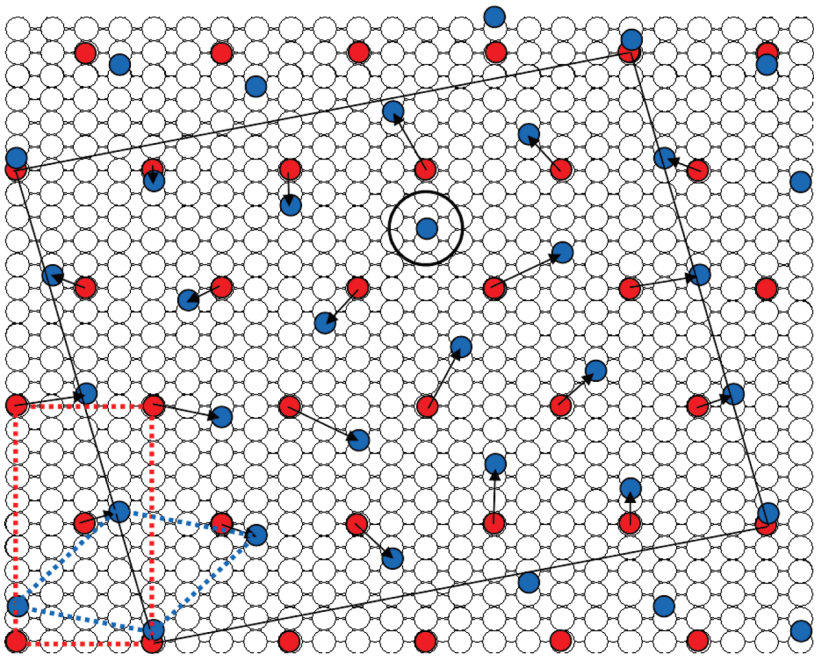

Figure 7. Structural relationship between the c(10 × 4) ML phase and the (1 4, 4 −3) bilayer/multilayer FePc phase on Ag (110). Substrate Ag atoms are represented by white circles. Only the Fe atoms of the FePc molecules (red for c(10 × 4); blue for (1 4, 4 −3)) are shown for clarity. The respective unit cells are highlighted by dashed lines. The (20 4, 5 −18) coincidence cell between the two superstructures (full black line) is shown. Black arrows mark the shortest molecular displacements required to accomplish the structural transition. One extra molecule per coincidence unit cell (circled) is needed to account for the higher density of the thicker phase.

reduces the superposition of neighboring molecules along the stack. If the phthalocyanine molecules are represented as squares, two limiting stacking configurations can be individuated: a partial offset along the square diagonal (as shown in the inset of Figure 6b), the so-called (+)-stacking, or a partial offset along the square side, the (×)-stacking.[33] Prototypical examples of such stacking configurations are the χ and β phases of H_2Pc, the metal-free phthalocyanine,[34] respectively. In Figure 6, (+)-stacking is apparent for a 4 ML-thick FePc film deposited on Ag(110), with a lateral shift of about (2.0 ± 0.5) Å between molecules belonging to two successive layers. Interestingly, the stacking sequence observed for our Ag (110)-supported films differs from that observed in the two most common polymorphs of solid FePc (namely the metastable α-FePc and the stable β-FePc phases) that are both characterized by an (×)-stacking sequence.[33,35] It is indeed known that size effects can alter the relative stability of phthalocyanine polymorphs.[36]

A further interesting issue concerns the transition between the 1 ML c(10 × 4)/p(10 × 4) superstructures and the bilayer/multilayer (1 4, 4 −3) phase and their mutual structural relationship. Data reported in Figure 6 and similar measurements on thinner films show that as soon as the coverage reaches 1 ML, the interfacial c(10 × 4)/p(10 × 4) FePc layer undergoes a reorganization into the new (1 4, 4 −3) superstructure. For coverages between 1 and 2 ML the two arrangements coexist: islands of the 2 ML-thick (1 4, 4 −3) phase are surrounded by 1 ML thick c(10 × 4)/p(10 × 4) areas. The latter are characterized by a lower surface density with respect to the former (0.422 nm^{-2} vs 0.444 nm^{-2}).

The projection of the two superstructures on the substrate surface is sketched in Figure 7, where the c(10 × 4) arrangement is adopted for the ML coverage (with no loss of generality: the p(10 × 4) arrangement is simply offset by half a substrate unit cell along the [1$\bar{1}$0] substrate direction). The coincidence of these structures, evidenced by the large (20 ± 4, 5 ∓18) supercell (solid line) suggests that the c(10 × 4)/p(10 × 4) → (1 4, 4 −3) transition does not involve long-range mass transport, as only small local molecular displacements, shorter than the mean molecular diameter, are needed to accomplish it. This is highlighted in Figure 7, where the shortest displacements necessary and sufficient to complete the transition are marked by black arrows (which are not obviously intended to represent the actual molecular diffusion paths). Since a single molecular layer of the (1 4, 4 −3) phase is denser than the c(10 × 4)/p(10 × 4) ML phases, one extra molecule per coincidence unit cell (circled in Figure 7) is needed to complete the interfacial restructured layer. This can be provided directly by the deposition flux. We remark that the large (20 ± 4, 5 ∓18) coincidence supercell is what one expects to see in LEED patterns if the c(10 × 4)/p(10 × 4) interfacial molecular layer survives beneath the topmost (1 ± 4, 4 ∓3) restructured layer. This has never been observed: the LEED patterns are a sum of the c(10 × 4)/p(10 × 4) and (1 4, 4 −3) superstructures in the 1− 2 ML coverage range, with relative intensities depending on the actual coverage. From the completion of the second ML onward, only the (1 4, 4 −3) spots are observed. In addition, if the coincidence superstructure were present, each individual FePc unit in the II ML (centered on blue spots in Figure 7) within the coincidence cell would have a different stacking relationship with I ML molecules (centered on red spots in Figure 7), i.e. the vertical FePc−FePc stacking would differ from molecule to molecule: some would sit nearly on-top FePc molecules of the I ML, some would be more or less offset from I ML molecules in either nearly (×)- or nearly (+)-stacking (a complex situation also due to the rotation of II ML with respect to the supposedly c(10 × 4) I ML molecules). This would have consequences on molecular heights and on tunneling paths from the STM tip to the substrate, which would show up as a modulation of the STM contrast within the coincidence unit cell. Nothing like this is ever observed at any bias - all molecules in the II and subsequent MLs in the (1 4, 4 −3) phase appear identical within the experimental uncertainty. Moreover, dif-

TABLE 2: Computational Results on 1 ML FePc Arranged in the (1 4, 4 −3) Phase[a]

		DFT	DFT-D′	DFT-D
on top	h_{Fe}	0.306	0.306	0.268
	E_{ads}	–0.51	–0.58	–5.81
short bridge	h_{Fe}	0.278	0.278	0.247
	E_{ads}	–0.70	–0.77	–5.94
	ΔE_{ads}	0.19	0.19	0.14

[a] Adsorption energies (E_{ads}, in eV/molecule) and Fe atom height (h_{Fe}, in Å) are reported. $\Delta E_{ads} = E_{ads}$ (on top) − E_{ads} (short bridge). Energies are in eV and distances in nm.

ferent local stacking geometries would contradict the results of the multilayer erosion down to the interface described above. These observations strongly suggest that the phase transition is not limited to the second ML, but involves the interfacial FePc layer as well. We show below that DFT calculations provide a rationale for the phase transition extending down to the interfacial layer.

The question to be answered thus concerns the reason driving 2 ML islands and thicker films to pack more densely with respect to single ML films. To address this issue, DFT, DFT-D and DFT-D′ calculations were carried out on a single FePc ML using the (1 4, 4 −3) monoclinic supercell shown in Figure 6a. As for the c(10 × 4) phase, the metal substrate was modeled by a periodic Ag slab of 5 atomic layers with a vacuum space larger than 1 nm. Calculations were performed for the FePc ML adsorbed either on an OT or on a SB site; molecules were adsorbed only on one side of the metal slab. Results are summarized in Table 2.

As for the p(10 × 4) case, calculations on the (1 4, 4 −3) ML predict the adsorption site to be the SB, but with a Fe−Ag distance $h_{Fe} = 0.278$ nm, that is fairly similar to that computed for the c(10 × 4) phase and significantly longer than that in the p(10 × 4) one. On the other hand, the role of dispersion is rather similar for the three phases (see results in Table 2). The inclusion of the intralayer dispersion terms (DFT-D′) increases the film stability with negligible effects on the geometry. Furthermore, when the dispersion terms of the metal support are turned on (DFT-D) the Fe−Ag distance decreases to 0.247 nm, while the vertical interaction increases of about 1 order of magnitude. In addition, the relative stability of the two adsorption sites is still not significantly affected by dispersion effects.

It is worth noting that the local adsorption geometry of the (1 4, 4 −3) arrangement closely resembles that of the stable minimum of the p(10 × 4) phase (see above): in both cases the FePc molecule is adsorbed on a SB site and is rotated by the same amount with respect to the main substrate surface directions. On this basis, the choice of the favored local adsorption site appears to be driven by the vertical molecule - substrate interactions, while the phase density (i.e., lateral intermolecular interactions) plays a secondary role in this context.

On passing to multilayer films, also the stacking FePc−FePc interaction plays a role in the energetics of the adsorbed phases. To estimate its importance, further calculations were performed on both the (1 4, 4 −3) and the c(10 × 4) arrangements at the 2 ML regime. In the former case, molecules were arranged as deduced from the STM images (see Figure 6a). An analogous stacking geometry was adopted to develop a model of a hypothetical c(10 × 4) bilayer. This set of calculations was performed using cells similar to those adopted for the adsorbed MLs, where the cell parameter perpendicular to the Ag surface was enlarged to 2.3 nm to keep the vacuum space between repeated slab images larger than 1 nm. Molecules in direct contact with the Ag surface were supposed to keep the same adsorption site as in the 1 ML regime. Since the pure DFT functional yields unphysically weak stacking interactions (lower than 0.06 eV/molecule for all the investigated arrangements), calculations on the adsorbed bilayer were performed by using the DFT-D′ and the DFT-D schemes only.

TABLE 3: Comparison of the Formation Energies (E_{ads}) of the OT-c(10 × 4) and SB-(1 4, 4 −3) Models, of the Relative Film Cohesion Energies (E_{coh}) and of the Surface-Film Adhesion Energies (E_{adh}) and Their Density-Weighted Analogues ε (See Text)[a]

		OT-c(10 × 4)		SB-(1 4, 4 −3)		ΔE ($\Delta\epsilon$)	
		PBE-D′	PBE-D	PBE-D′	PBE-D	PBE-D′	PBE-D
1 ML	E_{ads}	–0.93	–6.09	–0.77	–5.94	–0.16	–0.15
	ε_{form}	–0.38	–2.51	–0.33	–2.58	–0.05	+0.07
	ε_{coh}	–0.04	–0.04	–0.04	–0.04	0.00	0.00
	ε_{adh}	–0.34	–2.47	–0.29	–2.53	–0.05	+0.07
2 ML	$E_{ads}^{II\,ML}$	–1.88	–2.41	–1.84	–2.36	–0.04	–0.05
	$\bar{E}_{ads}$	–1.41	–4.25	–1.30	–4.15	–0.11	–0.10
	ε_{form}	–1.16	–3.50	–1.13	–3.60	–0.03	+0.10
	ε_{coh}	–0.87	–0.87	–0.92	–0.92	+0.05	+0.05
	ε_{adh}	–0.29	–2.63	–0.21	–2.68	–0.08	+0.05

[a] E values are in eV/molecule, whereas ε values are in eV/nm^2. ΔE are defined as $\bar{E}$[c(10 × 4)] − $\bar{E}$[(1 4, 4 −3)], i.e., for $\Delta E > 0$ the denser (1 4, 4 −3) packing is favored. An equivalent definition and meaning holds for $\Delta\varepsilon$.

Adsorption energies of the c(10 × 4) and (1 4, 4 −3) phases, at both 1 and 2 ML regimes, are summarized in Table 3. In the case of 2 ML films, adsorption energies are referred either to the second-layer molecules (E_{ads}^{IIML}) or computed as the average of the adsorption energies of both the MLs ($\bar{E}_{ads}$). Hence, given that each ML contains one molecule in the given slab models

$$E_{ads}^{IIML} = (E_{2ML-phase}^{tot} - E_{1ML-phase}^{tot} - E_{FePc}^{tot})$$

$$\bar{E}_{ads} = (E_{2ML-phase}^{tot} - E_{clean}^{tot} - 2E_{FePc}^{tot})/2$$

Because of the different surface densities of the two superstructures, in order to better compare the stability of different phases, formation energies per unit area have also been computed, defined as

$$\varepsilon_{form} = (E_{phase}^{tot} - E_{clean}^{tot} - nE_{FePc}^{tot})/A$$

where A is the area of the 2D unit cell of the considered phase. The cohesion energy of the unsupported film (ε_{coh}) is computed as

$$\varepsilon_{coh} = (E_{film}^{tot} - nE_{FePc}^{tot})/A$$

wherefrom an estimation of the surface-film adhesion (ε_{adh}) energy is finally obtained as

$$\varepsilon_{adh} = \varepsilon_{form} - \varepsilon_{coh}$$

In discussing the results reported in Table 3, it should be first realized that when two adsorption phases are in competition, one of which is characterized by a higher adsorption energy and a lower density, two regimes are to be expected in the

formation of the overlayer. In the first one, related to the sub-ML coverage, the system will prefer to maximize the interaction of each adsorbate molecule with the surface and with the neighboring molecules, i.e. the overlayer will grow in the phase where the interaction per molecule (viz. E_{ads} of Table 3) is most negative. The second regime is to be expected after the ML coverage is reached. In that case, the favored arrangement is decided by the interplay of two effects: the energy gain relative to each adsorbed molecule, and the number of molecules per unit area that are packed at the interface. Clearly, the interlayer molecule−molecule interaction is weaker of the adsorption energy, and if the latter quantity is similar for the two phases, the densest one will be favored, as it yields the largest total film−substrate interaction. In other words, as soon as the coverage is beyond 1 ML, the phase giving the most negative ε_{form} value is most stable. This will provide a driving force making molecules initially adsorbed in the second layer move into the first layer. Now, looking to the data of Table 3, we find that when the DFT-D′ approach is used, both ΔE_{ads} and $\Delta\varepsilon_{form}$ are always negative, not only in the 1 ML, but also in the 2 ML films. It thus appears that, in order to describe the c(10 × 4) → (1 4, 4 −3) phase transition experimentally observed for multilayer films, the dispersion contribution to the surface-film interaction energy term is needed. Accordingly, when the DFT-D calculations are considered, we find that for 1 ML films $\Delta E_{ads} < 0$ while $\Delta\varepsilon_{form} > 0$. Therefore, on the basis of the above qualitative discussion, the c(10 × 4) phase is preferred at low coverage, whereas the (1 4, 4 −3) one is preferred as soon as the coverage becomes higher than 1 ML, in agreement with the experimental observations. Furthermore, our results show that there is no difference in the cohesion energies between the two phases, so that the preference for the densest phase is indeed to be attributed to the optimization of the film-surface interaction. In other words, there would be no energy gain in restructuring from c(10 × 4) to (1 4, 4 −3) in a layer not in direct contact with the substrate: restructuring, if it is ever to occur, is bound to occur precisely at the interface with the metal, since only there it causes an energy gain in the form of an increase in adhesion energy.

For 2 ML films, the results essentially confirm those for 1 ML, with the dense phase being less favored as far as adsorption energies are concerned, and more favored as far as formation energies are concerned. A question to be answered is why the c(10 × 4) is never observed for multilayer films, even though the topmost layer is most likely incomplete. A calculation on model systems with two adsorbate layers in different arrangements is not feasible (they would require using the coincidence cell of Figure 7). However, it seems reasonable that, once the first ML is converted to the (1 4, 4 −3) arrangement, this is able to act as a template for the growing top layer.

As far as the structure of 2 ML films is concerned, the optimized distance between the two molecular layers is 0.32 nm in both phases. Moreover, no remarkable distance differences were found as the unsupported bilayer was adsorbed on the substrate. In addition, the height with respect to the substrate of the molecular layer in direct contact with Ag was found to be almost equal to that of the adsorbed ML.

4. Conclusion

A comprehensive study of FePc self-assembly patterns on Ag(110) in UHV conditions at RT has been carried out by means of high resolution STM and with the aid of DFT theoretical calculations including semiempirical dispersion interactions (DFT-D).

Two closely related phases have been identified in the sub-ML to ML coverage range, namely the p(10 × 4) and c(10 × 4) superstructures that are characterized by different local adsorption sites. Real time STM imaging shows that in the p(10 × 4) phase FePc molecule switch between two equilibrium orientations through a concerted set of alternated clockwise and counterclockwise in-plane molecular rotations, which seem to be promoted by the presence of molecular point defects in the overlayer. The existence of two local minima in the computed PES of the p(10 × 4) ML, corresponding to the observed rotated configurations, has been shown to be determined by intralayer interactions, while the energy barrier between the minima is set up by the interaction of the overlayer with the substrate.

A phase transition from the p(10 × 4)/c(10 × 4) phases to a (1 ± 4, 4 ∓3) superstructure is observed at RT as soon as the thickness of the overlayer exceeds the single ML. High resolution STM has allowed us to determine the vertical molecular stacking in the FePc multilayer, that is shown to differ from the arrangement found in main bulk FePc crystalline phases. We have shown that only calculations where the dispersion contribution to the film-surface interaction is accounted for are able to reproduce this transition. Calculations indicate that the transition to the dense (1 ± 4, 4 ∓3) structure is not driven by the strengthening of the interadsorbate interactions, but rather by the stronger adhesion energy resulting from the closer packing.

Acknowledgment. This work has been partially supported by Fondazione CARIPARO (Progetti di Eccellenza 2006 - "Multi-layer optical devices based on inorganic and hybrid materials by innovative synthetic strategies") and by the University of Padova (Progetti Strategici 2008 - HELIOS). Computational resources and assistance were provided by the "Laboratorio Interdipartimentale di Chimica Computazionale" (LICC) at the Department of Chemistry of the University of Padova, within the large scale computer facilities of the CR-INSTM "VILLAGE" network (http://village.unina.it), and by CINECA (Bologna, Italy). Molecular graphics has been generated by XCrysDen.[37]

References and Notes

(1) Maitrot, M.; Guillaud, G.; Boudjema, B.; Andre, J. J.; Strzelecka, H.; Simon, J.; Even, R. *Chem. Phys. Lett.* **1987**, *133*, 59.
(2) Temofonte, T.; Schoch, K. F. *J. Appl. Phys.* **1989**, *65*, 1350.
(3) Miyake, K.; Hori, Y.; Ikeda, T.; Asakawa, M.; Shimizu, T.; Sasaki, S. *Langmuir* **2008**, *24*, 4708.
(4) Oison, V.; Koudia, M.; Abel, M.; Porte, L. *Phys. Rev. B* **2007**, *75*, 035428.
(5) Kong, X. H.; Deng, K.; Yang, Y. L.; Zeng, Q. D.; Wang, C. *J. Phys. Chem. C* **2007**, *111*, 17382.
(6) Smolenyak, P.; Peterson, R.; Nebesny, K.; Torker, M.; O'Brien, D. F.; Armstrong, N. R. *J. Am. Chem. Soc.* **1999**, *121*, 8628.
(7) Gust, D.; Moore, T. A.; Moore, A. L. *Acc. Chem. Res.* **2001**, *34*, 40.
(8) Balzani, V.; Credi, A.; Venturi, M. *ChemSusChem* **2008**, *1*, 26.
(9) Zagal, J. H. *Coord. Chem. Rev.* **1992**, *119*, 89.
(10) Walzer, K.; Hietschold, M. *Surf. Sci.* **2001**, *471*, 1.
(11) (a) Lu, X.; Hipps, K. W. *J. Phys. Chem. B* **1997**, *101*, 5391. (b) Cheng, Z. H.; Gao, L.; Deng, Z. T.; Jiang, N.; Liu, Q.; Shi, D. X.; Du, S. X.; Guo, H. M.; Gao, H.-J. *J. Phys. Chem. C* **2007**, *111*, 9240. (c) Gao, L.; Ji, W.; Hu, Y. B.; Cheng, Z. H.; Deng, Z. T.; Liu, Q.; Jiang, N.; Lin, X.; Guo, W.; Du, S. X.; Hofer, W. A.; Xie, X. C.; Gao, H.-J. *Phys. Rev. Lett.* **2007**, *99*, 106402.
(12) Molodtsova, O. V.; Knupfer, M.; Ossipyan, Yu. A.; Aristov, V. Yu. *J. Appl. Phys.* **2008**, *104*, 083704.
(13) Palmgren, P.; Priya, B. R.; Niraj, N. P. P.; Göthelid, M. *Sol. Energy Mater. Sol. Cells* **2006**, *90*, 3602.
(14) Palmgren, P.; Priya, B. R.; Niraj, N. P. P.; Göthelid, M. *J. Phys.: Condens. Matter* **2006**, *18*, 10707.
(15) Scarfato, A.; Chang, S.; Kuck, S.; Brede, J.; Hoffmann, G.; Wiesendanger, R. *Surf. Sci.* **2008**, *602*, 677.

(16) Manandhar, K.; Park, K. T.; Ma, S.; Hrbek, J. *Surf. Sci.* **2009**, *603*, 636.

(17) Åhlund, J.; Schnadt, J.; Nilson, K.; Göthelid, E.; Schiessling, J.; Besembacher, F.; Mårtensson, N.; Puglia, C. *Surf. Sci.* **2007**, *601*, 3661.

(18) Palmgren, P.; Angot, T.; Nlebedim, C. I.; Layet, J.-M.; Le Lay, G.; Göthelid, M. *J. Chem. Phys.* **2008**, *128*, 064702.

(19) Horcas, I.; Fernandez, R.; Gomez-Rodriguez, J. M.; Colchero, J.; Gomez-Herrero, J.; Baro, A. M. *Rev. Sci. Instrum.* **2007**, *78*, 013705.

(20) Giannozzi, P.; Baroni, S.; Bonini, N.; Calandra, M.; Car, R.; Cavazzoni, C.; Ceresoli, D.; Chiarotti, G. L.; Cococcioni, M.; Dabo, I.; Dal Corso, A.; Fabris, S.; Fratesi, G.; de Gironcoli, S.; Gebauer, R.; Gerstmann, U.; Gougoussis, C.; Kokalj, A.; Lazzeri, M.; Martin-Samos, L.; Marzari, N.; Mauri, F.; Mazzarello, R.; Paolini, S.; Pasquarello, A.; Paulatto, L.; Sbraccia, C.; Scandolo, S.; Sclauzero, G.; Seitsonen, A. P.; Smogunov, A.; Umari, P.; Wentzcovitch, R. M. *J.Phys.: Condens. Matter* **2009**, *21*, 395502.

(21) Vanderbilt, D. *Phys. Rev. B* **1990**, *41*, 7892.

(22) Perdew, J. P.; Burke, K.; Ernzerhof, M. *Phys. Rev. Lett.* **1996**, *77*, 3865.

(23) Marzari, N.; Vanderbilt, D.; De Vita, A.; Payne, M. C. *Phys. Rev. Lett.* **1999**, *82*, 3296.

(24) Grimme, S. *J. Comput. Chem.* **2006**, *27*, 1787.

(25) Barone, V.; Casarin, M.; Forrer, D.; Pavone, M.; Sambi, M.; Vittadini, A. *J. Comput. Chem.* **2009**, *30*, 934.

(26) Dobson, J. F.; Wang, J.; Dinte, B. P.; McLennan, K.; Le, H. M. *Int. J. Quantum Chem.* **2005**, *101*, 579.

(27) Caciuc, V.; Atodirsei, N.; Lazić, P.; Morikawa, Y.; Blügel, S.; eprint arXiv.0811.3088.

(28) Dion, M.; Rydberg, H.; Schröder, E.; Langreth, D. C.; Lundqvist, B. I. *Phys. Rev. Lett.* **2004**, *92*, 246401.

(29) (a) Liao, M.-S.; Scheiner, S. *J. Chem. Phys.* **2001**, *114*, 9780. (b) Liao, M.-S.; Watts, J. D.; Scheiner, S. *J. Phys. Chem. A* **2005**, *109*, 7988. (c) Liao, M.-S.; Kar, T.; Gorun, S. M.; Scheiner, S. *Inorg. Chem.* **2004**, *43*, 7151.

(30) Tersoff, J.; Hamann, D. R. *Phys. Rev. Lett.* **1983**, *50*, 1998.

(31) Hofer, W. A. *Prog. Surf. Sci.* **2003**, *71*, 147.

(32) Witte, G.; Lukas, S.; Bagus, P. S.; Wöll, C. *Appl. Phys. Lett.* **2005**, *87*, 263502.

(33) Hoshino, A.; Takenaka, Y.; Miyaji, H. *Acta Crystallogr.* **2003**, *B59*, 393.

(34) Zugenmaier, P.; Bluhm, T. L.; Deslandes, Y.; Orts, W. J.; Hamer, G. K. *J. Mater. Sci.* **1997**, *32*, 5561.

(35) Miller, C. W.; Sharoni, A.; Liu, G.; Colesniuc, C. N.; Fruhberger, B.; Schuller, K. *Phys. Rev. B* **2005**, *72*, 104113.

(36) Iwatsu, F. *J. Phys. Chem.* **1988**, *92*, 1678.

(37) Kokalj, A. *Comput. Mater. Sci.* **2003**, *28*, 155 Code available from http://www.xcrysden.org/.

JP904260P